Acylindrical and aspherical microscale mirrors : principles, technology and applications to miniature optical benches

Yasser Mohammed Sabry Gad Aboelmagd

UNIVERSITÉ PARIS-EST

Ecole Doctorale

Mathématiques, Sciences de l'Information et de la Communication (MSTIC)

THÈSE

pour obtenir le grade de

Docteur de l'Université Paris-Est

Spécialité : Electronique, Optronique et Systèmes

Présentée et soutenue publiquement par

Yasser Mohammed Sabry Gad Aboelmagd

Le 24 Octobre 2013

Miroirs Acylindriques et Asphériques à Echelle Microscopique : Principes, Technologie et Applications aux Bancs Optiques Miniatures

Acylindrical and Aspherical Microscale Mirrors: Principles, Technology and Applications to Miniature Optical Benches

Directeur de thèse

Professeur Tarik BOUROUINA

Jury

Hans-Peter HERZIG, Professeur, EPFL, Switzerland	Rapporteur
Anne-Marie HAGHIRI, Directeur de Recherches CNRS, LPN, Marcoussis	Rapporteur
Diaa KHALIL, Professeur, Université Ain-Shams, EGYPTE	Examinateur
Yamin LEPRINCE , Professeur, LPMDI, UPE, UPEMLV	Examinateur
Bassam SAADANY, Head of MEMS Division, Si Ware Systems	Examinateur
Tarik BOUROUINA, Professeur, UPE, ESIEE Paris	Examinateur

ACKNOWLEDGMENTS

All praise is due to Allah, Most Gracious and Most Merciful, Whose bounties are ever dominating throughout my life.

First, I would like to express my deep gratitude to my supervisor, Professor Tarik Bourouina, for his support, guidance, patience and encouragement through the way of accomplishing my thesis. He is not only an outstanding advisor in research but also in daily life aspects. His humor sense, generosity and cleverness are really impressive. I am very proud to be graduated under his supervision.

Many thanks and great appreciation goes to Professor Diaa Khalil. I learned so many aspects from his solid background in optics, optimism and innovation. I consider myself lucky to have the chance to work closely to Professor Diaa during my thesis.

I wish to thank Si-Ware Systems for giving the opportunity and the financial support to conduct this study. Thanks to Doctor Bassam Saadany who has a great share in giving my thesis the industrial sense, thanks to Bassem Mortada for giving a hand in layout editing and thanks to all the MEMS team members for providing such an inspiring environment.

I am grateful to Professor Mahmoud Hanafe and Doctor Mohamed Shalaby for allowing part of the measurements conducted in this thesis to be carried out in the laser laboratory in the faculty of Engineering, Ain Shams University.

Thanks to the SMM team at ESIEE-Paris for providing help throughout the microfabrication work in this thesis. I am grateful to Bruno Mercier for his kindness, support and giving my first lessons in the clean room. I would like to thank Fredric Marty for his useful discussion and help on the deep etching process. I am also grateful to my colleague Noha Gaber who didn't hesitate in offering her help at any time.

I would never forget to thank my wife for her unrivaled encouragement, sacrifice, care and love; and for taking care of our son Malek who made our life more delightful. I am indebted to my parents who spent their lives raising me up and guiding me through my whole life. I pray to Allah I will always be a good faithful son to them.

Yasser Sabry
Cairo, Egypt
12 January, 2014

RÉSUMÉ SUBSTANTIEL

La photonique sur silicium est un pan de la science et de la technologie qui porte sur la manipulation de la lumière dans une puce de silicium et d'y effectuer une ou plusieurs fonctionnalités en vue d'applications. En outre, l'intégration sur la puce, de micro-actionneurs est très commode car les forces minuscules, de l'ordre du micronewton, sont suffisantes pour contrôler le mouvement de micro-composants optiques, ce qui donne ainsi des degrés de libertés supplémentaire pour le contrôle de la lumière. Cette approche a donné naissance au domaine des microsystèmes opto-électro-mécaniques, ou simplement MEMS optiques. En termes d'applications, ce sont les marchés de l'affichage et des télécommunications qui ont été les premiers moteurs des activités de recherche dans ce domaine. L'effondrement du marché des télécommunications suite à l'éclatement de la bulle internet au début des années 2000 a été suivi de l'apparition de nouvelles orientations de recherche plus intéressantes du point de vue scientifique. Elles portent sur l'instrumentation miniaturisée en biologie, chimie, physique et sciences des matériaux. Les applications les plus récentes incluent des nouvelles techniques d'imagerie médicale basées sur la tomographie à cohérence optique, des sources laser accordables en longueur d'onde, des microsystèmes d'analyse biochimique sur puce de type 'lab-on-chip', des spectromètres portables pour l'analyse de la composition de fluides incluant l'air et l'eau. Ceci a également donné un nouvel essor à

des domaines scientifiques transverses tels que l'optofluidique et l'opto-mécanique. Toutes ces avancées ont révélé des défis technologiques à lever et a soulevé des opportunités pour le progrès de la science.

Cette thèse a pour objectif ultime est d'accroître notre compréhension de la réflexion de la lumière sur des surfaces optiques micro-courbes, en particulier lorsque les dimensions physiques des surfaces sont comparables aux paramètres dimensionnels d'un faisceau optique Gaussien, typique des faisceaux issus d'une fibre optique ou d'un micro-laser. A cet effet, une étude théorique doit être menée et doit être confrontée à une étude expérimentale. Toutefois, la réalisation des micro-miroirs à concavité contrôlée n'étant pas chose aisée, un premier jalon de cette thèse a consisté à atteindre les avancées technologiques nécessaires à la réalisation de tels micro-miroirs en vue de leur caractérisation expérimentale. Une motivation importante du choix de ce sujet est son potentiel applicatif à la réalisation de micro-bancs optiques sur puce silicium, de sorte à augmenter les capacités de manipulation de lumière de façon intégrée dans un espace ultra-compact. A titre d'illustration des possibilités de la nouvelle micro-instrumentation optique que nous proposons, nous avons conçu et réalisé un microsystème de balayage spatial à grand angle d'un faisceau laser dont le spot optique ne se déforme pas tout au long de l'opération de balayage, ce qui en fait, entre autres, la pièce maitresse d'un système d'imagerie médicale par tomographie à cohérence optique

Tout d'abord, un procédé de fabrication a été développé pour la réalisation de micro-miroirs incurvés et de micro-bancs optiques. Le procédé est basé sur la technologie de gravure ionique réactive profonde et n'implique pas l'utilisation de longues étapes de gravure anisotropes alcalines. Par conséquent, les profils de surfaces arbitraires, y

compris les surfaces courbes, pourraient en principe être fabriqués sans restriction sur l'orientation de la surface. La gravure de profondeurs plus grandes que 300 μm a été démontrée, comme indiqué dans la Fig. 1, avec une verticalité des flancs meilleure que 0,1 degré et une rugosité de surface inférieure à 60 nm. La réflectivité optique des micro-miroirs micro-gravés avec un revêtement en aluminium a été mesurée à la longueur d'onde optique de 1550 nm et s'est révélée être supérieure à 90%. Cela indique une surface optique de haute qualité. Le procédé a été également positivement évalué en termes de verticalité pour différentes largeurs de tranchées et d'ouvertures carrées, ce qui permet la co-intégration, sur une même puce de silicium, d'actionneurs MEMS avec les surfaces optiques.

La réalisation d'un interféromètre de Michelson miniaturisé intégré monolithique à balayage a été démontrée sur puce silicium, en utilisant le procédé mis au point comme indiqué dans la Fig. 2. L'interféromètre a été réalisé sur des plaques de type SOI (*Silicon-On-Insulator*) avec des hauteurs de la couche utile de 90 μm et de 200 μm, dans le but de l'évaluation des améliorations apportées sur les performances Des fibres optiques multimodes avec des diamètres de base de 62,5 μm et de 200 μm ont été utilisées pour délivrer à la puce de silicium un signal optique en lumière blanche. Les interférogrammes obtenus ont été mesurés et comparés. L'interférogramme mesuré dans le cas d'une hauteur de 200 μm est représenté sur la Fig. 3. Le signal optique détecté a été comparé à celui qui a été obtenu avec une hauteur de 90 μm ; une amélioration d'environ 12 dB a été constatée, ce qui constitue une amélioration significative de la performance des instruments miniaturisés, grâce au micro-banc optique développé.

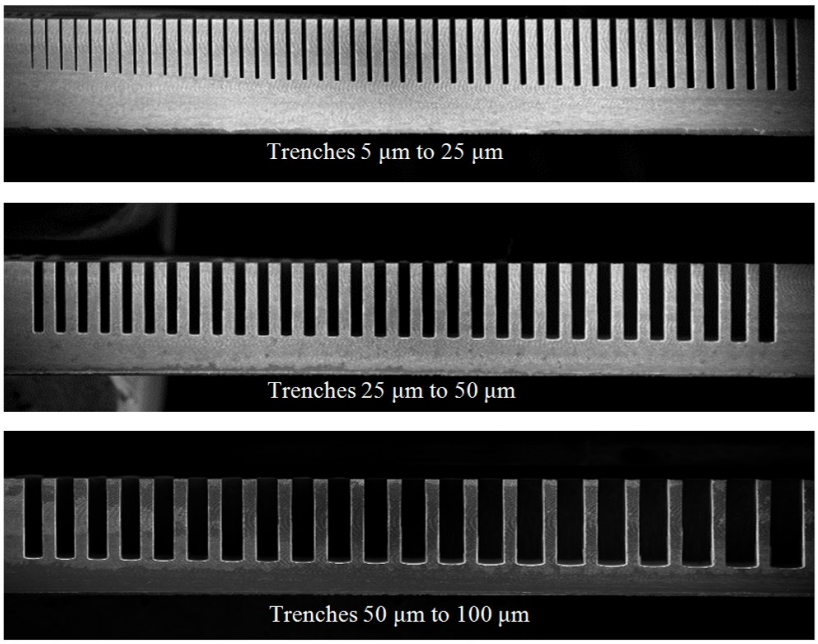

Fig. 1. Images au Microscope électronique à balayage (MEB) de tranchées profondes gravées avec un excellent profil au vu de l'angle qui décrit la verticalité des flancs.

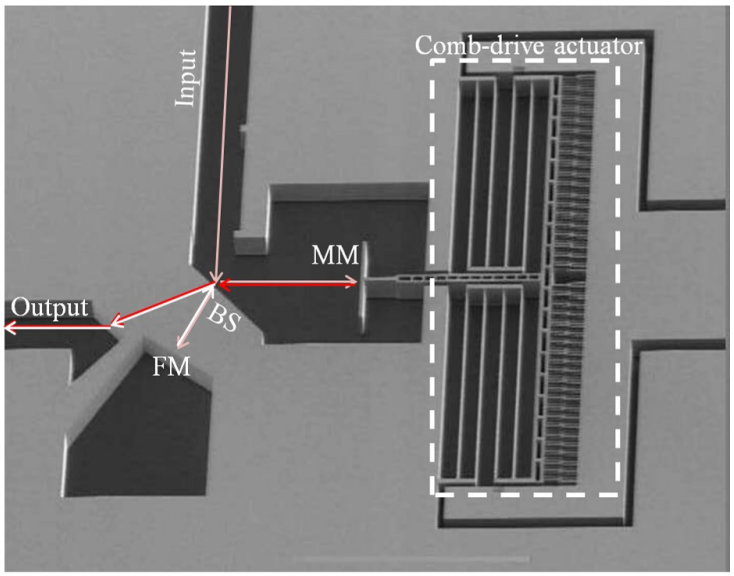

Fig. 2. Image MEB d'un interféromètre de Michelson monolithique, dans laquelle BS désigne un diviseur de faisceau, FM un miroir fixe et MM un miroir mobile.

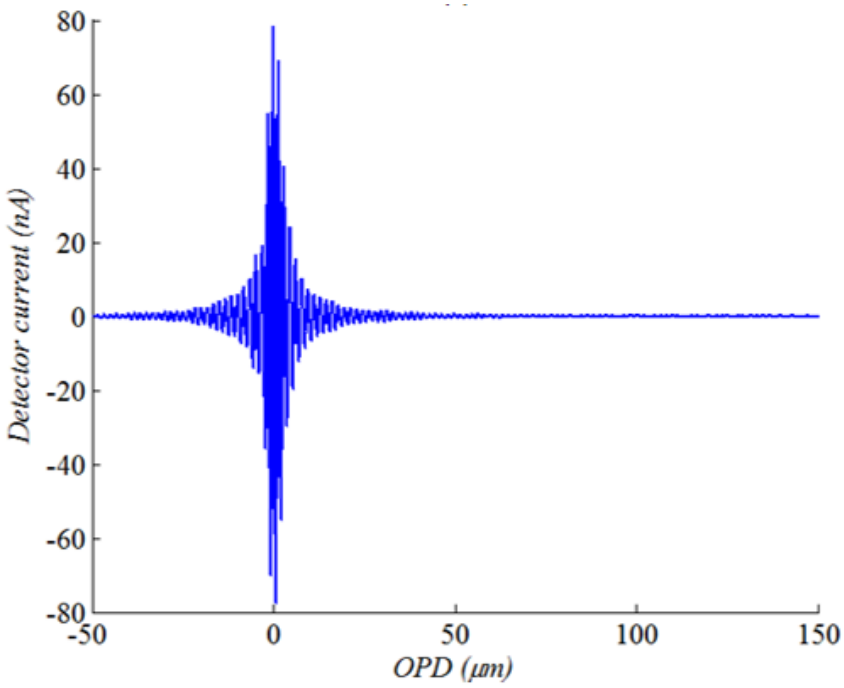

Fig. 3. Interférogramme en lumière blanche mesuré à l'aide de l'interféromètre fabriqué avec 200 µm de profondeur.

Une nouvelle architecture de microscanners optiques avec propagation dans le plan a été présentée comme le montre la Fig. 4. L'architecture est basée sur un mouvement de translation d'un micro-miroir incurvé par rapport à l'axe optique du faisceau incident. L'axe du faisceau optique étant parallèle au substrat, le microscanner a pu être réalisé sous forme d'un banc micro-optique. Des surfaces acylindriques de forme optimisée ont été conçues et réalisées pour maintenir les propriétés du faisceau optique insensibles au balayage. Contrairement aux méthodes courantes de génération de surfaces asphériques, la méthodologie de conception est basée sur la formulation d'une équation différentielle à partir des conditions appropriées puis à la résolution de la dite équation.

Deux types de surfaces ont été produites, selon que le mouvement de translation est d'un degré ou de deux degrés de liberté de mouvement.

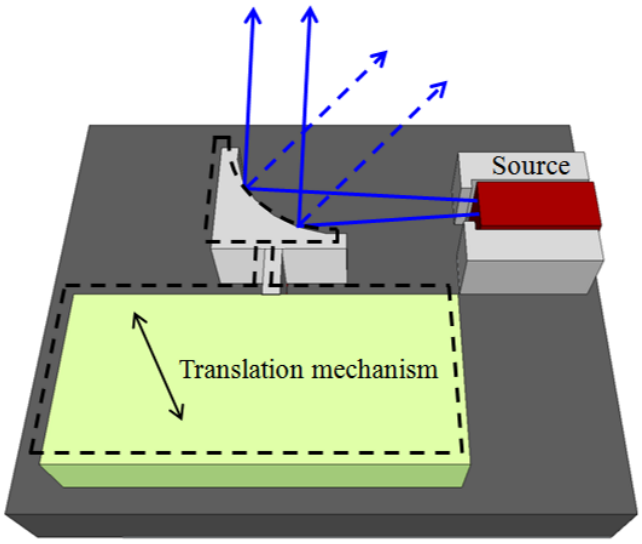

Fig. 4. Schéma de l'architecture du microscanner intégré, dans lequel un balayage à grand angle peut être facilement obtenu. Les dimensions du miroir peuvent être contrôlées indépendamment des composants mécaniques du système et de la source, ainsi que d'autres composants micro-optiques qui peuvent être intégrés sur la puce.

La fabrication et l'intégration monolithique d'une surface incurvée destinée à un actionneur électrostatique en forme de peignes interdigités a été effectuée sur la base de la technologie de gravure ionique réactive profonde sur une plaquette SOI comme montré en Fig. 5. Le peigne d'entraînement est dédoublé et fonctionne en *push-pull*, afin de produire de grands déplacements. Au centre du dispositif, une suspension doublement pliée est utilisée pour éviter la non-linéarité lors des flexions fortes. Un miroir acylindrique est fixé au peigne d'entrainement et une gorge est gravée en regard du

miroir, destinée à accueillir la fibre optique, avec une inclinaison par rapport à la direction de mouvement du miroir. La zone métallisée autour du miroir peut être observée par sa luminosité plus élevée dans la Fig. 5.

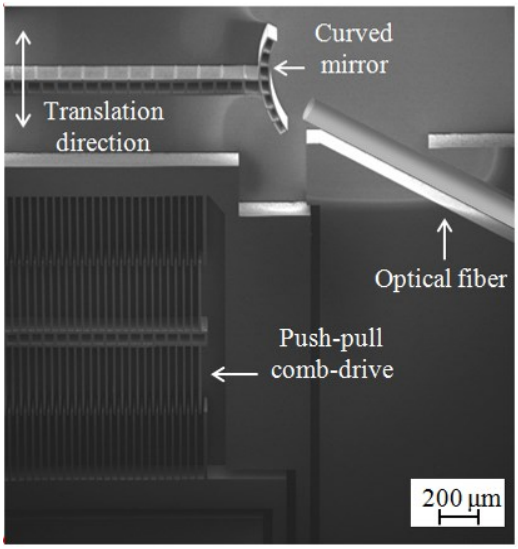

Fig. 5. Image MEB du microscanner fabriqué avec un zoom sur les doigts de l'actionneur à peignes relié au miroir incurvé et une fibre optique insérée dans le sillon gravé, qui est auto-aligné avec le miroir.

La fibre optique, insérée dans la rainure, se comporte comme une source optique dont la sortie est un faisceau Gaussien. Le faisceau est incident sur le miroir de façon désaxée et l'angle de balayage du faisceau de sortie peut être contrôléé par l'application d'une tension électrique sur les électrodes de l'actionneur à peignes. La fréquence de résonance du système est d'environ 329 Hz et il a été démontré expérimentalement que l'angle de déflexion optique pouvait atteindre jusqu'à 120° degrés, ce qui positionne le module de balayage bien au-delà des performances attendues. L'uniformité de la taille du spot

optique en fonction de l'angle de déviation a été mesurée comme indiqué dans la Fig. 6. La plage de variation de taille du spot variation à travers toute la gamme de balayage angulaire est inférieure à 5%, en bon accord avec les prévisions théoriques de la conception des micro-miroirs acylindriques. Cette bonne performance a été vérifiée aux longueurs d'ondes de 675 nm et de 1550 nm. Cela rajoute au micro-scanner une faculté de fonctionnement en large bande spectrale.

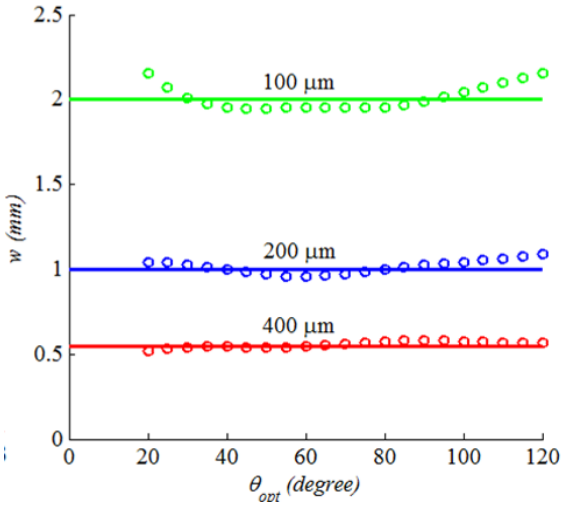

Fig. 6. Le rayon du spot du faisceau de balayage (théorique et expérimentale dans les lignes des marqueurs) fonction de l'angle de déviation optique utilisant des miroirs acylindrical avec des focales de 100, 200 et 400 µm.

Une technique de fabrication avancée a été démontrée, ciblant des microstructures incurvées en trois dimensions, présentant un axe principal dans le plan du substrat, comme indiqué dans la Fig. 7. Le but principal de la fabrication de ces structures est leur utilité dans des micro-bancs optiques, notamment pour la collimation en trois dimensions

et le couplage de faisceaux optiques en espace libre. Les surfaces incurvées sont créées en combinant la courbure dans le plan produite à partir d'un dessin de masque et de la lithographie correspondante avec une étape de gravure pour produire le profil voulu dans la direction hors du plan. Le procédé de gravure est soit un procédé à plusieurs étapes impliquant plusieurs dizaines de cycles de gravure ou alors un procédé à seulement deux étapes, ce qui est plus approprié pour la réalisation de structures avec une qualité de surface optique.

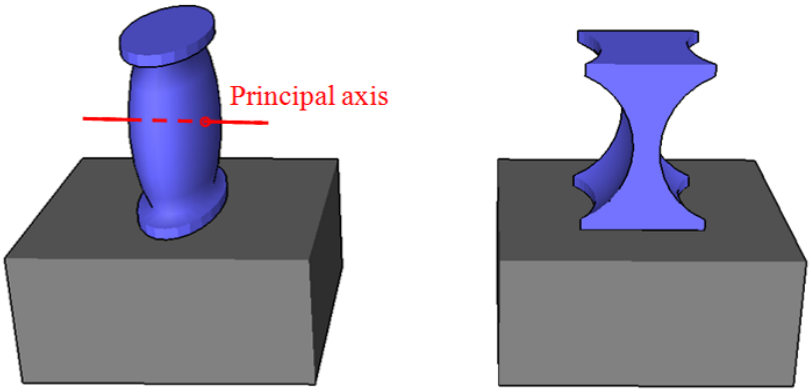

Fig. 7. Microstructures incurvées tridimensionnelles avec un profil convexe à gauche et concave à droite, dans lesquelles l'axe principal est dans le plan du substrat.

Les techniques ont été étudiées au moyen de simulations numériques (voir Fig. 8) au moyen du simulateur ELITE ainsi que d'un modèle que nous avons développé, qui s'est avéré plus efficace en temps de simulation et de mémoire. La qualité de la surface est liée au rapport entre la profondeur de gravure globale et le rayon de courbure visé. Afin d'atteindre des rapports profondeur/rayon plus petit que 0,25 un grand nombre d'étapes de gravure peut s'avérer nécessaire avec la nécessité d'une résolution de gravure

petite et bien contrôlée. A l'opposé, le rapport profondeur/rayon qui est supérieur à 1 implique une grande gravure latérale par cycle, ce qui peut être problématique en termes de rugosité de surface. Alternativement, la gravure en deux étapes, méthode inspirée de la gravure de micro canal enterré, est une technologie capable de produire des surfaces concaves avec une bonne qualité de surface optique.

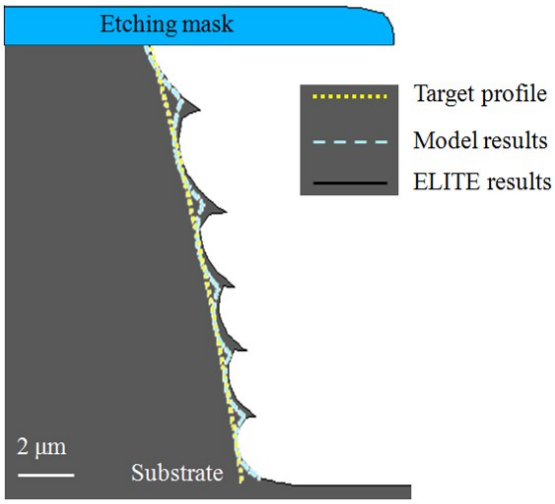

Fig. 8. Les résultats des simulations numériques pour les 6 premiers (environ 20 µm) cycles de gravure d'un profil convexe cible avec 160 µm rayon de courbure.

Les méthodes ont été appliquées sur des substrats de silicium en tirant profit du plasma à couplage inductif, dans lequel une gravure anisotrope, une gravure isotrope ainsi que la protection latérale des flancs peuvent être menées sans interruption. Les étapes ont été programmées dans la machine et leur temps ont été fixés en fonction des pré-calculs basés sur le mode de simulation. Le procédé de gravure en plusieurs étapes a été validé dans la production de surfaces convexes avec des dimensions millimétriques,

comme indiqué dans la Fig. 9. La rugosité de surface était d'environ 500 nm pic à pic, ce qui est trop élevé pour les surfaces optiques traitant de la lumière dans la gamme du visible et du proche infrarouge. D'un autre côté, le procédé de gravure en deux étapes a produit des surfaces concaves avec une bien plus petite rugosité de surface, comme le montre la Fig. 10. La microstructure concave réalisée présente une qualité de surface optique avec une réflectivité de puissance optique meilleure que 92%.

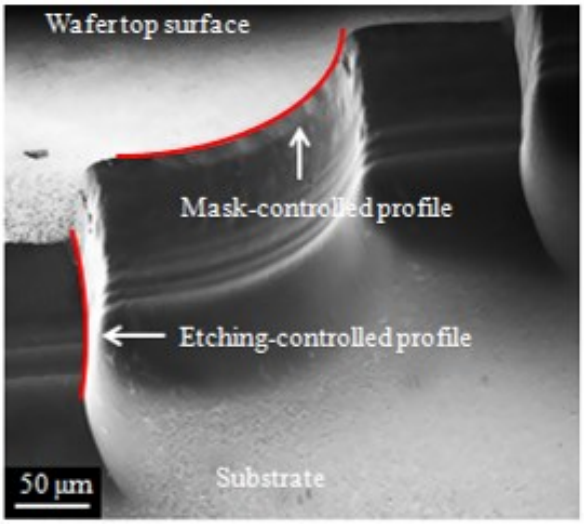

Fig. 9. Image MEB d'une surface convexe en trois dimensions gravée par la méthode multi-étapes.

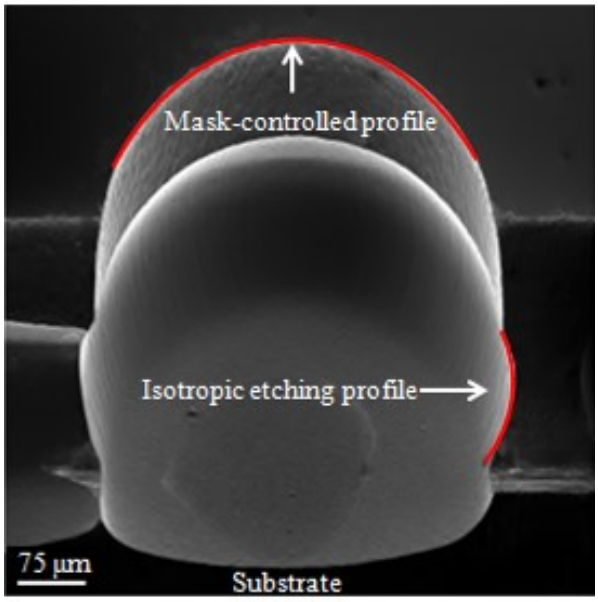

Fig. 10. Image MEB d'une surface concave en trois dimensions grave par la méthode en 2 étapes.

Le couplage des faisceaux gaussiens en utilisant des micromiroirs plats / incurvés a été minutieusement étudié, en nous concentrant sur le régime de dimensions dans lequel le rayon de courbure des miroirs et l'échelle globale est comparable à la taille du spot et à la gamme de Rayleigh du faisceau Gaussien. Les coefficients de couplage de champ et de puissance électromagnétique ont été calculés pour un (micro-) système optique, y compris dans le cas de courbures différentes dans les plans tangentiel et sagittal. Dans notre étude, la normalisation par rapport à la gamme de Rayleigh, à la taille et à l'angle de divergence a été effectuée, de telle sorte que nos résultats restent indépendants des valeurs spécifiques des paramètres du faisceau et de la longueur d'onde. Le couplage par micro-miroirs plats, qui présente une troncature possible du faisceau en raison de la taille finie de miroir, a été également étudié, en guise de référence. Il s’est avéré que la

troncature a un effet négligeable sur l'efficacité du couplage lorsque la taille du miroir est supérieure à 4 fois la taille du faisceau. Plus important encore, les micro-miroirs incurvés se sont révélés appropriés pour le couplage du faisceau gaussien lorsque le rayon de courbure du miroir est plus grand que la moitié de la distance de Rayleigh, comme indiqué dans la Fig. 11. L'effet de la non-idéalité a été comptabilisé et la dépendance importante sur la distance de Rayleigh vis-à-vis du rayon de courbure du miroir a été soulignée. Un désalignement en tilt s'est révélé efficace lorsque la taille du spot du faisceau Gaussien et la surface des miroirs sphériques sont proches alors que le désalignement latéral s'est avéré efficace pour de relativement grandes distances de séparation. Une différence des rayons de courbures tangentiel et sagittal des miroirs sphériques micro-usinés a été identifiée comme la cause de la détérioration de l'efficacité du couplage, similaire à celle rencontrée en raison d'un mauvais alignement.

Une technique de mesure a été introduite sur la base de l'utilisation d'une fibre optique monomode non revêtue pour des mesures de l'efficacité de couplage. Des micro-miroirs plats, cylindriques et sphériques fabriquées ont été mesurés en utilisant des fibres monomodes avec des longueurs d'onde de travail de 675 nm et 1550 nm, correspondant à des plages de Rayleigh de 30 μm et 45 μm, respectivement. Les résultats expérimentaux et théoriques sont présentés dans la Fig. 12, pour un micro-miroir sphérique concave de rayons de courbure dans le plan et hors du plan de 200 μm et 100 μm, respectivement. Le rendement de couplage de micro-miroir sphérique est supérieur à 50 % sur un trajet optique de 200 μm, contre moins de 10 % pourr un micro-miroir plat conventionnel.

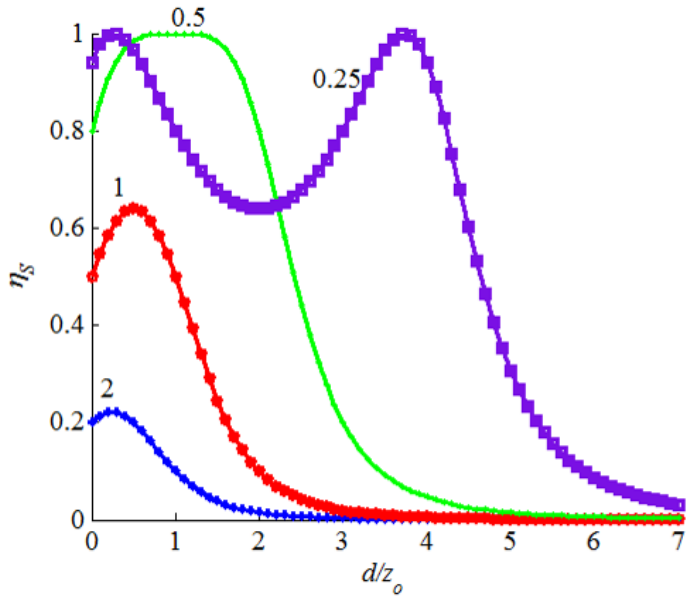

Fig. 11. Rendement de couplage d'un micro-miroir sphérique en fonction du rapport entre la séparation avec le miroir et de la plage de Rayleigh du faisceau, pour différents rapports entre la plage de Rayleigh et le rayon de courbure du miroir.

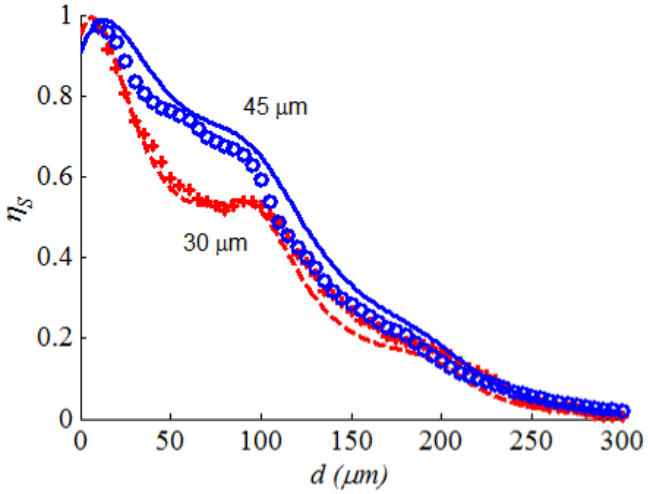

Fig. 12. Efficacités de couplage expérimentales (marqueurs) et théoriques (lignes) d'un micro-miroir sphérique en function de la distance de séparation miroir à faisceau pour une plage de Rayleigh variant de 30 à 45 µm.

Une cavité de Fabry-Pérot a été formée par une fibre monomode clivée en surface avec un revêtement réfléchissant multicouche inséré dans une tranchée, tout en faisant face au micro-miroir sphérique micro-usiné, les deux étant fabriqués par micro-usinage de silicium. La lumière est injectée dans et collectées à partir d'une fibre optique SMF-28 Corning avec une réflectivité de la surface revêtue de l'ordre de 98% à 1330 nm (bande O). La surface du miroir de silicium est revêtue d'aluminium avec une réflectivité d'environ 92%. La réponse spectrale de la cavité mesurée a une largeur de raie de 0,45 nm environ à 1330 nm, avec un intervalle spectral libre de 26 nm (Fig. 13). Les résultats obtenus indiquent qu'il y a peu de pertes par diffraction, avec un facteur de qualité proche de 3000, plus de 10 fois supérieur à celui d'une cavité à micro-miroir plat. Le facteur de qualité est limité par la surface de réflexion optique qui peut être amélioré à l'avenir par un procédé de fabrication de miroirs optimisé et une meilleure adéquation avec le revêtement de la fibre.

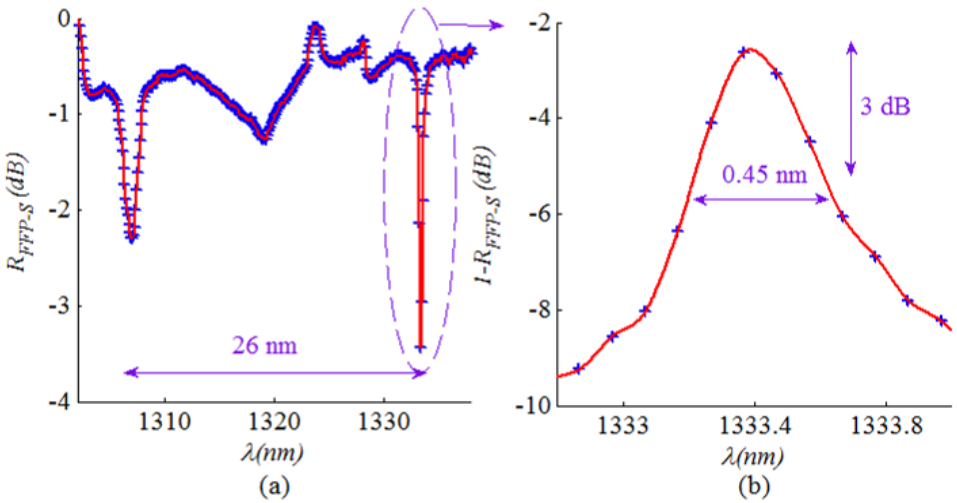

Fig. 13. (a) réponse spectrale mesurée en réflexion de la de la cavité à fibre-miroir courbe tridimensionnel. (b) La réponse complémentaire.

En vue d'une illustration supplémentaire des capacités du micro-miroir courbe tridimensionnel fabriqué, la collimation d'un faisceau gaussien à partir d'une fibre monomode a été démontrée et la divergence du faisceau réfléchi a été étudiée en utilisant l'instrument de mesure du profil de faisceau (voir Fig. 14). La sensibilité aux erreurs de micro-usinage et tolérance à l'alignement se sont révélés être assez faibles en limitant le ratio entre la distance focale du miroir et la distance de Rayleigh à moins de 5. Les résultats expérimentaux montrent un gain de collimation de l'ordre de 4 et un gain de puissance, due à la collimation de l'ordre de 12 dB par rapport au faisceau non collimaté original ayant une plage de Rayleigh de 25 μm à une longueur d'onde de 675 nm, en bon accord avec la modélisation théorique comme montré à la Fig. 15. En outre l'exploitation du micro-miroir courbe tridimensionnelle fabriqué, la collimation d'un faisceau gaussien à partir de la fibre monomode a été démontrée et la divergence du faisceau réfléchi a été étudiée en utilisant l'instrument de profilage de faisceau (voir Fig. 14).

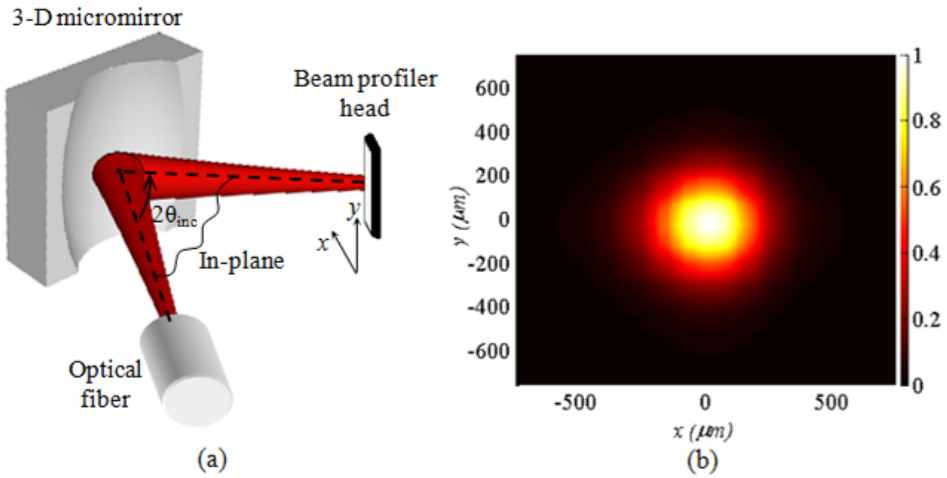

Fig. 14. (a) Mesure du profil du faisceau réfléchi sur surface reflechissante tridimensionnelle transformatrice de phase. (b) La capture du spot optique révèle une ellipticité d'environ 1,05.

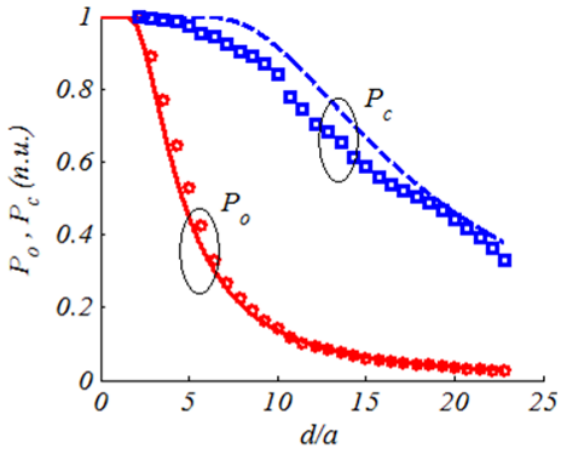

Fig. 15. (a) Puissance normalisée collectée par un détecteur avec une ouverture de rayon *a* dans le cas de faisceaux Gaussiens original (Po) et collimaté (Pc). Les données sont traces en function du rapport entre la distance de propagation distance *d* et le rayon d'ouverture du détecteur.

La réflexion d'un faisceau Gaussien désaxé (hors-axe optique) sur des micromiroirs incurvés a été soigneusement étudiée afin de faire progresser notre compréhension du sujet et d'examiner la validité de l'approche de l'optique de Gauss, dans laquelle un faisceau gaussien incident est supposé rester gaussien après réflexion ou réfraction par l'élément optique. Pour la configuration hors-axe, la méthode de l'optique de Gauss est basée sur l'hypothèse que le diamètre du faisceau est faible par rapport au rayon de phase du faisceau de courbure et le rayon de courbure des éléments optiques hors de l'axe. Cette hypothèse n'est plus acceptable pour les micro-réflecteurs où le diamètre du faisceau incident est comparable aux dimensions du réflecteur. La technique des matrices de diffusion, utilisée dans la littérature pour la gamme de longueurs d'onde millimétriques, a été examinée et appliquée sur les micro-réflecteurs incurvés, dans le

régime du proche infrarouge. La technique est basée sur le calcul de la diffusion de la puissance d'un faisceau Hermite-Gaussien sur les autres modes en raison de la réflexion hors-axe. Ensuite, le profil réfléchi est obtenu par superposition des modes excités. Cependant, les résultats ne sont pas toujours satisfaisants en raison du grand nombre de modes nécessaires à la convergence de la simulation comme indiqué dans la Fig. 16.

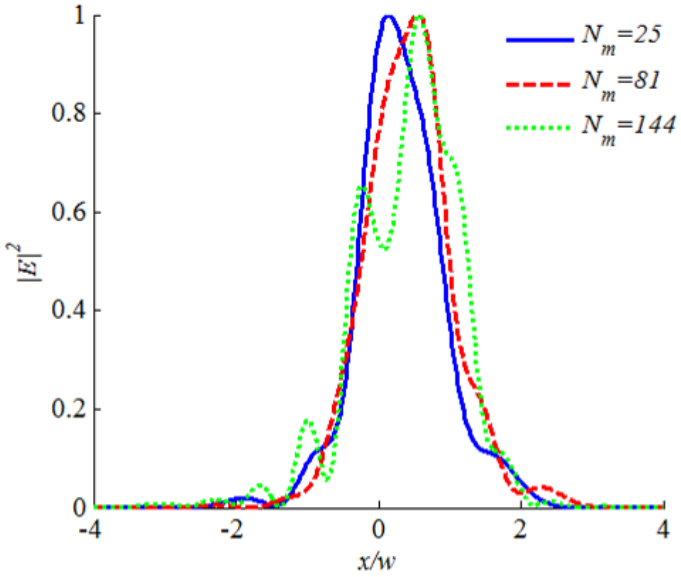

Fig. 16. Simulation basée sur la matrice de diffusion pour un faisceau Gaussien réfléchi par le micromiroir sphérique. Le profile obtenu n'est pas stable au fur et à mesure de l'augmentation du nombre de modes.

Une étude de simulation a été effectuée pour la réflexion du faisceau gaussien de micro-miroirs incurvés pour les deux cas de l'incidence normale et oblique à l'aide du simulateur GRASP9 basé sur l'approche optique physique. Dans cette étude, la longueur d'onde est de 1550 nm et une large gamme de rayons de courbure des micro-miroirs ont

été considérés, de 10 µm jusqu'à 1000 µm. La précision de l'approche de l'optique de Gauss a été jugée supérieure à 98% lorsque $w_m = 0{,}5R$ (voir Fig. 17) et autour de 90% lorsque $w_m = R$ où w_m est le rayon du faisceau Gaussien incident au miroir. La précision est mesurée en ajustant les résultats de GRASP9 sur les profils gaussiens, en comparant les angles de divergence. L'erreur a été évaluée positive ou négative en fonction des paramètres optiques spécifiques.

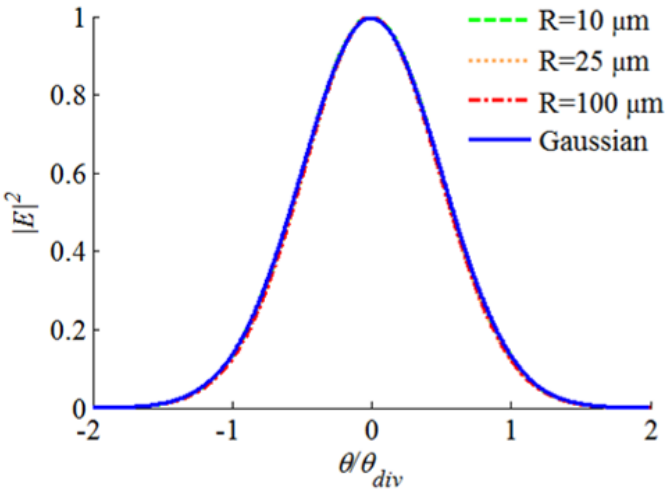

Fig. 17. Simulation sur GRASP9 comparée à une analyse en optique de Gauss avec $w_m/R = 0.5$.

Dans le cas d'incidence oblique, le faisceau Gaussian subit une distorsion et une transformation qui ne sont pas bien prédites par l'analyse gaussienne optique dans certains cas, tandis que d'autres cas elles conduisent à un bon accord. Pour un angle d'incidence de 45°, le faisceau résultant a été proche des résultats obtenus par l'optique de Gauss à la fois dans les plans tangentiel et sagittal lorsque la taille du faisceau d'entrée est

w_0 = 5 µm. Pour w_0 = 1,5 µm, le faisceau tangentiel a été complètement déformé (voir Fig. 18) et le faisceau sagittal a été jugé encore gaussienne mais avec un angle de divergence qui est loin de l'analyse gaussienne optique. En gardant le ratio w_m <0.1R, la distorsion du faisceau a révélé un petit décalage de pointe et un petit élargissement du faisceau. L'effet est plus prononcé lorsque l'angle d'incidence ou le rayon de courbure du miroir est augmenté. La direction de pointe de décalage a été constatée et dépend de la distance d'entrée tout en étant minimale lorsque le faisceau arrive sur le miroir avec son rayon de courbure de phase minimum. L'effet de polarisation croisée n'est pas significatif, inférieur à 20 dB, et plus prononcé lorsque l'angle d'incidence ou la distance d'entrée sont augmentés.

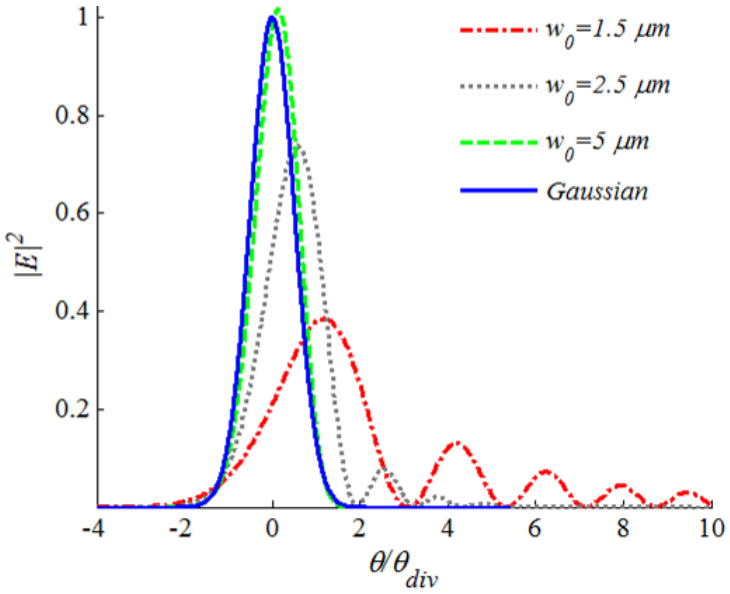

Fig. 18. Résultats de simulation sur GRASP9 dans le plan tangentiel comparés à l'analyse en optique de Gauss pour un rayon de courbure du miroir de 500 µm, un angle d'incidence de 45 degrés et différentes tailles de spot min du faisceau incident.

Un modèle simple a été élaboré sur la base du traitement du miroir incurvé comme un transformateur de phase dans lequel la transformation de phase est constituée de deux composantes, l'une est calculée à partir de la partie du faisceau incident et la deuxième composante est calculée à partir de la partie de faisceau réfléchi. En outre, le modèle prend en compte une troncature dissymétrique du faisceau sur la surface du miroir. La propagation du faisceau, après réflexion est effectuée en utilisant une technique d'optique de Fourier. Le modèle a été comparé aux résultats physique-optique et un excellent accord a été trouvé comme indiqué dans la Fig. 19.

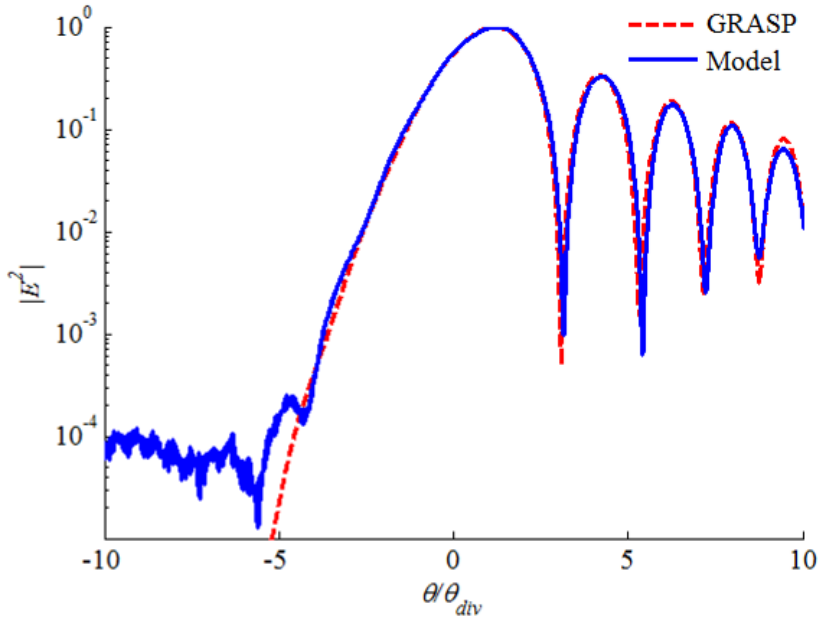

Fig. 19. Comparaison sur échelle logarithmique entre le modèle développé et GRASP9.

Enfin, une étude expérimentale a été réalisée en utilisant des micro-miroirs cylindriques fabriqués par la technologie de gravure ionique réactive profonde. Par

exemple, voir Fig. 20 pour les données expérimentales obtenues en utilisant différents rayons de courbure du miroir. Les résultats expérimentaux ne sont pas bien prédits par les simulations, en particulier pour les grandes distances entre l'origine du faisceau incident et la surface du miroir ou pour de petits rayons de courbure du miroir. La modélisation par éléments finis a également été utilisée mais elle n'a pas ajouté une nouvelle valeur à l'égard des résultats physiques optiques. Nous avons attribué cet écart entre simulations et mesures, au fait que les surfaces mesurées sont non idéales dans le sens où elles peuvent souffrir de rugosité de micro-usinage ou d'une ondulation. Ces non-idéalités couplent la puissance optique du mode gaussien fondamental vers les modes Hermite-Gaussiens d'ordre supérieur. Cette explication a été soutenue par des résultats de simulation à l'aide de notre modèle développé après l'ajout d'un terme de phase non-idéal pour la transformation de phase au niveau du miroir.

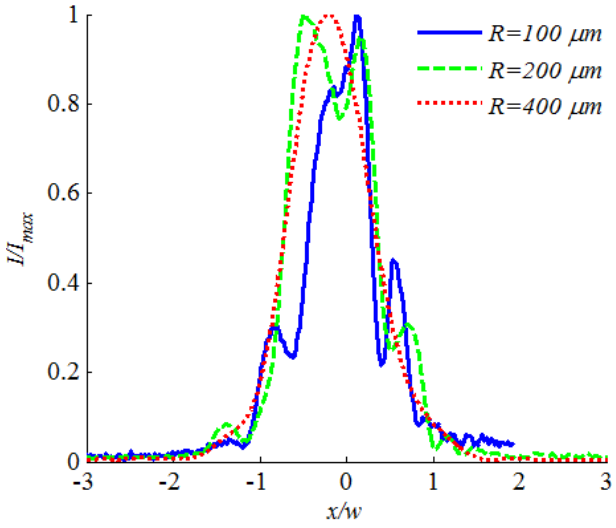

Fig. 20. Résultats expérimentaux dans le plan tangentiel à partir de fibres monomodes à 675 nm pour une distance initiale de 100 µm pour le faisceau incident, un angle d'incidence de 45 degrés et pour différents rayons de courbure de miroirs.

CONTENTS

Part 1: Micro-optical benches comprising flat and two-dimensional curved micromirrors

LIST OF FIGURES

LIST OF TABLES

CHAPTER 1

INTRODUCTION

Silicon photonics is the science and technology of using light within a silicon chip to perform one or more useful functionality. The integration of micro actuators within silicon photonic chip is very convenient since tiny forces in the order of micronewtons is enough for manipulating micro-optical components acting on the photons of light. The silicon material has excellent thermal and mechanical properties. Moreover, there is a great flexibility in design and manufacture of silicon substrates taking advantage of the well-established fabrication process. This gave rise to the field of micro-opto-electro-mechanical systems, or simply optical MEMS.

The display market was the first driver for the optical MEMS research and development activities. The digital micromirror device developed by Texas Instruments Incorporated was a pioneering and the most notable optical MEMS product with a great success. Its success story inspired great advancements and investments in the field of optical MEMS in the late 1990s; driven by the telecommunication revolution and the expected growth in the market at that time. The creation of new companies and the expansion of well established companies were vast. This unprecedented effort was subjected to the probability of vanishing due to the telecommunication bubble collapse in the beginning of the third millennium.

The previously mentioned collapse was, however, followed by the appearance of new directions of research with considerable momentum. The new directions were focused mainly on the realization and usage of micro-engines and miniaturized instrumentation in biology, chemistry, physics and materials science. The most recent applications include handheld spectrometers for fluid composition analysis, swept laser source for the non-invasive biomedical-imaging technique known as optical coherence tomography, optofluidic lab-on-chip sensors, etc… All these advances revealed technological challenges and raised opportunities for the progress of science.

In this thesis we tackle the problem of light reflection by miniaturized reflectors of planar, (a)cylindrical and (a)spherical shapes and their fabrication. The thesis is focused on deeply etched micro-optical benches, in which the light is propagating in-plane with respect to the silicon substrate. In this chapter, a brief introduction is given in section 1.1 about the deep reactive ion etching (DRIE), which is the enabling technology in our case. In section 1.2 a brief discussion is given on the deeply-etched micro-optical benches and the corresponding state of the art. The motivation, objectives, major contribution and the organization of the thesis are given in sections 1.3, 1.4, 1.5 and 1.6, respectively.

1.1 Deep reactive ion etching technology

Deep Reactive Ion Etching (DRIE) is a highly anisotropic dry etching technology used to steeply etch high aspect ratio features in a substrate. The technology is common in use for MEMS fabrication in addition to other structures such as high-density

capacitors in DRAM and through silicon via in advanced Three-Dimensional (3-D) packaging technology.

DRIE technology was enabled by the introduction of high density plasma etching equipment. A schematic representation of a typical Inductively Coupled Plasma (ICP) reactor is shown in Fig. 1.1. The major significant difference between this DRIE machine and the RIE machine, that is capacitively coupled, is the existence of two power sources. The first one is the high Radio Frequency (RF) power ICP source is responsible for the generation of high density plasma without sputtering of the reactor's walls and with a wide range of pressures. The second source is the RF or the Low Frequency (LF) substrate bias source responsible for wafer voltage biasing independent from the ICP source. The use of two sources leads to a high degree of isolation between the process of generating the plasma, including free radical and ions, and the acceleration of the ions toward the substrate. The free radicals transport to the substrate by a diffusion process. A wide range of pressures can be obtained by controlling the gas inlet mass flow and the mechanical valve interfacing to the pumping system. Laser interferometry can be used to monitor the progressing of the etching depth. A temperature controller implements a nitrogen cooling mechanism simultaneously with a heating mechanism to stabilize the process temperature. A good thermal contact between the chuck and the etched substrate is achieved though a helium gas.

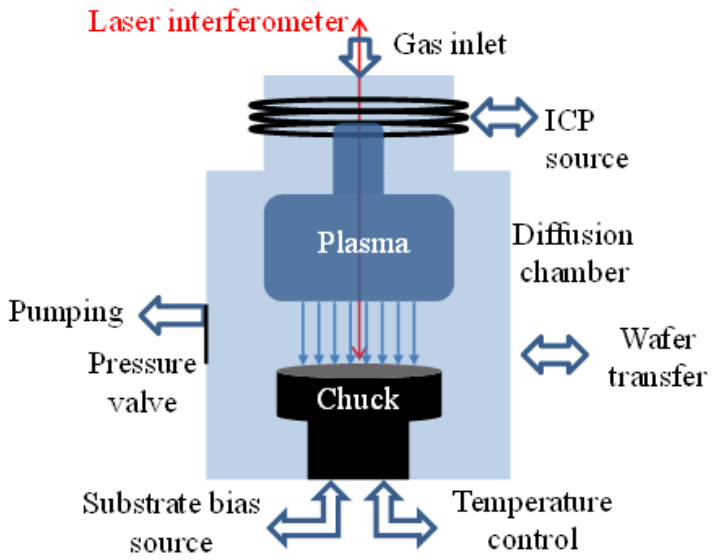

Fig. 1.1. The Inductively Coupled Plasma equipment used for DRIE process.

The DRIE Bosch process, named after the German company Robert Bosch GmbH who introduced this process, is a cyclic process switching alternately between two short cycles as shown in Fig. 1.2:

1. The etching cycle in which the substrate is etched in a nearly isotropic manner.
2. The passivation cycle in which the etched sidewalls are protected from further etching in the next etching cycles.

During the etching phase, ion bombardment selectively removes the passivation layer from the bottom of the trench, in a process known as depassivation, while the side walls are kept protected. For Si etching, sulfur hexafluoride (SF_6) and octafluorocyclobutane (C_4F_8) are the most commonly used gases for etching and passivation, respectively.

Etching and passivation cycle times of the Bosch process as well as the processing condition control the peak-to-valley extent of the scallops, formed due to the cyclic nature of the process. In addition to the scalloping amplitude, important performance metrics for the DRIE etching process are the lateral undercut below the mask, the verticality of the etched trench and the overall etch rate in relation to the mask opening, selectivity with respect to the mask material and the etching depth. It is important to mention here that continuous-mode DRIE processes also exist but the corresponding etching depth is usually limited with respect to the pulsed-mode Bosch process and the processes are highly sensitive to the temperature. An intensive review of the different DRIE process can be found in [1].

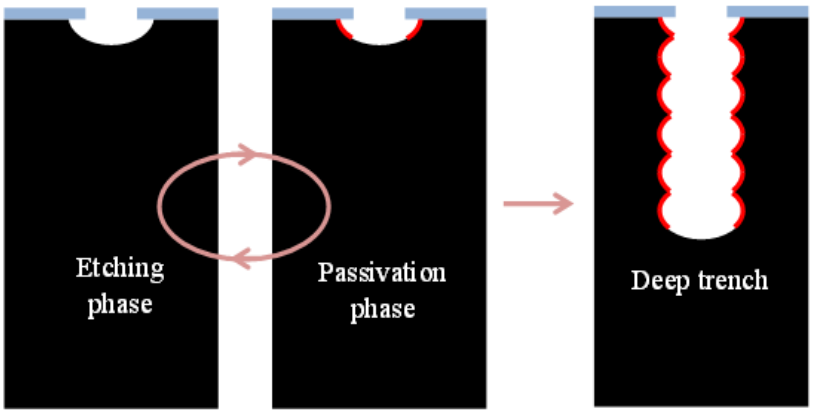

Fig. 1.2. The DRIE Bosch process is an alternation between etching and passivation phases until a deep trench is etched into a substrate.

1.2 Deeply etched micro-optical benches

Deeply etched micro-optical benches apply the DRIE technology on SOI substrates in order to produce micro-optical and MEMS components that are able to process free-space optical beams propagating parallel to the SOI substrate. The first SOI-based micro-optical bench implementing vertical micromirror fabricated using DRIE was introduced in 1997 by Marxer et al. for fiber optics switching applications [2-3]. The micromirror height was 75 μm and it was able to direct the output beam of a single-mode optical fiber to another one. The fibers are placed into grooves of equal depth, lithographically aligned and etched simultaneously with the micromirror. The buried oxide (BOX) layer serves as an etch-stop layer ensuring the uniform etch depth and as a sacrificial layer for releasing the movable structures. The motion was induced by the electrostatic-type comb-drive actuator. Indeed, this type of micro-optical benches has the advantages of robustness and lithographic self-alignment of the micro-components. Moreover, the micromirror size is suitable for manipulating optical beams with a spot size in the order of the core of the single-mode optical fibers. Therefore, it is an ideal candidate for production of inexpensive fiber-optic switched and variable optical attenuators targeting the optical telecommunication market. Following the telecommunication bubble in 2001, new directions came to light towards instrument miniaturization capitalizing on the optical MEMS emerging technology.

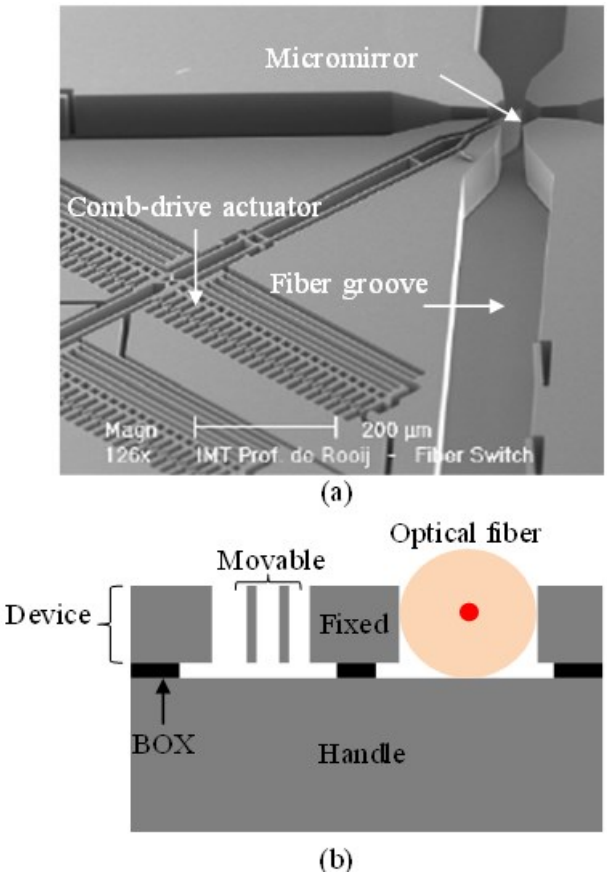

Fig. 1.3. SOI-based micro-optical bench introduced by Marxer for fiber-optic switching application [3].

A wide library of deeply etched micro-optical components has been introduced by our as well as other research groups (see Fig. 1.4 for example):

1. Flat and cylindrical metalized micromirrors
2. Flat and cylindrical distributed Bragg reflectors (DBRs)
3. Thin as well as half-plane Si beam splitters
4. Diffraction gratings including blazed-type and lamellar-type grating

A wide range of miniaturized optical devices has been implemented combining one or more of the micro-optical component together with MEMS actuators. More specifically, variable optical attenuators [4,5], optical tunable filters [6-8], optical delay lines [9], grating, Michelson, Mach-Zehnder as well as Fabry-Pérot interferometers [10-14], optical cavities [15], external cavity tunable lasers [16-17] and Fourier-transform spectrometry [11,18-22]. The special interest in SOI micro-optical benches is a consequence of their small size, low fabrication cost, self-alignment and integrability that serve the need for miniaturized instruments.

It is noteworthy to mention that other types of micro-optical benches can be occasionally found in literature based on either monolithic or hybrid integration [23-25]. The micro-optical components are first fabricated on micro-hinged polycrystalline Si plates using surface micromachining technology, and then 90 degree rotated around the micro-hinges central axis and held from sides by latching mechanism. The main advantage of this system is versatility in the size and shape of the micro-optical components. The definition of the optical axis is, however, governed by the accuracy and stability of the mechanical elements rendering the reliability of the system questionable. Besides, the intrinsic stress in the thin polycrystalline Si can deteriorate the performance. Since the optical axis lies above the substrate, the monolithic integration of micromachined grooves for optical fiber insertion is prohibited in addition to the difficulty in integrating MEMS actuators for moving the optical components.

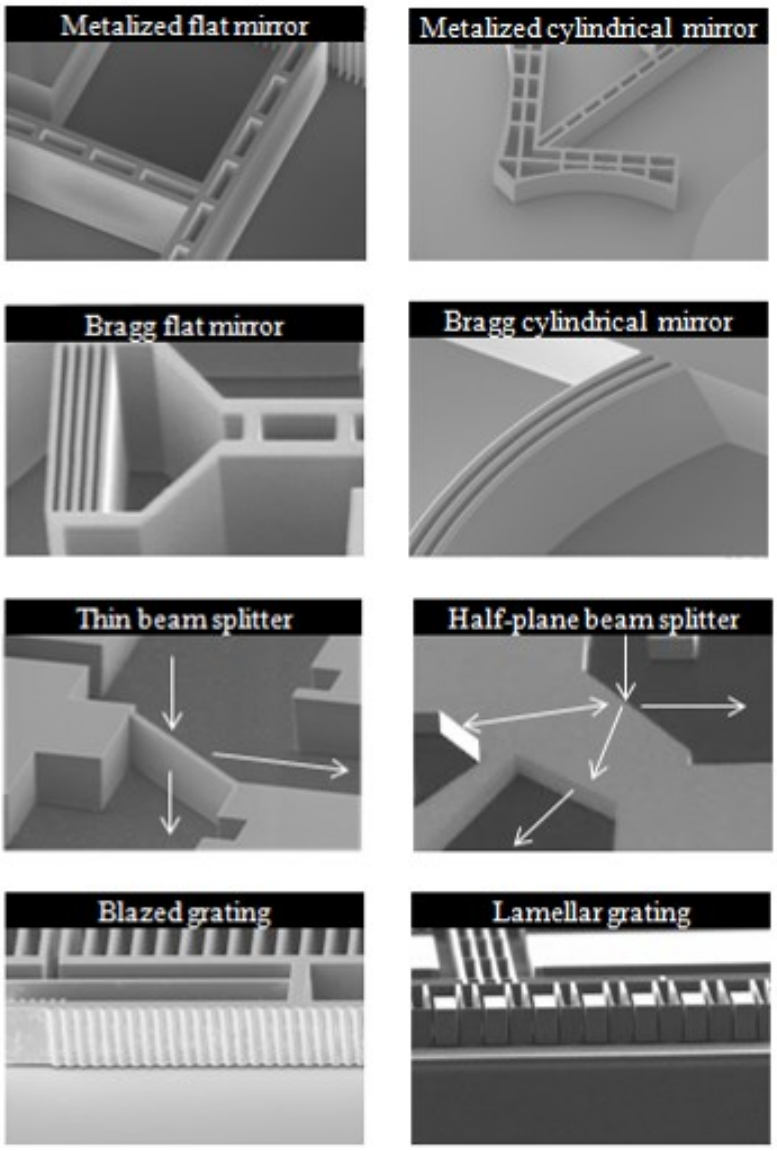

Fig. 1.4. Deeply etched micro-optical components library.

1.3 Motivation

In deeply etched micro-optical benches, the micromirror surface verticality and roughness are controlled by optimizing the DRIE process and by optionally reducing the

cycles' time [26-27]. Techniques for smoothing out the DRIE Bosch process scallops from the resulting surface based on oxidation followed by oxide etching or using short anisotropic wet etching have been proposed [28-31]. The combination of a DRIE continuous etching process together with the DRIE Bosch process was used to produce smooth mirror's surface at the top part of the mirror [6]. For more stringent verticality and smoothness requirements, the micromirrors were etched in a (110) wafer with the mask aligned to the (111) crystal planes [32].In the latter case, wet anisotropic etching yields very high surface quality and vertical surface close to ideal on the expense of: 1) restricting the realizable flat optical surfaces arrangement and 2) prohibiting the deep etching of in-plane curved surface, which is of particular interest in this thesis. Aside from the wet anisotropically-etched structures [33-34], the height of the micromirrors in the previously mentioned deeply-etched micro-optical benches was limited to 70-80 μm. Although deep surface with moderate verticality specification were reported for the purpose of through-wafer etching [56], up to our knowledge, deeper surfaces exhibiting measured optical quality simultaneously etched with the accompanying MEMS on the SOI wafer device layer, were not reported.

As a consequence of the limited micromirrors size in micro-optical benches, deeply-etched micro-optical benches have low optical throughput. The optical throughput, commonly called etendue in French, is a quantitative measurement of how much light energy gets through an optical instrument and transferred from a light source to a detector. The throughput is a geometrical quantity that is invariant in the system and defined by the least optimized part of it. Due to the micromirrors height in micro-optical

benches, the optical throughput of a micro-optical bench can be not large enough to serve an adequate signal to noise ratio in miniaturized instruments. This is especially true when dealing with non-coherent wideband sources typically used in OCT and spectrometry.

Deeply-etched micro-optical benches comprise optical elements that are flat in the direction perpendicular to the wafer surface. Although such optical elements are able to reflect, refract or diffract an impingent optical beam, they are unable to focus or collimate the optical beam in the out-of-plane direction. At the same time, the spot size of the optical beam cannot be increased- to reduce the beam expansion accompanying the propagation- due to the limit height of the micromirrors. As a result, the conventional micro-optical bench systems suffer from weak coupling efficiency, high propagation loss and/or limited allowable optical beam path traversed in the micro-optical bench. In fact, Silicon-based coupling micromirrors were reported in both flat and cylindrical shapes [35-36]. The allowable optical path was limited to tens of micrometers by the rapid decay of the coupling efficiency. Up to date, high coupling efficiency with sub-millimeter OP in OBs was not achieved without the assembly of a ball lens with flat mirrors [16], the insertion of a fiber rod lens with cylindrical mirrors [15, 17, 37] or the hybrid integration of 3-D mirrors that require further assembly or mounting steps [38-41]. These shortcomings again limit the overall optical performance of miniaturized instrument based on micro-optical bench technology.

Another challenge in micro-optical benches is their limited optical beam steering angle capability in the reported literature. Micro-optical bench microscanners based on rotating a flat vertically-etched micromirror using a rotary comb-drive actuator was

reported [42-43].The reported scanning angle was limited to ± 3 degrees set by the small angle of rotation usually achieved with rotary comb-drive actuators. Microscanners based on refraction of light from a translated microlens were also reported [44-46]. A micro stage attached to an electrostatic or piezoelectric actuator is usually micromachined, and then the lens is inserted and fixed on that stage. The assembly and fixation of the microlens on the stage and in conjunction with the source is not a trivial task. The weight of the lens harms the agility of the system while the scanning angle is limited by the optical properties of refraction. Typical maximum scanning angle of ± 5-10 degrees and speed in the order of 200 Hz were reported [44-46]. Indeed, non-integrated wide scanning angle microscanners have been reported in literature extensively [47-52].

1.4 Objectives

The ultimate objective of this PhD thesis is threefold; mainly achieving technological advancement in micro-optical benches, design and implementation of integrated wide-angle microscanner on a silicon chip and finally tackling the problem of light reflection on micro-curved optical surfaces.

The technological advancement is composed of two parts. The fabrication of high optical throughput micro-optical benches is one target. This is considered as an enabling technology for achieving miniaturized instruments dealing with low coherence light, for example in FTIR spectroscopy. The second technological target is the fabrication of three-dimensional curved micromirrors compatible with micro-optical benches; i.e. the principal axis of the micromirror lays in-plane with respect to the micro-optical bench

substrate. This technological advancement enables high coupling efficiency over a single- as well as multi-wavelength spectrum. High- quality-factor optical cavity in micro-optical benches is one example application.

The second objective of this thesis is to design and implement a wide-steering-angle integrated microscanner on a silicon chip. For this purpose, the use of curved micromirrors of acylindrical shape is explored. This allows on-chip integration of the microscanner with other micro-optical modules, which is an important asset allowing cost reduction and opening the door for instrument miniaturization, with OCT being a typical example.

Tackling the problem of coherent light reflection on micro-curved optical surface is the third objective of this thesis. An incident Gaussian beam on micro-curved surface doesn't necessarily imply a reflected Gaussian beam; i.e. the Gaussian optics approach may not be valid. A theoretical study complimented by experimental results can be of interest to a wide spectrum of researchers working in optical MEMS and photonics as well as other fields of micro-optics. The study will be focused on the fundamental Gaussian and the Hermite-Gaussian beams that represent a complete set of modes in free-space.

1.5 Major contributions

The major contributions of this thesis are summarized as the following:

A deep etch fabrication process is developed for realizing high optical throughput micro-optical benches. Micromirrors with verticality better than 0.1 degree and

scalloping depth less than 75 nm is demonstrated over a 300 μm etching depth, about 4*x* deeper than reported literature. The process is not based on alkaline etching or specific crystalline planes and, thus, is suitable for realizing flat as well as 2-D curved micromirrors and MEMS actuators without restriction on the orientation. A Miniaturized FTIR spectrometer with 200 μm depth is demonstrated using the developed process offering more than 12 dB improvement in the detected signal. We consider this a significant jump towards bringing miniaturized instrument to the practical life.

Ultra-wide steering-angle integrated microscanner is realized using micro-optical bench technology. The scanner is based on a novel optical architecture in which the angular deflection is achieved by displacing the principle axis of a curved silicon micromirror of acylindrical shape, with respect to the incident beam optical axis. The micromirror curvature is designed and precisely controlled by lithography to overcome the possible deformation of the scanned beam spot size during scanning. We have demonstrated optical deflection angles up to 110 degrees using a one-degree-of-freedom MEMS system. Larger deflection angles, up to 160-180 degrees, are also predicated theoretically when two-degree-of-freedom MEMS system is used.

A technological method is presented and experimentally validated for batch fabrication of three-dimensional curved microstructures with in-plane principal axis. The method is based on multi-step etching and protection technique, in which all the steps are performed in ICP reactor without process interruption. Concave as well as convex microstructures with out-of-plane radius of curvature in the submillimeter range are demonstrated.

Detailed analytical study of free-space Gaussian beam coupling using flat, cylindrical and spherical micromirrors is performed. The analytical formula can be used for more complex micro-optical benches, once their transformation matrix parameters are known. The study is focused on the regime where the confocal parameter of the Gaussian beam is comparable to the micromirror radius of curvature. Non-deal effects, such as limited micromirror size, astigmatic spherical micromirror radii of curvature and optical axis misalignment are taken into account.

A fabricated spherical micromirror, using the multi-step etching technique and further metallization, was used in demonstrating efficient wideband lens-less coupling of free-space light propagating in-plane with respect to the substrate. Then, an optical cavity is formed between a multi-layer coated optical fiber and the spherical micromirror demonstrating a quality factor of 3000, 10x higher than using a conventional flat micromirror. Finally, the fabricated spherical micromirror is used for collimating the output of a single-mode optical fiber and cutting down free-space propagation loss reduction by more than 10 dB.

A numerical study of Gaussian beam distortion upon reflection on micro-curved surface is carried out in the near-infrared spectral regime. The study explored different methods based on physical-optics, scattering-matrix and phase transformation approaches. The developed simple model based on phase transformation and Fourier-optics shows excellent agreement with the benchmarking physical-optics approach. The validity of the Gaussian optics approach is examined. The study is also complemented

using experimental data in the near-infrared spectral regime in addition to the visible regime.

1.6 Organization of the thesis

This thesis is concerned with light reflection on miniaturized reflectors of various shapes including flat, two-dimensional curved and three-dimensional curved micromirrors and its applications in micro-optical benches. It is divided into three parts and six chapters:

Chapter one gives a brief introduction of the motivation, objective, major contribution and organization of the thesis.

Part I: This part is focused on fabrication, design and measurements of micro-optical benches in which flat, cylindrical and acylindrical micromirrors are used. The theoretical work in this part is based on Gaussian optics.

Chapter two presents the results of developing a fabrication process for high optical throughput micro-optical benches with application on a Michelson interferometer used in FTIR spectrometer.

Chapter three demonstrates an integrated wide-angle microscanner based on translating acylindrical curved micromirrors in micro-optical benches.

Part II: This part is focused on fabrication, analysis and measurements of micro-optical benches in which three-dimensional micromirrors are used. The theoretical work in this part is also based on Gaussian optics.

Chapter four discusses the fabrication of three-dimensional curved microstructures having their principal axis laying in-plane with the respect to the substrate.

Chapter five presents the analyses and applications on Gaussian beam coupling using micro reflectors of various shapes.

Part III: This part is concerned with the study of Gaussian beam reflection on micro-curved mirrors. The study considers different approaches of non-Gaussian optics and examines the validity limits of Gaussian optics.

Chapter six gives the results and conclusions of studying Gaussian beam reflection on micro-curved mirrors based on non-Gaussian optics approach.

Finally, chapter seven gives the conclusion of this thesis and lists several recommendations for the future work.

CHAPTER 2
HIGH THROUGHPUT MICRO-OPTICAL BENCHES

2.1 Introduction

High aspect ratio trenches with a narrow width are of particular interest for MEMS inertial sensors and high density capacitors. High aspect ratio micromirrors with narrow gaps are usually used in micro-optical benches for creating 1-D photonic band gap filters [32]. In these structures, maintaining the deep progress of etching is challenging because of two main reasons. First, it is more arduous for the etchants to diffuse down to the bottom of the trench and for the etching products to diffuse out. The second reason is that due to scattering on the sidewalls of the trench, the amount of ions reaching the bottom of the trench are less for deeper trenches, which leads to less efficient removal of the bottom passivation layer in addition to hampering the passivation layer on the sidewalls. These two reasons lead to etched trenches with a positive profile and consequently set a limit for the achievable etching depth and aspect ratio. By using a low-pressure high-ion-bombardment process, using a separate depassivation cycle with optimized parameters and gas or by ramping up the etching cycle time and substrate bias during this cycle, high aspect ratios trenches up to 120 were reported [53, 55-56].

In contrast, free-space micromirrors are relatively widely separated in free-space and their surface verticality and smoothness quality are of crucial important more than its aspect ratio, except for the case of 1-D photonic band gap (Bragg) mirrors. The

micromirror surface verticality and roughness are controlled normally by optimizing the DRIE process and by optionally reducing the cycles' time [26-27]. Techniques for smoothing out the DRIE Bosch process scallops from the resulting surface based on oxidation followed by oxide etching or using short anisotropic wet etching have been proposed [28-31]. The combination of a DRIE continuous etching process together with the DRIE Bosch process was used to produce smooth mirror's surface at the top part of the mirror [6]. For more stringent verticality and smoothness requirements, the micromirrors were etched in a (110) wafer with the mask aligned to the (111) crystal planes [32].In the latter case, wet anisotropic etching yields very high surface quality and vertical surface close to ideal on the expense of: 1) restricting the realizable flat optical surfaces arrangement and 2) prohibiting the deep etching of in-plane curved surface, which is of particular interest in this thesis.

Aside from the wet anisotropically-etched structures with restricted shapes [33-34], the height of the micromirrors in the previously mentioned deeply-etched micro-optical benches was limited to 70-80 μm. Beyond this limit, the verticality of the etched surface deteriorates with a highly negative profile and significantly rough surface. Although deep surface with moderate verticality specification were reported for the purpose of through-wafer etching [56], up to our knowledge, deeper surfaces exhibiting measured optical quality simultaneously etched with the accompanying MEMS on the SOI wafer device layer, were not reported.

In this chapter, we report the fabrication of deeply etched vertical micromirrors with verticality close to 90^{o} and with depth up to 300 μm. The micromirrors are etched

using DRIE maintaining the versatility of etching arbitrary oriented flat surfaces as well in-plane curved surfaces. The high surface quality is obtained by process optimization and the incorporation of dummy surfaces that are removed in subsequent processing steps.

2.2 Problem statement

The process development in this chapter targets the fabrication of high throughout micro-optical benches with the monolithically integrated Michelson interferometer shown in Fig. 2.1 considered as an important application. The optical surfaces of the interferometer are a silicon-air beam splitter (BS), a metalized moving mirror (MM) attached to a long travel range comb-drive actuator and a metalized fixed mirror (FM). The separation distance between the optical surfaces is in the order of sub-millimeter. Simultaneous etching of the optical surfaces and the actuator is required to ensure the proper self-alignment of the components, simplify the processing steps and consequently reduce the processing time and cost.

The miniaturization of a Michelson interferometer is a key step forwards the production of a miniaturized Fourier-Transform Infrared (FTIR) spectrometer instrument used in chemical analysis. The input optical power of such spectrometer is usually supplied by means of multi-mode (MM) optical fiber, which serves as a carrier of the optical power from a wide band source, usually referred to as white light, to the spectrometer. The amount of power injected from the source into the miniaturized spectrometer is proportional to the area of the aperture of the spectrometer that is directly

proportional to the depth of the etched optical surfaces of Michelson interferometer. The amount of coupled power has a direct impact on the instrument signal to noise ratio. Besides, a stringent requirement exists on the parallelism of the optical surface which can significantly deteriorates the visibility of the resulting interferogram and again the instrument signal to noise ratio. For an extensive discussion on the effect of different parameters on the spectrometer performance, one may refer to the book by Griffiths and Haseth on FTIR spectrometry [57]. To summarize, there is a need for deeply etched surface in micro-optical benches with a high control on the verticality of the optical surfaces.

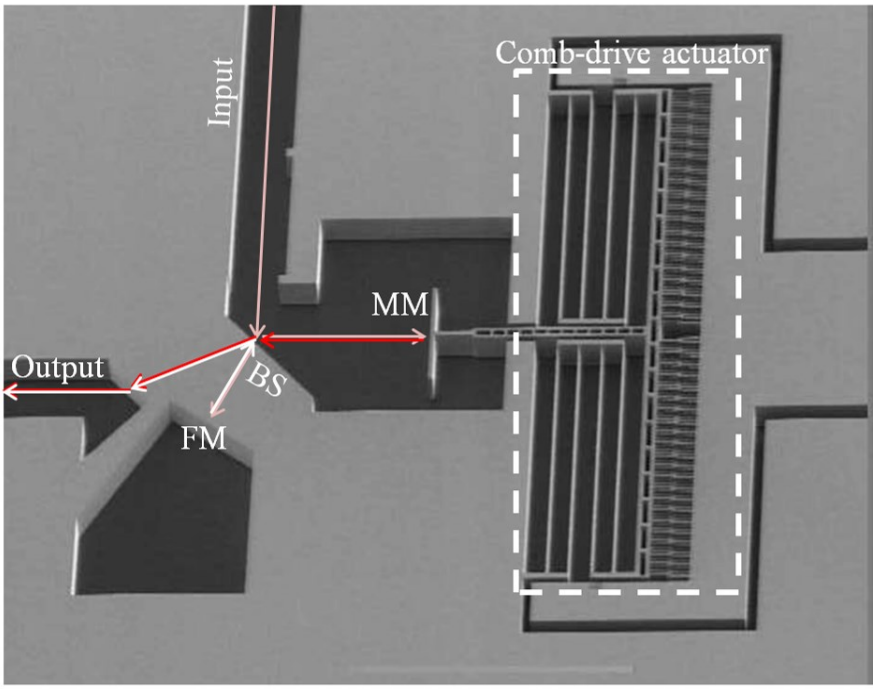

Fig. 2.1. Monolithically integrated Michelson interferometer in which BS is a beam splitter, FM is a fixed mirror and MM is a moving mirror.

2.3 Fabrication process

2.3.1 Target specifications

The specifications of the required etch profile are listed in Table 2.1. The profile parameters are illustrated in Fig. 2.2. The specifications of the trench width, the critical dimension and the undercut are mainly attributed to the geometry of the comb-drive actuator. The specifications of the etching depth, sidewall angle and the scalloping depth are related to the optical surface height and quality. At least 200 μm etching depth is required to maintain an acceptable optical throughput of the interferometer. Sidewall angle deviation from verticality is not allowed to exceed 0.15^{o}. The scalloping depth is required to be less than 50 nm that is about λ / 30 where λ is the wavelength of light in the near infrared spectrum, which is in the order of 1550 nm. For larger wavelength in the med infrared spectrum, the roughness effect will be less significant.

Table 2.1. Specifications of the required deep etching results

Trench width	$20\ \mu m < w < 30\ \mu m$
Critical dimension	$CD < 5\ \mu m$
Mask undercut	$u < 1.5\ \mu m$
Etching depth	$D = 200\ \mu m$
Sidewall angle	$\beta = 90^{0} \pm 0.1^{0}$
Scalloping depth	$s < 50$ nm

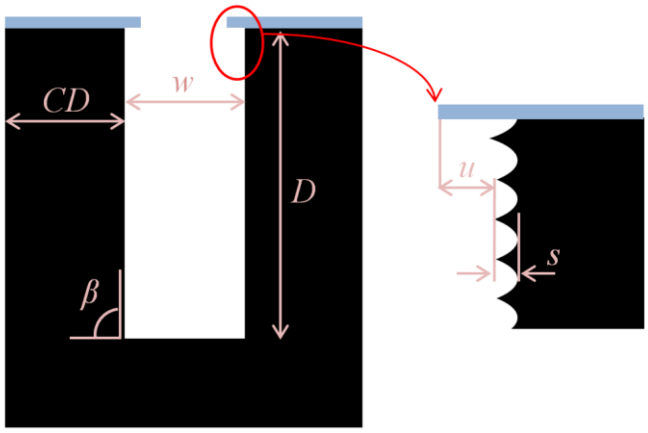

Fig. 2.2. DRIE profile parameters: D is the etching depth, *w* is the resulting trench width, CD is the resulting line critical dimension, *β* is the sidewall angle, *u* is the undercut or overetching and *s* is the scalloping depth.

2.3.2 Process flow

The fabrication steps are briefly given in Fig. 2.3. The starting substrate is an SOI wafer in which the device and handle layers are (100) silicon substrates. For DRIE process development, silicon wafers are used instead in which etching depths better than 300 μm could be achieved. For the Michelson interferometer fabrication, SOI wafers with device layer height of 200 μm are used, as listed in Table 2.1. The SOI wafers are double-side polished. The handle layer thickness of the SOI wafer is typically 525-550 μm. The SOI wafers are ordered with an oxide layer on the handle top surface to be used as a backside etching mask. The thickness of the oxide is typically the same as the BOX layer, which is typically 2-3 μm.

First, the top side etching mask is grown or deposited in step 2. As will be detailed hereinafter, both aluminum and oxide were used as an etching mask each with specific advantages and disadvantages. The aluminum mask is deposited by the sputtering technique while the oxide mask is thermally grown in a wet oxidation process. Then, bottom and top mask are patterned, in this order, using photolithography in step 3. In step 4, DRIE of the device is carried out using the optimized process recipe with the help of dummy walls in close proximity to the optical surfaces. The dummy walls prevent the removal of the sidewall passivation layer due to energetic ions with wide angular distribution. In this way, the angle of the etched surface could be well controlled by optimizing the ratio between etching and passivation. Without using the dummy walls, the sidewall angle can be hardly controlled by process optimization and can be larger than 90 degrees by more than one degree. The handle layer is then partially etched; allowing for separating the individual designs from the wafer after fabrication. The etched surfaces are then smoothed in step 5 in order to meet the required specifications of the scalloping depth. The sacrificial dummy walls are made thin enough such that it is totally consumed within the smoothing step. Alternatively, the dummy walls can be left to fall in the release step. Bottom and top oxides are etched in a 50% vapor HF as well as the BOX layer underneath the moving parts, as shown in step 6. The mirrors are then metalized using aluminum or gold in step 7 using a shadow mask, which is fabricated a priory. The aluminum has a higher reflectivity than gold in the visible regime while gold metallization reflectivity is higher in the near infrared regime. Then, the pads are gold metalized in step 8 using another shadow mask allowing for gold wire bonding. Even

when the mirrors and the pads are gold metalized, we found that separation their metallization into two different steps has the advantage of optimizing each step separately.

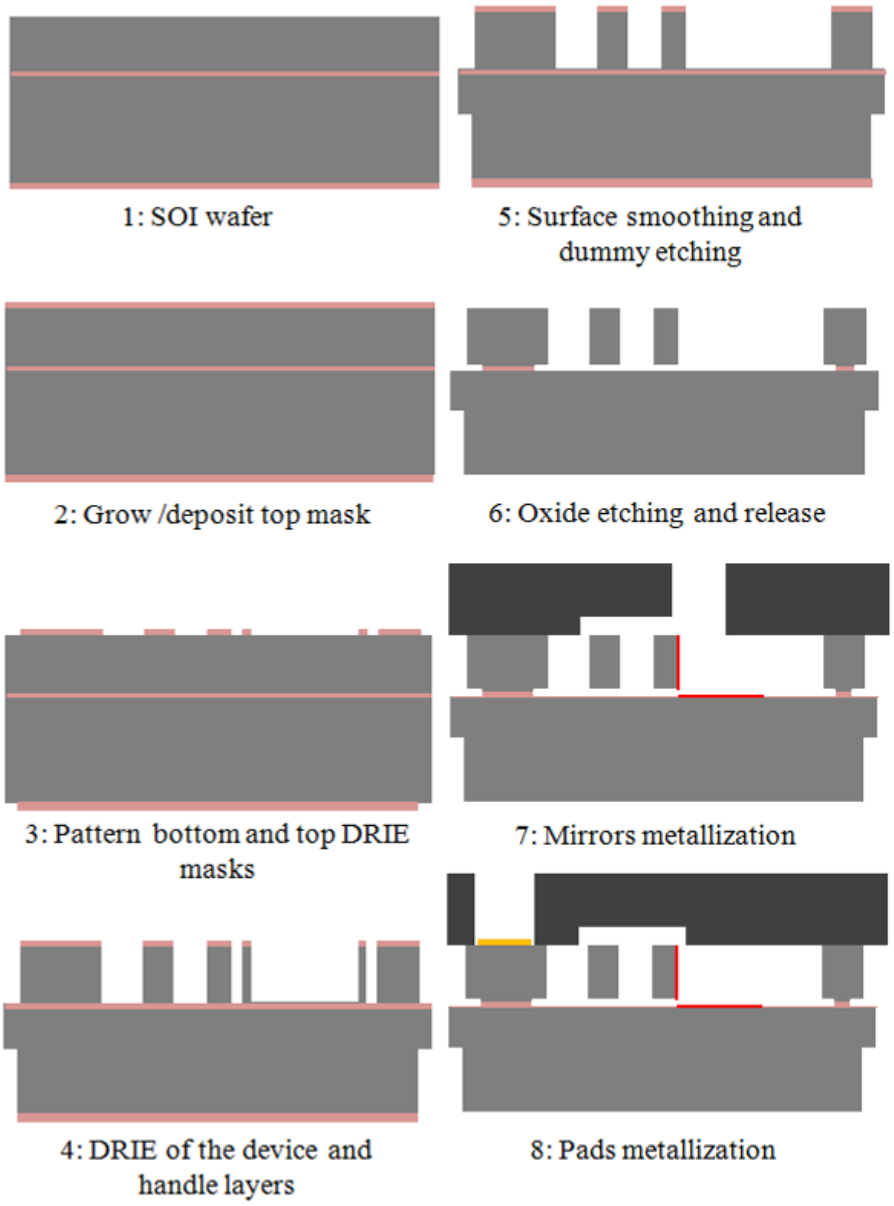

Fig. 2.3. Fabrication process steps of the SOI optical bench.

In the rest of this chapter, we were more concentrating on the optimization and characterization of the DRIE step of the device layer, post-DRIE cleaning and post-DRIE smoothing.

2.3.3 DRIE step optimization

The recipe by which we started the DRIE optimization was provided by the SMM team of the clean room in ESIEE Paris. We refer to this initial recipe as DRIEA. The etching equipment is Alcatel 601E with mechanical clamping supporting either low-frequency (LF) or radio-frequency (RF) mode of operation for the substrates bias source. In this section, we summarize the results obtained using the initial as well the developed recipes.

First, we started our experiments using a 500 nm aluminum mask. The aluminum was deposited on the top of a silicon wafer using the sputtering method. The aluminum was patterned using a photolithographic process with PFR7790G photoresist. We found that wet etching of the aluminum results in an excessive overetching that is larger than 2.5 μm. Therefore we used chlorine-based plasma for the etching, which results in overetching smaller than 1 μm that is acceptable in our case.

By using VECCO optical profiler for measuring the etching depth after 40 minutes long etching process, the average etch rate of the provided process was found to be 4.25 μm/min in wide etching areas. Unfortunately, the etched structure was full of silicon grass as shown in Fig. 2.4. After a few iterations, we found that the problem appears due to long time etching process using the low frequency substrate power. The

silicon grass was attributed to the micromasking phenomena [58]. Due to the highly energetic low frequency ions, the aluminum is sputtered inside the DRIE reactor and a redeposition process occurs on silicon blocking further etching in some places and resulting in the silicon pillars shown in Fig. 2.4.

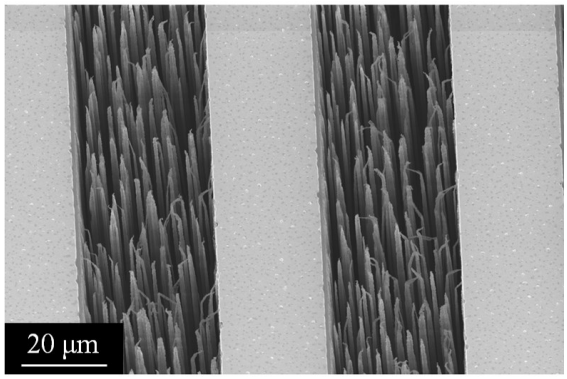

Fig. 2.4. Silicon grass appears upon applying recipe DRIE A for 40 minutes on a silicon wafer with aluminum mask.

To overcome this problem, the substrate source was switched to the RF mode. Indeed the LF mode is used to minimize the notching phenomenon that occurs when the BOX layer is reached during etching [1]. This puts a constraint on the use of aluminum with the SOI wafers. In this case, the mask has to be carefully designed allowing as much opening uniformity as possible and or the use of other techniques to reduce the nothing while still using the radio frequency substrate power [56]. For this purpose, the lag effect of the optimized DRIE process has to be characterized both for trenches and square openings. The experiment was repeated again using the RF mode and the resulting

structure became clean. The new average etch rate was found to 5.1 μm/min for wide areas measured along a 40 minutes etching process. However, the sidewall angles of the 20:30 μm width trenches were found to be larger than $90^0 + 0.3^0$, which indicates more passivation is needed.

The passivation flow rate was already set at its maximum limit afforded by the equipment. Moreover, we found that increasing the passivation flow rate leads to a silicon grass circle near the edge of the wafer under processing. This was attributed to the mechanical metallic clamping of the equipment disturbing the plasma at this region. In order to improve the side wall angle, the pressure was increased. Increasing the pressure was found to be an effective method to increase the sidewall passivation and reduce the corresponding etching angle without sacrificing the etch rate.

For etching depths larger than 100 μm, a deterioration the in the sidewall angle was observed with tendency to a closing behavior with depth. This behavior means the passivation layer can be too thick to be removed efficiently from the bottom of the trench. For this reasons, the substrate power was increased in order to maintain the enough bias voltage for the ions to arrive deeply inside the etched trenches and be sufficient for passivation layer removal. We refer to this new recipe as DRIEB. The DRIE time was increased to 80 minutes. The etching depth in wide areas was measured on different position across the wafer and found to be 417 μm ± 10 μm indicating an acceptable etching uniformity in the order of 2 % with an average etch rate 5.22 μm in wide areas. The resulting etch profile is shown in Fig. 2.5 for 5 μm to 100 μm trench width as drawn on layout. The corresponding sidewall angle was measured and recorded as shown in Fig.

2.6. Trench widths in between 20 μm and 30 μm have sidewall angles well fitting in the specifications window of $90^0 \pm 0.1^0$. The trenches length is 1 mm. The mask undercut of the DRIE is about 1.5 μm.

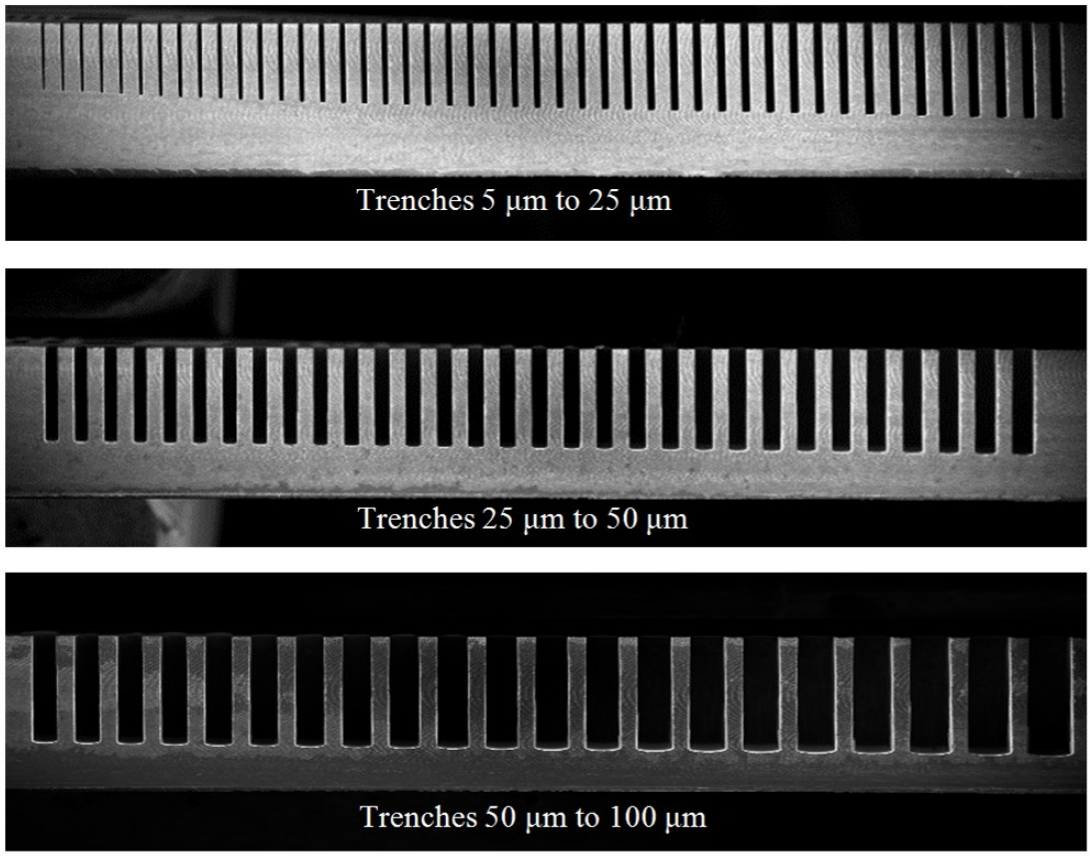

Fig. 2.5. Etched trenches with the developed recipe DRIEB. The etched profile is excellent in terms of the sidewall angle verticality.

Trenches as well as squares with different dimensions exhibits different etching due to the well-known DRIE lag effect [1]. Characterization this lag effect is important for mask design to guarantee that all of the mask features will reach the desired etching

depth simultaneously or at least without a significant difference. If this is not the case, notching effect may occur. In addition, an excessive mask undercut and sidewall angle deterioration can take place. The lag effect corresponding to the recipe DRIEB was characterized on trenches and squares with mask drawn features ranging from 5 µm to 100 µm and the corresponding depth is plotted in Fig. 2.7. The recommended mask features are 25 µm and 60 µm for trenches and squares, respectively corresponding to a depth of 325 µm. The 25 µm trenches have a corresponding sidewall angle of about 90^0.

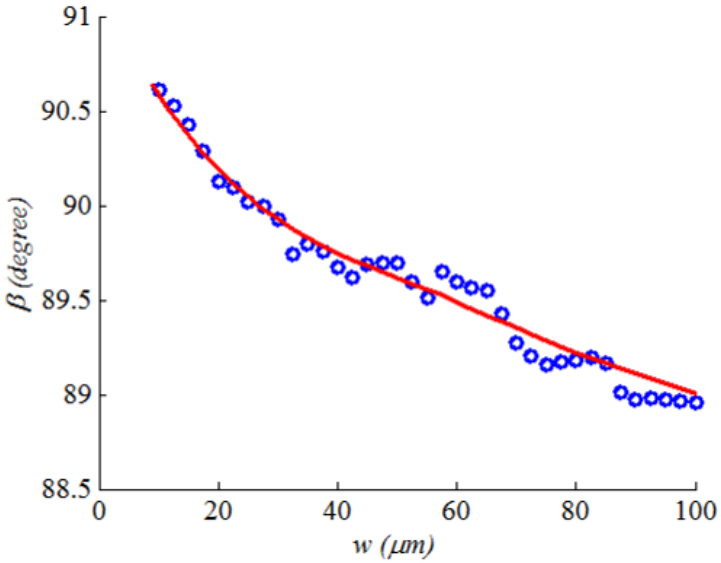

Fig. 2.6. The sidewall angle versus trench width of the developed recipe DRIEB.

Deep etching up to 325 µm with excellent surface verticality was obtained using aluminum mask as shown previously. The use of LF substrate pulses is, however, prohibited because of the micromasking effect. In this case, the notching phenomenon is avoided by a careful design of the mask using the rules extracted from Fig. 2.7. We also

investigated the use of oxide mask with deep etching, which allows using the LF substrate pulses with a less-constrained mask design.

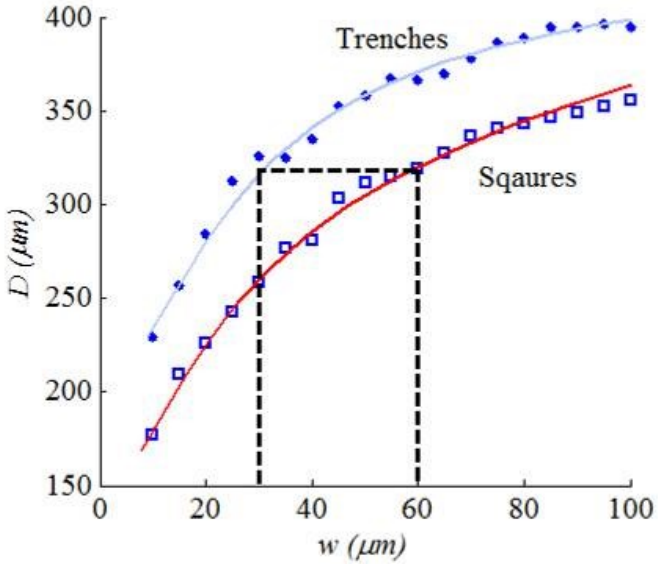

Fig. 2.7. Depth of the trenches and squares etched with recipe DRIEB. A depth of about 325 μm is obtained simultaneously for trench and square of 25 μm and 60 μm feature, respectively.

Oxide mask with a thickness of 2.5 μm was thermally grown on silicon by means of wet oxidation, which was a quite long process consuming about 14 hours in the oxidation furnace. The thickness was chosen based on our experiments from which the selectivity of oxide with respect to silicon in DRIE was found to be close to 100:1. The 2.5 μm oxide, thus, allows 200 μm etching in silicon that was decided to be enough for our application. The DRIE recipe had to be re-optimized with oxide mask to have similar results to those obtained with the aluminum mask. We refer to this new recipe as DRIEC. The oxide mask was found to result in etched surfaces exhibiting higher quality with

respect to the surfaces obtained with the aluminum mask. This was especially found in the case of wide etching areas as shown Fig. 2.8. We attributed this difference to the higher stability of oxide over silicon, in contrast to the micromasking occurring with aluminum. Besides, the etching usually results in mask undercut, which may lead to the falling of aluminum located close to the mask edges. For DRIE depth of 200 μm in 25 μm trenches, the mask undercut in case of using aluminum is about 1.25 μm while smaller value of about 0.75 μm was obtained using oxide mask.

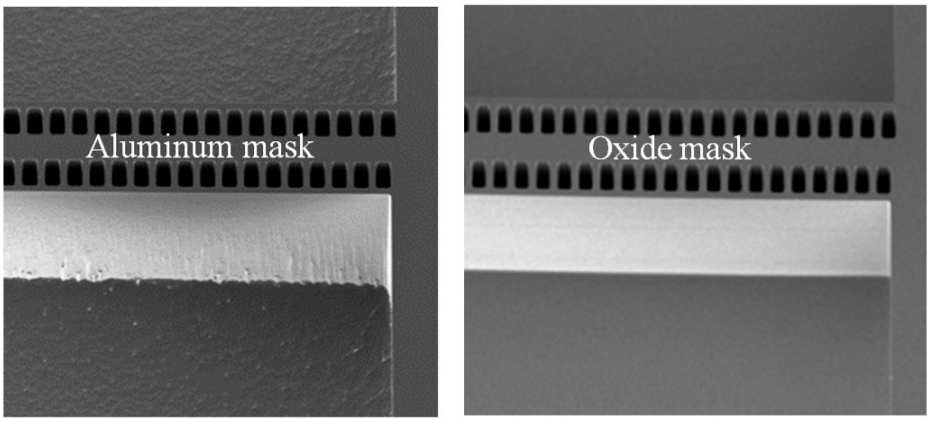

(a) (b)

Fig. 2.8. DRIE with oxide mask results in higher etching quality for sidewalls and bottom surfaces.

The scalloping depth of the DRIE was measured at a depth of about 100 μm and found to be about 150 nm as shown in Fig. 2.9. This value is unacceptable according to the specifications in Table 2.1 and consequently there is a need for applying a smoothing

technique. The alternative of modifying the DRIE process parameters by reducing the etching cycle time was not available due to the relatively long response time of the mass flow controllers of the equipment.

2.3.4 Post-DRIE cleaning

A post-DRIE cleaning process was performed to get rid of the accumulating polymer on the sidewalls and to prepare the wafer for insertion in the oxidation furnace without contaminating the furnace tube. The wafer was subjected to oxygen plasma in a MATRIX stripper at a temperature of 220^0 C, a pressure of 3 Torr and an RF power of 450 watt for 12 minutes. Then the wafer was immersed in a fuming nitric acid (HNO_3 99 %) for 10 minutes. We found that these two steps are effective in cleaning the accumulating polymer. For overall cleaning of the wafer, a piranha solution was formed by adding sulfuric acid (H_2SO_4) 96% to hydrogen peroxide (H_2O_2) 30% with volumetric composition of 1:1. The solution heats up by itself and lasts for about one hour. Because the mixture is a strong oxidizing agent, it removes most organic matters. The wafer is immersed in the piranha solution for 10 minutes. The wafer is subjected to DI water after each wet process. Then, the wafer was immersed in isopropyl alcohol or IPA (C_3H_8O) for 5 minutes and heated in 110^0C oven for 10 minutes. The IPA helps in disrupting the surface tension of water and results in traces-free cleaning of the wafer especially in deeply etched trenches.

2.3.5 Post-DRIE smoothing

The smoothing step was carried out by subjecting the wafer to 1 μm wet oxidation process at a temperature of 1100^0C process. We didn't use a special process step for removing the grown oxide. The oxide is, instead, removed during the release step in vapour HF 50 %. Indeed, we have tried another smoothing alternative by a short etching step in a solution of potassium hydroxide (KOH). The oxidation process was found to be more effective in reducing the scalloping depth without an excessive overetching. The resulting scalloping depth was measured and found to be about 60 nm as shown in Fig. 2.9. This value meets the specification listed in Table 2.1. A tilted view of the movable mirror from the front is shown after release in Fig. 2.10. The scalloping effect is barely observable, which indicates the high quality of the etched surface. Optical characterization of the mirror's reflectivity and the overall Michelson interferometer performance improvements will be given in the optical measurements section.

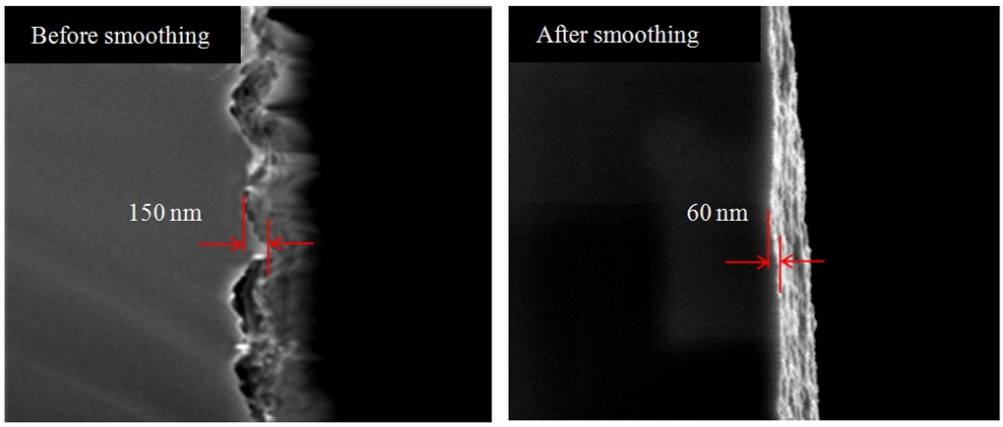

Fig. 2.9. DRIE scallops before and after smoothing by oxidation and oxide etching: the scalloping depth was reduced from about 150 nm to about 60 nm.

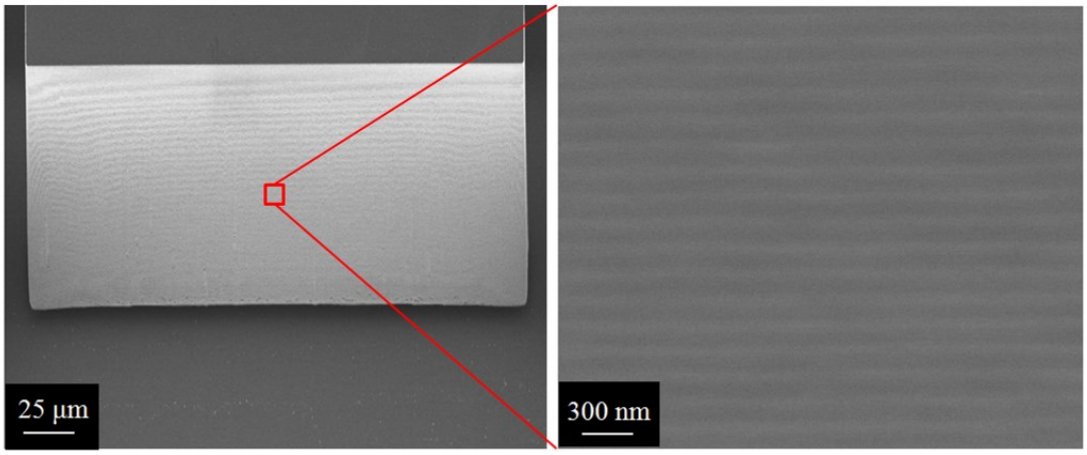

Fig. 2.10. Front view of the movable mirror after etching the BOX layer with zoom-in on the right emphasizing the quality of the mirror surface.

2.3.6 Packaging

Packaging of the Michelson interferometer was an important step to ensure the protection of the structure and for carrying out optical measurements outside of the clean environment. The individual designs were capped using Pyrex covers. The Pyrex covers were pre-fabricated by double-side etching of a Pyrex wafer for having opening above the electrical pads and for having a recess above the moving parts. The Pyrex wafer was diced and each individual covers was attached to the SOI wafer using a pick-and-place machine as shown in Fig. 2.11 (a). Then, the individual designs were separated and attached to PCB boards. Electrical connectivity is carried out by wire bonds connecting the electrical pads of the MEMS and the PCB board.

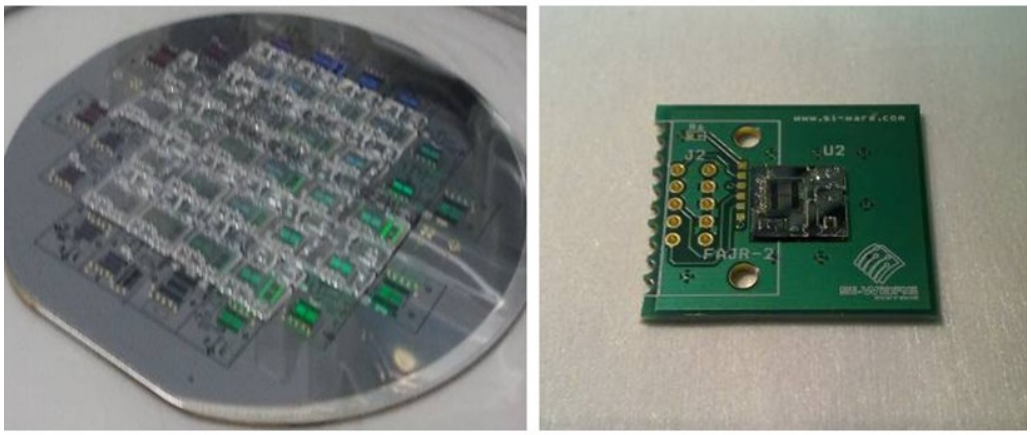

(a) (b)

Fig. 2.11. (a) Pyrex capping of the individual designs. (b) The individual designs are attached to PCB boards and wire bonding is carried out for electrical connectivity.

2.4 Optical measurements

The reflectivity of the fabricated micromirrors was measured at 1550 nm and was found to be larger than 90 %. This indicated a good quality optical mirror convenient for our application. In fact, the reflectivity of the unsmoothed mirror was also measured but found to be about 50 %. This means about 2.5 dB improvement due to the smoothing process. The reflectivity measurement was repeated using a white light source. This is of particular interest to the spectrometry application. More specifically, we used AvaLight-HAL Tungsten Halogen Light Source sold by AVANTES. The source has a spectral width extending from 360 nm to 2500 nm. The measured reflectivity was also about 90 %.

Michelson interferometers with device layer heights of 90 μm and 200 μm were fabricated for the sake of comparing their delivered signal level; i.e. to evaluate the impact of the developed process on the miniaturized instrument performance. For spectrometry applications, multi-mode optical fibers can

be used in delivering the optical power from the white light source to the Michelson interferometer. Multi-mode optical fibers haves the advantage of much larger core diameters, and hence larger power coupled from the source, than single-mode optical fibers. Therefore, 62.5/125 µm and 200/230 µm multi-mode fibers were used in the cases of Michelson interferometers with device layer heights of 90 µm and 200 µm, respectively.

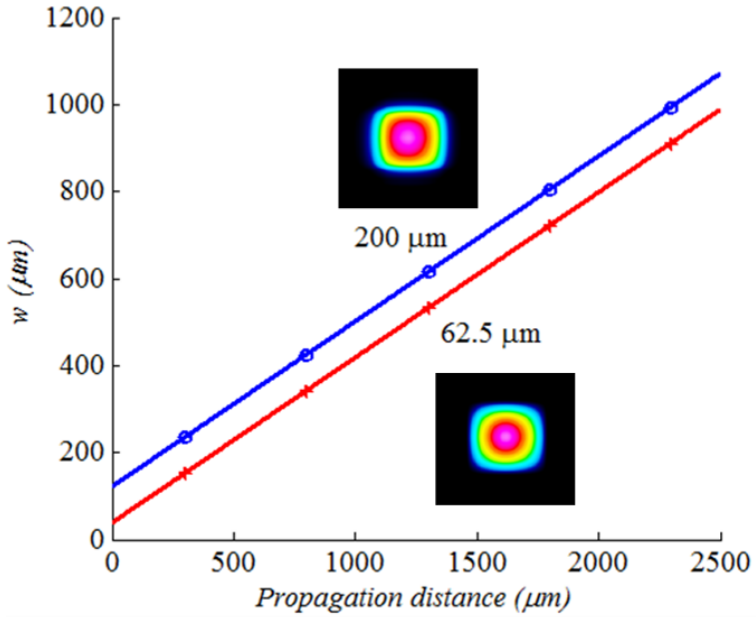

Fig. 2.12. Multi-mode fibers output beam radius versus the propagation distance measured for fiber core 62.5 µm and 200 µm with the fibers fed form white light source. Typical spot profiles are shown after 2000 µm propagation distance.

The multi-mode fibers output was characterized using using DataRay Inc. BeamScope^{TM}-P8 scanning slit beam profiling system [85]. This step helps in appreciating the need for micro-optical benches with larger device layer heights. From one end, the fibers were fed from the white light source previously mentioned and the fibers were bare and cleaved from their second end. The output beam is left to propagate in free space and then measured using the beam profiler. The measurement spot radius versus propagation distance is shown in Fig. 2.12. The cone divergence half-angle of the

propagating field is about 21 degree corresponding to a numerical aperture of about 0.38, which is much larger than the 0.22 numerical aperture specified at 1550 nm by the fiber manufacturer. We attributed this difference to the wide spectrum of the non-coherent white light. The spot intensity profiles, after 2000 μm propagation distance, are shown by the insets in Fig. 2.12. The profiles exhibit a tendency to a flat-top beam. The shape of the intensity pattern can be different for each wavelength component but the contributions from different wavelengths are averaged out. Theoretical details about the output beam of a multi-mode fiber can be found in [59].

The measurement setup, used for measuring the Michelson interferometers, is shown schematically in Fig. 2.13. Cleaved multi-mode fibers were inserted into micromachined grooves self-aligned with the interferometer in the input and output locations. The input fiber is fed from the source while the output fiber is connected to a detector working in the 1100-1800 nm spectral range.

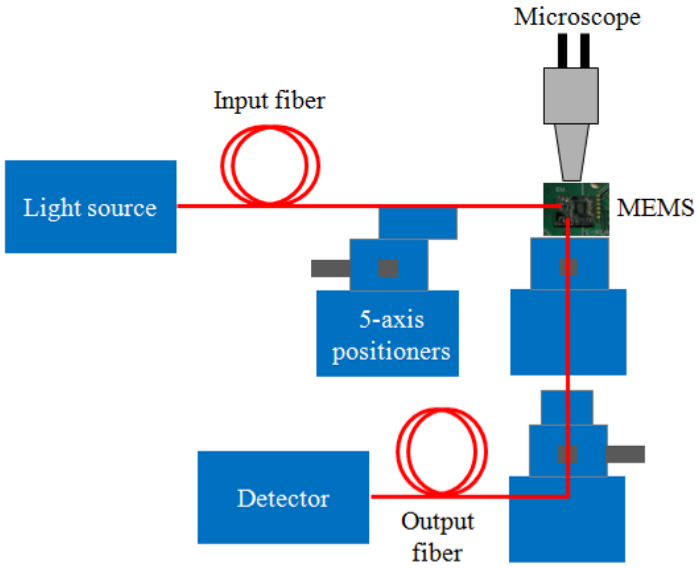

Fig. 2.13. Schematic drawing of the Michelson interferometer measurement setup.

First the input fiber is fed from a laser source working at 1550 nm for the purpose of calibrating the comb-drive motion versus the applied voltage. This is achieved by counting the interferogram fringes where the peak to peak separation is equivalent to an optical path difference (OPD) of λ/2. Once the x-v relation is obtained, the interferogram can now be plotted versus the OPD directly [22].

The measured Michelson interferometer is a more complicated version of the simple one shown in Fig. 2.1. The inherent dispersion problem in silicon is compensated using balancing interfaces [60]. The comb-drive is double-sided and works in push-pull operation in order to produce large displacement [78-79]. At the center of the device, a double-folded flexure is used to avoid non-linearity at large displacement [80].

As mentioned previously, Michelson interferometers with device layer heights of 90 µm and 200 µm were measured. The multimode fiber with cladding diameters of 125

μm was used in the case of 90 μm device layer height while the multimode fiber with cladding diameters of 230 μm was used in the 200 μm device layer height case. The resulting white light interferograms are shown in Fig. 2.14 (a) and (b), respectively. The signal level is improved 16 times using the 200 μm device layer height compared to the 90 μm device layer height. This 12 dB improvement is directly adding to the signal to noise ratio of the miniaturized instrument. Increasing the device layer height enabled the use of 200 μm core fibers which is about 10 times larger in area than the 62.5 μm core fibers. The collected power from the white source was increased by a similar ratio. We consider this a significant improvement in the instrument performance and a jump towards bringing micro-optical bench based instruments to the practical life. Indeed, the developed process is versatile enough to be used with many optical arrangements without restriction on the optical surfaces profiles or orientation. The same process will be used in demonstrating the wide-angle microscanner presented in chapter 3.

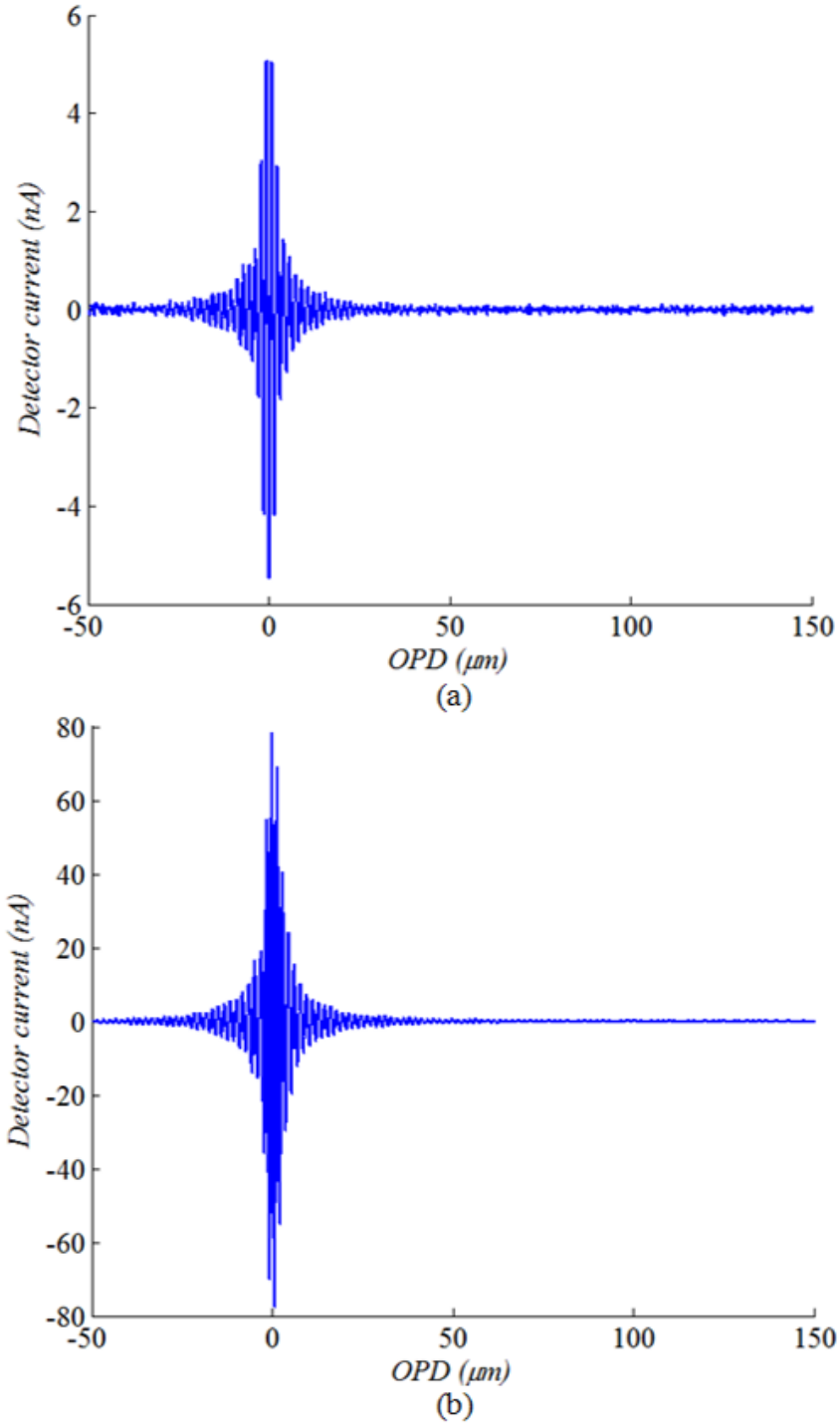

Fig. 2.14. Measured white light interferogram using the fabricated interferometer with 90 μm depth in (a) and 200 μm depth in (b).

2.5 Summary

A fabrication process was developed for the production of high optical throughput micro-optical benches. The process is based on deep reactive ion etching technology and doesn't involve the use of long anisotropic etching steps. Consequently, arbitrary surfaces profiles, including curved surfaces, could be fabricated without restriction on the surface orientation. Etching depths larger 300 μm was demonstrated with side wall angle verticality better than 0.1 degree and scalloping depth smaller than 60 nm. The process was characterized in terms of the verticality of different trench widths and square openings. The optical reflectivity of the deeply-etched micromirrors with aluminum metallization was measured at 1550 nm and found to be larger than 90 %. This indicates a high quality optical surface.

A miniaturized monolithic scanning Michelson interferometer was demonstrated on-chip using the developed process. The interferometer was realized on SOI wafers with device layer heights of 90 μm as well as 200 μm, for the sake of evaluating the performance improvement. Multi-mode optical fibers with core diameters of 62.5 μm as well as 200 μm were used for delivering the white light optical signal to the silicon chip. The resulting interferograms were measured and compared. There was about 12 dB improvement in the detector signal, which is a significant improvement in the miniaturized instrument performance.

CHAPTER 3
INTEGRATED WIDE-ANGLE MICROSCANNER

3.1 Introduction

Optical beam scanners are key components in a wide range of applications including displays, optical communications, imaging, printing and surgery [62-65]. Miniaturization of the scanners reduces their cost and size enabling new applications that were not possible using their original bulky form; these include handheld barcode readers, pico projectors, confocal microscopy, Optical Coherence Tomography (OCT) and endoscopy [66-49]. The integrability of the scanner with other optical components on the same substrate is an important asset that allows great cost reduction and opens the door for more applications. A good example of this application is the OCT in which the optical scanner could be integrated with a beam splitter and either a moving mirror or a tunable laser to form an integrated OCT head working in either time domain or frequency domain, respectively.

In the conventional microscanning architecture, incident beam from a laser source is first collimated using a lens in order to reduce its divergence angle, and then reflected into different directions using a flat mirror rotating around its central axis as shown in Fig. 3.1 (a). To this end, several actuation mechanisms were reported including electrostatic [47], piezoelectric [50], thermal [51] or magnetic [52] actuation with the aim of increasing the achievable scan angle and speed, which is a challenging task. Another

challenge in the rotating micromirrors architecture arises due to the static or the dynamic bending of the mirror surface during the micromachining process or during the scanner operation, respectively [70]. MEMS mirrors are usually coated with a thin metal film to improve the reflectivity. This coating, in addition to the method of fabrication, can cause stress gradient across the mirror thickness leading to a permanent curvature of the reflecting surface, which may be compensated by the accompanying optics. More seriously, dynamic bending during the operation cannot be compensated. Indeed, a radius of curvature equal to or smaller than the scanned beam Rayleigh range can lead to a severe increase of the far-field beam radius and renders the beam spot size vary significantly during the scanning [71]. Assembly cost of the scanner shown in Fig. 3.1 (a), bringing up the laser source, the collimating optics as well as the rotating mirror all aligned together, is a third challenging issue in this architecture. Monolithic integration of a diffractive Fresnel zone plate on a scanning micromirror was reported as a step towards simplifying the assembly [72], yet source integration and the possibility of monolithic integration of other micro-optical components were not possible.

Microscanners based on refraction of light from a translated microlens were also reported [43-46]. A micro stage attached to an electrostatic or piezoelectric actuator is usually micromachined, and then the lens is inserted and fixed on that stage. Again the assembly and fixation of the microlens on the stage and in conjunction with the source is not a trivial task. The weight of the lens harms the agility of the system while the scanning angle is limited by the optical properties of refraction. Typical maximum scanning angle of ± 5-10 degrees and speed in the order of 200 Hz were reported [43].

Therefore, there is a need for a wide angle scanner that can be monolithically integrated with other components on the same chip.

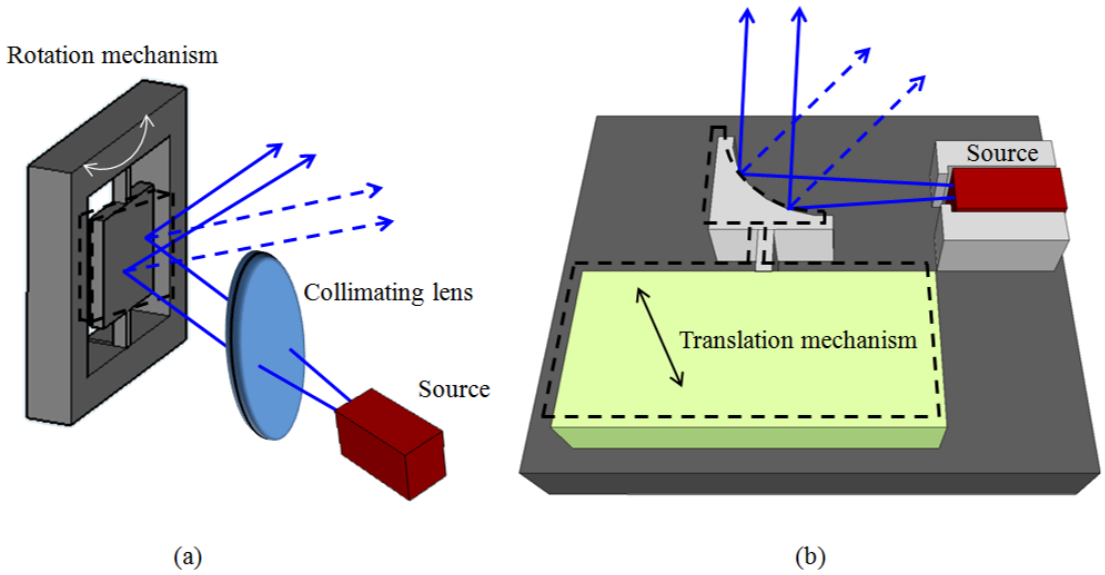

Fig. 3.1. Conventional scanning architecture based on a rotating flat mirror is shown in (a). The presented scheme based on a translating curved mirror is shown in (b). In the presented scheme, wide angle scanning can be easily obtained, the mirror dimensions can be controlled independent of the mechanical components of the system, the optical beam is collimated in-plane and the source, as well as other micro optical components,

In this chapter, we present an optical scanning architecture based on translating a curved mirror as shown in Fig. 3.1 (b) [73-77]. The incident beam from the source is simultaneously collimated and reflected by the micromirror while the latter is attached to a translational motion mechanism. At one position, the incident beam is reflected in a given direction. By translating the curved mirror to another position, a new deflection

angle is achieved. In this way, ultra-wide optical scanning angles, in principle up to 180 degrees, can be obtained. More importantly, the mirror surface and its translation path are designed carefully to maintain the uniformity of the beam spot size across the scanning window [75]. The optical beam propagates parallel to the wafer substrate and, thus, the optical source, the curved mirror and a microelectromechanical actuator can be all integrated on chip. This significantly reduces the alignment and assembly issue usually encountered in the conventional scanners. The source can be also replaced by an optical fiber inserted into a fiber groove where the latter can be lithographically aligned with the mirror. The presented architecture opens the door for a completely integrated laser scanner with beam splitters, filters and laser sources self-aligned on the same chip that allows low cost and mass production of this important product family.

3.2 Optical beam transformation

Before studying the performance of the presented scanner, this section briefly describes the transformation of a Gaussian beam (GB) after reflection on a surface, which is curved along one dimension. This allows to evaluate both cylindrical and acylindrical reflectors. For this purpose, consider an incident GB on a curved reflector with an angle of incidence θ_{inc} as shown in Fig. 3.2. In this case, the incidence plane is referred to as the tangential plane (t-plane) and the plan perpendicular to the tangential plan while containing the beam optical axis is referred to as the sagittal plane (s-plane). Let the reflector surface has a radius of curvature R in the t-plane while the surface cross section

is flat in the s-plane. The incident GB undergoes a transformation in the t-plane described by the ABCD matrix given by Eq. (3. 1) [82]:

$$M = \begin{bmatrix} A & B \\ C & D \end{bmatrix} = \begin{bmatrix} 1 & 0 \\ \frac{2}{R\cos\theta_{inc}} & 1 \end{bmatrix} \tag{3. 1}$$

The focal length of the transformation is given by Eq. (3. 2):

$$f = -0.5R\cos\theta_{inc} \tag{3. 2}$$

The output beam waist w_{out} and the distance d_{out} between the waist location and the point of incidence are related to their input beam counterparts by Eq. (3. 3) and (3. 4) [83]:

$$w_{out} = \frac{w_{in}}{\sqrt{\left(Cd_{in} + D\right)^2 + C^2 z_o^2}} \tag{3. 3}$$

$$d_{out} = \frac{\left(Ad_{in} + B\right)\left(Cd_{in} + D\right) + ACz_o^2}{\left(Cd_{in} + D\right)^2 + C^2 z_o^2} \tag{3. 4}$$

where w_{in} is the waist radius of the input GB, d_{in} is the distance between the location of the input GB waist and the point of incidence and z_o is the Rayleigh range of the input GB. Using the matrix parameters in Eq. (3. 1) the normalized output beam parameters are given by Eq. (3. 5) and (3. 6):

$$\frac{z_R}{z_o} = \frac{1}{\left(1 - \frac{d_{in}}{f}\right)^2 + \frac{z_o^2}{f^2}} \tag{3. 5}$$

$$\frac{d_{out}}{f} = \frac{z_R}{z_o}\left[\frac{z_o^2}{f^2} - \frac{d_{in}}{f}\left(1 - \frac{d_{in}}{f}\right)\right] \tag{3. 6}$$

where z_R is the Rayleigh range of the output GB. Eq. (3. 2), (3. 5) and (3. 6) will be used to study the deformation in the output GB spot size and waist location with scanning.

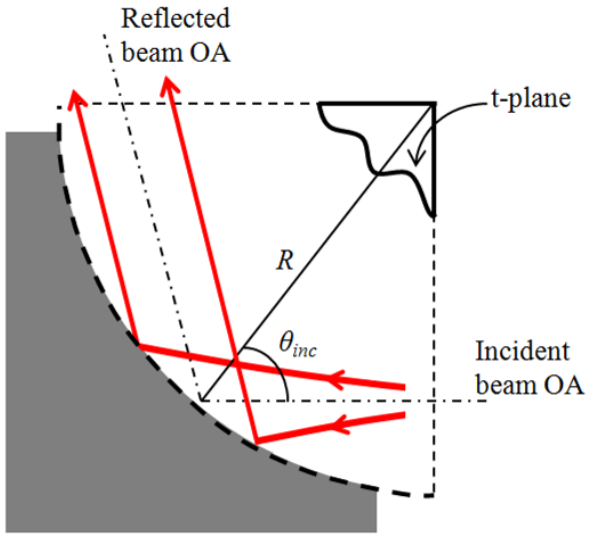

Fig. 3.2. A GB is incident on a curved reflector with an angle of incidence θ_{inc} where the reflector radius of curvature is R. The tangential plane contains the incident as well as the reflected beam Optical Axis (OA) while the sagittal plane is normal to the tangential one and contains the beam OA.

3.3 Scanning based on cylindrical mirrors

In its simplest form, the optical scanning architecture can be built using a cylindrical mirror. The proposed scanning architecture shown in Fig. 3.1 (b) can be achieved by shifting the mirror principle axis in a normal direction with respect to the incident beam optical axis while holding the input GB waist location fixed at a distance f_o from the mirror vertex, where f_o = -0.5R. The focal length of the curved reflector varies

with the incidence angle as given in Eq. (3. 2). As a result when a cylindrical mirror is used, the reflected beam parameters given by Eq. (3. 5) and (3. 6) vary significantly with scanning as shown in Fig. 3.3. The study is carried out for f_o / z_o ratios of 1, 5 and 10. The variation amplifies with f_o / z_o both for z_R / z_o and d_{out} / f_o. For example, a 10 % reduction in z_R / z_o is found at 10, 13 and 25 degrees for f_o / z_o of 10, 5 and 1 respectively. The negative peak in d_{out} / f_o is reduced and shifted to larger angles for smaller f_o / z_o. The variation of the output beam waist location may not be critical as long as we are interested in the output beam at the far field. The significant roll off in the Rayleigh range of the output beam is, however, a critical drawback in the scanner performance based on a cylindrical reflector. This deteriorated output limits the overall scan angle of the curved reflector and the Rayleigh range of the output beam that are predominate factors in defining the scanner performance.

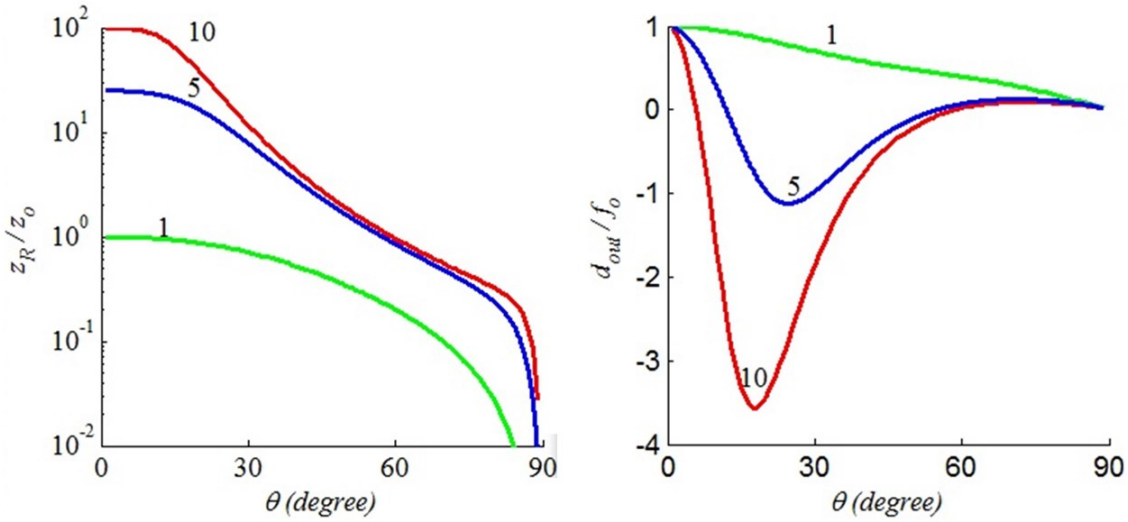

Fig. 3.3. The variations of the output beam normalized parameters with the incidence angle for mirror focal length to input beam Rayleigh range (f_o / z_o) ratios of 1, 5 and 10. The variations of the output beam Rayleigh range is shown in (a) while the variation of the output beam waist location is shown in (b).

3.4 Scanning based on acylindrical mirrors

The aforementioned drawback of cylindrical reflector based scanning is encountered due to the reduction in focal length by the inclined incidence factor *cos* (θ_{inc}). In addition, a mismatch arises between the focal length and the distance between the input GB waist and mirror surface, which varies according to Eq. (3. 7):

$$d_{in} = f_o - 2f_o\left[1-\cos\left(\theta_{inc}\right)\right] \qquad (3.\ 7)$$

The focal length is maximized at zero degree angle of incidence where d_{in} is matched to the focal length only at this specific angle. Therefore, a special design for the mirror

curved profile coupled to its translation path is needed. The translation motion of the mirror can be in the form of one or two degrees of from as shown in Fig. 3.4.

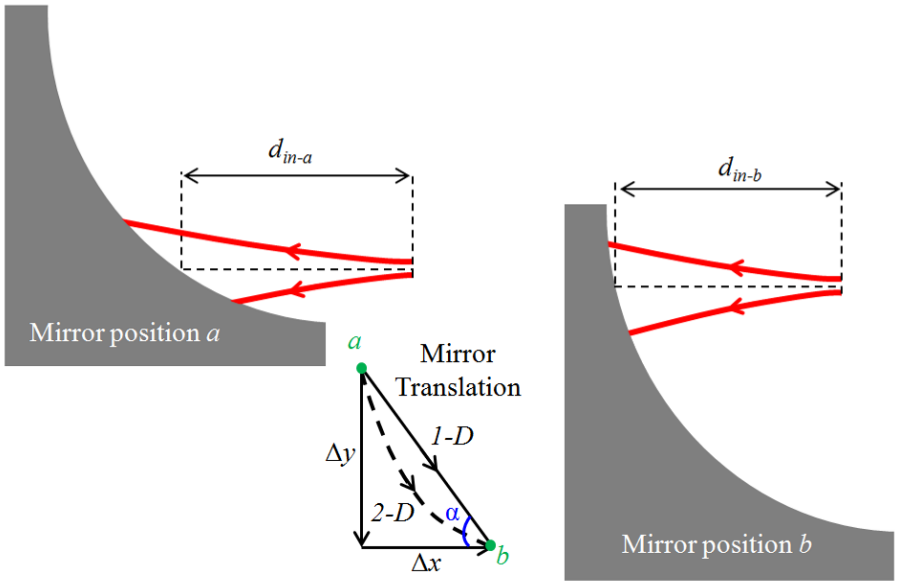

Fig. 3.4. Two-Degree (2-D) of freedom motion of the mirror follows a curved path from position a to position b while One-Degree (1-D) of freedom motion of the mirror follows a linear path.

3.4.1 Two-degree of freedom translation

Maintaining a constant separation between the beam waist and the mirror surface at incidence point can be achieved by a 2-degree of freedom motion on a curved path as shown in Fig. 3.4. The normal motion in one direction Δ*y* performs the scanning function while an additional motion Δ*x*, parallel to the incident beam optical axis, keeps d_{in} constant. Keeping the focal length of the curved surface constant and independent of the

incidence angle is imposed by the introduction of a new acylindrical surface profile satisfying Eq. (3. 8):

$$-0.5R(\theta_{inc})\cos(\theta_{inc}) = \text{constant} = f_o \qquad (3.\ 8)$$

where $R = R\ (\theta_{inc})$ is now a function of the incidence angle, leading to an acylindrical shape for the mirror. Substituting for the radius of curvature of the surface and the cosine of the angle of incidence in terms of the surface first and second derivatives, Eq. (3. 8) can be rewritten as a second order non-linear differential equation:

$$2f_o y'' - y'^3 - y' = 0 \qquad (3.\ 9)$$

The analytical solution of Eq. (3. 9) was found and arranged in the expression in Eq. (3. 10):

$$y = y_v - 2f_o \tan^{-1}\left(\exp\left[\frac{-x_v}{2f_o}\right]\sqrt{\exp\left[\frac{x}{f_o}\right] - \exp\left[\frac{x_v}{f_o}\right]}\right) \qquad (3.\ 10)$$

where (x_v, y_v) is the curved surface vertex coordinates, and x and y are the Cartesian coordinate system. The reflected beam parameters are depicted in Fig. 3.5 versus the incidence angle for f_o / z_o of 10, 5 and 1. Uniform spot size and waist location are obtained without degradation versus the incidence angle and up to 90 degrees; corresponding to 180 degrees optical deflection angle.

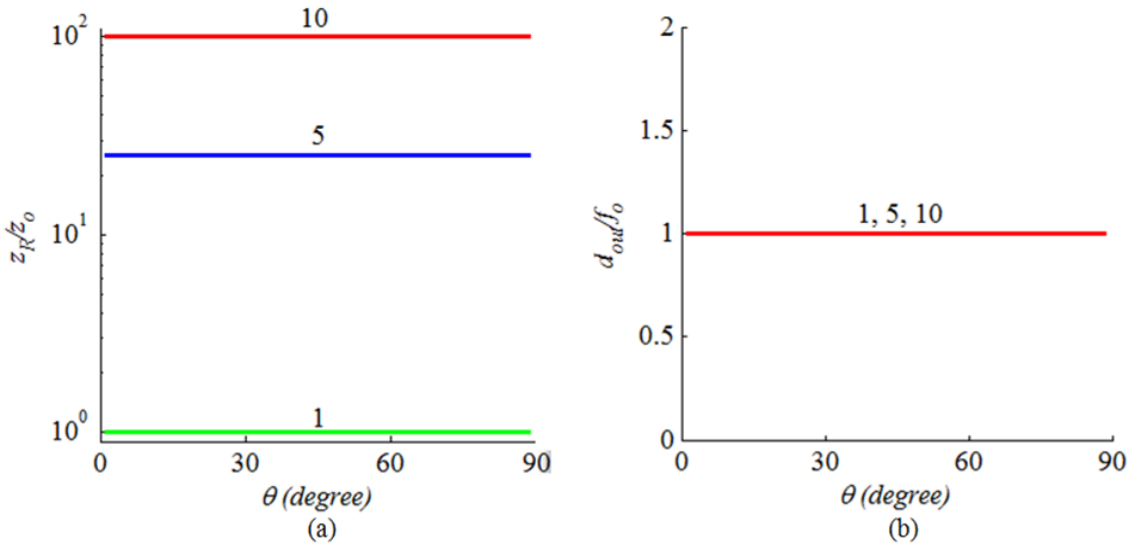

Fig. 3.5. Uniform output beam parameters can be obtained using the surface described by Eq. (3. 10) up to 180 degrees optical deflection angle. The study is carried out for f_o / z_o ratios of 1, 5 and 10.

Skew GB simulation capability in ZEMAX® was used to verify our theoretical expectation from the simple ABCD matrix. In contrast to the paraxial GB analysis, skew GB can account for tilt and decenter of the optical axis from one component to another. The simulation wavelength was set at λ = 1550 nm and the mirror focal length was set to f_o = 200 μm. The GB waist size was varied in order to have f_o / z_o ratios of 10, 5 and 1. Indeed, using a polynomial representation fitting the surface in Eq. (3. 10) results in a non-accurate result because of the radius of curvature of the surface described by the polynomial being not matching that of the surface in Eq. (3. 10). Therefore, the surface has to be described, in terms of its sag, as a user-defined surface in a "dll" file. The

surface sag used in this definition is found by the inverse function of (3. 10) when (x_v,y_v) = (0,0):

$$sag = -f_o \ln\left[\cos^2\left(-0.5y / f_o\right)\right] \qquad (3.\ 11)$$

The results of this simulation were exactly matching to those presented in Fig. 3.5. Then a physical optics propagation simulation was carried out to examine the quality of the reflected beam spot from the presented surface in Eq. (3. 10) and estimate the practical limits on the scanning. The intensity profile was obtained for incidence angles of 0^o, 25^o, 50^o and 75^o as shown in Fig. 3.6. The profiles are distortion-free even for the case of 75^o incidence angle when $f_o / z_o = 1$. For $f_o / z_o = 5$, the output profile peak shifts to the left with increment in the incidence angle and side lobes appears clearly for 75^o incidence angle. These artifacts are larger for the case of $f_o / z_o = 10$ while seem to be still acceptable for many scanning applications. The collimation gain is given by f_o / z_o and, therefore, the smaller the collimation gain needed from the scanning mirror, the larger the scanning angle that can be achieved while maintain the output beam with minimum distortion.

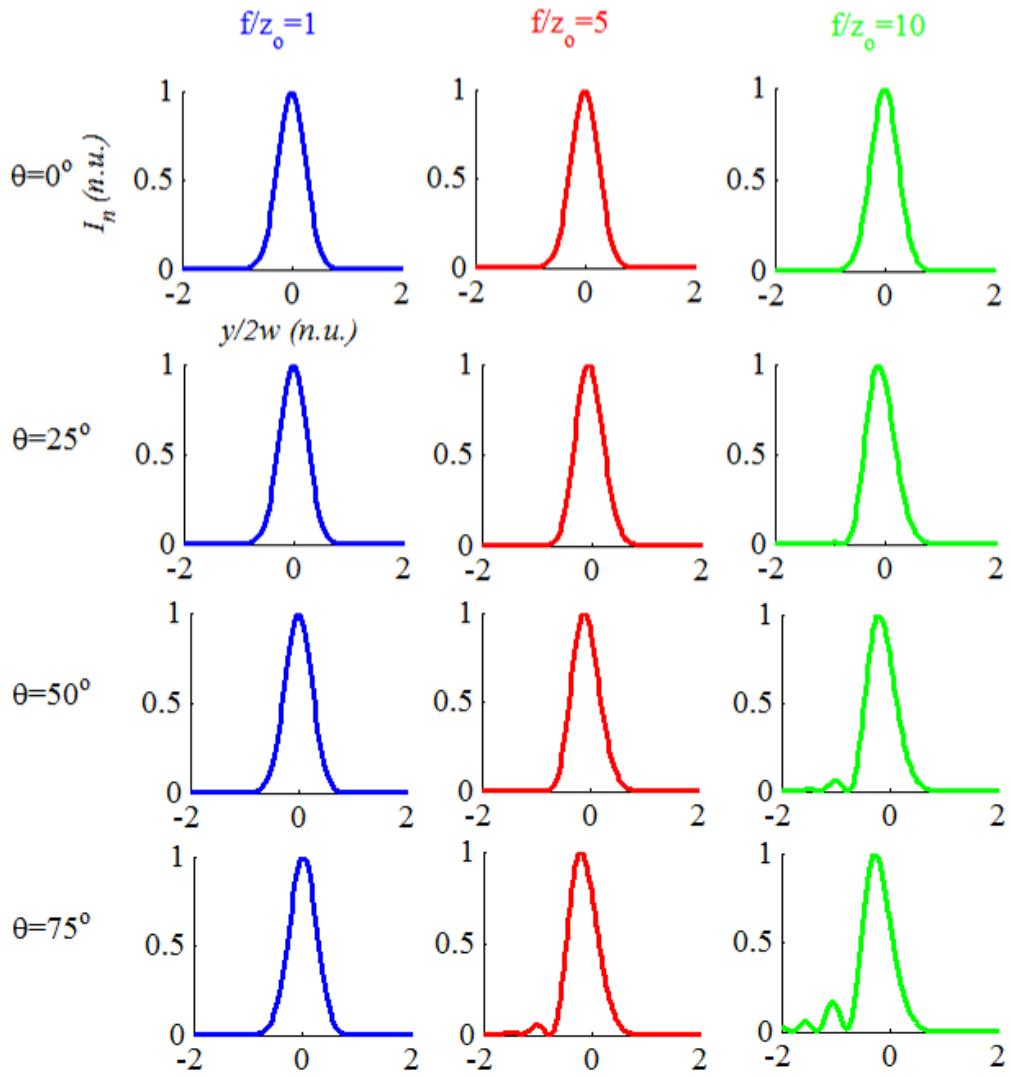

Fig. 3.6. Reflected beam intensity profile from the curved mirror described by Eq. (3. 10) upon the inclined incidence of a GB on the mirror surface. The profile is examined for f_o/z_o ratios of 10, 5 and 1 and for incidence angles of 0, 25, 50 and 75 degrees.

3.4.2 One-degree of freedom translation

Although an in-plane translational motion with two-degree of freedom is achievable, it can be challenging and lead to complicated MEMS design. An alternative solution is to tilt the translation path of the curved mirror with the appropriate angle α with respect to the incident beam optical axis as shown in Fig. 3.4. This tilting can play an important role in minimizing the input distance variation. The mirror surface has to be designed carefully, in accordance. The differential equation describing the mirror surface is formulated by equating the effective focal length of the mirror surface to the input distance in conjunction with keeping the tilted motion path mentioned previously:

$$-0.5R(\theta_{inc})\cos(\theta_{inc}) = d_{in} \qquad (3.\ 12)$$

By substituting for the radius of curvature of the mirror surface as well as the cosine of the angle of incidence in terms of the surface first and second derivatives, Eq. (3. 12) can be put in the form:

$$\frac{0.5y'(1+y'^2)}{y''} = f_o - x + y/m \qquad (3.\ 13)$$

The right hand side in Eq. (3. 13) represents the input distance and the factor m = 1/ *tan* (α). The solution of Eq. (3. 13) could be found numerically as a family of curves resulting from different values of m. For example, Figure 5 depicts the solution for m = 1, 2, 10 and infinity where the latter value describes the case of translating the mirror in a normal direction with respect to the incident beam optical axis. The cylindrical cross sectional profile is close to the solution of Eq. (3. 13) when m = 10. Indeed, the different values of m don't change the starting behavior of the curve as governed by the derivative boundary

value at the vertex which was set to infinity in our case. For smaller values of m, the curve tends to be more linear at larger y-coordinate values. This will, consequently, limit the maximum obtainable scanning angle for a given translation.

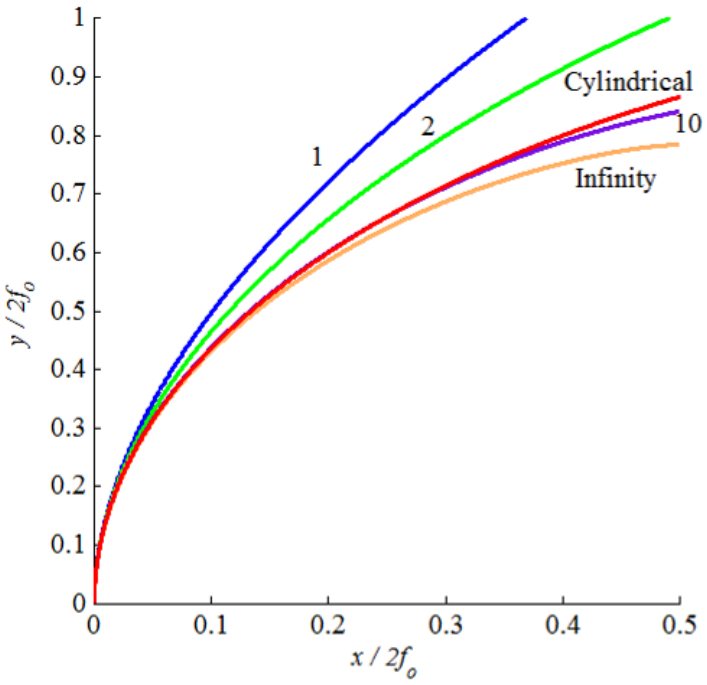

Fig. 3.7. Solution of Eq. (3. 13) for different values of m compared to the cylindrical cross sectional profile.

A study was carried out seeking the appropriate tilt angle that minimizes the output beam parameters variations on a wide scanning angle range. The tilt angle was found to be $\alpha \approx 26.5$ degrees corresponding to $m \approx 2$. For this case, the reflected beam parameters are depicted in Figure 6 versus the incidence angle for f_o / z_o of 10, 5 and 1. Nearly uniform spot size and waist location are obtained versus incidence angle up to 55

degrees; corresponding to 110 degrees optical deflection angle. Indeed, there is a significant improvement as compared with the scanning performance shown in Fig. 3.8.

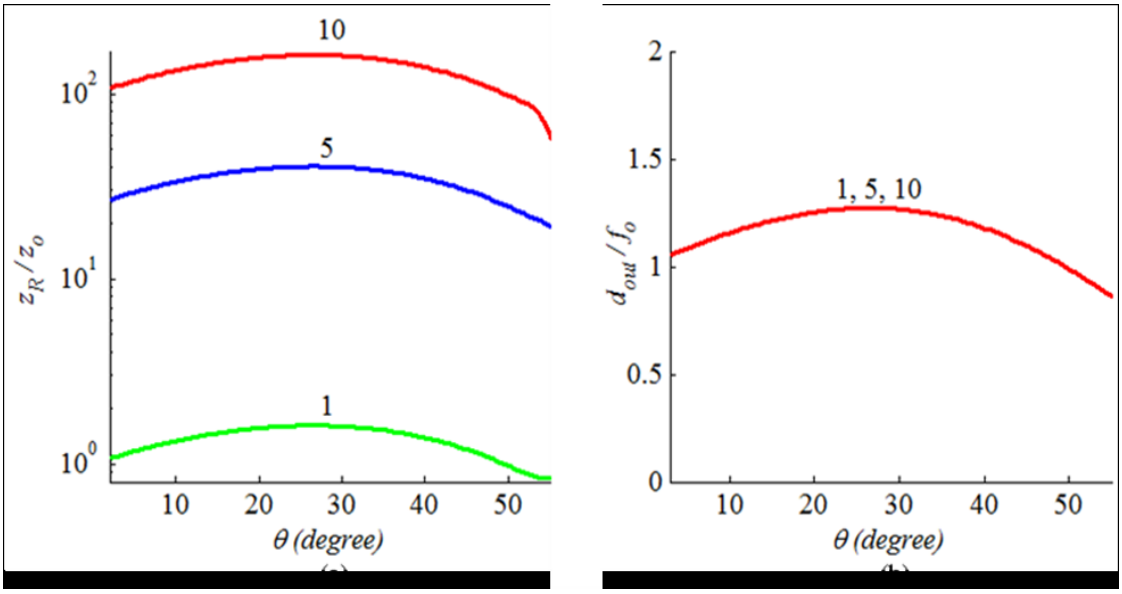

Fig. 3.8. Nearly uniform output beam parameters can be obtained using the surface described by Eq. (9) for m = 2 up to 110 degrees optical deflection angle. The study is carried out for f_o / z_o ratios of 1, 5 and 10. For the different ratios, the same normalized output distance (d_{out} / f_o) can be obtained as shown in (b).

3.5 Micro-optical-bench scanner

An SOI optical bench was designed and fabricated using deep reactive ion etching of silicon making use of the developed fabrication process presented in chapter 2 of this thesis. The overall layout of the design is shown in Fig. 3.9 (a). An electrostatic comb-drive was used in order to produce the desired translational motion. In principle, other

actuation mechanisms are also possible. The comb-drive is double-sided and works in push-pull operation in order to produce large displacement [78-79]. At the center of the device, a double-folded flexure is used to avoid non-linearity at large displacement [80]. The electrical routing to the electrodes is made using the silicon layer while the electrodes as well as the mirrors are metalized using the shadow mask technique. A scanning electron microscope image of the fabricated device is shown Fig. 3.9 (b). Acylindrical mirror with f_o = 200 μm is attached to the comb-drive and a fiber groove is etched facing the mirror where the optical fiber axis is tilted with respect to the comb-drive motion direction. The metalized area around the mirror can be observed by its higher brightness in Fig. 3.9 (b). The optical fiber, inserted into the fiber groove, is working as an optical source with a GB output. The beam is incident on the mirror in an off-axis manner and the output beam deflection angle can be scanned by applying an electrical voltage on the comb-drive electrodes. Aside from the mirror attached to the actuator, acylindrical mirrors with focal length f_o of 100, 200 and 400 μm were also fabricated. The both types of profiles related to two-degree and one-degree of freedom motions were considered. These mirrors enable the static testing of the optical performance in terms of the reflected beam spot size and intensity profile. In the latter case, the relative motion between the fiber and the mirror was achieved using external mechanical motion stage while the optical fiber is left free to move with respect to the mirror.

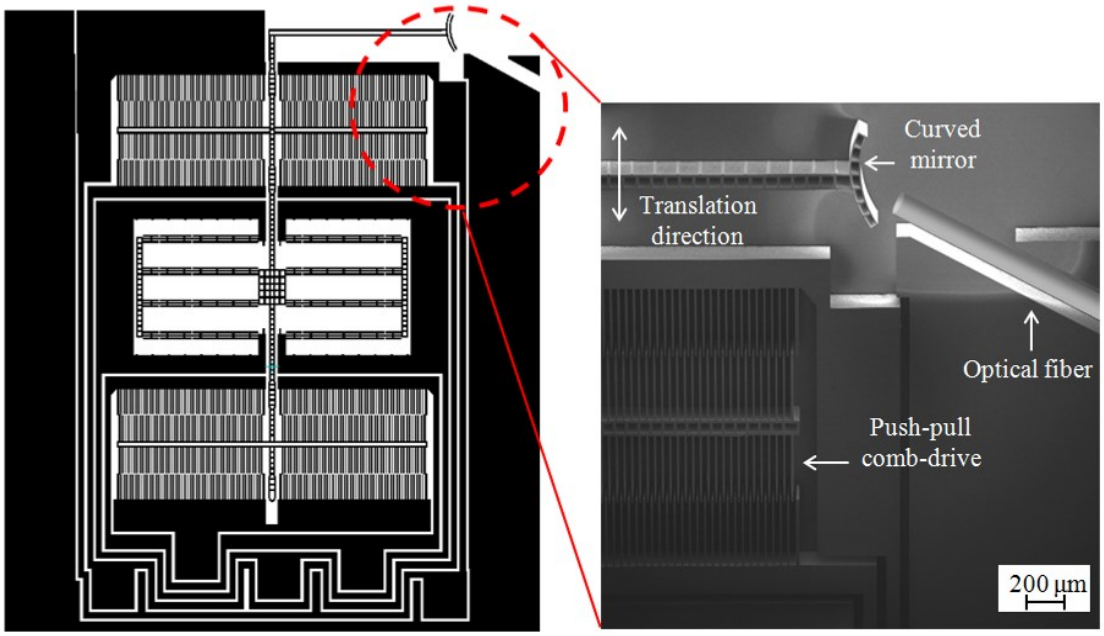

Fig. 3.9. Overall structure of the microscanner device in (a) and a Scanning Electron Microscope (SEM) image of the fabricated device in (b) with a zoom-in on the comb-drive fingers, attached curved mirror and an optical fiber inserted into the etched groove self-aligned with the mirror.

3.5.1 Electrical measurements

Electrical measurements were carried out to characterize the comb-drive resonance frequency and quality factor. The equivalent parallel conductance and capacitance of the comb-drive actuator were measured using an HP 4149A impedance analyzer instrument [81]. The low voltage terminal of the instrument was connected to the electrode of the movable fingers while the high voltage terminal was connected to the fixed fingers. In order to prevent sticking between the movable fingers and the handle

layer (substrate), the electrodes of both of them have to be at the same electrical potential. This could be achieved by connecting the movable fingers electrode to the instrument virtual ground while the substrate was connected to the real ground. The comb-drive was biased by a DC voltage and a small superimposed ac signal. The ac signal frequency was swept from 270 to 390 Hz around the expected comb-drive resonance frequency. The measurement results for the conductance and the capacitance are depicted in Fig. 3.10 (a) and (b), respectively, using markers. The motional parameters of the equivalent circuit were extracted [81] and fitting of the data was applied (see lines in Fig. 3.10). The estimated quality factor is close to 22 with a resonance frequency of about 329 Hz. These measurements were carried out at atmospheric pressure.

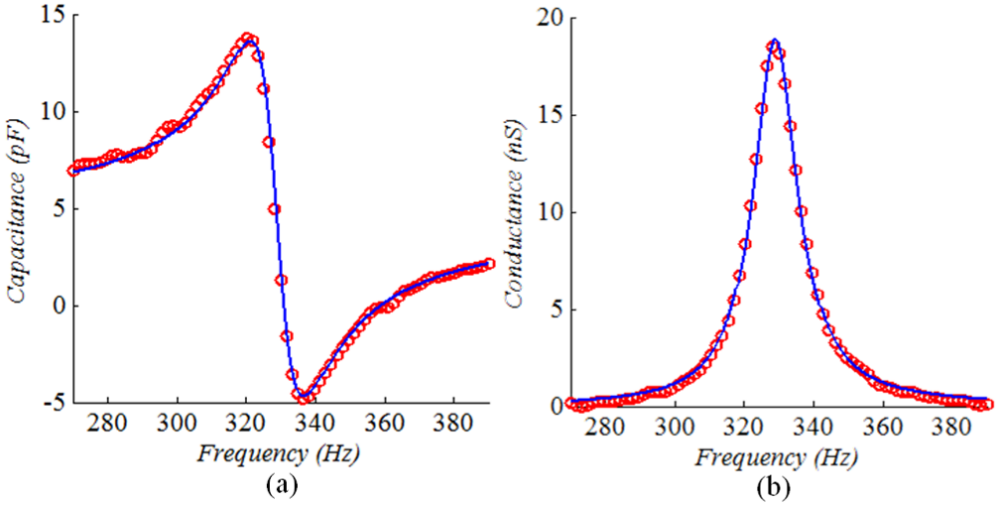

Fig. 3.10. Measured electrostatic actuator equivalent parallel conductance is given in (a) and parallel capacitance in (b) versus frequency. The measured data is depicted in markers while equivalent circuit data fitting is depicted in lines. The resonance frequency is 329 Hz and the quality factor is 22.

Long travel range by the comb-drive actuator was achieved by applying a half-wave rectified sinusoidal signal on the push electrode simultaneously with a 180 degree phase shifted signal on the pull electrode. More than one combination of applied signal offset voltage and amplitude can be used to achieve the required displacement of 400 μm which corresponds to about 100 degrees optical deflection angle using acylindrical mirror with f_o = 200 μm. Microscope images for the comb-drive in static case as well as in resonance are given in Fig. 3.11 (a) and (b) respectively where the scale etched in the silicon has a pitch of 25 μm. The oscillation envelope at resonance can be observed in Fig. 3.11 9 (b) with a peak-to-peak displacement slightly larger than 400 μm.

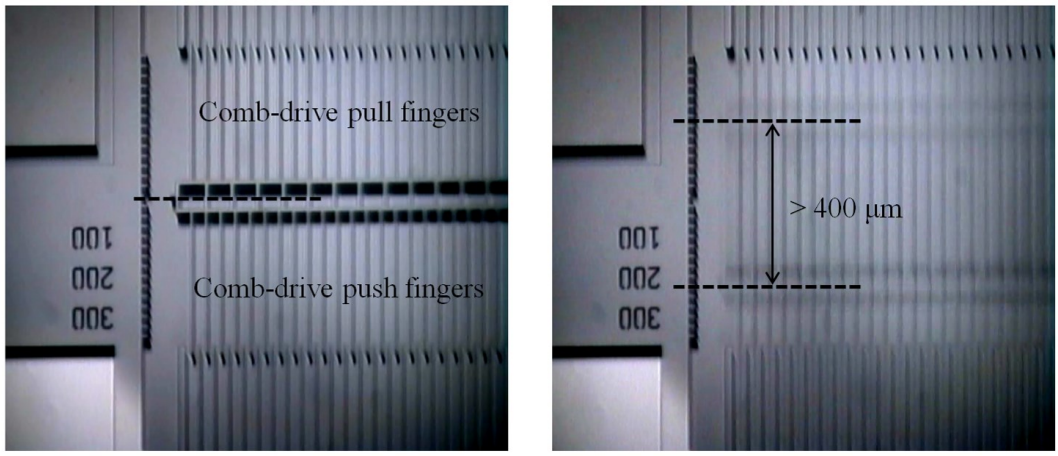

(a) (b)

Fig. 3.11. Microscope image for the comb at rest position is given in (a) and at resonance in (b). The scale etched in the silicon has a pitch of 25 μm. A peak-to-peak displacement slightly larger than 400 μm can be observed.

3.5.2 Optical measurements

The SOI optical bench microscanner was attached and wire bonded to a PCB daughter board as shown in Fig. 3.12 (a). A 4/125 OZ Optics optical fiber was used to ensure single mode operation at the visible spectrum. The optical fiber was inserted into the micromachined fiber groove which is lithographically aligned with the acylindrical micromirror and the comb-drive actuator. The fiber was fed from Thorlabs S1FC675 Fabry-Perot laser source working at a wavelength of 675 nm. The comb-drive was operated at the resonance condition resulting in the scanning window shown in Fig. 3.12 (b). A window width of about 21.5 cm could be projected on a screen 10 cm away from the scanning MEMS.

An experiment was carried out in order to characterize the scanned beam spot size and intensity profile. For this purpose, fabricated acylindrical mirrors aside from those attached to the actuator, were used in conjunction with an external mechanical motion stage enabling the characterization of the beam in a static manner. First, the acylindrical mirrors designed for one-degree of freedom in-plane motion were examined. A typical scanned beam spot shape after 10 cm propagation is shown in the inset of Fig. 3.13 (a) for an optical deflection angle of 100 degrees with the input beam obtained from the single-mode fiber fed from the 675 nm laser source. An elliptical spot is obtained offering a flying-line scanning type instead of the dot scanning. Indeed, the scanned beam spot shape can be changed by controlling the incident or the reflected GB wavefront radius of curvature. This can be achieved using a lensed fiber or additional curved micromirrors integrated within the SOI optical bench [83].

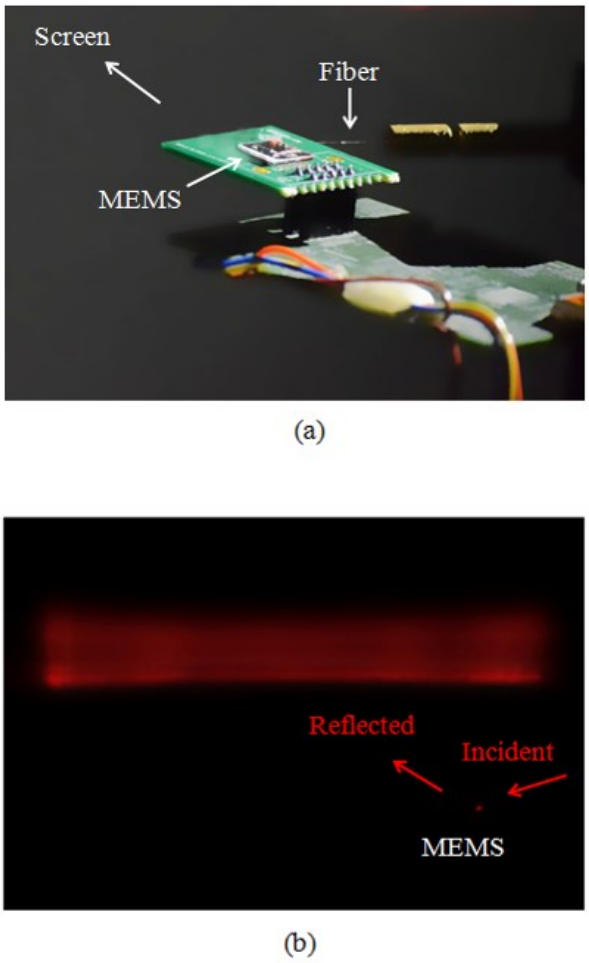

Fig. 3.12. Microscope image for the comb at rest position is given in (a) and at resonance in (b). The scale etched in the silicon has a pitch of 25 μm. A peak-to-peak displacement slightly larger than 400 μm can be observed.

The scanned beam spot size and intensity profile were captured using DataRay Inc. BeamScope^{TM}-P8 scanning slit beam profiling system [85]. The measured normalized intensity profile of the beam along the *x*-direction is shown in Fig. 3.13 (a) in markers where *w* is the spot radius of the beam. Gaussian fitting of the data is also presented in solid line with a root mean square error less than 0.03. The spot radius was

recorded for various optical scanning angles in the range of 20 to 110 degrees and the results are shown in Fig. 3.13 (b). In order to validate the scalability the design of the acylindrical mirror, the experiment was repeated for mirror focal length f_o of 100, 200 and 400 μm. There is a good agreement between the measured data (markers) and the theoretical prediction (lines). A scanning spot size variation of about ±10% around the mean value is obtained for optical deflection angles up to 100°. There is a larger deviation between theory and experiment for smaller focal length which can be referred to axial misalignment in the process of fiber insertion. However, the deviation is still relatively small for a 100 μm focal length.

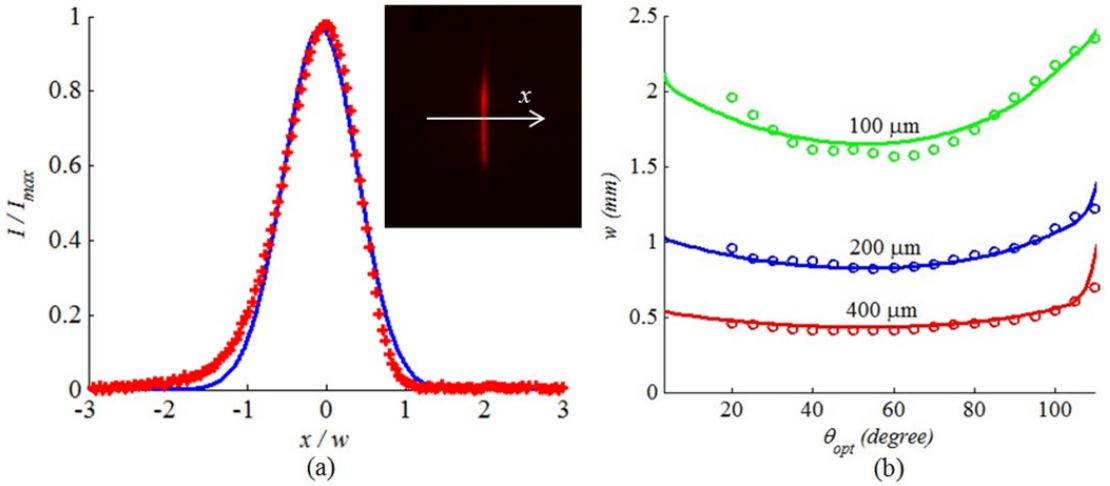

Fig. 3.13. The intensity profile of the scanned beam (measured in markers and Gaussian fitting in line) at an optical deflection angle of 100 degree is given in (a) versus the transverse direction. The inset shows the spot shape of the beam. The spot radius of the scanned beam is given in (b) versus the optical deflection angle using acylindrical mirrors with focal length (f_o) of 100, 200 and 400 μm.

Acylindrical mirrors designed for two-degree of freedom in-plane motion were also examined. The measured normalized intensity profile of the 120 degrees-deflected beam is shown in Fig. 3.14 (a) in markers. Gaussian fitting of the data is also presented in solid line with a root mean square error less than 0.03. The spot radius was recorded for various optical scanning angles in the range of 20 to 120 degrees and the results are shown in Fig. 3.14 (b). A scanning spot size variation of about ±5% around the mean value is obtained for optical deflection angles up to 120°. Again there is a larger deviation between theory and experiment for smaller focal length.

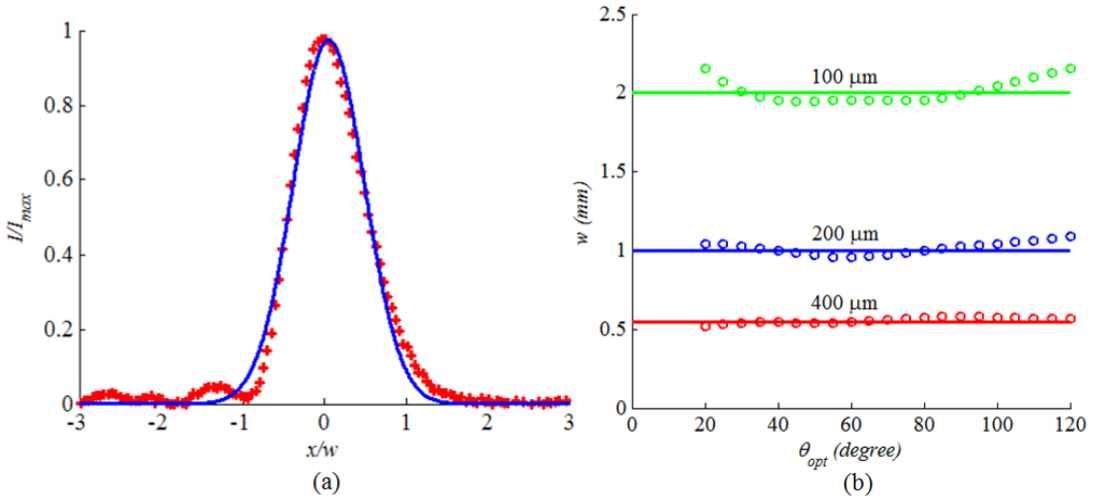

Fig. 3.14. The intensity profile of the scanned beam (measured in markers and Gaussian fitting in line) at an optical deflection angle of 120 degree is given in (a) versus the transverse direction. The spot radius of the scanned beam is given in (b) versus the optical deflection angle using acylindrical mirrors with focal length (f_o) of 100, 200 and 400 µm.

Optical measurements were also carried out using a standard single-mode fiber fed from laser source operating at 1550 nm. Near Infrared (NIR) operation of the scanner has direct application in biomedical imaging, for example OCT. Similar results were obtained so those shown in Fig. 3.13 and Fig. 3.14, validating the scanner performance in this spectral range. The integration of the scanner with a swept laser source is ongoing by our research group targeting the production of a miniaturized OCT probe.

3.6 Summary

A novel architecture for in-plane microscanners was introduced. The architecture is based on translation motion of a curved micromirror with respect to the incident beam optical axis. Thanks to the optical beam axis being parallel to the wafer substrate, the composition of the microscanner in the form of a micro-optical bench was enabled. Acylindrical surfaces were designed to maintain the properties of the scanned beam almost constant during the scanning. In contrast to the common methods of aspherical surfaces generation, the design methodology was based on formulating a differential equation from the appropriate conditions and the subsequent solving of the equation. Two types of surfaces were produced depending on whether the translational motion is one-degree or two-degree of freedom motion.

The proper performance of the designed surfaces was experimentally validated, for different focal length, up to 120^0 deflections angles. The fabrication and monolithic integration of one type of the designed surface with an electrostatic comb-drive actuator

was carried out based on deep reactive ion etching technology on SOI wafer. The system resonance frequency is about 329 Hz and optical deflection angle up to 110^0 degrees was demonstrated; positioning the presented scanner ahead of the wide-angle performing scanners specification. Moreover, the possible integration of laser sources, filters and beam splitters within the microscanner is a major advantage in the presented scanner architecture opening the door for a wide range of applications with a special potential in biomedical imaging.

CHAPTER 4
THREE-DIMENSIONAL MICROFABRICATION

4.1 Introduction

Fabrication of three-dimensional (3-D) microstructure was extensively reported in literature over the last two decades. Different methods were reported for 3-D microstructures production on different substrates, among which the most common are glass and silicon. The most commonly used methods can be divided into two main categories: 1) production of 3-D curved microstructures on the substrate top surface; and 2) etching of 3-D microstructures into the substrate.

On one hand, batch fabrication of 3-D microstructures on the substrate top surface was basically reported using the combination of multiple steps of standard lithography and etching resulting in discrete levels of height [86]. Advanced techniques of 3-D microstructure fabrication on silicon substrate were then followed in literature among which the main methods are stereo lithography [87], grayscale lithography [88-89], MEMSNAS process and other methods taking advantage of the reactive ion etching lag effect [90-91], boron doping and subsequent selective etching [92], photoresist thermal reflow [93-94] and deposition thorough spaced apertures over a substrate [95]. On the other hand, work-piece microfabrication based on localized etching / deposition was reported. This is usually carried out by using focused laser /electron beam [96, 102-103] or miniaturized electrical / ultrasonic tip [97-101] in combination with mechanical

scanning over the work piece area. In the previously mentioned methods, the produced 3-D microstructures were fabricated on the substrate top surface and, consequently, having their principal axis oriented with respect to the substrate in out-of-plane manner as shown in Fig. 4.1 (a). The produced micro-optical using such methods are, therefore, not compatible with the micro-optical bench technology.

The use of multiple etching steps were reported in literature for the specific purposes of improving the anisotropic nature of etched trenches [104], overcome step coverage problems in metallization [105], release MEMS structures [106], fabrication of buried micro-fluidic channels [107], fabrication of micro needles [108] and producing micro notches in photonic crystals or barcode fingers [53,109]. In this chapter, we present a technique for batch fabrication of 3-D microstructures overcoming the orientation challenge in the reported methods [110-111]. The technique is based on achieving a truly 3-D shape using, first standard lithography to define the shape cross section in the x-y plane (plane parallel to the substrate surface) and then, secondly by applying a multi-step time-controlled etching and protection steps in a pre-calculated manner to define the shape cross section along the z-direction (out-of-plane direction). The out-of-plane profile can be of concave or convex shape while the 3-D microstructure has its principal axis oriented in-plane with respect to the substrate as shown in Fig. 4.1 (b).

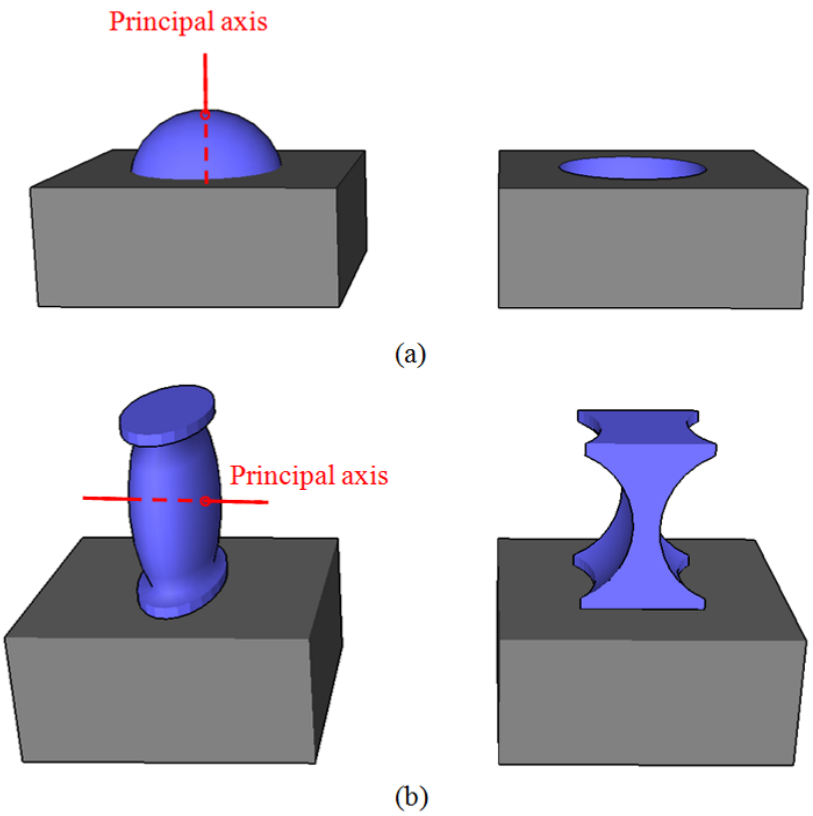

Fig. 4.1. 3-D curved microstructures with convex profile to the left and concave profile to the right. The principal axis is out-of-plane in (a) and in-plane in (b).

4.2 Multi-step etching principle

The fabrication method involves the use of a series of etching and protection steps to create the desired profile in the z-direction while the 2-D etching mask, created by standard lithography, controls the cross section in the x-y plane. For illustration, consider the cross sections drawn in Fig. 4.2 and the fabrication flow chart in Fig. 4.3 (a). First, an isotropic etching is used to achieve the desired lateral etching under the mask. The imaginary cross sectional etching circle created by the isotropic etching has a radius of

curvature R_1 which is equal to the desired lateral etching extent. The starting step can be either isotropic or anisotropic etching depending on the targeted profile. For the starting convex profile shown in Fig. 4.2, the first step should be isotropic etching. During isotopic etching, both lateral and vertical etching occurs where the etching time is adjusted to achieve the desired lateral etching. The vertical etching advances the etching deeper automatically. If the resulting depth is not enough, an anisotropic etching step can be carried out in order to reach the required depth for the next lateral etching step. Then, the etched surface has to be protected from any to the further etching during the next cycles. A passivation step, side wall protection layer, is applied to achieve the required protection. Indeed, this protection step is important to prevent interaction between the multiple etching steps. The surface protection layer has to be removed from the bottom so as not to block the etching. The second cycle starts by another isotropic etching step and so on… When the targeted profile and depth are achieved, the accumulated passivation layer is removed in a surface cleaning step. The resulting surface will be rough due to the cyclic nature of the process. Therefore, a finishing surface smoothing step is needed to obtain a surface of better quality as shown in Fig. 4.2.

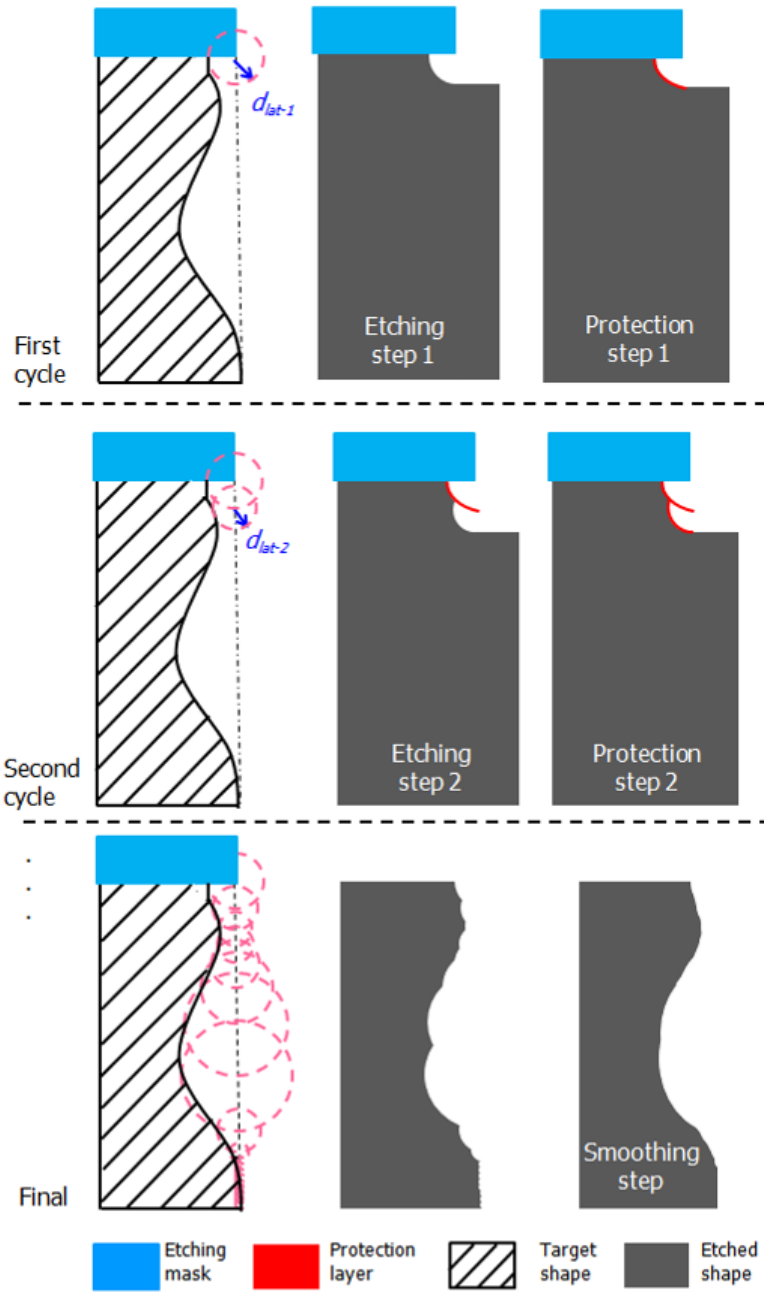

Fig. 4.2. Multi-step etching and protection for achieving arbitrary profile in the direction normal to the wafer substrate (z-direction). Protection layer cleaning and surface smoothing are applied after etching completion.

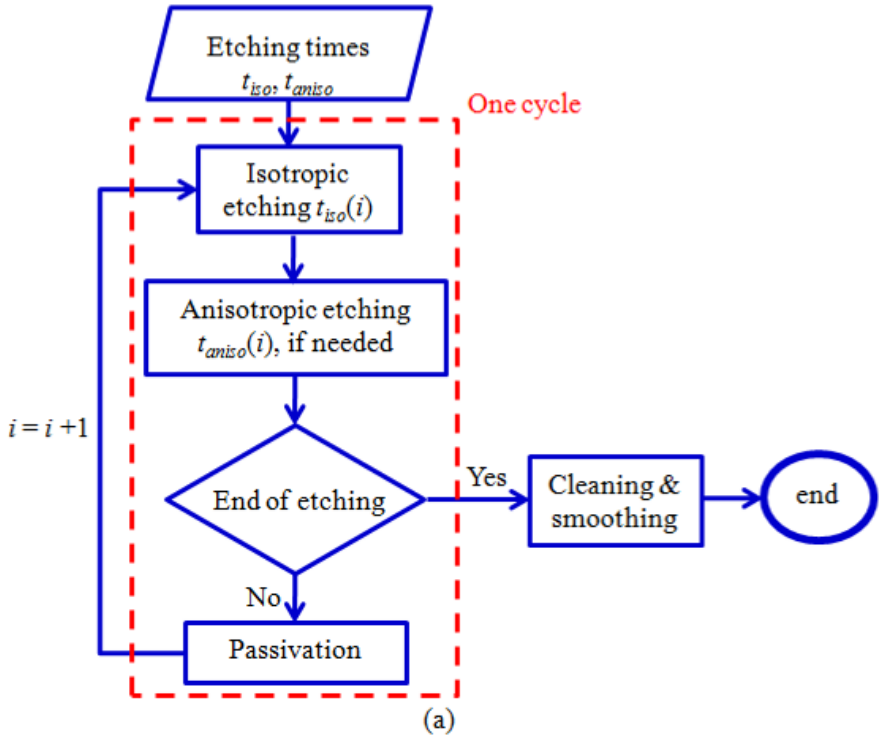

Fig. 4.3. (a) Fabrication flow chart for the multi-step technique shown in Fig. 4.2. (b) Algorithm for calculation of the etching times corresponding to the target profile.

The isotropic and anisotropic etching times are calculated by the algorithm shown in Fig. 4.3 (b). The isotropic etching process is assumed to result in equal penetration per cycle in all directions, which is denoted by d_{lat}. For instance, the lateral etching extent at a given height is calculated by Eq. (4. 1) or (4. 2) for a curved surface with a spherical concave or convex profile, respectively:

$$\frac{d_{lat-conv}}{\phi} = \frac{R}{\phi} - \sqrt{\left(\frac{R}{\phi}\right)^2 - \left(0.5 - \frac{h}{\phi}\right)^2} \qquad (4.\ 1)$$

$$\frac{d_{lat-conc}}{\phi} = \sqrt{\left(\frac{R}{\phi}\right)^2 - \left(0.5 - \frac{h}{\phi}\right)^2} - \sqrt{\left(\frac{R}{\phi}\right)^2 - 0.25} \qquad (4.\ 2)$$

where R is the radius of curvature of the surface, $\emptyset \leq 2R$ is the overall profile height of the surface. If needed, anisotropic etching is carried out and the resulting vertical penetration per cycle is denoted by d_{ver} . The overall cycle-accumulated depth is denoted by h. The etch rates are dependent on the process parameters as well as the mask geometry including feature size and density. Therefore, the etch rates are given as input to the algorithm and have to be determined from appropriate modelling and technology calibration. A minimum advancing pitch p should be specified in order to determine if anisotropic etching steps are needed or not. In some cases, such as for a convex shape around the vertex when located under the etching mask edge, the lateral etching extent tends to zero. Consequently, if no anisotropic etching is applied, a huge number of isotropic etching steps are needed in an impractical manner.

Since the fabrication method presented in Fig. 4.2 suffers from the cyclic nature

of the process and the resulting roughness in the fabricated surface, hence the use of this method to produce curved surface with high optical surface quality can be challenging. A second method that is suitable for the production of optical concave surfaces, not suffering from a large scale roughness, is inspired from the method used to fabricate buried micro-fluidic channels [107]. The processing steps are shown in Fig. 4.4. First, the substrate is etched anisotropically with a specific etching depth defining the principle, or the optical, axis of the targeted concave surface. Then, a sidewall protection step is applied in order to prevent etching of the sidewalls. The protection also ensures the desired start of the next etching step at the optical axis. The out-of-plane concave surface is obtained by further etching of the substrate in an isotopic manner. The etching depth of this last step defines the radius of curvature of the fabricated surface.

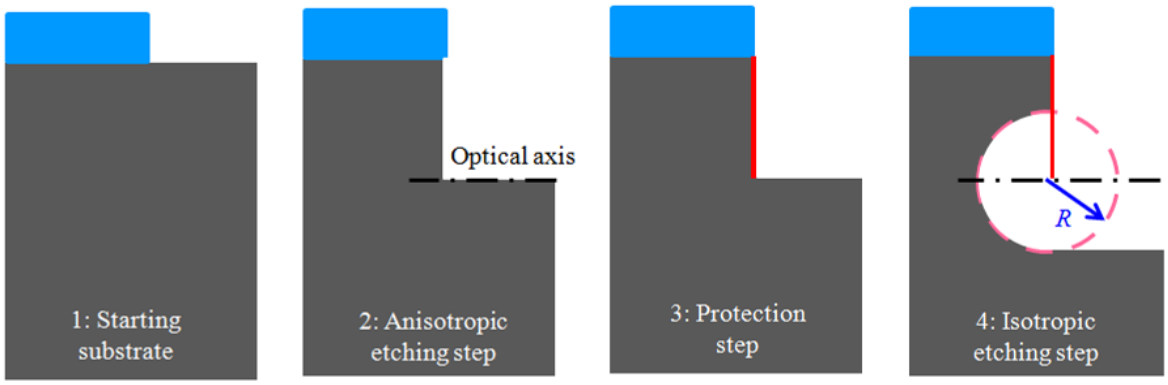

Fig. 4.4. Out-of-plane concave surface fabrication steps. The resulting curved surface doesn't suffer from the surface roughness of the cyclic process in Fig. 4.2

4.3 Simulation study

The presented techniques have been verified using CAD simulation, namely using ELITE; an advanced 2-D simulator within ATHENA process simulation framework provided by SILVACO. The substrate was (100) silicon wafer. The etching mask was chosen to be a thermally grown layer of 1 μm SiO_2. A 500 nm passivation layer of SiN was deposited with step coverage of 0.8 for the sake of emulating the protection layer. An etching step is then applied to remove the passivation layer from the bottom. In principle the protection layer can be SiO_2, SiN, C_4F_8 (Teflon-like) or any other material with good selectivity in terms of isotropic etching of silicon. Now, consider the simulation results depicted in Fig. 4.5. The figure shows the resulting structure from the first 6 etching cycles (about 20 μm depths) targeting a convex profile with a radius of curvature of 180 μm and height of 80 μm. The target profile is also drawn in the figure for the sake of comparison. We have found that the number of segments used by ELITE in discretization of the structure increases significantly each cycle leading at the end to a memory limit and termination of the simulation. Therefore, only the first 6 etching cycles were simulated in this case.

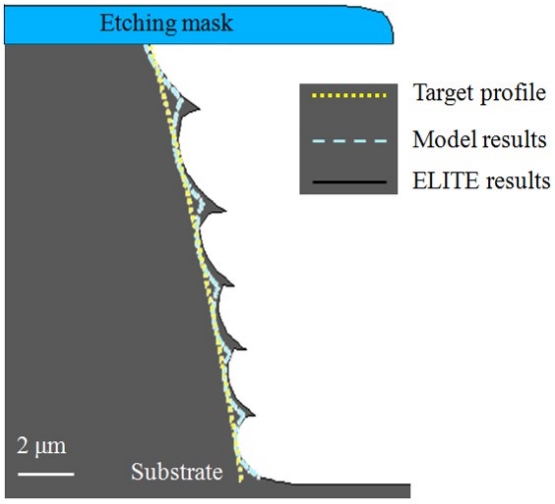

Fig. 4.5. ELITE as well as the developed numerical model simulation results for the first 6 (about 20 μm) etching cycles of a target convex profile with R =160 μm and Ø=80 μm.

In order to study the effect of the multi-step etching method on the resulting shape for different target profile parameters, we created our numerical model for etched profile prediction. The model is based on finding the intersection between the isotropic etching circles and plotting the result thereof. The model results agree well compared to ELITE results as shown in Fig. 4.5. The model will be then used hereinafter to carry out the simulation study.

The developed model was used to study the versatility of the method for producing concave and convex profile, which can be considered as the building blocks for producing arbitrary profiles. Multi-step etched concave profiles with height to radius of curvature ratios of $Ø/R$ = 0.25, 0.5, 0.75 and 1.0 are shown in Fig. 4.6 (a), (b), (c) and (d) respectively. In order to achieve ratios of $Ø/R$ smaller than 0.25, a large number of

etching steps may be required with a small and well-controlled etching resolution. On the contrary, $\emptyset/R$ ratio that is larger than 1 implies a large lateral etching per cycle size. Depending on the application, the etching depth may be too large to have a polished surface quality after the smoothing process with small deviation from the original targeted profile. The absolute numbers are dependent on the scale of the structure, which can be from the nanometers scale up to hundreds of micrometers depending on the actual target profile and the micromachining etch rate and precision. Since the vertex of a concave shape is always away from the etching mask edge, the depth advances well with isotropic etching steps without a need for anisotropic etching.

Turning to the convex profiles, multi-step etched profiles with height to radius of curvature ratios $\emptyset/R$ = 0.25, 0.5, 0.75 and 1.0 are shown in Fig. 4.7 (a), (b), (c) and (d) respectively. Similar conclusions can be drawn regarding the number of cycle and smoothness of the produced surface. The smoothness problem is, however, less pronounced in the case of convex profiles that can be observed by comparing the cyclic size in Fig. 4.6 (d) and Fig. 4.7 (d). Etching close to the vertex of a convex surface is more challenging to achieve when the vertex is located below the edge of the etching mask (i.e. zero radial position). The difficulty arises due to the small lateral etching depth required, the vertical etching doesn't advance and, consequently, anisotropic etching steps are added in between the isotropic steps as shown in Fig. 4.7 (a).

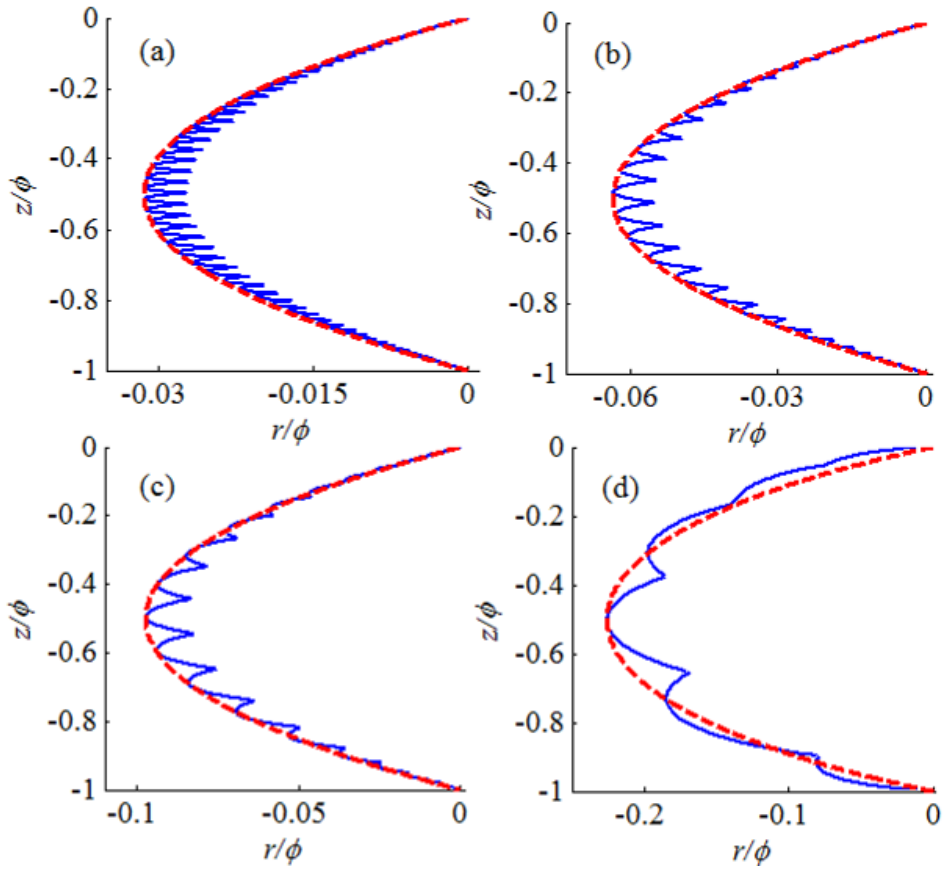

Fig. 4.6. Multi-step etched concave surface (solid line) compared to the target profile (dashed line). The diameter to radius of curvature ratios are 0.25, 0.5, 0.75 and 1.0 in (a), (b), (c) and (d) respectively.

The effect of a small shift *S* between the mask edge and the vertex of a target convex profile is studied in Fig. 4.8 for shift to diameter ratios S / Ø =1 /10, 1/25, 1/50 and 1/100 where Ø / *R* = 0.25. Interestingly, shifting the mask edge offers a trade-off between the number of cycles and the cyclic size. The number of cycles is reduced when the shift is increases and the cyclic size becomes larger. Moreover, even for S / Ø =1 /50 (i.e. a relative small shift) the anisotropic etching steps are no more needed close to the

vertex of the profile. This method can be utilized to achieve ∅/R ratios smaller than 0.25.

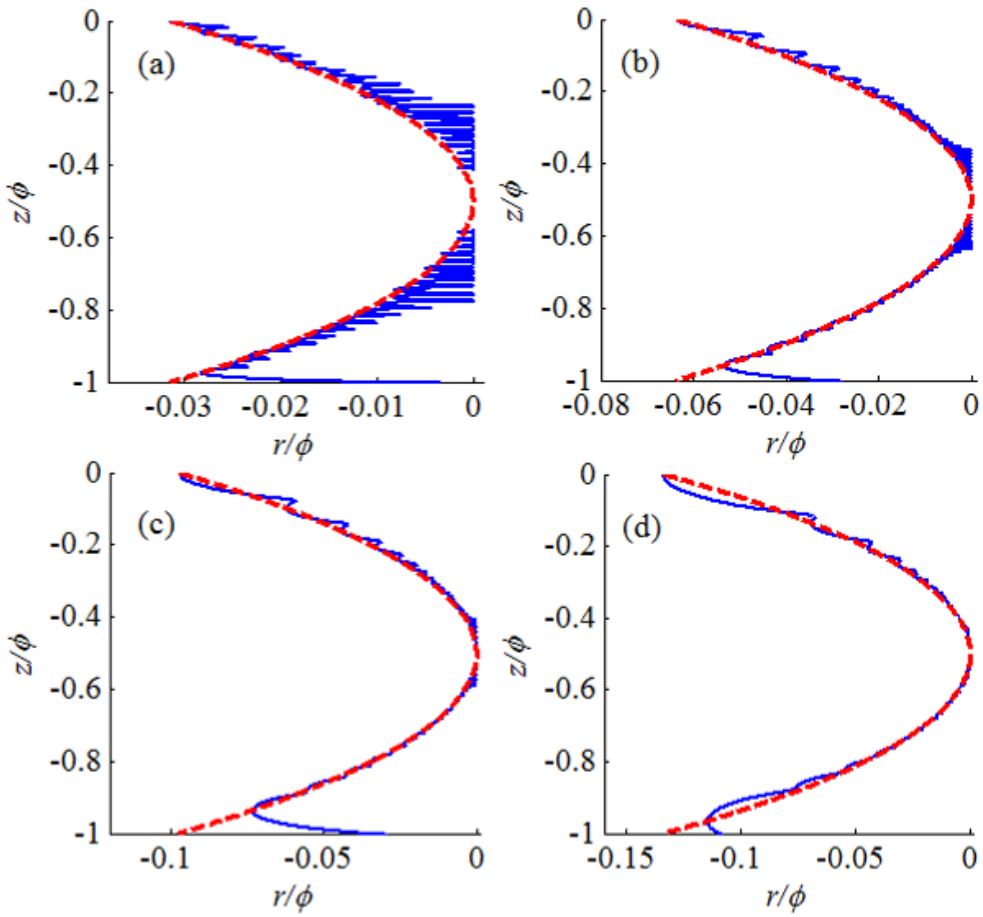

Fig. 4.7. Multi-step etched convex surface (solid line) compared to the target profile (dashed line). The diameter to radius of curvature ratios are 0.25, 0.5, 0.75 and 1.0 in (a), (b), (c) and (d) respectively.

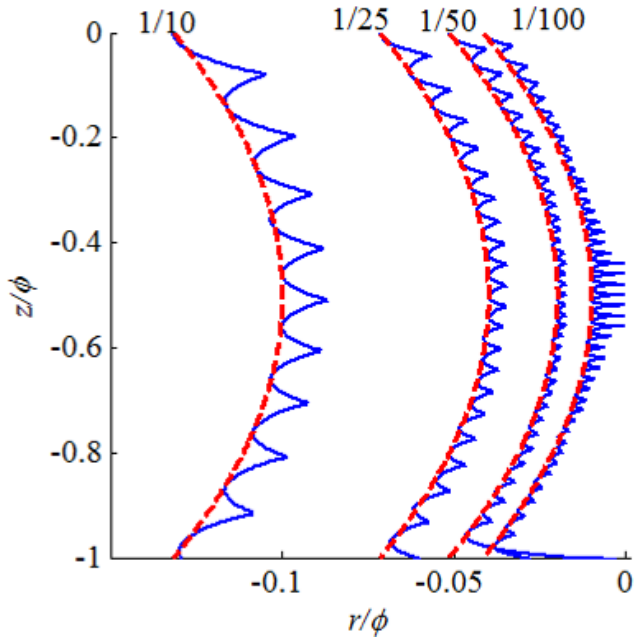

Fig. 4.8. The effect of shifting the mask edge from the vertex of a convex profile the resulting surface when $Ø / R = 0.25$. The shift to diameter ratio S/$Ø$ =1 /10, 1 /25, 1 /50 and 1 /100.

The method presented in Fig. 4.4 was verified using ELITE simulation. The substrate thickness was set to 550 µm. The anisotropic etching depth was chosen to be 100 µm while isotropic etching depths of 50 µm, 100 µm, 150 µm and 200 µm were simulated as shown in Fig. 4.9 (a), (b), (c) and (d), respectively. By reaching an isotropic etching depth close 100 µm, the sidewall behind the protection layer gets consumed and the layer falls down. However, we found that further isotropic etching is still able to increase the fabricated radius of curvature.

Practical limits come from the substrate thickness and the possibility of substrate breakage if become too thin, due to excessive etching. The mechanical stability of the etching mask can be an issue also but this depends on the overall mask shape that cannot be included in the 2-D simulation of Elite. The fragility challenge can be overcome by forming the concave surface in the device layer of an SOI wafer, instead of the silicon wafer. The SOI wafer has an etch stop BOX layer. This layer can resist the isotropic etching and prevent its extent in the handle layer of the SOI wafer.

The fabrication of more than one concave surface with different out-of-plane radii of curvature on an SOI wafer was also simulated on ELITE. The idea is based on the protection of the first surface before the formation of the second one as shown in Fig. 4.10. A first concave surface of 75 μm is fabricated using the method presented previously. The surface is then coated by a protective layer from further etching. The protective layer on the surface is not subjected to any physical etching, for example ion bombardment of a deep etching process, because it exists in the shadow region under the etching mask. The second surface is formed. The optical axis of the two surfaces can be adjusted at the same level by giving carefulness for the anisotropic etching steps. In this case, low etch rate anisotropic etching process with high uniformity is preferred.

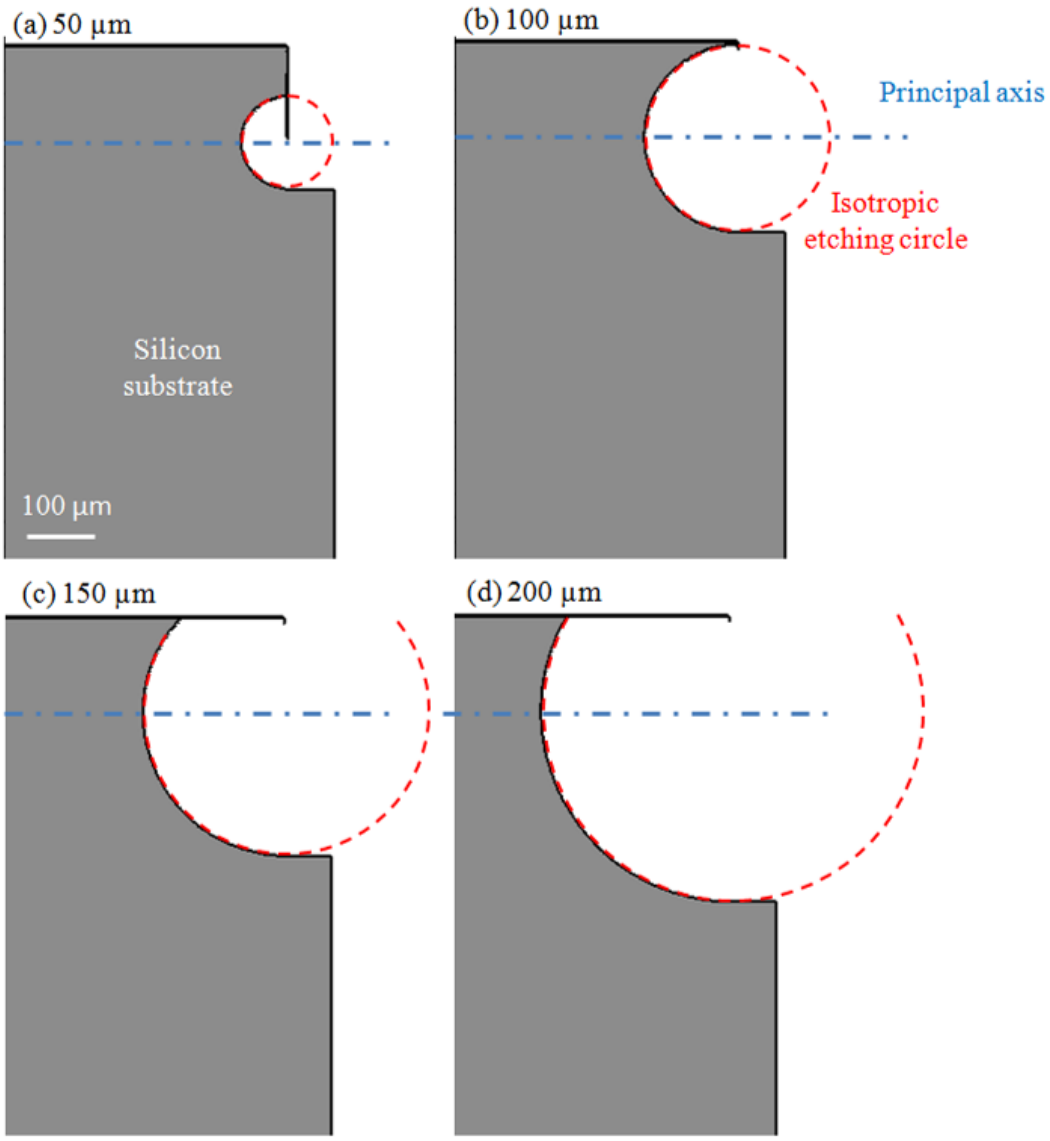

Fig. 4.9. ELITE simulation for the production of a concave surface by a 100 µm deep anisotropic etching followed by sidewall protection and isotropic etching. The principal axis is defined by the anisotropic step while its radius of curvature is defined by the isotropic step which is 50 µm, 100 µm, 150 µm and 200 µm in (a), (b), (c) and (d), respectively.

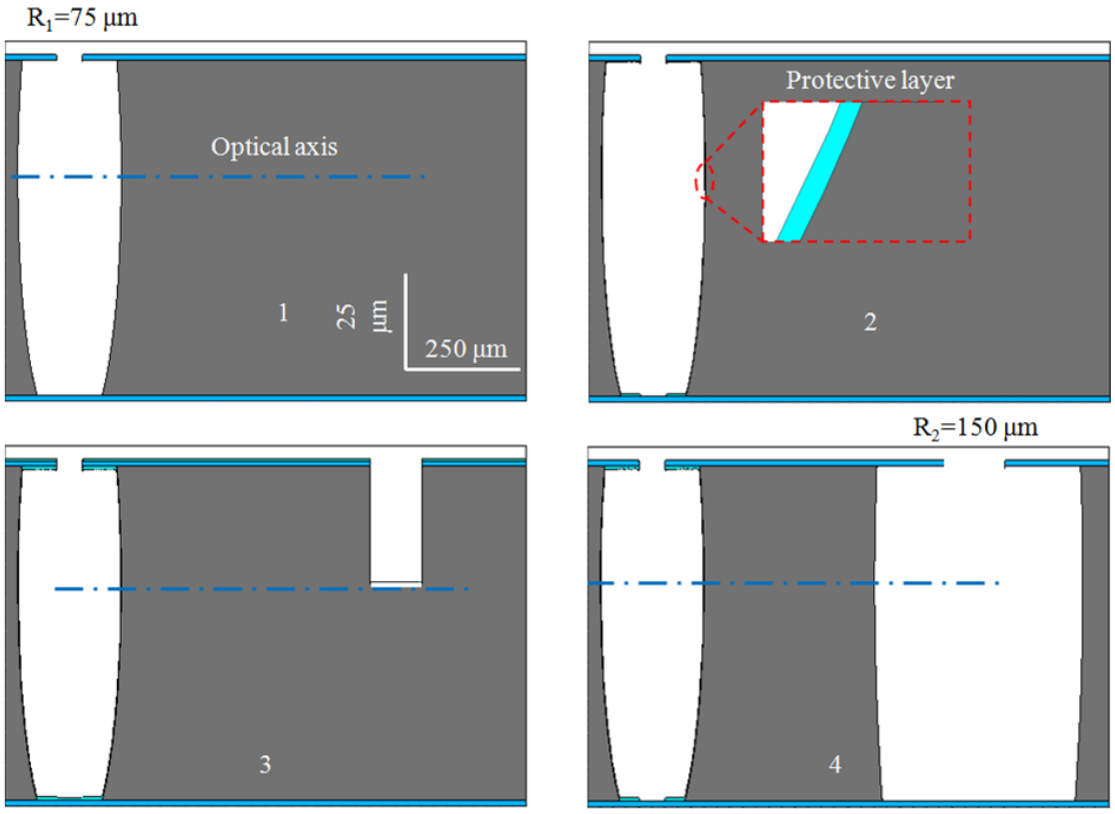

Fig. 4.10. ELITE simulation for the production of two concave surfaces with different out-of-plane radii of curvature. The first surface fabricated is protected then the second surface is formed.

Taking advantage of the etching lag effect can be another way for the production of different out-of-plane radii of curvatures, by assigning smaller mask opening for the concave surface with the smaller radius of curvature. Indeed, the lag effect can be cancelled or even reversed using the appropriate etching conditions [112]. The concave surfaces are all fabricated simultaneously. The anisotropic etching step parameters can be adjusted to cancel the lag effect in order to have the principal axis of the surfaces aligned.

In contrast, the isotropic etching conditions should be in the direction of favouring the lag effect, ending up with the desired surfaces.

4.4 Demonstration on silicon substrate

The proposed methods for 3-D microstructures and curved surfaces productions are validated on silicon substrate in this section. The demonstration takes advantage of the Alcatel 601E Deep Reactive Ion Etching (DRIE) machine with Inductively Coupled Plasma (ICP) source. A significant difference in this machine compared to capacitive coupled reactors (RIE machines) is the existence of two power sources: 1) the high RF power ICP source responsible for the generation of high density plasma without reactor walls sputtering and with a wide range of pressures; 2) the RF power substrate source responsible for wafer voltage biasing independent from the ICP source leading to a high degree of isolation between the process of generating the plasma (free radical and ions) and the acceleration of the ions toward the substrate. Therefore, the machine can be utilized in both anisotropic and isotropic dry etching of silicon by raising and lowering the substrate power, respectively in addition to the sidewall protection using Fluorocarbon gas. Indeed, we used the ICP machine to carry out all the etching/protecting steps of silicon, which rendered the application of multiple cycles of anisotropic/isotropic etching feasible. The machine was programmed to apply the cycles with the pre-calculated times and without interruption between the cycles by holding the plasma source active.

The cyclic BOSCH process was used to achieve the anisotropic etching of silicon. The Bosch process parameters are chosen carefully in order to have high enough etched rate without sacrificing the verticality of the etching. The process recipe is referred to as DRIED. A smooth etched substrate surface with no appearance of silicon grass is obtained as shown in Fig. 4.11. The SiO_2 was chosen as the etching mask because of its higher selectivity with respect to PR mask while not subjected to sputtering inside the reactor; and so not leading to micromasking usually appears using an Al mask. The etch rate of this process was measured using VEECO optical profiler on wide etching areas and found to be 5.5 μm / min with a uniformity better than 3 % across the wafer. The SiO_2 mask thickness was measured before and after etching using the ellipsometer and the obtained selectivity is found close to 250:1.

A detailed discussion on the dry isotropic etching of silicon using sulfur hexafluoride (SF_6) and the effect of different process parameters on the resulting surface quality can be found in [113-114]. The isotropic etch rate has a weak sensitivity to the pressure, as long as the pressure is not too high or too low. In addition, increasing the pressure has the effect of increasing the roughness of the etched surface. Therefore, we used a moderate pressure value of 3 Pa. The substrate source (RIE source) power was set to zero in order to minimize any anisotropic tendency in the etching. This could increase the roughness in the bottom surface of the etched trench, which is not important in our case. The ICP source power was set at a moderate value to further improve the isotropic nature of the etching.

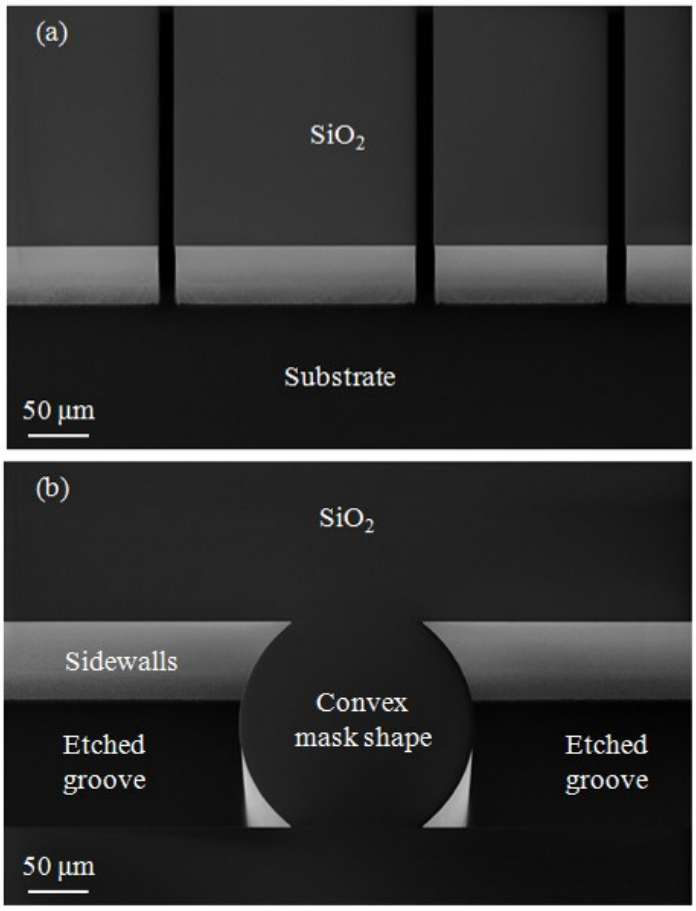

Fig. 4.11. Tilted view SEM images for the fabricated structures using the Bosch process DRIED. Etched trenches are shown in (a) while a 2-D convex mask shape is shown in (b) where the resulting surface is cylindrical. The etching depth is 150 µm.

We have encountered more than one effect regarding the isotropic etching of silicon using SF_6. First, a significant dependence of the etch rate on the trench width was observed, as shown in Fig. 4.12. The data markers represent the measured normalized data while the solid line is a logarithmic fitting. The etch rate for a 10 µm trench width is about one fifth the rate for a 500 µm trench width.

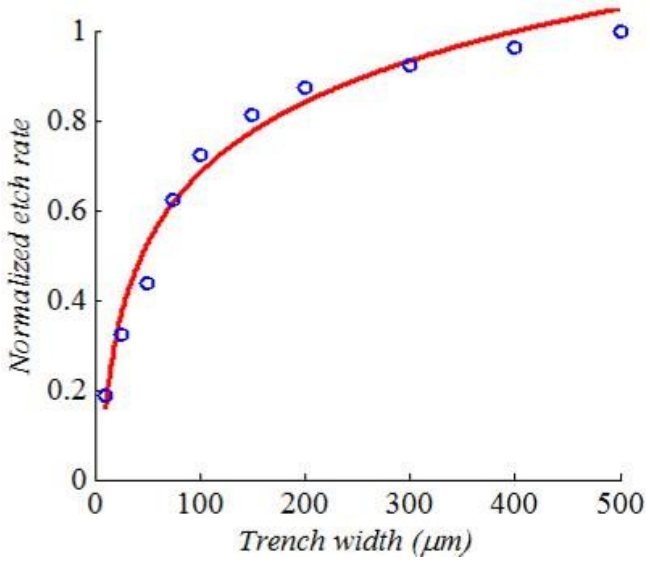

Fig. 4.12. Normalized isotropic etching rate versus the etched trench opening width while. The trench length is 300 μm. The measured data (in markers) is fitted to a logarithmic function (in line).

The second observation is the correlation between the trench width and the isotropic etching roughness as shown in Fig. 4.13. The smaller the trench width is, the higher the roughness. Considerable roughness can be observed in the 75 μm using bare eye inspection while the roughness in the 500 μm is much less, but still observable. The Atomic Force Microscope (AFM) instrument was used in order to have a quantitative measurement for the roughness of the 500 μm trench. The AFM probe was brought to the etched surface at the edge of a sample and an area of 10 μm by 10 μm was measured. Top and as well as 3-D titled view of the surface topology, obtained using the AFM, is shown in Fig. 4.14 (a) and (b) respectively. The measured roughness has a peak of 319 nm, an

average of 16 nm and a root mean square of 22 nm. The lag effect as well as the surface roughness of the isotropic etching roughness can be interpreted knowing that a diffusion process governs the transport of the etching radicals from the plasma, where it is created, to the substrate, where a chemical etching occurs. Due to this diffusion process, less amount of etchants are received in thinner trenches. This directly relates to the lag effect. At the same time when the amount of etchants is not enough, rough surface results from the etching process because the surface is not overwhelmed by the etchants.

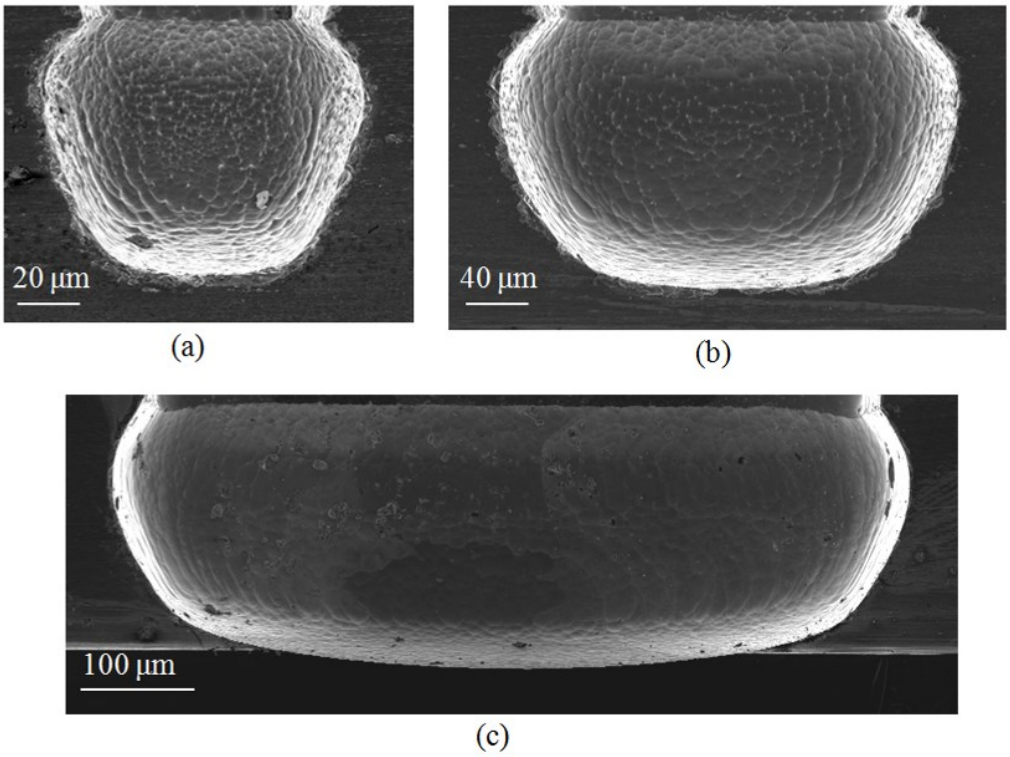

Fig. 4.13. Scanning electron microscope (SEM) images showing the roughness of the isotropically-etched trenches. The trench widths are 75 µm in (a), 150 µm in (b) and 500 µm in (c).

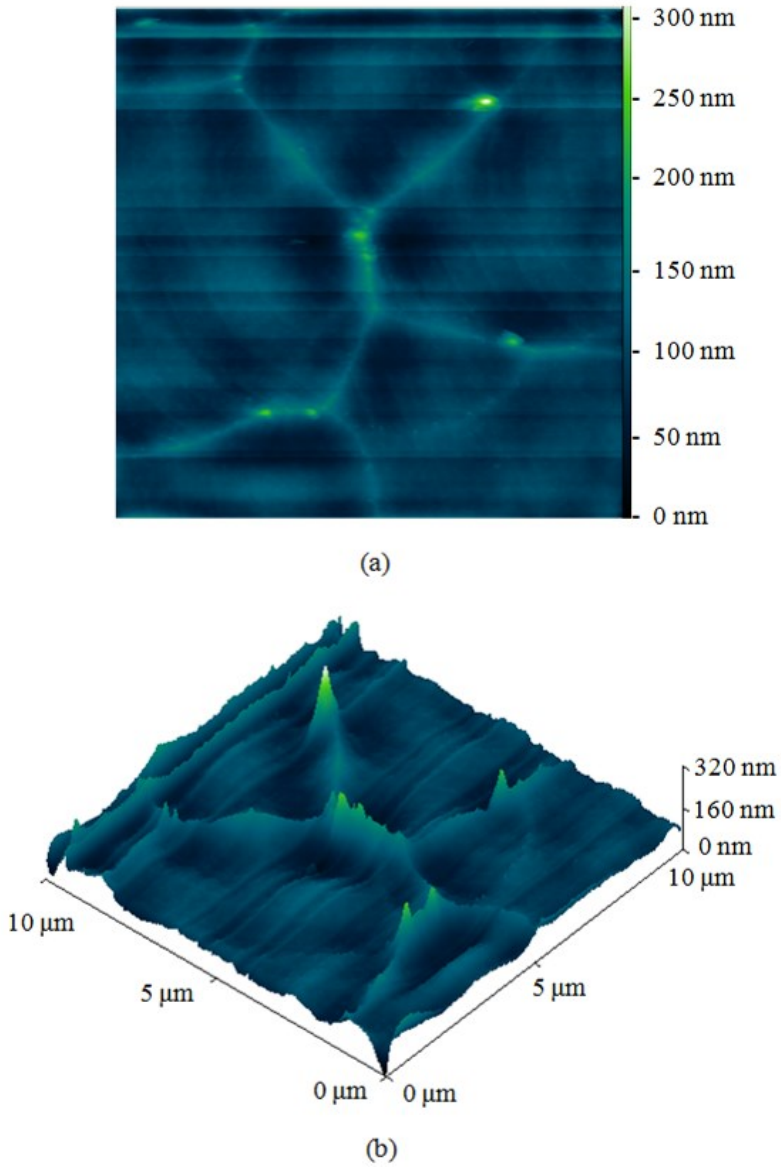

Fig. 4.14. The isotropic etching roughness measured in a 500 µm trench using the AFM. A top view of the measured surface is shown in (a) while a tilted 3-D view is shown in (b).

Turning to the sidewall protection step, the passivation layer was deposited and the deposited layer on the top the wafer was measured using the ellipsometer. A deposition rate of 100 nm / minute was found with uniformity better than 5 %. Increasing the source power and or gas flow rate leads to higher non-uniformity across the wafer. The relatively low pressure value was used to improve the conformity of the passivation layer inside the trenches. The high substrate power was used to accelerate the ions such that removal of the passivation layer from the bottom of the trench is competing with the deposition process. The deposition rate resembles the net of this competition. SEM images of the passivation layer in an etched cross mark are shown in Fig. 4.15. Both the walls and the bottom surfaces look well passivated, where the DRIE scallops cannot be observed on the sidewalls. The bottom surface passivation looks creamy in shape and a zoom-in down to the sub-micrometer scale is enough to show the grain size of the passivation layer. Regarding the stability of the layer, it has been reported in literature that post deposition and depassivation curing of the polymer for 30 minutes at 200^{o}C in vacuum would improve its stability [115]. However, this method requires too many interruption of the process by removing the wafer from the ICP reactor and transferring to an oven, which is not convenient in our case. Therefore, we didn't perform any dedicated stability-improvement step and, however, the results were satisfying.

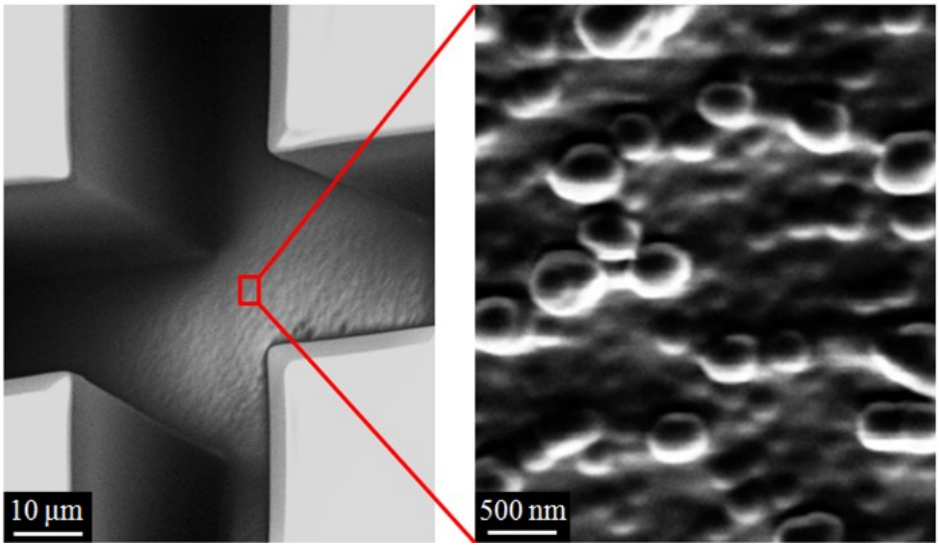

Fig. 4.15. SEM images of an etched cross mark with 20 µm features after passivation. The passivation layer on the bottom looks creamy. A zoom-in on the bottom shows the grain size of the layer.

Depassivation of the Teflon-like layer from the bottom of the trenches was carried out using mainly SF_6 plasma while a small amount of C_4F_8 is added to help in keeping the pre-passivated sidewalls. Indeed, the index of refraction of the passivation layer was found to be $n_t \approx 1.4$, measured using the ellipsometer. Knowing this value is useful in monitoring the deposition/etching of the passivation layer in the ICP reactor using the laser (λ = 675 nm) and the interferometric camera as shown in Fig. 4.16. In the shown case we have about 1.5 fringe; i.e. $0.75\lambda/n_t$, indicating the etching of a passivation layer with about 360 nm. A step in the detected power occurs by the end of etching due to the change in the gas composition in the plasma and another step occurs by switching off the

plasma.

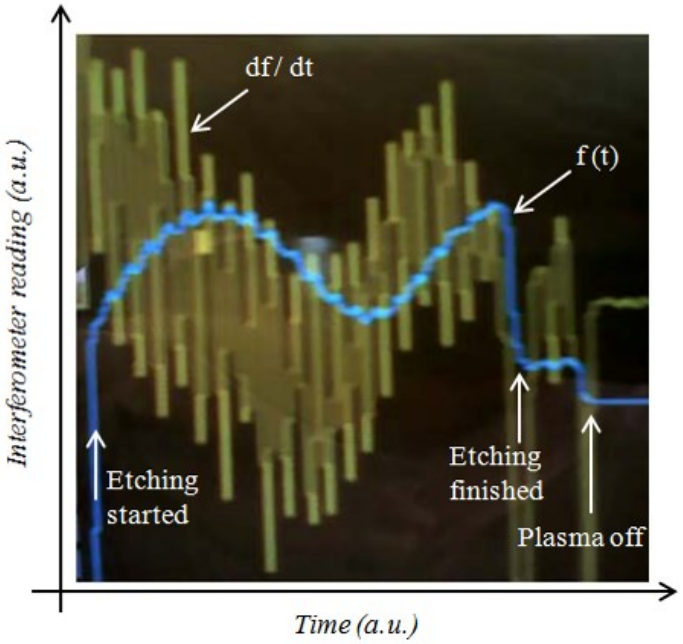

Fig. 4.16. Laser interferometric monitoring of the passivation layer removal.

The multi-step etching method was applied targeting a 3-D concave surface with a 250 μm out-of-plane radius of curvature and a 140 μm height. An SEM image for a resulting structure with a tilted view is shown in Fig. 4.17. The SiO_2 etching mask resides on the top head of the structure. The cyclic nature of the etching process has a clear mark on the etched sidewalls. The bottom surface (the substrate) has a rough topology as a result of using the dry isotropic etching with the reactor RIE source switched off. A small amount of silicon grass appears which can be related to an incomplete removal of the passivation layer from the bottom of the etched trench. Another reason can be due to the accumulation of the C_4F_8 on the reactor walls and its re-deposition on the substrate. The

latter explanation is supported by observing more than 25% increment in the process pressure with time. We ascribed this increment to the accumulation of the C_4F_8 on the pressure valve acting as an effective valve closure with time. Post etching cleaning of the reactor was carried out using 15 minutes long O_2 plasma.

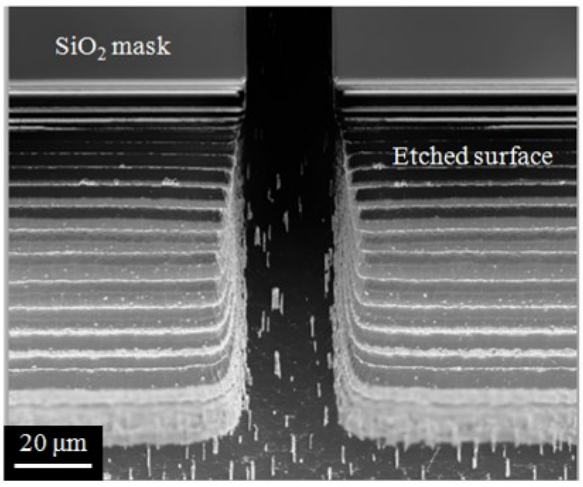

Fig. 4.17. SEM image showing a tilted view for the multi-step etched surface targeting a concave out-of-plane radius of curvature of 250 µm. The cyclic nature of the etching process is clearly seen before the application of a smoothing step.

Post-etching cleaning of the passivation layer was carried out, before the smoothing step, using a combination of dry ashing and wet chemical stripping. First, the wafer has been subjected to oxygen plasma and heated chuck in a Matrix Plasma Asher usually used to strip out polymers and photoresists. The Matrix applies a 4 minutes process with a high pressure of about 250-300 Pa, a temperature of 220^o and an RF substrate power of 450 watt. The process has been repeated three times with an

improvement. Then the wafer was inserted into a fuming HNO_3 acid with a 99% concentration for 15 minutes. The wafer then has been rinsed/dried and subjected to a post-cleaning smoothing step. The smoothing was carried out in the ICP reactor using a long isotropic etching step with about 50 μm etching depth. A SEM image of the resulting etched surface is shown in Fig. 4.18 with a zoom-in around a roughness peak. Roughness peaks in the order of 500 nm were observed.

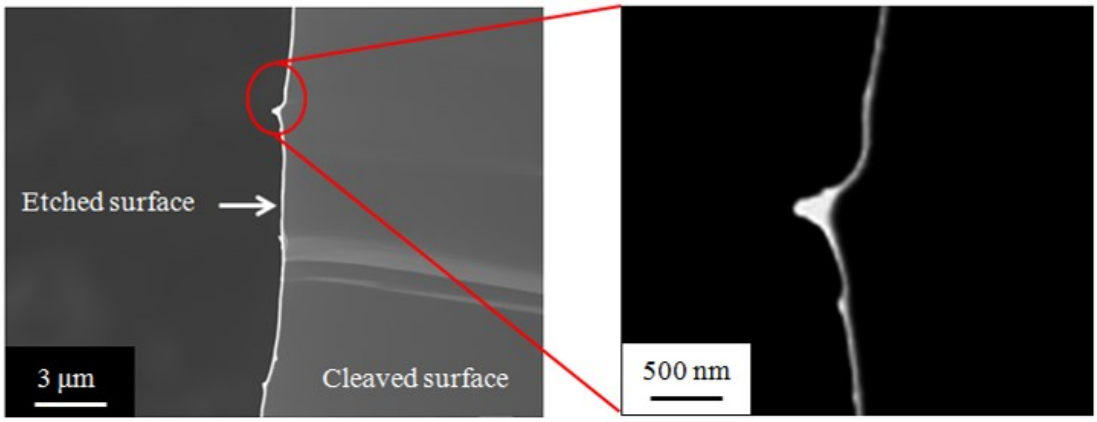

Fig. 4.18. Post-smoothing SME image of the etched surface in Fig. 4.17 with a zoom-in on around the roughness peak.

A tilted view of a smoothed 3-D concave structure is shown in Fig. 4.19 (a) where the in-plane and out-of-plane profiles are emphasized. The in-plane profile can be controlled using a drawn shape that could be transferred to the etching mask using standard lithography. The out-of-plane profile is controlled using the multi-step etching step and the subsequent smoothing process. Out-of-plane radius of curvature of about 270

μm was obtained as shown in the front view in Fig. 4.19 (b).

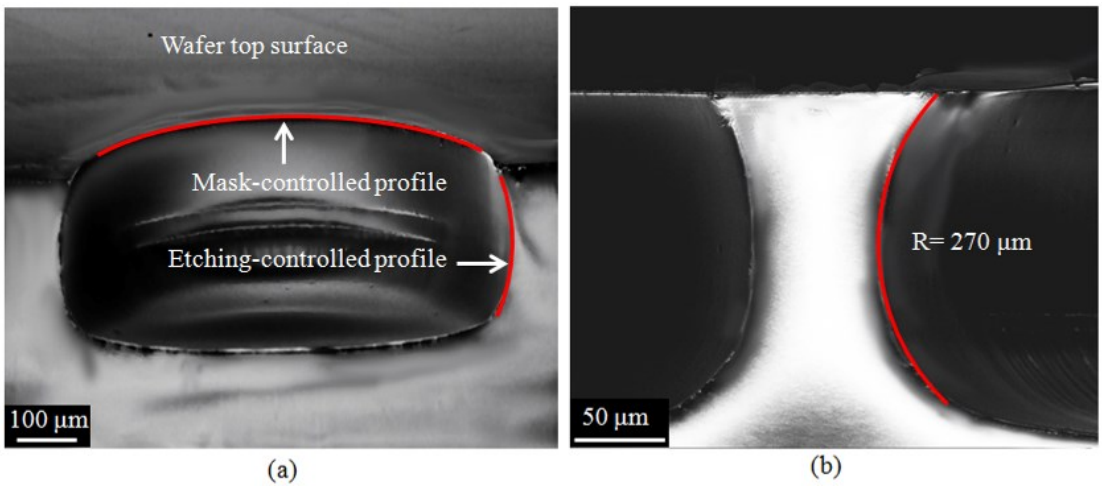

Fig. 4.19. SEM images showing the multi-step etched concave surface after dry etching smoothing. (a) Tilted 3-D view of the structure. (b) Side view of the structure. The out-of-plane radius of curvature is 270 μm.

The technique has been also applied targeting a 3-D convex surface with a 100 μm out-of-plane radius of curvature and a 140 μm height. An SEM image of a resulting structure after etching is shown in Fig. 4.20. In contrast to the concave surface case, the fabricated convex-profile suffered from sidewalls bites. We refereed these bites to the attack of the passivation layer on the sidewall during the step of passivation removal from the bottom surface. This occurred in the convex profile when its vertex is located under or close to the etching masks edge. Shifting the targeted profile a few micrometers in the shadow region under the etching mask mitigate this problem.

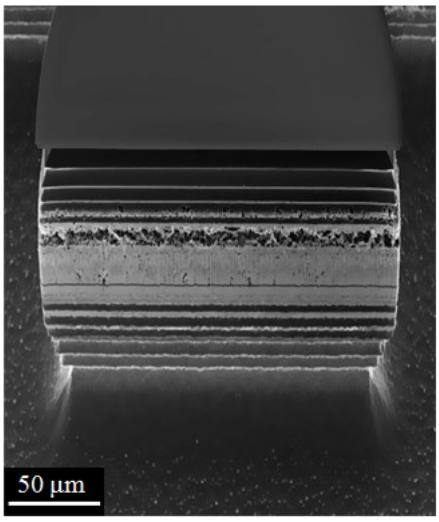

Fig. 4.20. SEM image showing a tilted view for the multi-step etched surface targeting a convex out-of-plane radius of curvature of 100 µm.

Dry isotropic etching was not efficient enough in smoothing the fabricated convex surface. Alternatively, the post-etching smoothing process was carried out using a mixture of hydrofluoric, nitric and acetic acids (HNA). The mixture is used for the sake of polishing when the appropriate acid concentrations and volumetric amounts in conjunction with the continuous stirring of the solution are applied [116]. An SEM image of a 60 minutes HNA smoothed surface is shown in Fig. 4.21. The wafer top has a rough surface due to the attack of the SiO_2 mask by the HNA solution.

A tilted view of a smoothed 3-D convex structure is shown in Fig. 4.22 (a) where the in-plane and out-of-plane profiles are emphasized. Again, the in-plane profile can be controlled using a drawn shape that could be transferred to the etching mask using standard lithography. The out-of-plane profile is controlled using the multi-step etching

step and the subsequent smoothing process. Out-of-plane radius of curvature of about 130 μm was obtained as shown in the front view in Fig. 4.22 (b).

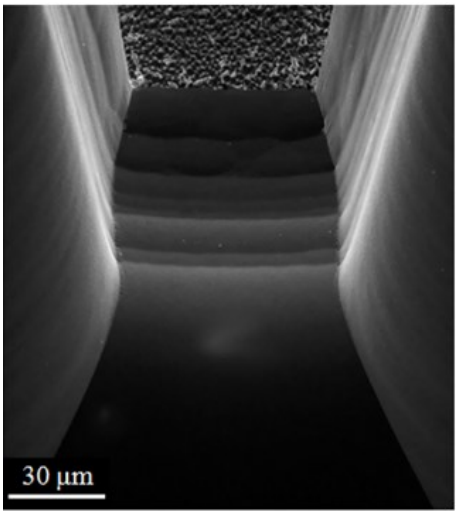

Fig. 4.21. SME image showing a post-smoothing tilted view of an etched surface targeting a convex out-of-plane radius of curvature of 100 μm.

The two-step etching method was applied targeting 3-D concave surfaces with higher finishing optical quality. Although this method is limited to concave surfaces, the out-of-plane curved profile is defined in one isotropic etching step getting rid of the cyclic nature of the multi-step etching, thus allowing for optical surface quality. An example of a resulting structure after etching completion is demonstrated by the SEM images shown in Fig. 4.23. The surface etched in the isotropic etching step has a cylindrical profile except at the mask corners. An intentional undercut has been created by performing a short isotropic etching step after the DRIE step. This helps in creating a

shadowed region under the mask where the protection polymer will be deposited and will remain safe from removal [107].

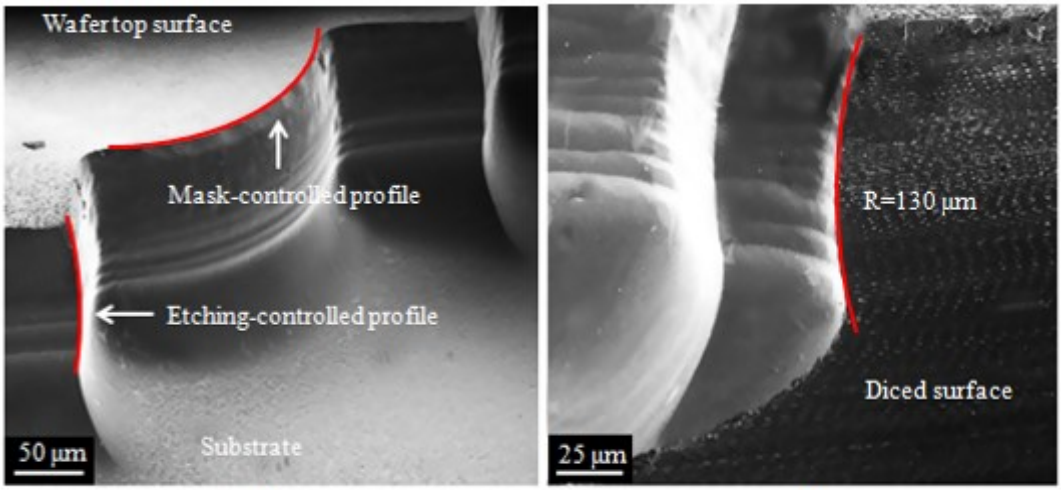

Fig. 4.22. SEM images showing the multi-step etched convex surface after HNA smoothing. (a) Tilted 3-D view of the structure. (b) Side view of the structure obtained after dicing the wafer. The out-of-plane radius of curvature is 130 μm.

Combing the out-of-plane cylindrical profile with a curved profile drawn on the mask, a 3-D curved surface could be achieved as shown in Fig. 4.24 (a). It is interesting to note that the presented structure can perform as either a cylindrical or spherical mirror depending whether the optical beam is incident on the top part or the bottom part of the mirror, respectively. The principle axis of the curved surface is controlled by the mask shape as well as the etching depth preceding the long isotropic etching step while the resulting out-of-plane radius of curvature is controlled by the isotropic etching step.

Principle axis depth, measured from the wafer top, in the range of 100 μm to 200 μm and out-of-plane radii of curvatures in the range of 30 μm to 200 μm were successfully demonstrated as shown in Fig. 4.24 (b) and (c). For single crystal silicon substrate, the maximum obtainable value was limited by the substrate thickness, which is normally around 525 μm.

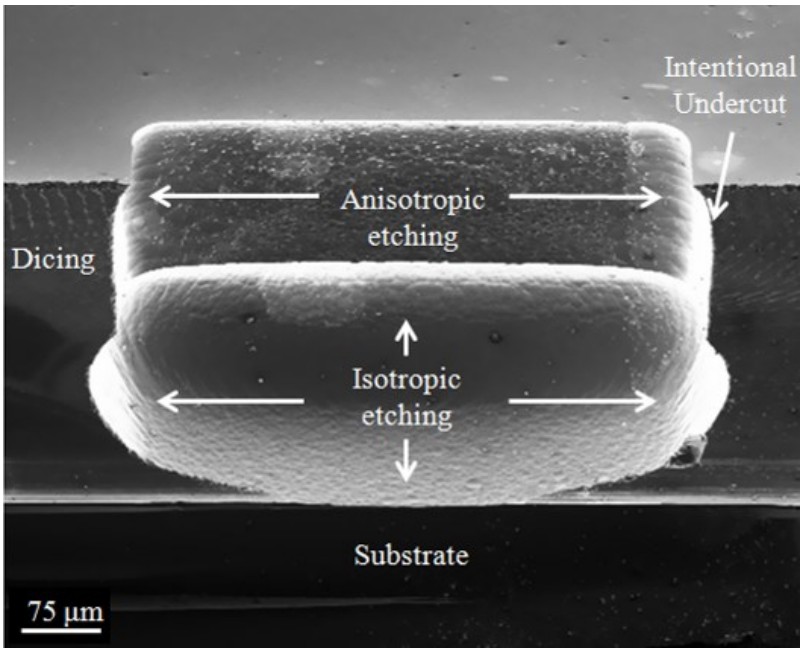

Fig. 4.23. Resulting structure from a rectangular mask shape combined with the two-step etching method.

Optical surface quality required also post-etching smoothing process using HNA. SEM images for the micromirror surface before and after smoothing are shown in Fig. 4.25 where the improvement of the surface quality can be observed. Measured peak-to-

peak roughness on the SEM after 15 minutes of smoothing is smaller than 50 nm compared to more than 300 nm before smoothing. Finally, the micromirror surface was coated with an Aluminum layer using the metal sputtering technique. This can be done through a shadow mask in case we need to protect some parts from metallization. The resulting Al layer has a thickness of nearly 100 nm in order to maintain a high optical reflectivity with wide spectral bandwidth [117]. The mirror reflectivity was measured at 675 nm and 1550 nm wavelengths and found to be larger than 92 %.

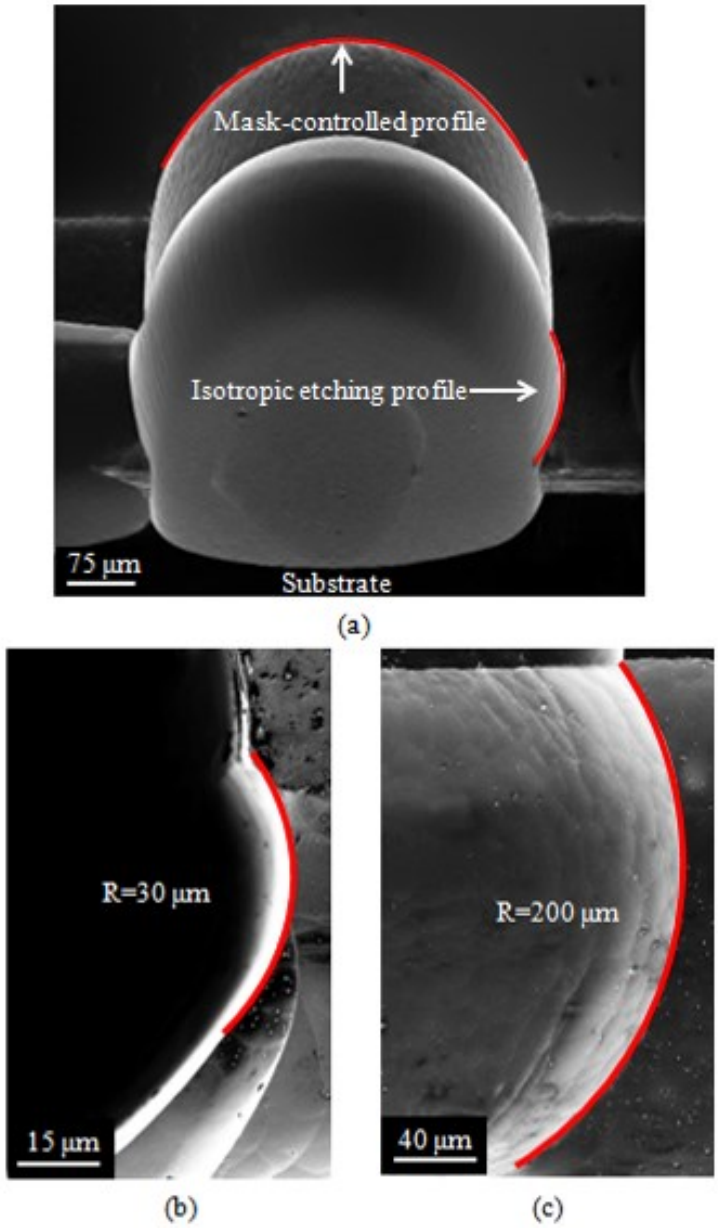

Fig. 4.24. SEM images showing the two-step etched concave surfaces. (a) Tilted 3-D view of the structure. (b) Side view of a resulting structure with a 30 µm out-of-plane radius of curvature. (c) A 200 µm out-of-plane radius obtained with longer isotropic etching.

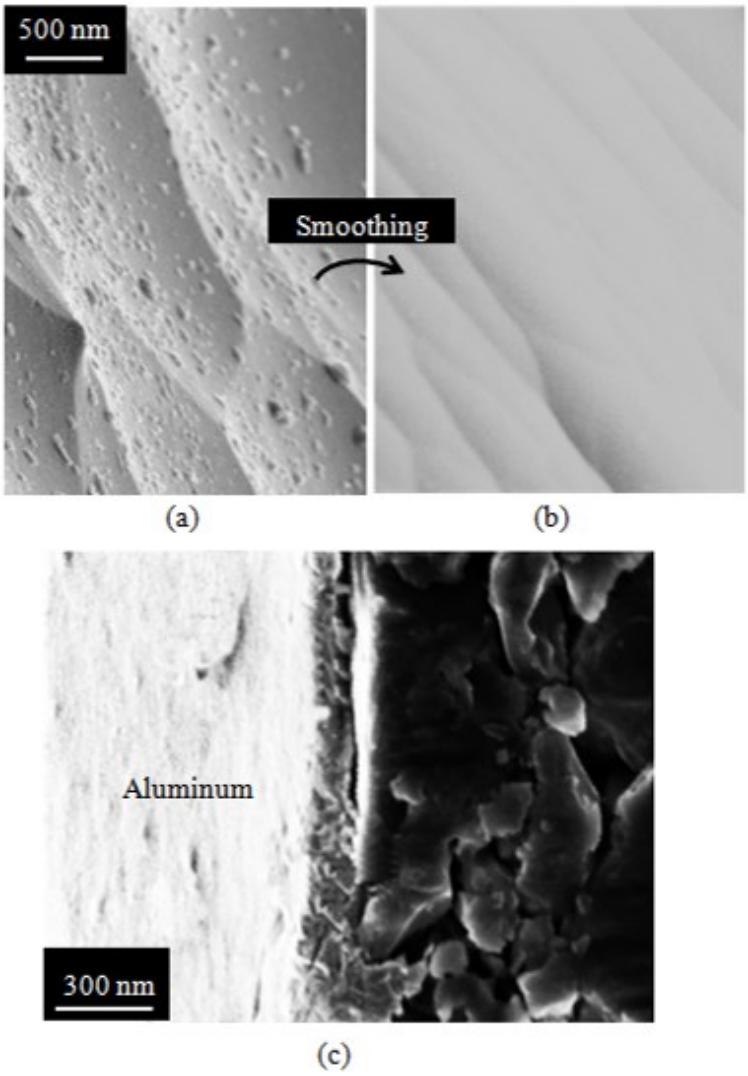

Fig. 4.25. SEM images for the two-step etched concave surface with a zoom-in scale. (a) The peak roughness before smoothing is about 300 nm. (b) The peak roughness after HNA smoothing is about 50 nm. (c) An aluminum layer is deposited on the surface using the sputtering technique.

4.5 Summary

Etching methods for fabrication of three-dimensional curved microstructures exhibiting in-plane principal axis were introduced. The curved surfaces are created by combining the in-plane curvature produced from a drawn mask layout and lithography together with an etching technique to produce the required profile in the out-of-plane direction (e.g., the direction perpendicular to the plane of the substrate). The etching process is either a multi-step method involving tens of etching cycles or a two-step method.

The multi-step etching method is able to produce both concave and convex curved surfaces. The introduced technique was studied by means of numerical simulation using ELITE simulator as well as our simple developed model. The surface quality was related to the ratio between the overall etching depth and the targeted radius of curvature. In order to achieve depth to radius ratio smaller than 0.25, a large number of etching steps may be required with a small and well-controlled etching resolution. On the contrary, depth to radius ratio that is larger than 1 implies a large lateral etching per cycle size, which can be problematic in terms of surface roughness. Alternatively, the two-step etching method –inspired from buried micro channel technology–is able to produce concave surfaces with higher surface quality.

The methods were applied on silicon substrates taking advantage of the ICP reactor, in which anisotropic/ isotropic etching as well as sidewall protection could be carried out without human interruption. The steps were programmed in the machine and their times were set according pre-calculation based on simulation mode. The multi-step

etching method was demonstrated in producing convex surfaces with out-of-plane radius of curvature of 130 μm and concave surfaces with out-of-plane radius of curvature of 270 μm. The surface peak roughness was about 500 nm, which is too high for optical surfaces dealing with light in visible and near infrared wavelength range. In contrast, the two-step etching method yielded concave surfaces with out-of-plane radius of curvature in the order of 30-200 μm and surface peak roughness of about 50 nm. The produced concave microstructure has an optical surface quality with optical power reflectivity better than 92 %.

CHAPTER 5
FREE-SPACE GAUSSIAN BEAM COUPLING

5.1 Introduction

Optical coupling is a critical performance feature in micro photonic components either when considering guided or free-space propagation of light. Guided wave coupling usually focuses on mode shapes, sizes and evanescent tails, where tapering [118], diffraction grating [119] and proximity coupling [120] are typically used. On the other hand, free space coupling elements are usually designed to mitigate optical beam divergence phenomena associated with GB propagation and achieve phase/mode matching. Photonic applications in which the sources and destinations are separated by free-space optical path (OP) were reported such as fiber to fiber [121], laser to fiber[122-124], photonic crystal to fiber [125], waveguide to fiber [126-128] , laser to laser [16,129] and intra chip coupling [132]. In many applications, high coupling efficiency over a relatively long OP is of a crucial importance. For example they have a direct impact on the output power and tunable range of external cavity tunable lasers [17], the finesse and free spectral range of Fabry-Perot resonators [15] and the insertion loss and number of the input/output ports in optical switches [126] as well as in optical interconnects [132].

Micro lenses in the form of lens array [131], ball lenses [133], graded-index lenses [121,127] or lensed fibers [5] are the most commonly used optical components for

focusing and matching GBs. The use of lenses, however, increases the system complexity and cost due to the required assembly process standing out as an obstacle against system integration. To the best of our knowledge, there has not been any 3-dimensional monolithic microlens designed for micro-optical benches; however, it is worth mentioning that several demonstrations of two-dimensional counterparts have been implemented based on surface-micromachined Fresnel lenses [134]. In addition to their inherent material absorption, optical lenses usually exhibit their chromatic behavior caused by their material dispersion as well as the spectral response of their anti-reflective coating that limits the system wavelength range. We therefore explore in this paper the potential of monolithically integrated silicon 3-D micromirrors, which appears as an efficient alternative to lenses for use in micro optical benches (OBs).

Silicon-based coupling micromirrors were reported in both flat and cylindrical shapes [35-36]. The allowable OP was limited to tens of micrometers by the rapid decay of the coupling efficiency. The decay is caused by the optical beam divergence as shown in Fig. 5.1 (a) and (b) in which the flat and the cylindrical micromirrors can be easily obtained by a well-known microfabrication technique, namely using Deep Reactive Ion Etching (DRIE) starting from photolithography-defined straight and curved patterns, respectively. Up to date, high coupling efficiency with sub-millimeter OP in OBs was not achieved without the assembly of a ball lens with flat mirrors [16], the insertion of a fiber rod lens with cylindrical mirrors [15-17] or the hybrid integration of 3-D mirrors that require further assembly or mounting steps [132-134].

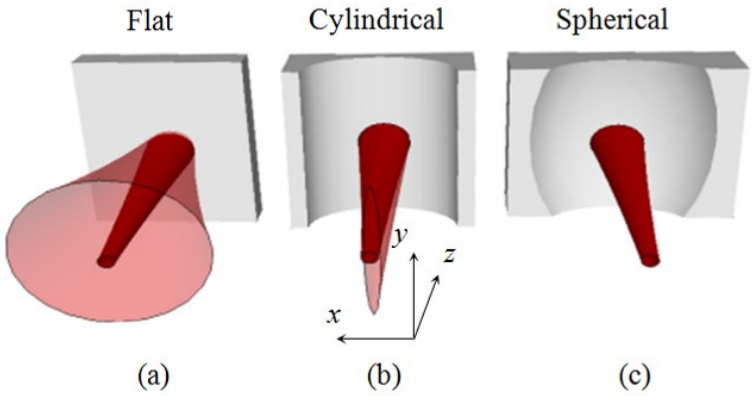

Fig. 5.1. Impact of micromirror's shape in GB reflection: (a) flat mirror where no focusing effect occurs on the reflected beam, (b) cylindrical mirror where the reflected beam can be focused in the tangential plane only, (c) 3-D spherical mirror where full 3-D focusing of the reflected beam can be achieved.

In section 5.2, we study the properties of Gaussians beam coupling using 3-D curved micromirrors and the capability of focusing both the tangential and sagittal divergence of optical beams propagating in-plane of the substrate (xz plane) as shown in Fig. 5.1 (c). The study is focused on a specific microscale range of dimensions where mirror radii of curvature are in the same order of magnitude of the Rayleigh range of the GB [110]. The study also takes into account the effect of having different radii of curvature for the micromirror in the sagittal and tangential planes. The theory is complemented by measuring the coupling efficiency of the fabricated mirror for wavelengths both in the visible and near IR spectrums, also demonstrating the potential use of the device over a wide spectrum. The effect of misalignment between the incident GB and the optical system will be considered. The classical analysis originally introduced

by Marcuse studies the effect of misalignment between two GBs [135], not taking into account a transformation by an optical system.

In section 5.3 an optical resonator is formed making use of the presented 3-D micromirror [136-137]. The optical cavity is formed from the out-of-plane etched 3-D micromirror and a multi-layer coated optical fiber inserted into a groove facing the micromirror. The 3-D curved micromirror demonstrates more than one order of magnitude enhancement in the measured quality factor of the resonator, as compared with the similar device based on a planar mirror. The applications of such a resonator can be exploited for instance in optical filtering, bio sensing and chemical analysis.

Finally in section 5.4, we demonstrate GB collimation using a 3-D curved micromirror as cheap and wide-band alternative to the use of micro lenses as shown in Fig. 5.2 [138]. Sensitivity to micromachining and alignment tolerance is shown to be low enough by restricting the ratio between the mirror focal length and the GB Rayleigh range. The beam incidence angle in the tangential plane together with the mirror focal lengths in tangential and sagittal planes are designed to generate a stigmatic collimated beam. Indeed, 3-D curved micromirrors have the potential of significantly increasing the allowable propagation distance in micro-optical bench systems paving the way for more optical processing and functionality performed inside lensless micro systems.

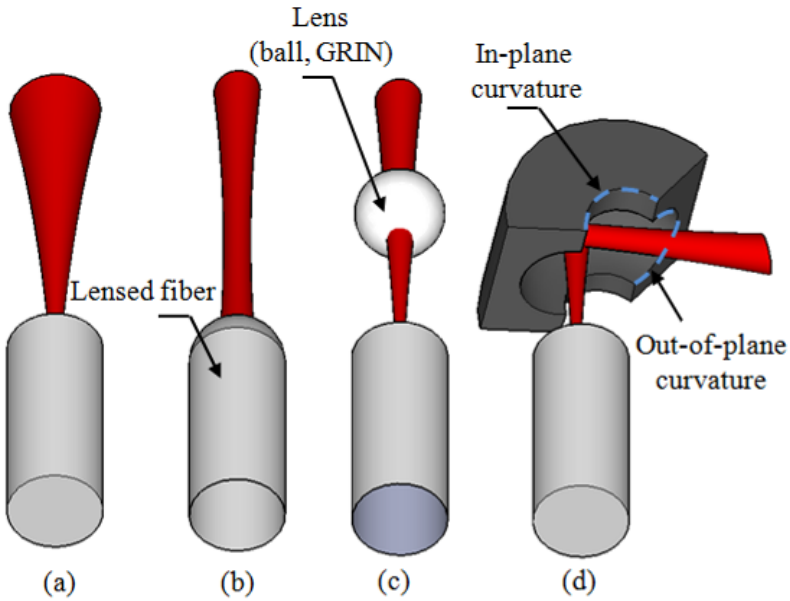

Fig. 5.2. The optical arrangement and output beam of (a) a cleaved single-mode fiber, (b) a lensed fiber, (c) a ball lens and (d) the proposed 3-D curved micromirror. The GB is propagating in a direction parallel to the mirror substrate.

5.2 Gaussian beam coupling efficiency

Field coupling coefficient between a normalized incident GB and another GB reflected back from (or transmitted through) an optical system is given by the overlap integral [83,135]:

$$k = \iint E_i E_r^* dA = \frac{2j\lambda}{\pi}\left[w_{it} w_{is} w_{rt} w_{rs} \left(\frac{1}{q_{it}^*} - \frac{1}{q_{rt}} \right)\left(\frac{1}{q_{is}^*} - \frac{1}{q_{rs}} \right) \right]^{-0.5} \qquad (5.\ 1)$$

where the subscripts i and r stand for the incident and reflected GBs respectively, w is the spot radius, q is the complex phase radius of curvature and the subscripts t and s stand for the tangential and sagittal planes respectively. Note that the field coefficients are chosen

such that overlap integral is normalized to unity. For an optical system with different properties in the tangential and sagittal planes, the reflected and incident beams are related by an ABCD matrix in the form:

$$M = \begin{bmatrix} A_t & 0 & B_t & 0 \\ 0 & A_s & 0 & B_s \\ C_t & 0 & D_t & 0 \\ 0 & C_s & 0 & D_s \end{bmatrix} \tag{5. 2}$$

The ABCD matrix in Eq. (5. 2) with its sparse nature is applicable as long as the optical system understudy poses mirror symmetry in the transverse directions [139]. The corresponding GBs complex phase radii are connected by:

$$q_{rt,s} = \frac{A_{t,s} q_{it,s} + B_{t,s}}{C_{t,s} q_{it,s} + D_{t,s}} \tag{5. 3}$$

By assuming that the incident GB has its waist location at the input plane of the optical system, where any offset can be accounted for in Eq. (5. 2) without loss of generality, then we have:

$$q_{rt,s} = \frac{A_{t,s} q_{it,s} + B_{t,s}}{C_{t,s} q_{it,s} + D_{t,s}} \tag{5. 4}$$

$$w_i = w_o \tag{5. 5}$$

$$q_i = jz_o = j\frac{\pi w_o^2}{\lambda} \tag{5. 6}$$

$$\frac{1}{q_r} = \frac{jz_o C + D}{jz_o A + B} = \frac{z_o^2 AC + BD - jz_o}{z_o^2 A^2 + B^2} \tag{5. 7}$$

$$w_r = \sqrt{-\frac{\lambda}{\pi \,\mathrm{Im}(1/q_r)}} = \sqrt{\frac{\lambda(A^2 z_o^2 + B^2)}{\pi z_o^2}} \tag{5. 8}$$

$$\frac{1}{q_i^*} - \frac{1}{q_r} = -\frac{jz_o(A+D) + B - Cz_o^2}{jz_o B - Az_o^2} \tag{5. 9}$$

where the condition $AD\text{-}BC = 1$ was incorporated to simplify Eq. (5. 7). Substituting back in Eq. (5. 1) yields the following expression for the field complex coupling coefficient:

$$k = \frac{\sqrt{2jz_{ot}}\sqrt{A_t z_{ot} - jB_t}}{(A_t^2 z_{ot}^2 + B_t^2)^{0.25}\sqrt{jz_{ot}(A_t + D_t) + B_t - C_t z_{ot}^2}} \mathrm{x} \\ \frac{\sqrt{2jz_{os}}\sqrt{A_s z_{os} - jB_s}}{(A_s^2 z_{os}^2 + B_s^2)^{0.25}\sqrt{jz_{os}(A_s + D_s) + B_s - C_s z_{os}^2}} \tag{5. 10}$$

The power coupling efficiency is obtained by squaring the magnitude of the field coupling coefficient and is given below:

$$\eta = \frac{2z_{ot}}{\sqrt{B_t^2 + z_{ot}^2(A_t^2 + D_t^2 + 2) + z_{ot}^4 C_t^2}} \mathrm{x} \\ \frac{2z_{os}}{B_s^2 + z_{os}^2(A_s^2 + D_s^2 + 2) + z_{os}^4 C_s^2} \tag{5. 11}$$

The derived relation in Eq. (5. 11) expresses the power coupling efficiency between the input and the output GBs to an optical system with known ABCD matrix parameters in the system tangential and sagittal planes. The GBs can be of elliptical or circular cross section. In the case of elliptical beams, the incident beam and the optical system should have the same orientation of the tangential and the sagittal planes so that the ABCD

matrix preserves its sparsity. The expression in (10) can be applied to the cases of flat, cylindrical and spherical micromirrors with the aid of Table 5.1.

Table 5.1. The ABCD matrix elements connecting incident and reflected beams by flat, cylindrical and spherical mirrors where d is the distance between the incident beam waist and the mirror (i.e. the optical path of the beam is $2d$).

Element	**Flat mirror**	**Cylindrical mirror**	**Spherical mirror**
$\boldsymbol{A_t}$	1	$1-2d/R_t$	$1-2d/R_t$
$\boldsymbol{B_t}$	$2d$	$2d(1- d/R_t)$	$2d(1- d/R_t)$
$\boldsymbol{C_t}$	0	$-2/R_t$	$-2/R_t$
$\boldsymbol{D_t}$	1	$1-2d/R_t$	$1-2d/R_t$
$\boldsymbol{A_s}$	1	1	$1-2d/R_s$
$\boldsymbol{B_s}$	$2d$	$2d$	$2d(1- d/R_s)$
$\boldsymbol{C_s}$	0	0	$-2/R_s$
$\boldsymbol{D_s}$	1	1	$1-2d/R_s$

Practically, the overall coupling efficiency of a micro-optical bench's micromirror should account for its reflectivity which is strongly dependent on the micromachined surface quality. The expression in Eq. (5. 11) can be applied to more complicated optical systems once their ABCD matrix parameters are derived.

Coupling losses can arise between the incident and the reflected GBs due to a misalignment between the incident GB optical axis and the principal axis of a micro-optical component. This misalignment can be in the form of lateral shift Δy or angular shift $\Delta\theta$. Consequently, there will be a shift misalignment Δ_c and an angular misalignment α_c between the incident and the reflected GBs. These misalignments can be calculated from the problem geometry. Their effect on the field coupling coefficient is given by [83]:

$$k_M = k \exp\left[-j\pi\lambda^{-1}\Delta_c^2\left(q_{rt} - q_{it}^*\right)^{-1}\right]\exp\left[j\pi\lambda^{-1}\alpha_c^2\left(\frac{1}{q_{rt}} - \frac{1}{q_{it}^*}\right)^{-1}\right] \quad (5.\ 12)$$

In addition to its direct impact on the coupling coefficient, misalignment of the incident GB to the spherical mirror causes the GB to undergo a slightly different transformation from that described by the ABCD matrix given in Table 5.1. The modified matrix parameters given in Table 5.2 should be used instead, which account for the incidence angle θ_{inc} and the difference in the propagation distances before and after reflection d_1 and d_2, respectively with the assumption of the misalignment befalling in the tangential plane. Following a similar analysis to the one used to derive Eq. (5. 11), the coupling efficiency between an incident GB and another GB reflected back from (or transmitted through) an optical system in the presence of misalignment in the tangential plane between the incident beam and the system is given by:

$$\eta_M = \eta \exp\left[\frac{-2\pi\Delta_c^2}{\lambda}\frac{z_o(1+D_t^{\,2})+C_t^{\,2}z_o^3}{[B^2+z_o^2(A_t^{\,2}+D_t^{\,2}+2)+z_o^4C_t^{\,2}]} - \frac{2\pi\alpha_c^2 z_o(B_t^{\,2}+A_t^{\,2}z_o^2)}{\lambda(B_t^{\,2}+A_t^{\,2}z_o^2+z_o^2)}\right] \quad (5.\ 13)$$

Eq. (5. 13) can be used for any optical system one its ABCD matrix parameters are known. The expression for the coupling efficiency in the presence of misaligned in the sagittal plane is similar.

Table 5.2. Modified ABCD matrix elements for GB transformation in the presence of misalignment.

Element	**Flat mirror**	**Cylindrical mirror**	**Spherical mirror**
$\boldsymbol{A_t}$	1	$1-2d_2/R_t\cos(\theta_{inc})$	$1-2d_2/R_t\cos(\theta_{inc})$
$\boldsymbol{B_t}$	d_1+d_2	$d_1+d_2-2d_1d_2/R_t\cos(\theta_{inc})$	$d_1+d_2-2d_1d_2/R_t\cos(\theta_{inc})$
$\boldsymbol{C_t}$	0	$-2/R_t\cos(\theta_{inc})$	$-2/R_t\cos(\theta_{inc})$
$\boldsymbol{D_t}$	1	$1-2d_2/R_t\cos(\theta_{inc})$	$1-2d_2/R_t\cos(\theta_{inc})$
$\boldsymbol{A_s}$	1	1	$1-2d_2\cos(\theta_{inc})/R_s$
$\boldsymbol{B_s}$	d_1+d_2	d_1+d_2	$d_1+d_2-2d_1d_2\cos(\theta_{inc})/R_s$
$\boldsymbol{C_s}$	0	0	$-2\cos(\theta_{inc})/R_s$
$\boldsymbol{D_s}$	1	1	$1-2d_2\cos(\theta_{inc})/R_s$

Beam truncation effect in micro-optical systems starts to interact and further reduces the coupling efficiency, when the micromirrors size is smaller than the limits

mentioned above. In this case, the coupling losses can divide into three parts. The first of these parts is already given by Eq. (5. 16). The second part arises from the power escaped out of the micromirror physical dimension and is not reflected by the micromirror. Finally, the third part is related to the additional coupling loss, which takes place as a result of the projection of the truncated beam on the fundamental GB. It was previously shown that the latter two parts of the losses can be accounted for by squaring of the truncation power loss formula [71]. In case of a rectangular micromirror of width w_m and height h_m typically encountered in micro-optical bench systems, the truncation power loss formula is given by [140]:

$$K = erf\left(\frac{w_m}{\sqrt{2}w}\right)erf\left(\frac{h_m}{\sqrt{2}w}\right) \qquad (5.\ 14)$$

where erf is the error function. Combining the square of Eq. (5. 14) with Eq. (5. 11), the overall coupling efficiency in the presence of truncation:

$$\eta_T = \eta\left[erf\left(\frac{D_w / w_o}{\sqrt{2+2(d/z_o)^2}}\right)erf\left(\frac{D_h / w_o}{\sqrt{2+2(d/z_o)^2}}\right)\right]^{2^{-1}} \qquad (5.\ 15)$$

where D_w and D_h are the physical width and height of the micro-optical components. In the following sections, detailed analysis of the coupling properties of micromirrors is given.

5.2.1 Coupling efficiency of flat micromirrors

Substituting with the ABCD parameters of a micro-optical system containing or more or more flat mirrors into Eq. (5. 11) yields the following expression for the coupling efficiency:

$$\eta_F = \frac{4z_o^2}{4d^2 + 4z_o^2} = \left[1 + \left(\frac{d}{z_o}\right)^2\right]^{-1} \qquad (5.\ 16)$$

The coupling efficiency decays with propagation distance and the decay rate is more significant for smaller beam Rayleigh range. The 3-dB coupling propagation distance of the optical system is $d = z_o$ while the 10-dB coupling distance is $d = 3z_o$. To avoid GB truncation in the micro-optical system, the size of the micromirrors should be at least four times the beam spot radius at the mirror, i.e. $4\sqrt{2}w_o$ or $4\sqrt{10}w_o$ in the specific cases of 3-dB or 10-dB coupling, respectively. Indeed, 3- to 10-dB coupling efficiency can be adequate for specific micro-optical system used, for instance in variable optical attenuators, tunable filters and chemical analysis applications.

Combining the square of Eq. (5. 14) with Eq. (5. 16), the total power coupling efficiency for a flat micromirror in the presence of truncation is given by:

$$\eta_{FT} = \left[erf\left(\frac{D_w / w_o}{\sqrt{2 + 2(d / z_o)^2}}\right) erf\left(\frac{D_h / w_o}{\sqrt{2 + 2(d / z_o)^2}}\right)\right]^2 \left[1 + \left(\frac{d}{z_o}\right)^2\right]^{-1} \qquad (5.\ 17)$$

where D_w and D_h are the physical width and height of the micromirror. The expression in Eq. (5. 17) is depicted in Fig. 5.3 . The micromirror width is kept large enough at $4\sqrt{10}$ w_o while its height –usually limited by the micromachining technology–, is assigned the

values of $4\sqrt{10}\ w_o$, $4\sqrt{2}\ w_o$, $4\ w_o$, $2\ w_o$ and w_o. The 3-dB coupling distance is about $d = 0.75\ z_o$ for $2\ w_o$ and is about $d = z_o$ for the larger widths. The 10-dB coupling distances are about $d = 3\ z_o$, $d = 2.8\ z_o$, $d = 2.5\ z_o$, $d = 1.85\ z_o$ and $d = 1.15\ z_o$ for $4\sqrt{10}\ w_o$, $4\sqrt{2}\ w_o$, $4\ w_o$, $2\ w_o$ and w_o respectively. The design rules for any other value of the coupling efficiency can be deduced in the same way. The truncation effect has a similar impact on the cylindrical and the spherical micromirrors.

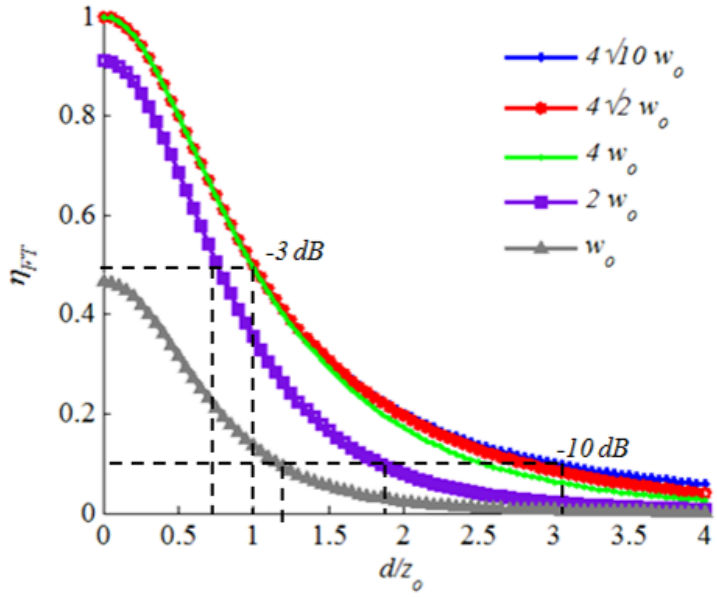

Fig. 5.3. Coupling efficiency of a flat micromirror in the presence of truncation versus the ratio between the mirror-to-beam-waist distance and the incident GB Rayleigh range. The mirror width is $4\sqrt{10}w_o$ and its heights are $4\sqrt{10}w_o$, $4\sqrt{2}w_o$, $4w_o$, $2w_o$ and w_o.

For the particular case of small misalignment with a flat micromirror, Eq. (5. 13) can be put in the form:

$$\eta_{FM} = \eta_F \exp\left[-\frac{\Delta_c^2}{w_o^2} \frac{1}{1+d^2/z_o^2} - \frac{\alpha_c^2}{\theta_o^2} \frac{1+4d^2/z_o^2}{1+2d^2/z_o^2} \right] \qquad (5.\ 18)$$

where d_1 was set equal to d_2. The expression in Eq. (5. 18) assumes a small tilt angle misalignment, for which there is no need to use trigonometric functions. Eq. (5. 18) has the advantage of being function in normalized quantities. This helps to gain insight about the dominate factors. It also preserves the physical sense that a GB with larger beam waist is less sensitive to shift misalignment and a GB with larger divergence angle is less sensitive to angular misalignment. The impact of tilt misalignment on the coupling efficiency was studied for d/z_o = 0, 1 and 3. The quantities Δ_c/w_o *and* α_c/θ_o were deduced from the problem geometry to be $2(\Delta\theta/\theta_o)(d/z_o)$ and $2(\Delta\theta/\theta_o)$, respectively. The corresponding misalignment coupling loss is depicted in Fig. 5.4. The coupling loss increases with increasing the distance d between the incident beam waist and the micromirror surface. This is a direct result of the proportionality between the Δ_c and d. The rate of increment decreases with the distance d as a result of the GB expansion with propagation.

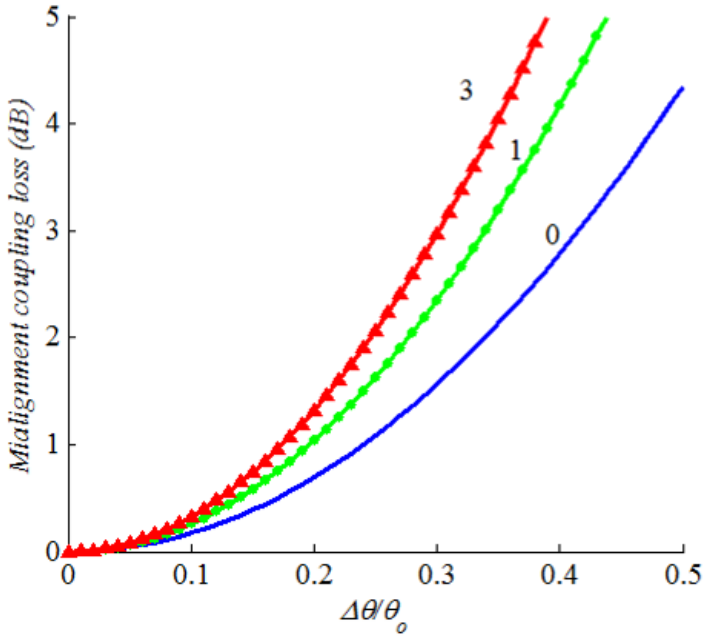

Fig. 5.4. The loss in coupling efficiency of a flat micromirror versus the relative tilt misalignment for different d/z_o.

5.2.2 Coupling efficiency of cylindrical micromirrors

Substituting with the cylindrical mirror ABCD parameters listed in Table 5.1 into Eq. (5. 11) yields the following expression for the coupling efficiency:

$$\eta_C = \left[1+\left(\frac{d}{z_o}\right)^2\right]^{-0.5}\left[0.5+\left(\frac{d}{z_o}\right)^2\left(1-\frac{d}{z_o}\frac{z_o}{R}\right)^2+0.5\left(1-2\frac{d}{z_o}\frac{z_o}{R}\right)^2+\left(\frac{z_o}{R}\right)^2\right]^{-0.5} \qquad (5.\ 19)$$

The first multiplication term in Eq. (5. 19) represents the coupling efficiency in the sagittal plane due to the flat cross section of the mirror surface. The second multiplication term expresses the coupling efficiency in the tangential plane accounting for the curvature in that plane. Indeed, Eq. (5. 19) reduces to Eq. (5. 16) when the radius of curvature is infinite. The truncation effect to the finite size of the micromirror can be

accounted for in a similar way to the flat micromirror. The second term in Eq. (5. 19) has maxima versus d / z_o that can be found by means of partial differentiation and nulling of the derivative, which yields:

$$\left(1-2\frac{d}{z_o}\frac{z_o}{R}\right)\left[\left(\frac{d}{z_o}\right)^2-\frac{d}{z_o}\frac{R}{z_o}+1\right]=0 \qquad (5.\ 20)$$

Thus the extremes are located at:

$$d_{m1}=0.5R \qquad (5.\ 21)$$

$$d_{m2,3}=0.5R\left(1\pm\sqrt{1-\left(\frac{2z_o}{R}\right)^2}\right) \qquad (5.\ 22)$$

A single extreme is found at d_{m1} when $z_o>R/2$, while two additional extremes are found at $d_{m2,3}$ when $z_o<R/2$. Back substitution in the second term of Eq. (5. 19) when $z_o<R/2$ yields unity maxima for the $d_{m2,3}$ locations while the maxima located at d_{m1} is smaller than unity. Note that for the specific case of curved micromirror, the radius of curvature of the surface can be in the order of the incident GB Rayleigh range. In contrast to the flat micromirrors, the zero-distance coupling efficiency of the cylindrical micromirrors is always smaller than unity and given by:

$$\eta_C\big|_{d=0}=\left[1+\left(\frac{z_o}{R}\right)^2\right]^{-0.5} \qquad (5.\ 23)$$

The cylindrical mirror coupling efficiency expression in Eq. (5. 19) is depicted in Fig. 5.5 versus the ratio d/z_o for z_o/R = 2, 1, 0.5 and 0.25. The zero-distance coupling is much smaller than unity unless the ratio z_o/R is small enough, for example 0.25. There is only

one peak location and close to zero when $z_o/R>0.5$. For smaller z_o/R, the peaks located close to $d/z_o \approx R/z_o$ start to be recognized. The coupling efficiency of the cylindrical micromirrors can be non-satisfactory when efficient coupling is needed. The effect of misalignment with a curved surface is better illustrated in the case of a spherical micromirror. The reason why the curved surface power coupling is smaller than unity for zero distance and the appearance of more than one maximum in the coupling behavior will be also explained in the next section after considering the coupling efficiency of the spherical micromirrors.

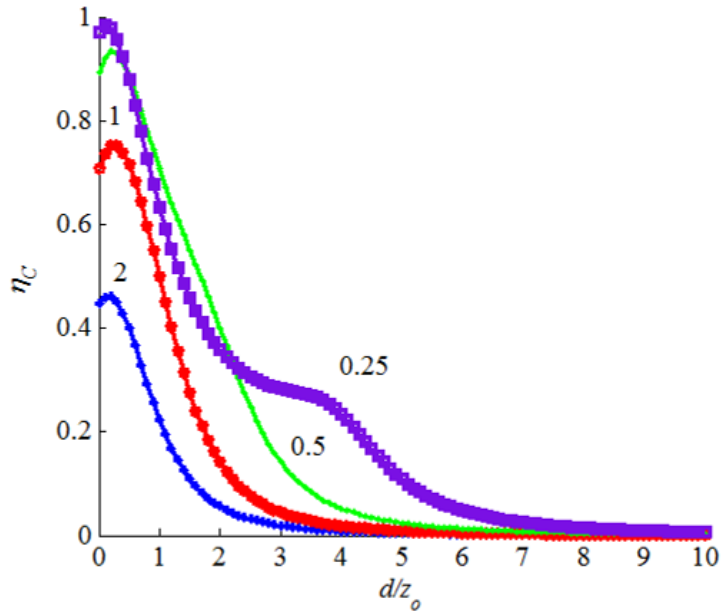

Fig. 5.5. Coupling efficiency of a cylindrical micromirror versus the ratio between the mirror-to-beam-waist distance and the incident GB Rayleigh range. The curves are plotted for different ratios between the GB Rayleigh range and the mirror radius of curvature.

5.2.3 Coupling efficiency of spherical micromirrors

Substituting with the spherical mirror ABCD parameters listed in Table 5.1 into Eq. (5. 11) and setting $R_s = R_t = R$ yields the following expression for the coupling efficiency:

$$\eta_S = \left[0.5 + \left(\frac{d}{z_o}\right)^2 \left(1 - \frac{d}{z_o}\frac{z_o}{R}\right)^2 + 0.5\left(1 - 2\frac{d}{z_o}\frac{z_o}{R}\right)^2 + \left(\frac{z_o}{R}\right)^2 \right]^{-1} \qquad (5.\ 24)$$

The expression is depicted in Fig. 5.6 versus the ratio d/z_o for z_o/R = 2, 1, 0.5 and 0.25. Again the zero-distance coupling efficiency is much smaller than unity unless the ratio z_o/R is small enough. The zero-distance coupling efficiency is given by:

$$\eta_S\big|_{d=0} = \left[1 + \left(\frac{z_o}{R}\right)^2 \right]^{-1} \qquad (5.\ 25)$$

Unity coupling efficiency can be obtained when z_o/R *is* smaller than or equal to 0.5. The coupling efficiency at the location d_{m1} is given by:

$$\eta_S\big|_{d=d_{m1}} = \frac{1}{\frac{1}{2} + \frac{R^2}{16 z_o^2} + \frac{z_o^2}{R^2}} \qquad (5.\ 26)$$

The special case of z_o/R= 0.5 has a unique flat response centered on d/z_o = 1. The 1-dB width of the response is extending from zero distance up to d/z_o = 2. Indeed, this response is very convenient to consider implementing a wide tuning mechanism for the mirror position centered on d/z_o = *1(i.e. d*=0.5 *R)* with nearly a flat response over a distance $\Delta d = \pm z_o$. This is of particular interest for applications like optical delay lines and external cavity tunable lasers. For larger ratios of mirror radius of curvature to beam Rayleigh range, there are two unity extremes at the locations d_{m2} and d_{m3}, with the latter becomes

closer to $d=R$ when z_o/R is much smaller than 0.5. For instance, consider the coupling efficiency shown in Figure for the case of R = 200 μm and the three values of GB Rayleigh range of 10 μm, 30 μm and 50 μm. The coupling efficiency curved around the extremes becomes sharper and the extremes locations become weakly dependent on z_o when z_o/R is small enough. In such situation, the spherical micromirrors pose the capability of efficiently coupling both elliptical as well as circular beams for a relatively wide wavelength range. From the application perspective, elliptical GBs are the typical output of semiconductor lasers while the utilization of wide bandwidth optical source is mandatory in low coherence applications.

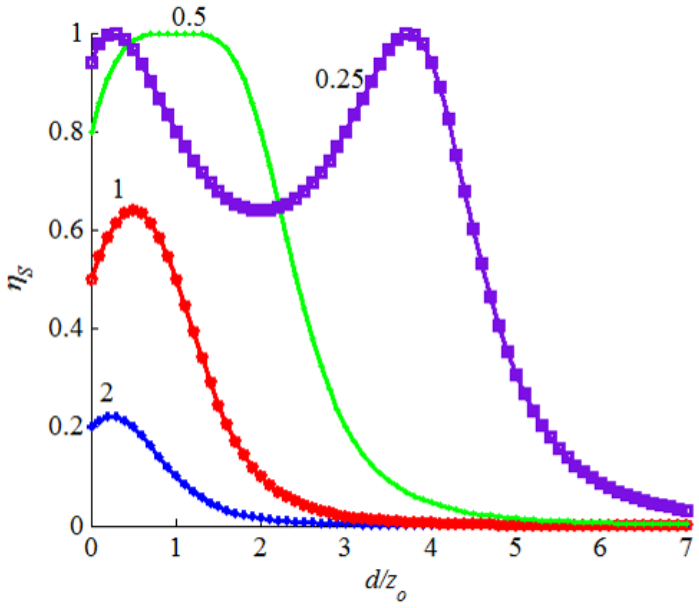

Fig. 5.6. Coupling efficiency of a spherical micromirror versus the ratio between the mirror-to-beam-waist distance and the incident GB Rayleigh range. The curves are plotted for different ratios between the GB Rayleigh range and the mirror radius of curvature.

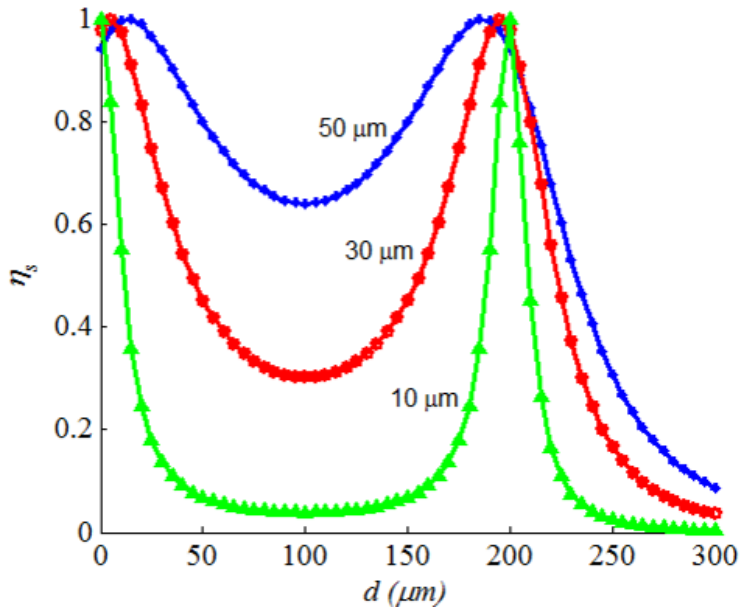

Fig. 5.7. Coupling efficiency of a spherical micromirror with a 200 µm radius of curvature versus the mirror-to-beam-waist distance for different GB Rayleigh range. The z_o/R ratios are 0.25, 0.15 and 0.05 for the GB Rayleigh ranges 50 µm, 30 µm and

The encountered behavior related to the ratio z_o/R can be explained as follows. For perfect beam focusing, the mirror radius of curvature should match the incident GB phase radius of curvature R_b where the later exhibits the dependence shown in Fig. 5.8 versus the distance z to the beam waist. The minimum phase radius is twice as the GB Rayleigh range ($R_b = 2z_o$). If the mirror radius of curvature is smaller than $2z_o$, the maximum achievable coupling will be always smaller than 100 % posing a single extreme value and preventing high coupling over a long distance. This extreme gets closer to 100 % and its location approaches z_o when the mirror radius of curvature approaches $2z_o$ (see point p_1). When the mirror radius of curvature is greater than $2z_o$, a

full-coupling condition can be satisfied at two different locations simultaneously (see points p_2 and p_3), before and after the location where $z = z_o$. As the mirror radius of curvature becomes larger, the first of these locations approaches zero while the second location becomes approximately equal to the mirror radius of curvature.

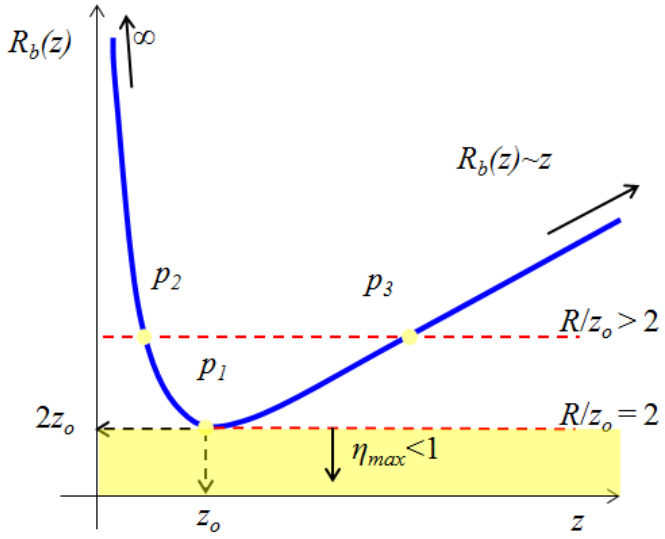

Fig. 5.8. The coupling efficiency behavior of the spherical micromirror is related to how the GB phase radius of curvature R_b varies with distance to beam waist z.

Practical coupling situations may involve the use of spherical micromirrors with unmatched radii of curvature in the tangential and sagittal planes. This is likely to occur due to the micromachining process tolerance. Substituting with the spherical mirror ABCD parameters listed in Table 5.1 into Eq. (5. 11) and assuming that $R_s \neq R_t$ yields the following expression for the coupling efficiency:

$$\eta_{SU} = \left[0.5 + \left(\frac{d}{z_o}\right)^2 \left(1 - \frac{d}{z_o}\frac{z_o}{R_t}\right)^2 + 0.5\left(1 - 2\frac{d}{z_o}\frac{z_o}{R_t}\right)^2 + \left(\frac{z_o}{R_t}\right)^2\right]^{-0.5} \text{x}$$
$$\left[0.5 + \left(\frac{d}{z_o}\right)^2 \left(1 - \frac{d}{z_o}\frac{z_o}{R_s}\right)^2 + 0.5\left(1 - 2\frac{d}{z_o}\frac{z_o}{R_s}\right)^2 + \left(\frac{z_o}{R_s}\right)^2\right]^{-0.5} \quad (5.27)$$

For the sake of evaluating the mismatch impact, the radii are assumed to be $Rs = R_o + \Delta R / 2$ and $Rs = R_o - \Delta R / 2$ where R_o is the mean value and ΔR is the total deviation. The coupling efficiency is depicted in Fig. 5.9 for the cases $z_o/R = 0.5$ and 0.25 with $\Delta R/R$ of 0.1, 0.25 and 0.5. The mismatch causes deterioration in the coupling efficiency peak values and change in their locations. The effect is more significant for smaller z_o/R_o. Again the case of $z_o/R_o=0.5$ shows a special interest because the effect of mismatch on the coupling efficiency is minimal in this case. The coupling loss (in dB) versus the mismatch $\Delta R/R$ is depicted in Fig. 5.10 for different z_o/R. The loss represented by dashed lines is obtained by dividing the maximum value of the ideal coupling efficiency, which is unity, by the maximum value of reduced coupling efficiency due to mismatch. Note that the location of the maximum value is different for the ideal and the reduced efficiencies. On the other hand, the loss represented by solid lines is obtained by evaluating the reduced coupling efficiency at $d=0.5R$ for the case of $z_o/R=0.5$ and $d=R$ for the other cases. Depending on the application, different values for mismatch can be tolerated and the data shown in Fig. 5.10 can be used to set the requirements on the fabrication tolerance.

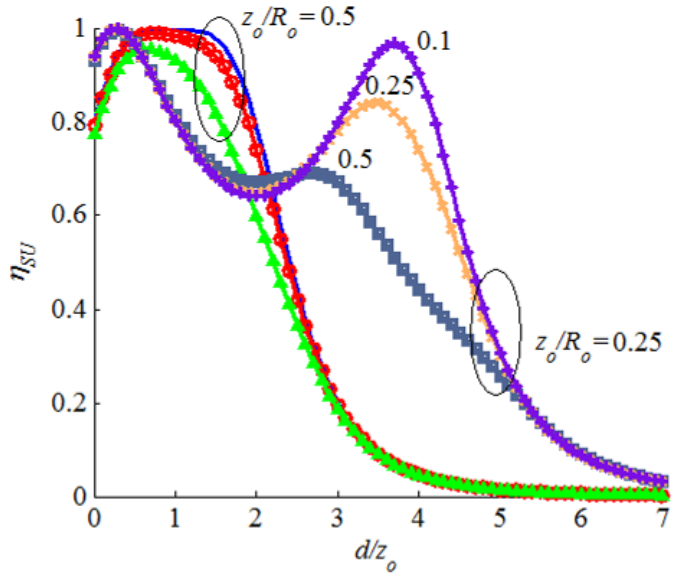

Fig. 5.9. Effect of the radii of curvature relative mismatch $\Delta R/R_o$ on the coupling efficiency of spherical micromirros.

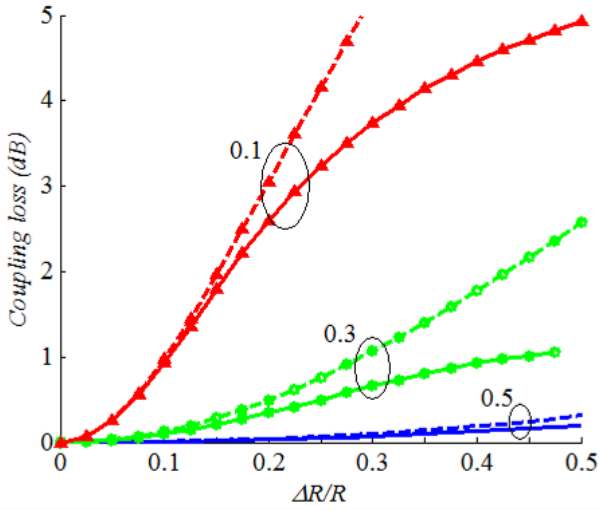

Fig. 5.10. The loss in coupling efficiency versus the relative mismatch in the radii of curvature. Solid lines: the distance d is chosen according to the shifted peak location. Dashed line: d is set equal to 0.5 R in the case of z_o/R=0.5 and set equal to R in the cases of z_o/R=0.3 and 0.1.

For the particular case of small misalignment with a spherical micromirror, Eq. (5. 13) can be put in the form:

$$\eta_{SM} = \eta_S \exp\left[-2\frac{\Delta_c^2}{w_o^2}\frac{1+(1-2d/R)^2+4(z_o/R)^2}{2+2(1-2d/R)^2+4(z_o/R)^2+(d/z_o)^2(1-d/R)^2} \right.$$
$$\left. -2\frac{\alpha_c^2}{\theta_o^2}\frac{(d/z_o)^2(1-d/R)^2+(1-2d/R)^2}{1+(d/z_o)^2(1-d/R)^2+(1-2d/R)^2} \right] \quad (5.\ 28)$$

The impact of lateral shift misalignment on the coupling efficiency was studied for z_o/R_o = 0.5 and 0.25; each with a shift $\Delta y/w_o$ = 0.1, 0.3 and 0.5. The corresponding factors Δ_c/w_o *and* α_c/θ_o were deduced from the problem geometry to be $2(\Delta y/w_o)(d/R)$ and $2(\Delta y/w_o)(z_o/R)$, respectively. The corresponding coupling efficiency curves are depicted in Fig. 5.11. Close to the mirror surface; i.e. $d = 0$, the effect of misalignment is worse for $z_o/R_o = 0.5$. On the hand, the effect is less pronounced around and around the peak value of the coupling efficiency. In addition, the misalignment causes a small shift in the peak location to be closer to the mirror surface. This is ascribed to the decaying behavior of the misaligned coupling coefficient with distance. Ignoring this small shift and focusing on the loss factor given by the exponential term in Eq. (5. 28), the coupling loss (in dB) is depicted in Fig. 5.12 versus the relative shift misalignment. The loss for z_o/R_o = 0.5, which is evaluated at d = 0.5R, has the advantage of being less affected by lateral misalignment and tolerates almost double the misalignment of other cases, which are evaluated at $d = R$. Apart from this case when $z_o/R_o < 0.5$, the loss is more pronounced for larger z_o/R_o and the dependence on z_o/R_o is weak as long as the misalignment is not relatively large.

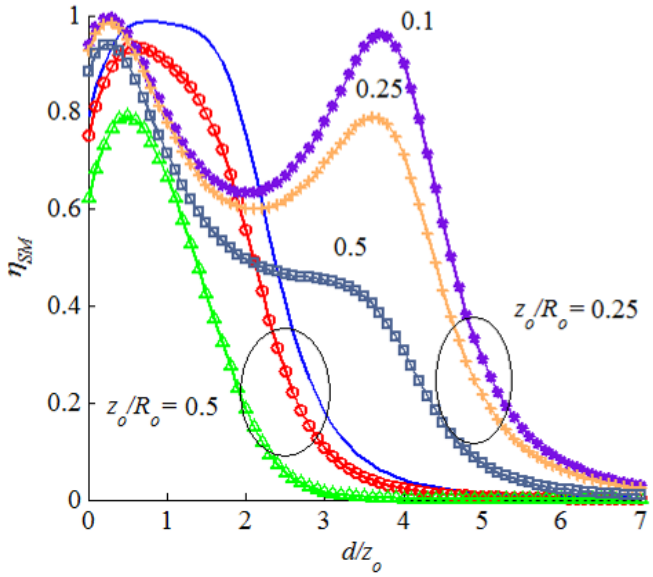

Fig. 5.11. Effect of relative shift misalignment $\Delta y/w_o$ on the coupling efficiency of spherical micromirros.

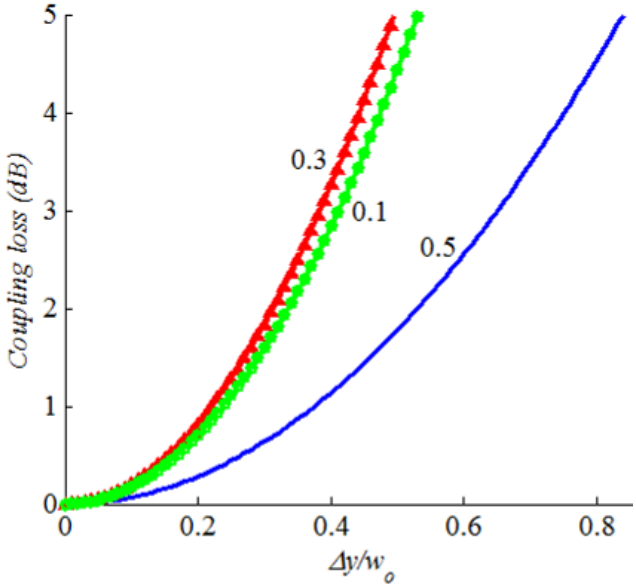

Fig. 5.12. The loss in coupling efficiency versus the relative shift misalignment for different z_o/R with d = 0.5 R for z_o/R_o=0.5 and d= R for the other cases.

The impact of tilt misalignment on the coupling efficiency was studied for z_o/R_o = 0.5 and 0.25; each with a relative tilt $\Delta\theta/\theta_o$ = 0.1, 0.3 and 0.5. Δ_c/w_o *and* α_c/θ_o were deduced from the problem geometry to be $2(\Delta\theta/\theta_o)(d/z_o)(1\text{-}d/R)$ and $2(\Delta\theta/\theta_o)(1\text{-}d/R)$, respectively. The corresponding coupling efficiency curves are shown in Fig. 5.13. Tilt misalignment hardly affects the case of z_o/R_o = 0.25 (or smaller) around $d = R$. Indeed, the tilt misalignment factors are null at $d = R$ because of the fact that a ray passing through the spherical mirror center of curvature will reflect back on itself whatever its tilt angle with respect to another reference axis passing through the center. Note also that the original power coupling coefficient itself in (20) has a peak value that is slightly less than unity around $d = R$ and becomes closer to unity for smaller z_o/R_o. In contrast to the shift misalignment, tilt causes a small shift in coupling peaks towards larger d locations; i.e. away from the mirror surface. The misalignment has its maximum impairment occurring close to $d = 0$ and is larger for larger z_o/R_o as shown in Fig. 5.14.

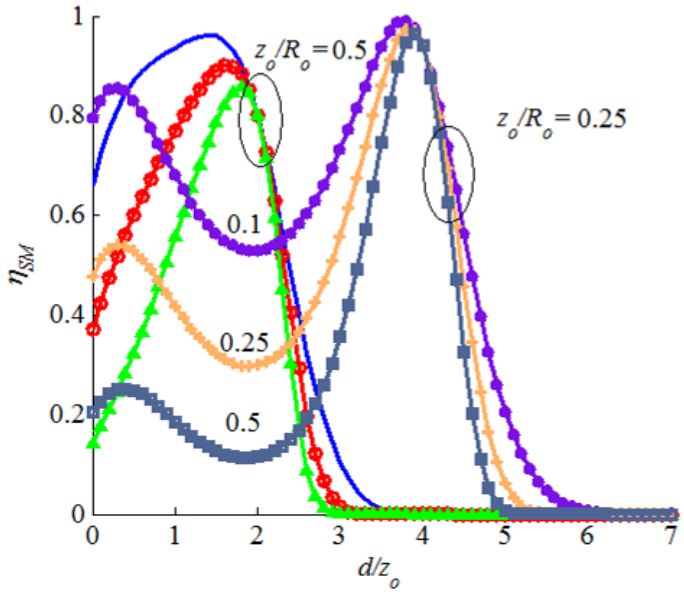

Fig. 5.13. Effect of relative title misalignment $\Delta\theta/\theta_o$ on the coupling efficiency of spherical micromirros.

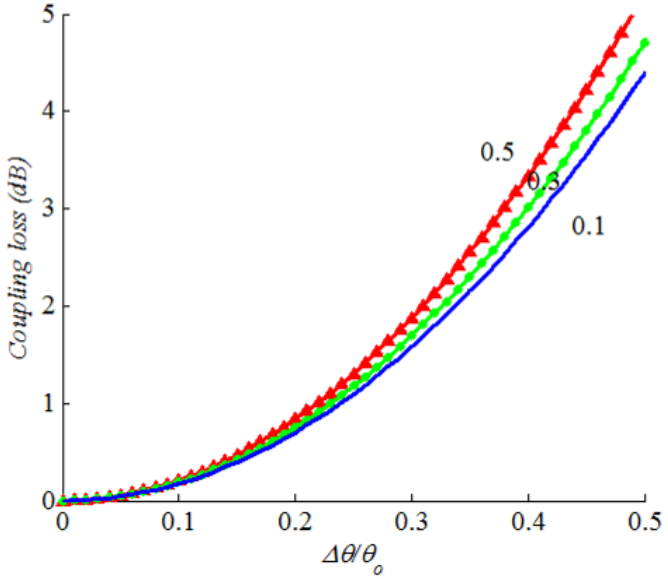

Fig. 5.14. The loss in coupling efficiency of a spherical micromirror versus the relative tilt misalignment for different z_o/R at $d = 0$.

5.2.4 Double-mirror coupling configuration

Consider the double-mirror coupling configuration shown in Fig. 5.15 in which the beam can be either coupled back to the source as shown in (a) or coupled to a destination as shown in (b). In both cases, a spherical micromirror is used to collimate the input beam when the beam waist is located at focus the micromirror. Then, the collimated beam is either reflected back by a flat mirror or refocused using another spherical mirror. The total coupling distance is $2(d_1 + d_2)$. The ABCD matrix parameters of this coupling configuration are given in Table 5.3. The radii of curvatures of the spherical mirror, as seen by the incident beam, will be dependent on the incidence angle. In order to have a single value for the focal length of the spherical mirror, the mirror should be astigmatic with the radii of curvatures related by the incidence angle such that $R_s / cos(\theta_{inc}) = R_t \, cos(\theta_{inc}) = R$.

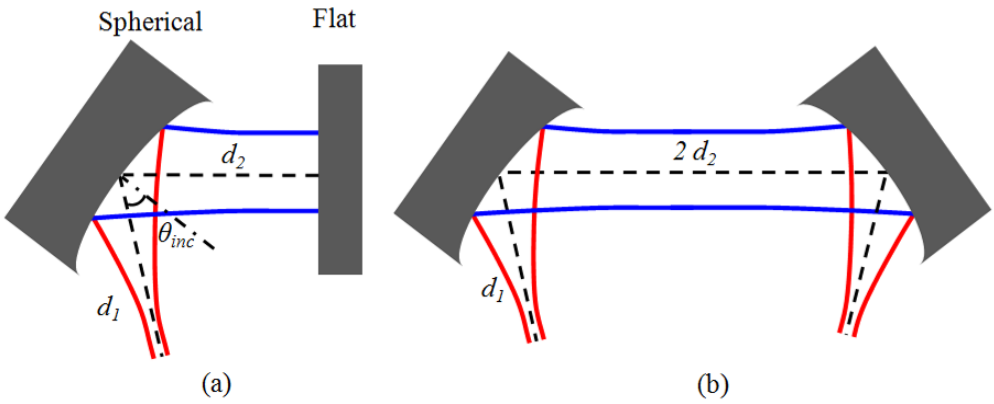

Fig. 5.15. Double-mirror coupling configuration using (a) one spherical mirror or (b) two.

Table 5.3. The ABCD matrix parameters of the double-mirror coupling configuration in Fig. 5.15.

$\boldsymbol{A_t}$	$1\text{-}4(d_1+d_2)/R_t\cos(\theta_{inc})+8d_1d_2/R_t^2\cos^2(\theta_{inc})$
$\boldsymbol{B_t}$	$2(d_1+d_2)\text{-}(8d_1d_2+4d_1^2)/R_t\cos(\theta_{inc})+8d_1^2d_2/R_t^2\cos^2(\theta_{inc})$
$\boldsymbol{C_t}$	$-2(1+4d_2/R_t\cos(\theta_{inc}))/R_t\cos(\theta_{inc})$
$\boldsymbol{D_t}$	$1\text{-}4(d_1+d_2)/R_t\cos(\theta_{inc})+8d_1d_2/R^2{}_t\cos^2(\theta_{inc})$
$\boldsymbol{A_s}$	$1\text{-}4(d_1+d_2)\cos(\theta_{inc})/R_s+8d_1d_2\cos^2(\theta_{inc})/R_s^2$
$\boldsymbol{B_s}$	$2(d_1+d_2)\text{-}(8d_1d_2+d_1^2)\cos(\theta_{inc})/R_s+8d_1^2d_2\cos^2(\theta_{inc})/R_s^2$
$\boldsymbol{C_s}$	$-2(1+4d_2\cos(\theta_{inc})/R_s)\cos(\theta_{inc})/R_s$
$\boldsymbol{D_s}$	$1\text{-}4(d_1+d_2)\cos(\theta_{inc})/R_s+8d_1d_2\cos^2(\theta_{inc})/R_s^2$

Setting $d_1 = R/2$ and substituting with the ABCD matrix parameters in Eq. ((5. 11) yields the following simple expression for the coupling efficiency:

$$\eta_D = \left[1+4\left(\frac{z_o}{R}\right)^2\left(1-\frac{2d_2}{R}\right)^2\right]^{-1} \qquad (5.\ 29)$$

The expression in Eq.(5. 29) is depicted in Fig. 5.16 versus the ratio d_2/z_o for z_o/R =1, 0.5 and 0.25. The zero-distance coupling efficiency of the double-mirror configuration is always smaller than corresponding efficiency of the single-mirror. The ratio between the zero-distance coupling efficiencies reaches a quarter when the ratio z_o/R is much larger than one and approaches unity when z_o/R is much smaller than one. In contrast to the single-mirror coupling configurations, there is a single peak located at $d_2 = R/2$ and it becomes flatter and wider for smaller z_o/R ratios. The maximum achievable coupling

efficiency is unity independent of the ratio z_o/R. For $z_o/R \geq 0.5$ the single-mirror configuration offers a wider response while for $z_o/R < 0.5$, the double-mirror configuration coupling efficiency response width can be much larger. For example, the 1 dB width of the response extends from zero up to $d_2/z_o = 12$ when $z_o/R = 0.125$. The appropriate choice of which configuration to use is, thus, dependent on the application and on the z_o/R ratio. Non-ideal effects, including tolerance in the spherical micromirrors radii of curvatures as well as misalignment between the incident GB and the optical micromirrors arrangements, can be accounted for using a similar analysis to previous section.

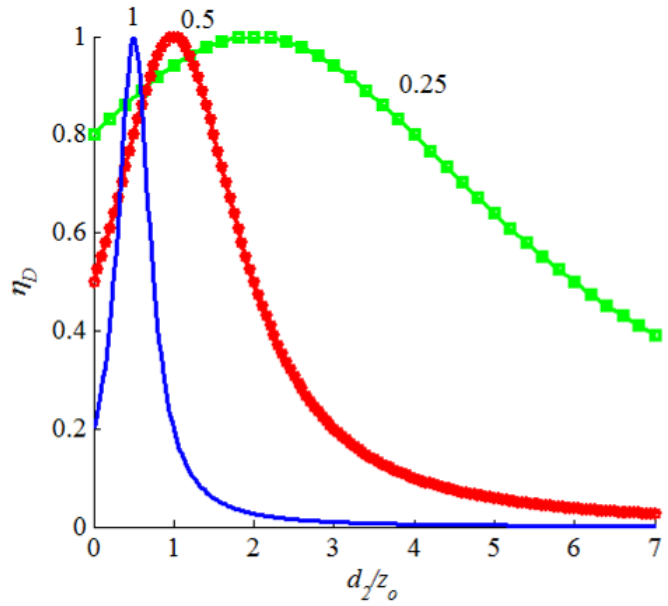

Fig. 5.16. Coupling efficiency of the double-mirror configuration versus the ratio between the mirror-to-beam-waist distance and the incident GB Rayleigh range. The curves are plotted for different ratios between the GB Rayleigh range and the mirror radius of curvature.

For the particular case of a misalignment with the double-mirror configuration when $d_1 = R/2$, Eq. (5. 13) can be put in the form:

$$\eta_{DM} = \eta_D \exp\left[-4 \frac{\Delta_c^2}{w_o^2} \frac{1+\zeta}{2+\zeta} - \frac{\alpha_c^2}{\theta_o^2} \right] \tag{5. 30}$$

where

$$\zeta = 2\left(\frac{z_o}{R}\right)^2 + 16\left(\frac{d_2}{z_o}\right)\left(\frac{z_o}{R}\right)^3 + 32\left(\frac{d_2}{z_o}\right)\left(\frac{z_o}{R}\right)^3 \tag{5. 31}$$

5.2.5 Optical measurements

A single-mode fiber was used to generate the GB incident on the micromirror and collects back the reflected beam as shown Fig. 5.17. To separate the reflected signal, the fiber was fed from a laser source through an optical Directional Coupler (DC) while the power coupled back was detected using an optical power meter. The fiber was mounted on a 5-axis positioner in order to assure good alignment between the fiber and the mirror while the latter is mounted on a variable height post. The measurements were carried out with the aid of a microscope.

Practically, a weak Fabry-Perot effect occurs between the optical fiber cleaved surface and the micromirror surface due to the refractive index mismatch at the fiber-air interface and the mirror reflectivity R_m. Knowing that the fiber-air interface reflectivity is much smaller than one, higher-order terms of the Airy function can be neglected and the detector power is given by:

$$P = P_o\left[R_m T_f^2 \eta + R_f + 2\sqrt{R_f R_m} T_f \sqrt{\eta}\cos\left(\frac{2\pi}{\lambda} 2d + \phi_k\right)\right] \qquad (5.32)$$

where P_o is a normalization factor, R_f is the fiber-air interface reflectivity, T_f is the fiber-air interface transmission and ϕ_k is the phase angle of the field coupling coefficient.

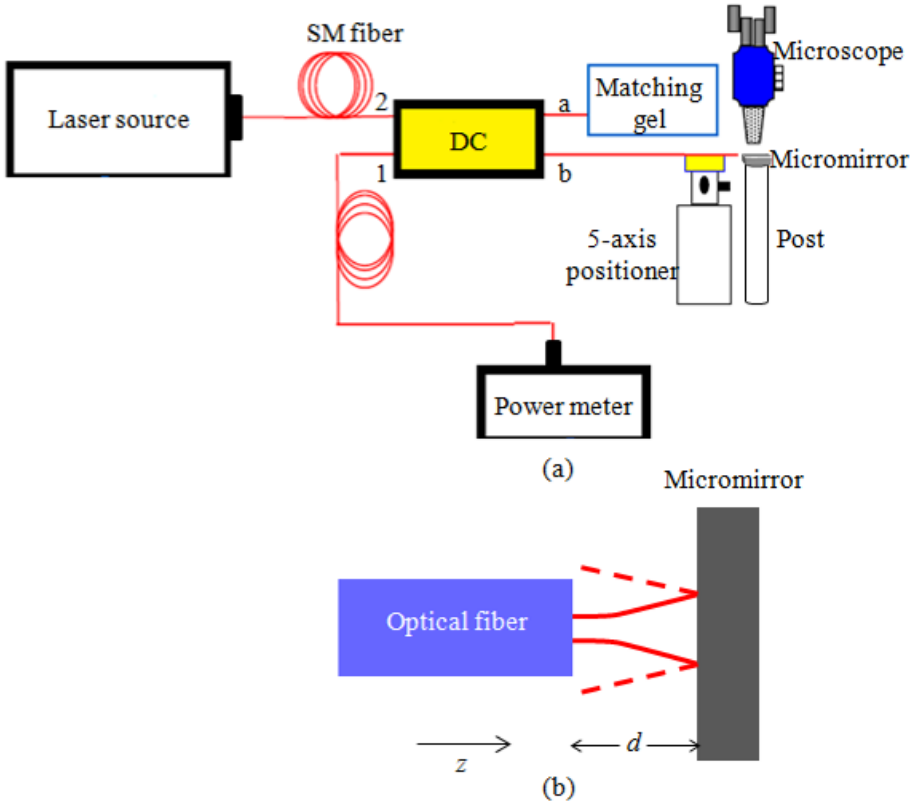

Fig. 5.17. (a) Coupling efficiency measurement setup using a directional coupler (DC) and a single-mode fiber is used as a GB source for the incident beam and to couple back the reflected beam shown in (b).

The variation of the cosine term is effective only within submicron resolution and, therefore, can be neglected. This is particularly applicable for working distance measurement, as in our case, and the cosine term is replaced by unity assuming that we are always seeking the peak power value. The coupling efficiency η can be solved for knowing the mirror reflectivity and fiber interface transmission and reflectivity. Rearranging Eq. (5. 32) using the peak value of the power P_{peak} yields:

$$\eta + \frac{2\sqrt{R_f}}{\sqrt{R_m}T_f}\sqrt{\eta} + \frac{R_f}{R_m T_f^2} - \frac{P_{peak}}{R_m T_f^2 P_o} = 0 \qquad (5.\ 33)$$

The solution of Eq. (5. 33) for η is given by:

$$\eta = \frac{P_{peak} + R_f P_o - 2\sqrt{P_o R_f}\sqrt{P_{peak}}}{R_m P_O T_f^2} \qquad (5.\ 34)$$

Flat and cylindrical as well spherical micromirrors were fabricated using DRIE and isotropic etching technologies on a silicon substrate. The flat and the cylindrical micromirrors is height 150 μm and their width is 300 μm. The cylindrical mirror in-plane radius of curvature is 150 μm precisely controlled using lithography. The spherical micromirror has in-plane and out-of-plane radii of curvature of 200 μm and 100 μm, respectively. The micromirror height and width are 200 μm and 300 μm, respectively. In-plane tilt angle between the optical fiber and the mirror surface could be minimized using a long and narrow fiber groove aligned with mirror in lithographic manner. The out-of-plane tilt angle alignment was carried seeking the maximum reflected power. The cylindrical micromirror required more attention to avoid lateral shift between the optical fiber axis and the cylindrical surface principal axis. The alignment was more critical in

the case of the spherical micromirror where the four-axis tilts and shifts are important. Each source of misalignment is minimized in the zone were its effect is dominant. The tilt angles were adjusted when the fiber is close to the micromirror while the shift misalignments were adjusted when the fiber is far from the micromirror and close to the maximum coupling efficiency location. GBs with estimated Rayleigh ranges of 30 µm and 45 µm were generated using single-mode optical fibers with core radius of 2 µm and 4.5 µm at wavelengths of 675 nm and 1550 nm, respectively. The measured as well as theoretical data of the flat, cylindrical and spherical micromirrors are shown in Fig. 5.18, Fig. 5.19 and Fig. 5.20 respectively. There is a good agreement between the measured and the theoretical data. A small discrepancy appears in the results that can be attributed to slight misalignment in the measurements in addition to the uncertainty in the optical fiber mode-filed diameter and cleaving quality.

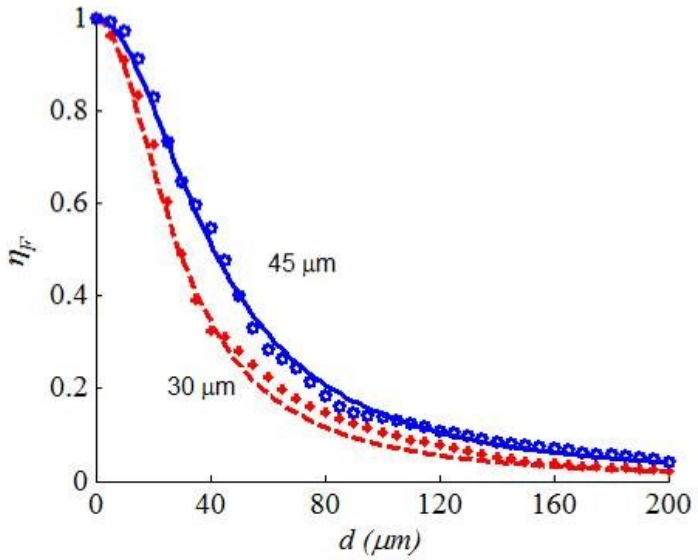

Fig. 5.18. Measured (markers) and theoretical (lines) coupling efficiency of the flat micromirror for GB Rayleigh ranges 30 and 45 µm.

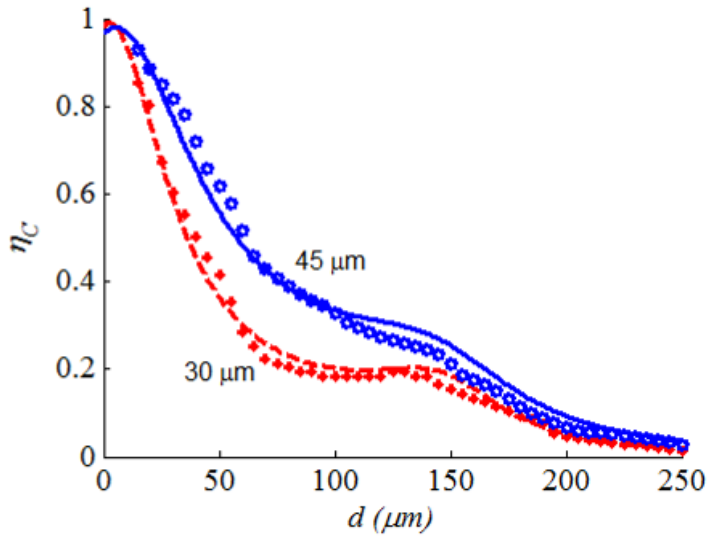

Fig. 5.19. Measured (markers) and theoretical (lines) coupling efficiency of the cylindrical micromirror for GB Rayleigh ranges 30 and 45 µm.

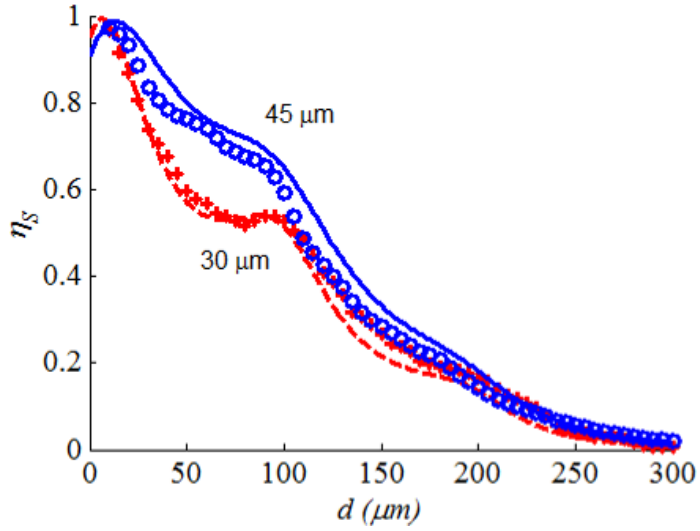

Fig. 5.20. Measured (markers) and theoretical (lines) coupling efficiency of the spherical micromirror for GB Rayleigh ranges 30 and 45 µm.

5.3 External-mirror fiber Fabry-Perot cavity

Optical cavities are used in a tremendous number of applications in the field of optical telecommunications, biomedical optics, atomic studies, and optical sensors [141-144].One of the commonly used cavities is the Fiber Fabry-Perot (FFP) type. In extrinsic FFP cavities, the cavity is formed between the fiber end and a facing mirror resulting in a cavity length the order of tens of micrometers [145]. Since the light is not guided in the cavity, diffraction effect plays an important role in determining the resulting performance. Several attempts were reported making use of a curved mirror formed on the fiber end to overcome the effect of diffraction [146-147]. In addition to the expensive methods of forming such a mirror, most of these reports use a special mechanical fixture and a piezoelectric actuator for fixing the fiber and tuning the cavity; preventing low cost and wafer level production of the cavity. In this context, forming the cavity from a cleaved fiber inserted in a groove and facing a micro silicon mirror fabricated by MEMS technology has the advantage of achieving cavity tuning with a MEMS actuator in a simple and low cost manner. Moreover, the MEMS solution can perform as a high speed tunable filter demanded in many applications. The use of a coated single-mode fiber facing a metalized silicon mirror was reported [148]. Both the fiber cleaved surface and the silicon mirror were of flat-surface kind leading to unavoidable diffraction losses. Moreover, coupling back the optical power from such a cavity into the single-mode fiber causes asymmetrical widened behavior in the filter response. In this section, we report on the analysis and measurements optical cavity formed form a coated single-mode fiber and a metalized spherical silicon mirror.

5.3.1 Cavity reflection coefficient

The reflection coefficient of a conventional Fabry-Perot cavity with input and output mirrors reflection coefficient r_f and $r_{m,}$ respectively and a cavity length L is given by the summation:

$$r_{FP} = r_f + \frac{1-|r_f|^2}{r_f}\sum_{n=1}^{\infty} r_m^n r_f^n \exp\left[-j\frac{2\pi}{\lambda}2nL\right] \qquad (5.\ 35)$$

where n is the round trip number. In Eq. (5. 35), the cavity is assumed to be lossless and the bouncing beam expansion in the cavity is neglected; i.e. a plane wave is assumed. In a realistic situation, the bouncing wave in the cavity has a finite extent and suffers from the diffraction effect.

For a fiber Fabry-Perot cavity, a single-mode fiber is used as a GB source and the beam expands during travelling from one cavity side to the other side as shown in Fig. 5.21, where t_f is the fiber mirror transmission coefficient and k is the coupling coefficient between the field cavity and the optical fiber propagating mode. The field reflected back into the fiber may not be matched to the fiber mode at the interface with regard to the mode size and phase front. Consequently, only a specific amount of energy is coupled back into the fiber mode while a portion is lost in radiation modes. This effect is modeled by the coupling coefficient k_n between the reflected field into the fiber and the fiber mode. For the special case of using a flat micromirror, the reflection coefficient of a fiber Fabry-Perot cavity is given by [148]:

$$r_{FFP-Flat} = r_f + \frac{1-|r_f|^2}{r_f}\sum_{n=1}^{\infty}\frac{r_m^n r_f^n}{1-jnL/z_o}\exp\left[-j\frac{2\pi}{\lambda}2nL\right] \qquad (5.\ 36)$$

In our case, a curved micromirror is used to balance the diffraction effect of the propagating field in the cavity. The field coupling coefficient k_n can be different from one round trip to another depending on the micromirror radius of curvature. The cavity reflection coefficient is more generally given by:

$$r_{FFP} = r_f + \frac{1-|r_f|^2}{r_f}\sum_{n=1}^{\infty} r_m^n r_f^n k_n \qquad (5.37)$$

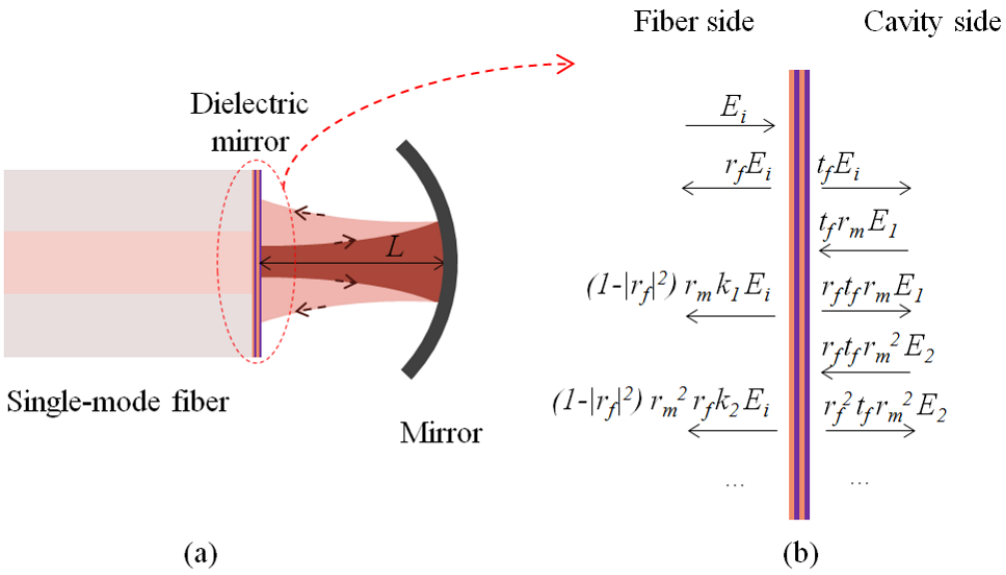

Fig. 5.21. (a) A fiber Fabry Perot cavity is formed between a dielectric-coated single-mode optical fiber and a silicon micromirror. (b) Multiple-reflection analyzes of the complex amplitude of the field in the cavity and the fiber side.

5.3.2 Cavity round-trip coupling

The round trip coupling coefficient can be deduced from Eq. (5. 10) by using the appropriate transformation matrix elements of the round trip $A_{t,s}^{(n)}$, $B_{t,s}^{(n)}$, $C_{t,s}^{(n)}$ and $D_{t,s}^{(n)}$. The coupling coefficient is given by:

$$k = \frac{\sqrt{2jz_{ot}}\sqrt{A_t^{(n)} z_{ot} - jB_t^{(n)}}}{(A_t^{(n)^2} z_{ot}^2 + B_t^{(n)^2})^{0.25}\sqrt{jz_{ot}(A_t^{(n)} + D_t^{(n)}) + B_t^{(n)} - C_t^{(n)} z_{ot}^2}} \text{x} \\ \frac{\sqrt{2jz_{os}}\sqrt{A_s^{(n)} z_{os} - jB_s^{(n)}}}{(A_s^{(n)^2} z_{os}^2 + B_s^{(n)^2})^{0.25}\sqrt{jz_{os}(A_s^{(n)} + D_s^{(n)}) + B_s^{(n)} - C_s^{(n)} z_{os}^2}} \tag{5. 38}$$

which the round trip matrix elements can be calculated from the elements in Table 5.1 by means of raising the matrix to the power of n:

$$\begin{bmatrix} A_{t,s}^{(n)} & B_{t,s}^{(n)} \\ C_{t,s}^{(n)} & D_{t,s}^{(n)} \end{bmatrix} = \begin{bmatrix} A_{t,s} & B_{t,s} \\ C_{t,s} & D_{t,s} \end{bmatrix}^n \tag{5. 39}$$

The round trip coupling efficiency in this case is given by:

$$\eta = \frac{2z_{ot}}{\sqrt{B_t^{(n)^2} + z_{ot}^2(A_t^{(n)^2} + D_t^{(n)^2} + 2) + z_{ot}^4 C_t^{(n)^2}}} \text{x} \\ \frac{2z_{os}}{B_s^{(n)^2} + z_{os}^2(A_s^{(n)^2} + D_s^{(n)^2} + 2) + z_{os}^4 C_s^{(n)^2}} \tag{5. 40}$$

Fiber Fabry-Perot cavities making use of the different types of the micromirrors can be studied using the expressions above.

For the simplest case of flat micromirror, the matrix in Eq. (5. 40) has a unitary diagonal and its n^{th} power is given by:

$$\begin{bmatrix} A_{t,s}^{(n)} & B_{t,s}^{(n)} \\ C_{t,s}^{(n)} & D_{t,s}^{(n)} \end{bmatrix} = \begin{bmatrix} 1 & 2nL \\ 0 & 1 \end{bmatrix} \tag{5. 41}$$

Using Eq. (5. 38) and (5. 41), it can be shown that the cavity reflection coefficient in Eq. (5. 37) reduces to Eq. (5. 36).

5.3.3 Cavity finesse

The finesse F of an optical cavity is defined as:

$$F = 2\pi N \tag{5.42}$$

where N is the number of round trips after which the energy inside the cavity drops to 1/e of its starting value. In Fabry-Perot cavities, the energy loss occurs due to many reasons. One source of loss is having the mirror's reflectivity being smaller than one. A second source of loss is light absorption within the cavity volume. The diffraction effect can be a major source of energy loss if the energy escapes out of the cavity from one round trip to another. The diffraction effect is overcome by making a proper design for the cavity mirrors resulting in a stable cavity. In Fiber Fabry-Perot cavities the diffraction effect causes a coupling loss between the cavity field and the optical fiber propagating mode. Assuming lossless cavity medium, the corresponding round trip number for the finesse calculation can be deduced from the equation:

$$2N \ln\left|r_m r_f\right| + \sum_{n=1}^{N} \ln(\eta_n) + 1 = 0 \tag{5.43}$$

Seeking the maximum value of the finesse limited by the coupling loss, the mirrors can be assumed ideal by setting $|r_m r_f| = 1$ and N is calculated by equating the second and the third terms in Eq. (5.43) to zero.

The finesse of a fiber Fabry-Perot cavity based on flat mirrors is depicted Fig. 5.22. The maximum attainable finesse is obtained when the mirrors reflectivity is unity. Typical MEMS mirrors reflectivity is 0.98 limited by the micromachined surface roughness in addition the metallization reflectivity limit. Unless the cavity length is very

short, the finesse of the cavity is very low because of the cavity length being comparable to the GB Rayleigh range. For instance, the typical GB Rayleigh range of the standard telecommunication optical fiber is close to 50 μm. For a cavity length L=10, the maximum attainable finesse is about 19 and is reduced to 13 when or L=25 μm.

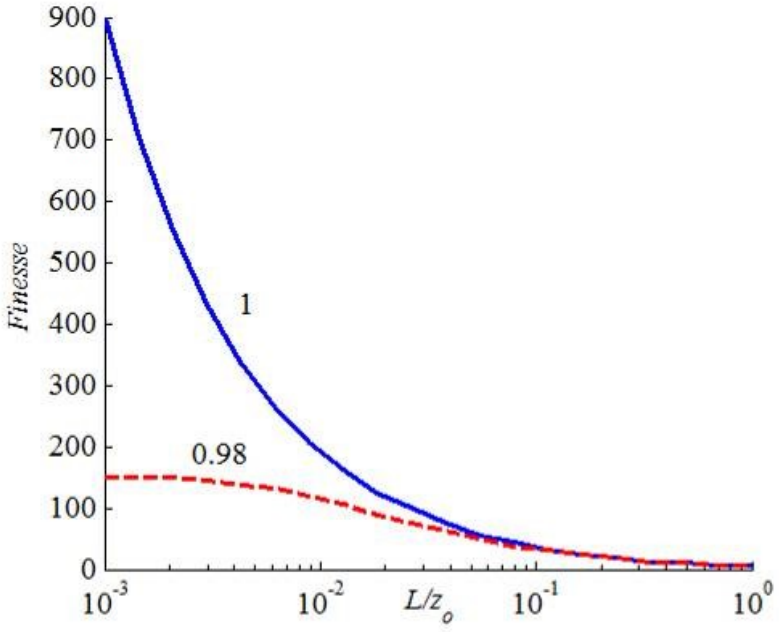

Fig. 5.22. Finesse of a fiber Fabry-Perot cavity based on flat mirrors versus the ration between the cavity length and the GB Rayleigh range L/z_o.

The finesse of a fiber Fabry-Perot cavity based on one flat mirror on the fiber surface and a spherical micromirror is studied in Fig. 5.23 for mirrors reflectivity of 0.98. The optical fiber mode GB Rayleigh range to the spherical micromirror radius of curvature z_o/R = 0.25, 0.5 and 0.75. Although the cavity stability condition is satisfied as

long as $L<R$ the finesse posses its maximum value for specific cavity lengths, which correspond to the maximum coupling efficiency locations in Fig. 5.6.

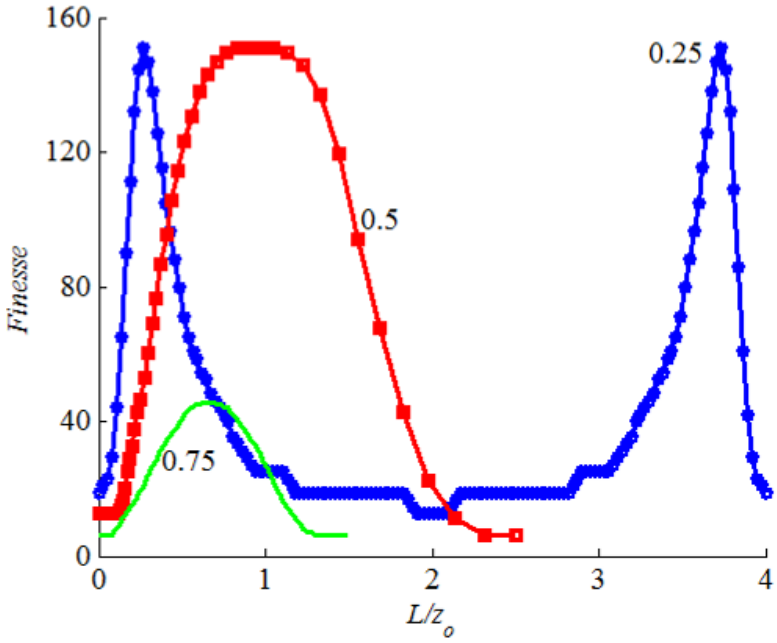

Fig. 5.23. Finesse of a fiber Fabry-Perot cavity based on one flat mirror on the fiber surface and a spherical micromirror for different z_o/R. The reflectivity of the mirrors is 0.98.

The behavior of the cavity finesse in can be also understood by considering the mode-matching condition. Consider the optical arrangement shown in Fig. 5.21 (a) where a single-mode optical fiber is facing a spherical micromirror. Let the mirror radius of curvature be denoted by R and the cavity GB wavefront radius of curvature R_{GB}. For mode matching between the optical fiber mode and the cavity mode, the optical fiber GB emitted at $z = 0$ should propagate into the cavity and have a wavefront radius of curvature

at the spherical mirror equal to the latter's radius of curvature, i.e. $R_{GB} = R$ at $z = L$. Using the well-known GB relation connecting its wavefront radius of curvature to the axial distance, the following condition can be found:

$$z_o = z_{oc} = L\sqrt{\frac{R}{L} - 1} \tag{5.44}$$

where z_o is the Rayleigh range of the optical fiber GB and z_{oc} is the Rayleigh range of the cavity mode. Then the relation between the optical fiber GB and the cavity mode Rayleigh range in Eq. (5.44) can be put in the form:

$$\frac{z_o}{z_{oc}} = \frac{R/L}{R/z_o\sqrt{R/L - 1}} \tag{5.45}$$

Eq. (5.45) is plotted in Fig. 5.24 for illustration versus R/L for R/z_o = 1.5, 2, 2.5 and 3. Unitary ratio can be achieved only when $R/z_o \geq 2$. For $R/z_o = 2$, a single solution is found at $R/L = 2$. For $R/z_o > 2$, two solutions can be found; one solution for a short cavity and the other one for a much longer one where the difference between the two cavity lengths depends on how much R/z_o is larger than 2.

The effect of having a spherical micromirror with unmatched radii of curvature in the tangential and sagittal planes is considered in Fig. 5.25. The finesse of matched radii of curvature with $z_o/R_t = z_o/R_t = 0.5$ is plotted as a reference. The reflectivity of the mirrors is assumed 0.98. The wide finesse response is deteriorated with mismatch. Relatively high finesse, with respect to the flat micromirror cavity, can still be obtained for a shorter cavity length. Operating the cavity at a short cavity length is important for having large free spectral range.

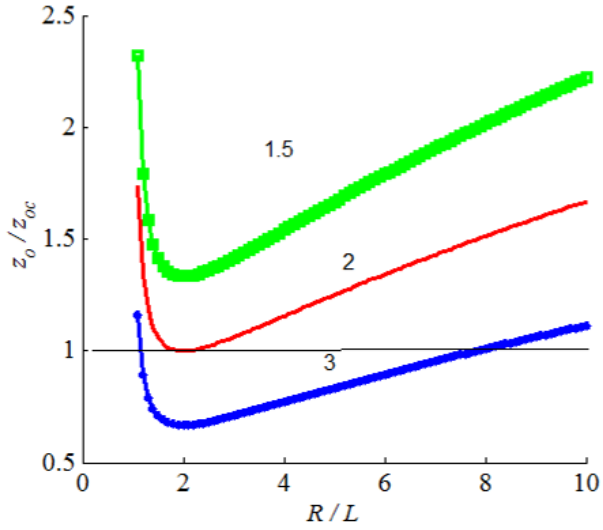

Fig. 5.24. The ratio between the Rayleigh ranges of the optical fiber GB and the cavity mode z_o/z_{oc} for different mirror radius of curvature to GB Rayleigh ratio R/z_o.

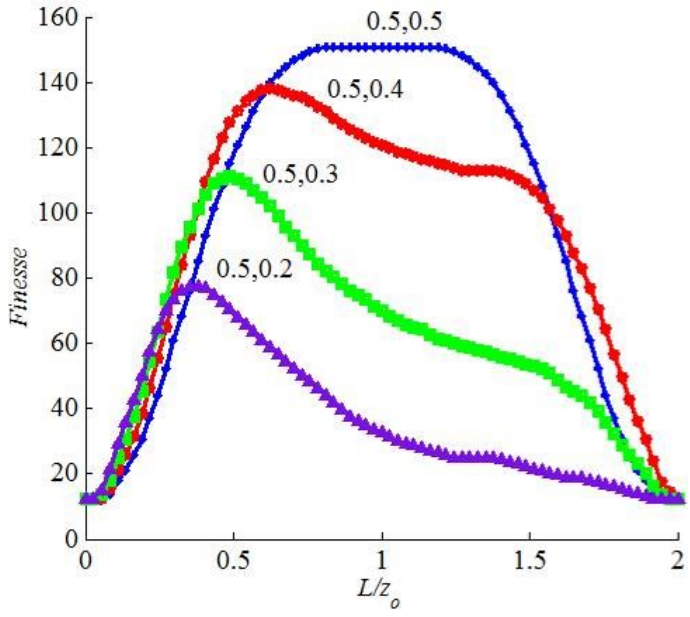

Fig. 5.25. Effect of the spherical micromirror radii of curvature mismatch on the Finesse of the fiber Fabry-Perot cavity. The finesse if plotted for different for different z_o/R_t and z_o/R_s.

5.3.4 Optical measurements

A single-mode optical fiber with a cleaved dielectric-coated surface was used to form an optical cavity with the 3-D micromirror. The experimental setup is shown in Fig. 5.26. The micromirror was previously demonstrated in efficient coupling of light with wavelengths of 1550 nm and 675 nm. In this experiment the cavity is operated around a wavelength of 1330 nm. The fiber surface multi-layer coating has a reflectivity of about 0.98 at 1330 nm and decrease rapidly with wavelength reduction. The fiber was fed from a Super Luminescent Diode (SLD) with a central wavelength of 1330 nm also and the power returned from the directional coupler was monitored on an Optical Spectrum Analyzer (OSA).

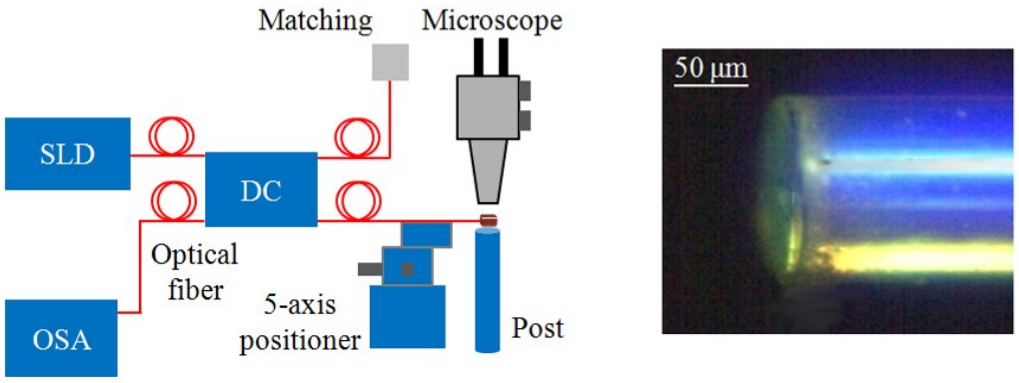

Fig. 5.26. (a) Schematic drawing of the experimental setup for the external fiber Fabry-Perot cavity measurements. (b) Microscopic image of the coated surface of the fiber.

The cavity length was adjusted for obtaining a narrow notch in the measured reflection response, yielding a free spectral range of about 26 nm as shown in Fig. 5.27 (a) with a corresponding cavity length of about 33 μm. The notch at 1333 nm is narrower than the preceding one at 1307 nm because of the lower reflectivity of the fiber coating at lower wavelengths. A zoom-in on the sharp notch complimentary response is shown in Fig. 5.27 (b). The obtained response has a line width that is slightly smaller than 0.45 nm demonstrating a quality factor of about 3000 for the formed cavity. For the sake of comparison, the cavity is formed once again but with a flat micromirror instead. The measured reflection response is shown in Fig. 5.27 (c) while their line width calculation is shown in Fig. 5.27 (d). In this case the contrast of the response around 1330 nm is very low due to the encountered diffraction loss causing a significant mismatch between the power returned from the cavity to the fiber and the power reflected from the fiber end face. The line width of the flat micromirror cavity is about 6 nm which is about 13 times worse than the line width obtained by the 3-D micromirror. Given that the reflectivity of the coated fiber and the metalized mirror are 0.98 and 0.92, respectively, the round-trip loss of the 3-D micromirror was estimated and found to be about 0.996 for a quality factor of 3000. Therefore, the obtained cavity performance is relatively diffraction-loss free and mainly limited by the mirrors reflectivity that can be improved. In addition, optimization of the spherical mirror radii of curvature can further reduce the diffraction loss potentially leading to order of magnitude(s) improvement in the quality factor.

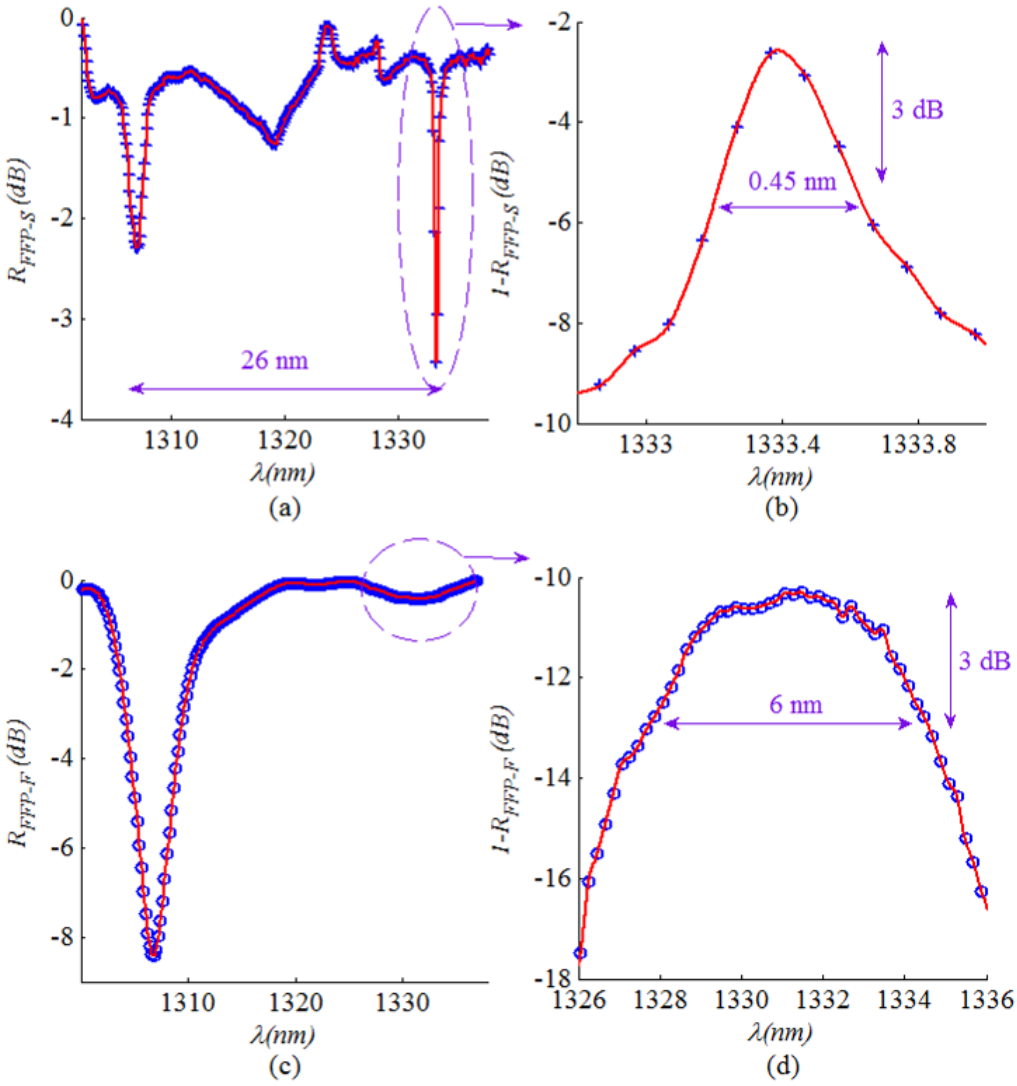

Fig. 5.27. Measured reflection spectral response of the coated fiber-mirror cavity. The response using the presented 3-D micromirror is shown in (a) with a free spectral range of about 26 nm where a corresponding line width of 0.45 nm could be obtained as calculated in (b). The response using a flat micromirror is shown in (c) where the corresponding line width is about 8 nm as shown in (d).

5.4 Optical fiber beam collimation

In this section, we study the possibility of GB collimation using 3-D curved mirrors exhibiting microscale focal lengths, i.e. is not so large compared to the incident GB Rayleigh range. The proper choice of the astigmatic micromirror curvatures as well as the incident GB incidence angle is considered. The achievable free-space propagation loss reduction due to the beam collimation is derived, when the beam size is much larger than the detector size. The utilization of the fabricated 3-D micromirrors in beam collimation / shaping is demonstrated experimentally for wavelengths of 675 nm and 1550 nm; serving as a potential replacement for lenses in micro-optical benches. The expected improvement in the allowable propagation distance in micro-optical benches is discussed for various systems sizes.

5.4.1 Theoretical study

Consider the incidence of a GB beam on a curved micromirror as shown in Fig. 5.28. The parameters of the output reflected GB are related to the input incident GB by:

$$G_c = \frac{w_{out}}{w_{in}} = \frac{1}{\sqrt{(1-d_{in}/f)^2 + z_o^2/f^2}} \tag{5.46}$$

$$\frac{d_{out}}{f} = \frac{z_o^2/f^2 - d_{in}/f(1-d_{in}/f)}{(1-d_{in}/f)^2 + z_o^2/f^2} \tag{5.47}$$

where w_{in} and w_{out} is the GB min waist radius for the incident and reflected beams, respectively, d_{in} and d_{out} is the distance between the GB wait location and the mirror surface at the point of incidence, f is the focal length of the mirror and z_o is the Rayleigh

range of the incident GB. The ratio w_{out}/w_{in} represents the collimation gain and denoted by G_C. The dependence of the collimation gain and the ratio d_{out}/f on the ratio d_{in}/f for different ratios of f/z_o is shown in Fig. 5.29. The collimation gain has a maximum value occurring when then input distance and the focal length are equal ($d_{in}=f$). The maximum gain is given by:

$$G_c = \frac{f}{z_o} = \frac{f\lambda}{\pi w_{in}^2} \tag{5.48}$$

The output beam waist is directly proportional to the wavelength, the focal length of the reflector and inversely proportional to the input beam waist. The variation of the collimation gain around $d_{in}/f=1$ is symmetric. The variation of ratio d_{out}/f possess an odd symmetry around the point ($d_{in}/f=1$, $d_{out}/f=1$). The output beam waist location doesn't change with the input beam Rayleigh range when the input beam waist location is located at the focus of the mirror. Negative values of d_{out}/f are obtained when $d_{in}/f<1$, which means the output beam waist is located virtually behind the mirror and the beam is diverging after reflection. The opposite case occurs when $d_{in}/f>1$ and the beam is reflected in a converging state. The output beam waist may have its waist just at the mirror surface. This case can be obtained at a single value of d_{in}/f when $z_o/f = 2$. It can be also obtained two times when $z_o/f = 0.5$; one time for a very small value of d_{in}/f and the second time for d_{in}/f that is slightly smaller than unity.

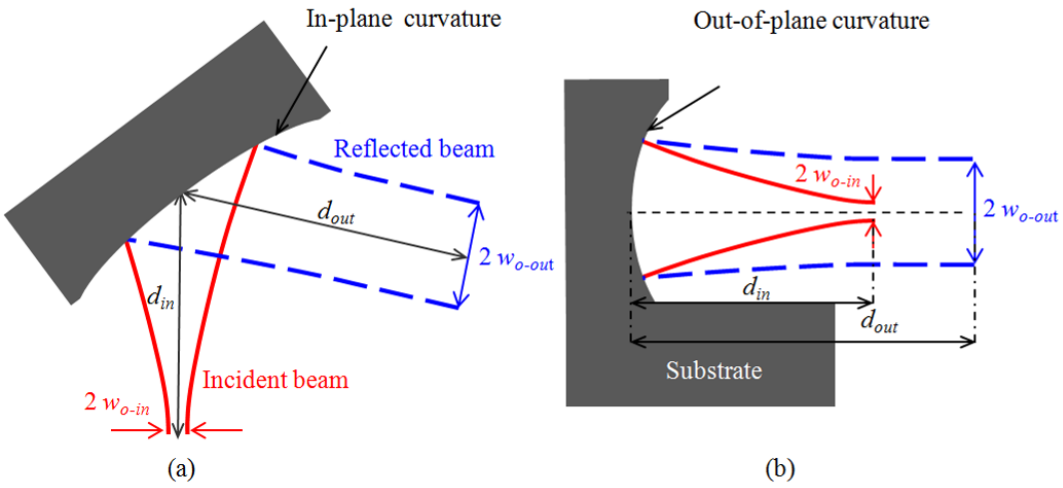

Fig. 5.28. 3-D curved micromirror used in beam collimation with the in-plane cross section shown in (a) and the out-of-plane cross section shown in (b).

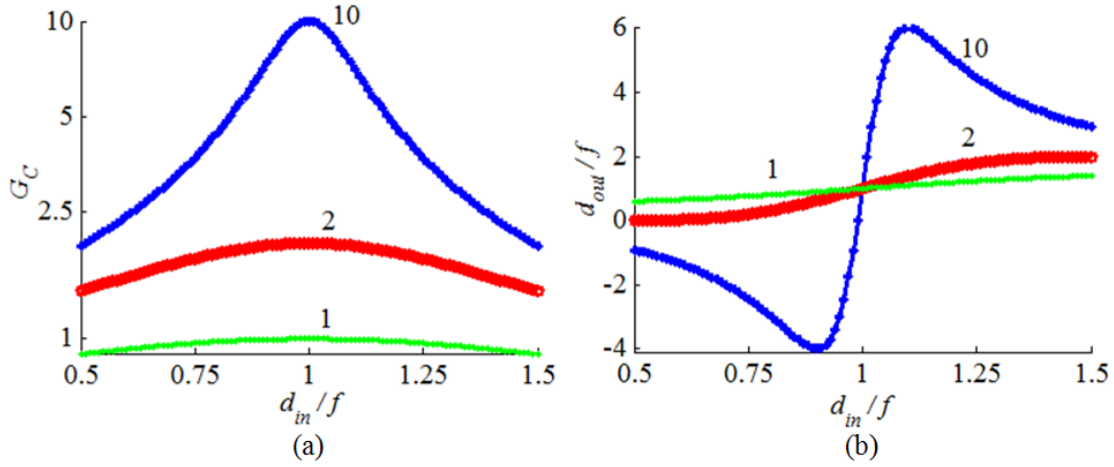

Fig. 5.29. Dependence of the collimation gain G_c and the ratio d_{out}/f on the ratio d_{in}/f in (a) and (b), respectively for different f/z_o ratios.

The microfabrication process tolerance may results in a variation of the curved micromirror radius of curvature, which affects the obtainable beam collimation gain. The impact depends on the gain sensitivity to the curved surface focal length. The corresponding change is by:

$$\Delta G_c = \frac{\Delta f}{f} \frac{r_{dif}(1-r_{dif}) + (z_o / f)^2}{[(1-r_{dif})^2 + (z_o / f)^2]^{3/2}}$$
$$= \frac{\Delta f}{f} \left(\frac{z_o}{f} \right)^{-1}, r_{dif} \approx 1 \qquad (5.49)$$

For a given percentage change in the focal length, the gain sensitivity becomes very high when the ratio z_o / f is very small. As depicted in Fig. 5.30 (a), the collimation gain is less sensitive to focal length variation when z_o / f is larger than 0.2. The output beam waist location is, however, very sensitive to the variations as shown in Fig. 5.30 (b). In the case of $z_o / f > 0.2$, the fabrication tolerance impact on the output beam waist location can be compensated by active axial alignment.

The inclined incidence of the beam on the mirror in tangential plane, while being normal in the sagittal plane, has the effect of splitting the focal length as well as the input ratio r_{dif} of the mirror each into two different values:

$$f_t = 0.5 R_t \cos(\theta_{inc}) \qquad (5.50)$$

$$f_s = 0.5 R_s / \cos(\theta_{inc}) \qquad (5.51)$$

$$\left(\frac{d_{in}}{f} \right)_t = \frac{2 d_{in}}{R_t \cos(\theta_{inc})} \qquad (5.52)$$

$$\left(\frac{d_{in}}{f}\right)_s = \frac{2d_{in}\cos(\theta_{inc})}{R_s} \tag{5.53}$$

where the subscripts t and s are used for the tangential and sagittal planes respectively and R is the radius of curvature of the mirror in the indicated plane.

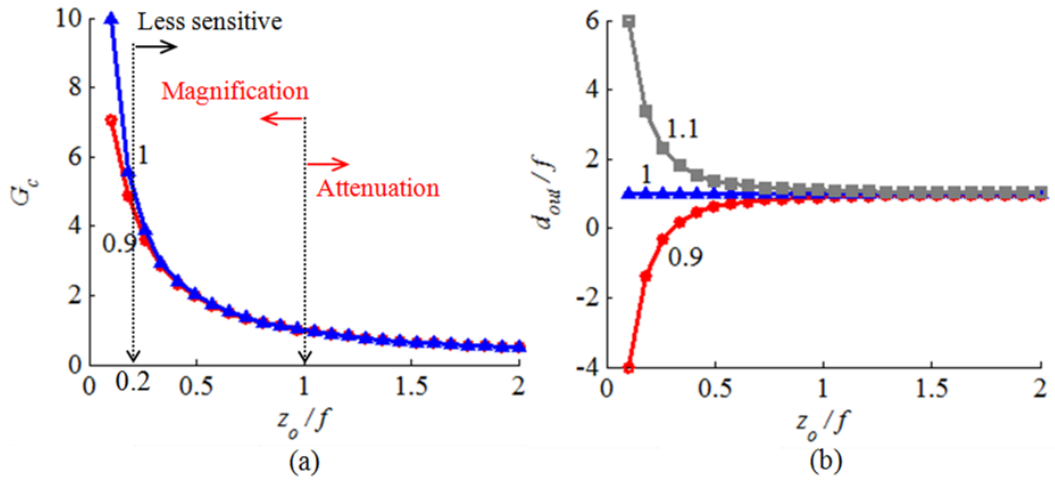

Fig. 5.30. Dependence of the collimation gain G_c and the ratio d_{in}/f on the ratio z_o/f in (a) and (b), respectively for different d_{in}/f ratios.

The inclined incidence has the effect of effectively increasing the sagittal focal length of the curved surface while at the same time decreasing its tangential focal length, and therefore, a stigmatic inclined curved surface should have non-equal radii of curvature in the two orthogonal planes. For our case, the sagittal plane radius of curvature is limited by the microfabrication technology as discussed in chapter 4. Fortunately, increasing angle of incidence compensates for this limit. For instance, focal length matching occurs at incidence angles $\theta_{inc} = 0^o$, 45^o and 60^o for $R_s / R_t = 1$, 0.5 and 0.25 respectively. Away

from the stigmatic beam generation angle, the reflected beam will have an elliptical cross section as well different beam waist location for sagittal and tangential planes. This is of particular interest in beam shaping / matching applications.

5.4.2 Optical measurements

In this experiment, a 3-D micromirror was used with radii of curvature of 300 μm and 150 μm in tangential and sagittal planes, respectively. The optical fiber is inserted such that its optical axis is in-plane and tilted with respect to the mirror optical axis while the reflected beam is observed in the far field on a scanning head beam profiler as shown in Fig. 5.31 (a). The in-plane incidence angle on the mirror was adjusted to about 45^{o} such that the observed beam ellipticity, defined by the ratio of the spot size in the in-plane direction to the out-of-plane direction, is close to unity (about 1.05). The axial position of the optical fiber was adjusted at the micromirror focus by minimizing the observed output beam diameter at the far field. The collimated output beam spot diameter was measured at different locations away from the micromirror and compared to the measurements of the optical fiber output beam without using the micromirror. In the case of the standard single-mode fiber fed from 1550 nm laser source, a reduction in the divergence angle of the beam by a factor of 2 was achieved by the micromirror. The output beam has a min waist radius of about 10 μm. A typical captured beam profile at one location *d* is shown in Fig. 5.31 (b). The profile was fitted to a Gaussian profile with average root mean square errors smaller than 0.01 and 0.015 in the *x*- and *y*- directions respectively as shown in Fig. 5.31 (c) and Fig. 5.31 (d). This is an indication of the good

performance offered by the fabricated 3-D micromirror, using the presented method, in terms of its wavefront transformation functionality. This experiment was repeated with the special single-mode fiber working at 675 nm wavelength. A reduction in the divergence angle of the beam by a factor of 4.25 was achieved.

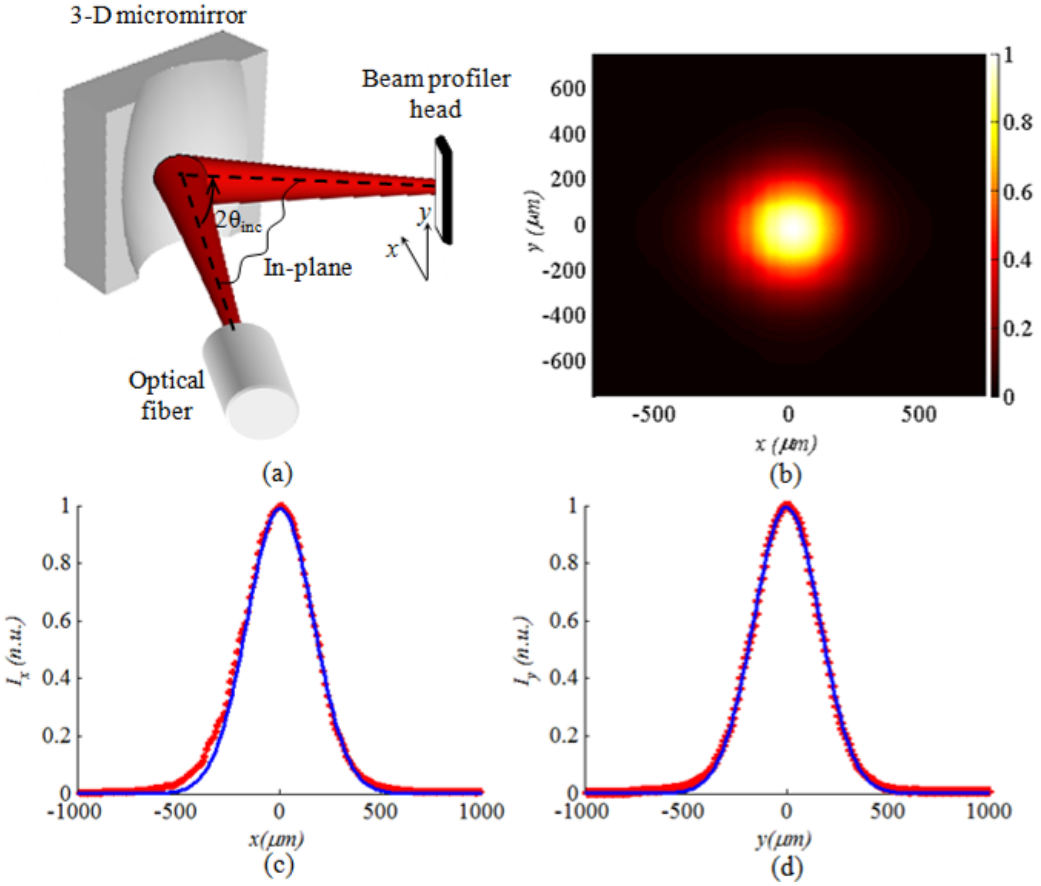

Fig. 5.31. Measurement of the beam profile reflected from the phase transforming 3-D micromirror surface using the setup in (a) resulting in a beam spot of 1.05 ellipticity captured by the beam profiler as shown in (b). The beam profile is fitted to a Gaussian profile in the x-direction as shown in (c) and in the y-direction as shown in (d) indicating a high phase transformation quality.

The collimation of the GB by the 3-D micromirror was also verified by measuring the detected power in free-space with a limited-aperture detector. Theoretically, the transmitted power in terms of the system aperture radius a and the GB spot radius at the detector is given by [140]:

$$P = 1 - \exp\left(-2\frac{a^2}{w^2} \right) \tag{5.54}$$

The power collected by a detector with 3.5 mm aperture radius is shown in Fig. 5.32 (a). The power was measured at different distance d in the far field away from the GB waist. The measurements were carried out at a wavelength of 675 nm; one time for the collimated GB by the micromirror, denoted by P_c, and another time for GB originally emitted by the single-mode fiber, denoted by P_o. The experimental data is depicted using markers while the theoretical data is depicted using lines. The power is normalized with respect to the initially maximum power. The measured power starts to fall clearly when the GB diameter starts to exceed the detector aperture as given by Eq. (5.45). The 3-D micromirror significantly reduces the propagation losses with respect to the original fiber output. The detected power from the 3-D micromirror has a slower roll-off and drops to half its maximum value 25 cm far from the micromirror compared to less than 8 cm from the optical fiber without the micromirror. The ratio between the two detected powers is depicted in Fig. 5.32 (b) where the improvement reaches about 11-12 dB.

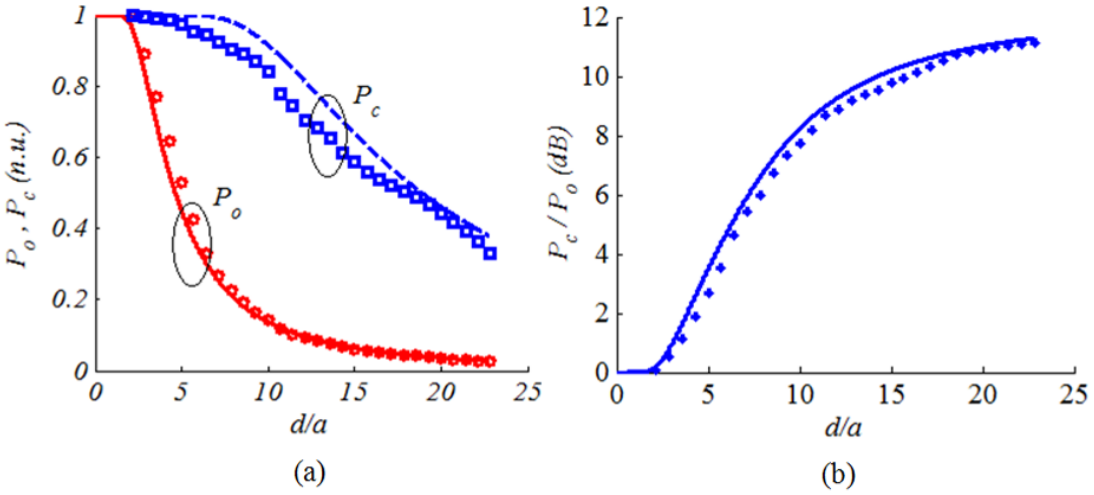

Fig. 5.32. (a) The normalized power collected by a detector with 3.5 mm aperture radius for the case of collimated and original GBs denoted by Pc and Po, respectively. The data is plotted versus the ratio between the propagation distance and the detector aperture radius. (b) The power gain in dB using the 3-D micromirror. The measured data is given in markers when the theoretical is given in lines.

In the far field, the ratio between the detected powers is given by:

$$G_p = \frac{P_c}{P_o} = \frac{1-\exp\left(-2\dfrac{a^2}{\theta_{div-c}^2 d^2}\right)}{1-\exp\left(-2\dfrac{a^2}{\theta_{div-0}^2 d^2}\right)} \qquad (5.55)$$

where the GB spot radius in the far field was replaced by $wd/z_o = d/\theta_{div}$. The maximum improvement is achieved when the spot radius becomes much larger than the detector aperture. In this case, Taylor expansion of the exponential terms can be applied to second order and Eq. (5.55) becomes:

$$G_{p-\max} = \frac{\theta_{div-c}^2}{\theta_{div-o}^2} = G_c^2 \qquad (5.56)$$

The maximum power gain due to the usage of the collimating mirror is given by the collimation gain squared. For the fabricated micromirror and using the single-mode fiber at 675 nm, the power gain is $G_p = (4.25)^2 = 18$ that is about 12.5 dB in good agreement with the measured data. This value is independent of the specific sizes of the beam spot and the detector aperture, as long as significant truncation loss is encountered.

5.5 Summary

Coupling of GBs using flat and curved micromirrors was thoroughly studied in this chapter focusing on the regime in which the mirrors radius of curvature and overall scale is comparable to the GB Rayleigh range and spot size. An ABCD matrix-based field and power coupling coefficient were derived for coupling using any optical system with different parameters in tangential and sagittal planes. In our study, normalization with respect to the GB Rayleigh range, waist and divergence angle is carried out such that our findings are independent of the specific values of the beam parameters and wavelength

Coupling by flat micromirrors accounting for possible beam truncation due to limited mirror size was studied. The truncation was found to be has a negligible effect on the coupling efficiency when the mirror size is larger than $4w_o$ (the GB min beam waist). Curved micromirrors were found to be suitable for GB coupling when the mirror radius of curvature $R \geq 0.5z_o$ (the GB Rayleigh range) such that unity coupling on relatively long optical paths can be obtained. Mismatch in the micromachined spherical mirror tangential

and sagittal curvatures causes deterioration in the coupling similar to that encountered due to misalignment. The deterioration effect was found to be strongly dependent on the z_o/R ratio. Tilt misalignment was found to be effective when the GB waist and the spherical mirrors surface are close while the shift misalignment was found to be effective for relatively large separation distance.

A measurement technique based on using a cleaved non-coated single-mode optical fiber for coupling measurements was introduced and used to verify the optical model. Flat, cylindrical and spherical silicon micromirrors were measured using GBs with z_o=30 and 45 μm with a good agreement with the model. The measured coupling efficiency is higher than 50 % over a 200 μm optical path compared to less than 10 % afforded by a conventional flat micromirror.

A Fabry-Perot cavity formed by a multilayer-coated cleaved-surface single-mode fiber inserted into a grove while facing the micromachined spherical micromirror; both are fabricated by silicon micromachining. The light is trapped inside the cavity while propagating in-plane of the wafer substrate. The light is injected in and collected from a Corning SMF-28 optical fiber with a coated surface reflectivity of about 98% at 1330 nm (O-band). The silicon mirror surface is aluminum metalized with a reflectivity of about 92%. The measured cavity has a line width of 0.45 nm around 1330 nm with a FSR of 26 nm. The obtained results indicate an almost diffraction-loss free optical cavity with a quality factor close to 3000, limited by the optical surfaces reflectivity that can be improved in future by an optimized mirror fabrication process and better matching of the fiber multilayer coating.

Finally, we demonstrated GB collimation using a micro-optical bench compatible three-dimensional (3-D) curved micromirror. Sensitivity to micromachining and alignment tolerance was shown to be low enough by restricting the ratio between the mirror focal length and the GB Rayleigh range below 5. Experimental results show a collimation gain of about 4 and power gain due to collimation of about 12 dB with respect to the original non-collimated beam with a Rayleigh range of 25 μm at a 675 nm wavelength; that are in a good agreement with theoretical modeling.

CHAPTER 6
GAUSSIAN BEAM REFLECTION ON OFF-AXIS CURVED MICRO REFLECTORS

6.1 Background and literature review

6.1.1 Gaussian and Hermite-Gaussian beams

GBs are special but very common class of fields which maintain their Gaussian shape as the field propagates through an optical system containing quadratic surfaces or index profiles. The propagation is accompanied with size scaling and phase front radius of curvature change. This class of fields is a solution of the Helmholtz wave equation under the paraxial approximation that holds as long as the beam divergence due to diffraction is smaller than 30^{o} (0.5 rad) or even larger [83]. A stigmatic GB has a normalized electric field in the form:

$$E(x,y,z)=\left(\frac{2}{\pi w(z)^2}\right)^{0.5}\exp\left[-\frac{x^2+y^2}{w(z)^2}\right]\exp\left[-j\left(\pi\frac{x^2+y^2}{\lambda R(z)}+kz-\phi_0(z)\right)\right] \quad (6.\ 1)$$

where the intensity spot radius $w(z)$ is given by:

$$w(z)=w_0\left[1+\left(\frac{\lambda z}{\pi w_0^2}\right)^2\right]^{0.5} \quad (6.\ 2)$$

, the phase radius of curvature $R(z)$ is given by:

$$R(z) = z + \frac{1}{z}\left(\frac{\pi w_0^2}{\lambda}\right)^2 \tag{6. 3}$$

and the Guoy phase shift is given by:

$$\phi_0(z) = \tan^{-1}\left(\frac{\lambda z}{\pi w_0^2}\right) \tag{6. 4}$$

The main properties of this beam can be summarized as follows. The beam has a minimum spot radius of w_o at the $z = 0$ plane (see Fig. 6.1). The beam radius increases with z reaching $\sqrt{2}\ w_o$ at $z = z_o$, where $z_o = \pi\ w_o^2 / \lambda$ is the Rayleigh range of the GB and the distance $2z_o$ is the depth of focus or the confocal parameter. In the far field $z >> z_o$ and the spot radius increases linearly with z in the form $w(z) \approx w_o / z_o = \theta_{div} z$ where θ_{div} is called the beam half divergence angle. The phase radius of curvature $R(z)$ is infinite at $z = 0$ similar to a plane wave (see Fig. 6.2). The radius of curvature poses a minimum value of $2z_o$ at $z = z_o$. In the far field, the radius of curvature can be approximated by $R(z) \approx z$ resembling a spherical wave. Due to its circular symmetry, the beam defined by Eq. (6. 1) is referred to as a circular GB. On the other hand, an elliptical or a simple-astigmatic GB exhibits unequal radii in the x- and y-directions are. It electric field is given by:

$$E(x,y,z) = \left(\frac{2}{\pi w_x(z) w_y(z)}\right)^{0.5} \exp\left[-\frac{x^2}{w_x(z)^2} - \frac{y^2}{w_y(z)^2}\right] \exp\left[-j\left(\frac{\pi x^2}{\lambda R_x(z)} + \frac{\pi y^2}{\lambda R_y(z)} + kz - \frac{\phi_{0x}(z)}{2} - \frac{\phi_{0y}(z)}{2}\right)\right] \tag{6. 5}$$

where Eqs. (2), (3) and (4) hold true by writing them twice; one for the x-direction and one for the y-direction.

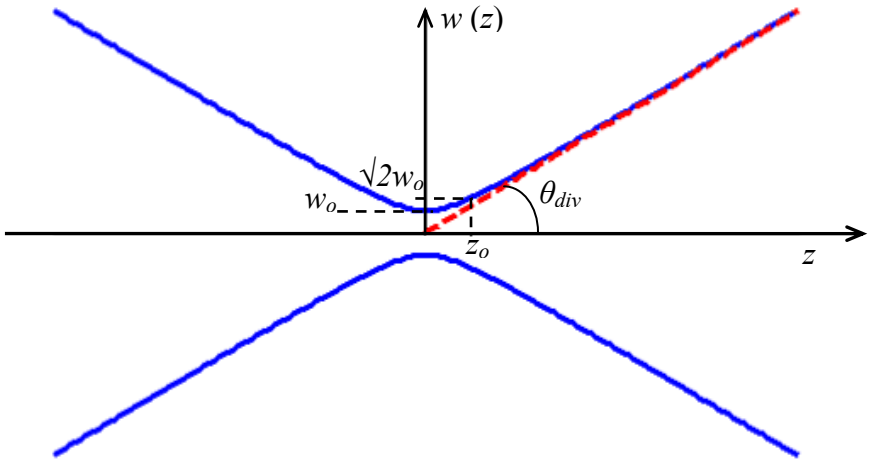

Fig. 6.1. Axial variation of a GB spot radius. At far field, the beam diverges linearly with z governed by the divergence angle θ_{div}. For illustration of the beam shape with propagation, the spot radius mirror around the z-axis is also shown.

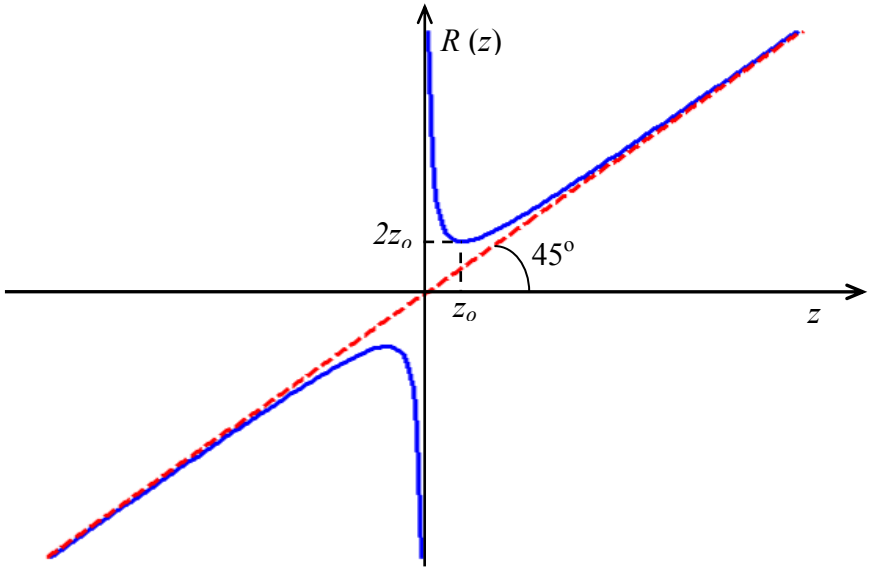

Fig. 6.2. Axial variation of the phase front radius of curvature. The beam is similar to plane wave at z = 0 and tends to spherical wave in the far field.

Hermit-Gaussian (HG) modes represent a general solution to the paraxial wave equation in rectangular coordinate system and serve as a complete set. The two-dimensional HG mode is simply the product of two one-dimensional functions. An HG mode of order (n,m) is defined by:

$$E_{mn}(x,y,z)=\left(\frac{1}{\pi w_x w_y 2^{m+n-1} m!\, n!}\right)^{0.5} H_m\left(\frac{\sqrt{2}x}{w_x}\right)H_n\left(\frac{\sqrt{2}y}{w_y}\right)$$
$$\exp\left[-\frac{x^2}{w_x{}^2}-\frac{y^2}{w_y{}^2}\right]\exp\left[-j\left(\frac{\pi x^2}{\lambda R_x}+\frac{\pi y^2}{\lambda R_y}+kz-\frac{(2m+1)\phi_{0x}}{2}-\frac{(2n+1)\phi_{0y}}{2}\right)\right] \quad (6.\ 6)$$

where H_n is the Hermite polynomial of order. The intensity profile of different modes is shown in Fig. 6.3. The axial variation of the spot size of arbitrary beam propagating in free space is given by [149]:

$$w(z)=Mw_0\left[1+\left(\frac{\lambda z}{\pi w_0^2}\right)^2\right]^{0.5} \quad (6.\ 7)$$

where M^2 is the beam quality factor and is greater than or equal to unity. In this case, the focused beam waist is Mw_o and the far-field half-divergence angle is $M\lambda/\pi w_o$. Poor beam quality results, for instance, from non-ideal optical components causing wave front aberration or beam truncation at the apertures. This is associated with the excitation of higher-order HG modes. The mode fundamental mode has the highest beam quality with $M^2 = 1$. Other HG modes with indices n and m have an M^2 factor given by [150]:

$$M^2 = n+m+1 \quad (6.\ 8)$$

It is noteworthy that the Gaussian modes form a complete set in free space such that any field can be expanded in terms of it. The field is projected on the fundamental and the higher-order HG modes and, then it possible to pass the field through paraxial optical components and predict the resulting field using Gaussian optics formulas.

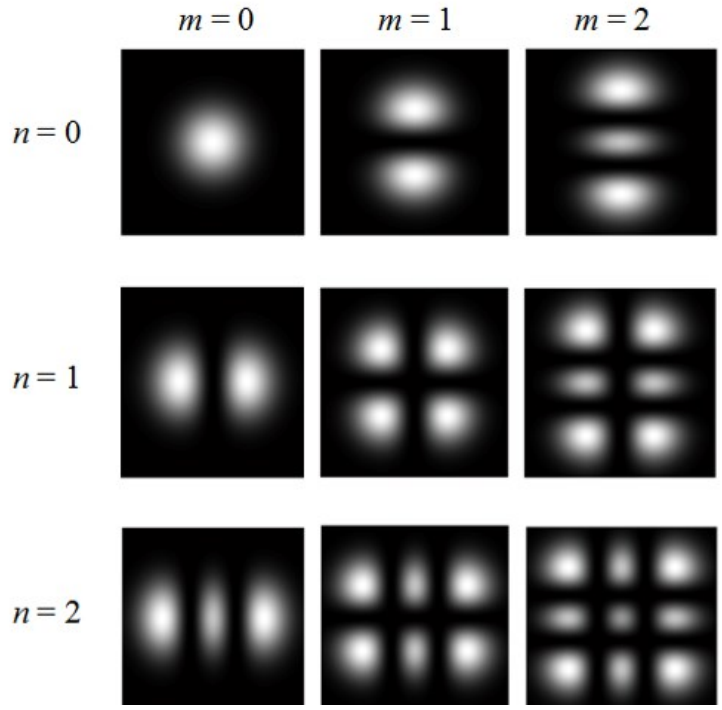

Fig. 6.3. Intensity profile of different Hermit-Gaussian modes

6.1.2 Gaussian-optical approach

In Gaussian-optical treatment of optical systems, an incident GB is assumed to remain Gaussian after reflection or refraction from the optical element. As will be shown in this section and when dealing with off-axis configuration, this approach is based on the

assumptions that the beam diameter is small relative to the beam phase radius of curvature and the radius of curvature of the off-axis optical elements. A symmetric quadratic expansion for the curved surface is assumed around the incidence point. The polarization states are treated independently not accounting for any cross coupling occurrence. Finally, the approach does not account for any diffraction effects associated with beam clipping on a mirror with a relatively small size.

Consider the off-axis incidence of a GB on a curved spherical mirror having a radius of curvature R with an incidence angle θ_{inc} as shown in Fig. 6.4. This can be considered a rotation of the reflector around the x-axis. The spherical reflector has an elliptical projection on the x-y plane with the minor axis along the y-axis. In this case, the y-z plane is called the tangential plane while the x-z plane is the sagittal plane. Now the elliptical projection of the mirror is still having mirror symmetry around x- and y-directions such that each direction can be treated independently. The mirror becomes an astigmatic component with different focal lengths f_t and f_s in the tangential and sagittal planes, respectively and given by [Col64]:

$$f_t = -R\cos\theta_{tilt}/2 \tag{6. 9}$$

$$f_s = -R\sec\theta_{tilt}/2 \tag{6. 10}$$

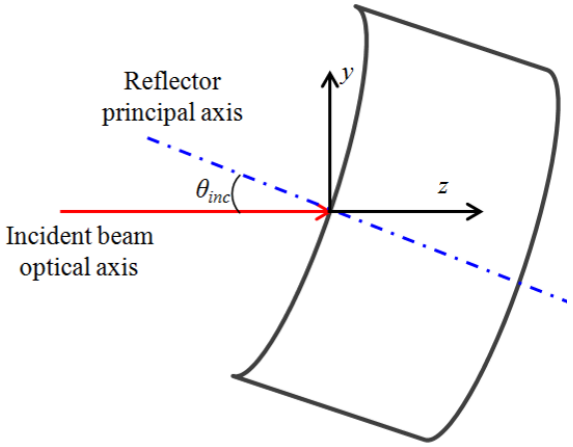

Fig. 6.4. Off-axis incidence on a curved reflector

Reflection and refraction of a GB incident on a tilted ellipsoidal surface were considered when the ellipsoidal surface has one of its principal axes lies in the plane of incidence [152]. The treatment was based on based on matching the complex phase of the incident, reflected and refracted beam at the interface. The surface equation, the refracted beam and the reflected beam were written in terms of the incidence beam coordinate system assuming the beam diameter is much smaller than the radius of curvature of the beam phase front and radii of curvature of the ellipsoid in the tangential and sagittal plane:

$$2w(z) << R(z)\,,\ 2w(z) << R_t \text{ and } 2w(z) << R_s \qquad (6.\ 11)$$

The transverse dimensions were approximated to the 2nd order, within the assumptions in Eq. (6. 11) and the ABCD matrix elements where derived as given in Table 6.1. The case of incidence with inclination on both the x-axis and the y-axis on a curved mirror was treated in [153] based on geometrical ray analysis. Expressions for

equivalent mirror radii of curvatures in the x- and y-directions (see Fig. 6.5) are were given below:

$$R_{eqx} = R_x \frac{\sin\theta_x}{\sin\theta_y} \tag{6. 12}$$

$$R_{eqy} = R_y \frac{\sin\theta_y}{\sin\theta_x} \tag{6. 13}$$

Table 6.1. ABCD matrix parameters for incidence on a tilted ellipsoidal surface [152].

Element	Reflection	Refraction
$\boldsymbol{A_t}$	1	$(n^2 - \sin\theta_{tilt}{}^2)^{0.5} / n\cos\theta_{tilt}$
$\boldsymbol{A_s}$	1	1
$\boldsymbol{B_t}$	0	0
$\boldsymbol{B_s}$	0	0
$\boldsymbol{C_t}$	$2/R_t\cos\theta_{tilt}$	$[\cos\theta_{tilt} - (n^2 - \sin\theta_{tilt}{}^2)^{0.5}]/R_t\cos\theta_{tilt}(n^2 - \sin\theta_{tilt}{}^2)^{0.5}$
$\boldsymbol{C_s}$	$2\cos\theta_{tilt}/R_s$	$[\cos\theta_{tilt} - (n^2 - \sin\theta_{tilt}{}^2)^{0.5}]/nR_s$
$\boldsymbol{D_t}$	1	$\cos\theta_{tilt}/(n^2 - \sin\theta_{tilt}{}^2)^{0.5}$
$\boldsymbol{D_s}$	1	$1/n$

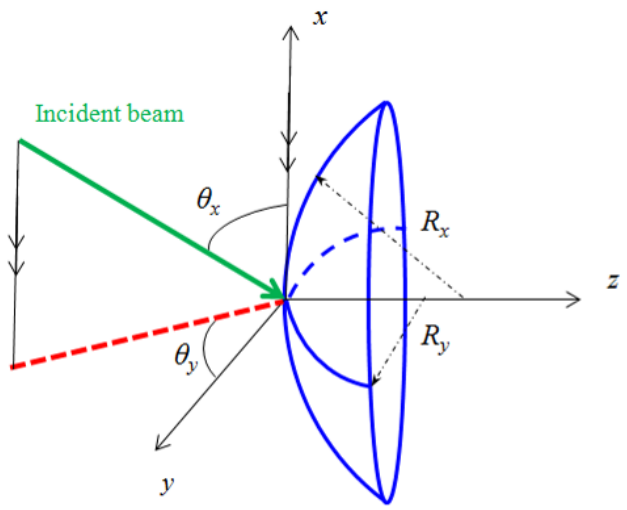

Fig. 6.5. Inclined incidence on both the *x*- and *y*-axes.

Extension to general curved surface profiles was reported in [154]. The approach is also based on the approximation of the curved surface by a quadratic expansion around the incidence point and phase matching of the incident and reflected GBs. The polarizations of the field were treated independently and the reflection and refraction coefficients were obtained from Fresnel coefficient depending on the polarization state. Numerical tracing of multiple reflections and transmissions was possible and the directions of the reflected and refracted beam were given by Snell's law.

6.1.3 Distortion of Gaussian beams

GB distortion occurs in mirrors when the beam is incident in off-axis configuration [155]. The reason can be illustrated with the aid of Fig. 6.6. The beam is incident normally on the curved mirror in Fig. 6.6 (a). In the framework of the thin-lens approximation [157], a point *O* on the optical axis and any arbitrary point *P* on the mirror

surface have approximately the same z. Therefore, the beam has a uniform spot radius and wave-front radius of curvature across the mirror surface. Indeed, this situation is the ideal one which produces also a GB after reflection but with transformed wave-front radius of curvature. On the other hand, when the beam is incident on the mirror surface obliquely as shown in Fig. 6.6 (b), the reflected field is not kept an ideal GB. One can explain the reason why the reflected beam is distorted by considering the mirroring of the mirror surface and the reflected beam around the tangent plane to the mirror surface at the central incident point O [158]. First, the thin-lens approximation may be no more valid due to a significant different in the axial position between the central point O and other point P_i. Consequently, the incident beam will have different spot radius and wave-front radius of curvature across the mirror surface. More significantly, if we considered similar points on the incident and reflected beams such as P_i and P_r, they have different transverse positions ($x_{pi} \neq x_{pr}$) as well as axial positions ($z_{pi} \neq z_{pr}$). This results in a mismatch in the phase and the amplitude between the incident and an ideal reflected GB. This mismatch gives rise to the excitation of higher-order HG modes.

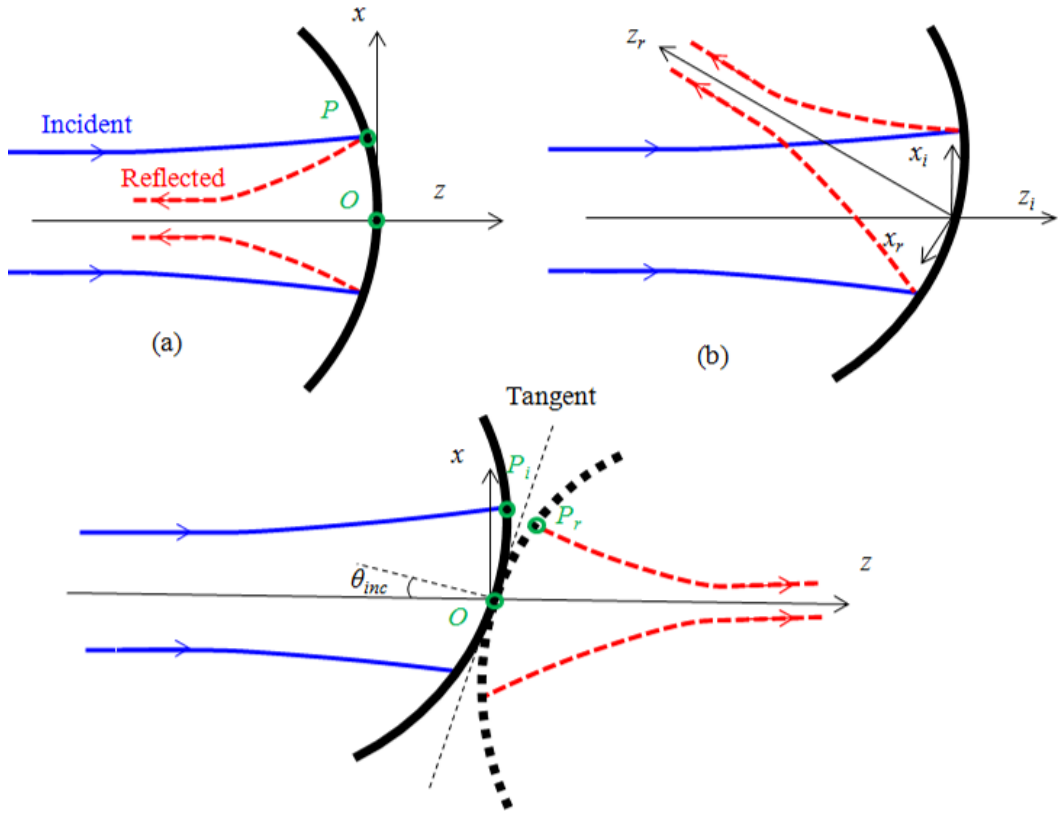

Fig. 6.6. Illustration for the case of normal incidence in (a), tilted incidence in (b) and tilted incidence with the mirror and the reflected beam mirrored around the tangent plane to mirror at the point of incidence O.

For the special case of off-axis ellipsoidal mirrors, it was shown in [155] that the phase mismatch effect is neglected, when the incident stigmatic beam and the ideal reflected beam wavefront radii of curvature match the radii of curvatures of the ellipsoidal mirror. This result makes sense with the geometrical phase aberration theory, which considers the ellipsoidal mirrors being as the ideal off-axis reflector phase transforming elements without introducing aberrations. In fact, analyzing the wavefront

aberrations in off-axis spherical mirrors was reported in [156]. The basic assumption in this study small pupil, which corresponds to small beam diameter, in addition to the inclination angles up to 10 degrees. In contrast to the geometrical phase aberration theory and by matching the incident and the reflected field within the scalar field approximation; i.e. $E_{ref} = -E_{inc}$, it was shown that the amplitude mismatch results in the excitation of the E_{30} and E_{12} modes when an E_{00} mode is incident on an off-axis ellipsoidal mirror [155]. The field amplitude of the higher-order modes was shown to be proportional to the factor $w_m \tan(\theta_{inc}) / f$ where w_m is the spot radius at the mirror and f is the focal length of the ellipsoid. Using a perturbation analysis technique in which amplitude distortion is neglected but including the vectorial nature of the fields, cross-polarization was found to occur for an incident linearly-polarized E_{00} mode and an E_{01} mode is excited with the perpendicular polarization. The excited field amplitude is also proportional to the factor $w_m \tan(\theta_{inc}) / f$. The vectorial nature was treated using the physical optics approximation description of wave beam reflection at a mirror; i.e. $\overline{E_{ref}} = -\overline{E_{inc}} + 2(\bar{n}.\overline{E_{inc}})\bar{n}$ where the dot represents a dot-product and $\bar{n}$ is the normal inward vector on the mirror surface at the incidence point. All the analysis mentioned above was based on the paraxial approximation such that the ratio w_m / f is much smaller than unity and for the special case of an ellipsoidal mirror.

6.1.4 Scattering matrix of Hermite-Gaussian beams

The off-axis incidence of a GB on a curved reflector results in the excitation of higher-order HG modes. In general, the incidence of a HG mode can excite other higher- or lower-order modes. A scattering matrix can be used to represent the relation between

the input set of modes and the output set [159-160]. First, an arbitrary incident field is projected onto the input HG modes set and the projection coefficients are calculated by the means of an overlap integral. Then, the scattering matrix elements are used to calculate coefficient of the resulting output HG modes set. The reflected field is calculated by recombination of the output modes. Indeed, the reflected field can be calculated after propagation of a certain distance by propagating its equivalent HG mode set, using the simple Gaussian optics approach, and then recombining them to give the total field. The method can be applied on a sequence of off-axis curved mirrors. Indeed, the scattering matrix is calculated numerically allowing for the diffractive spreading of the beam within the volume of the mirror to be taken into account. It allows also for the analysis of curved mirrors with arbitrary surface profile. The scattering-matrix approach has the following implications:

a) The mirror is considered as an inclined phase transforming element. Consider the cross section shown in Fig. 6.7 where the mirror surface is given by the solid line and its mirroring, around the tangent line x' , is given by the dashed line. The incident/reflected beams coordinate system is (x', z') and the mirror coordinates system is (x, z). The phase transformation effect is represented by the relation:

$$E_{out} = E_{in} e^{j2\Delta z' \cos\theta_{inc}} \qquad (6.\ 14)$$

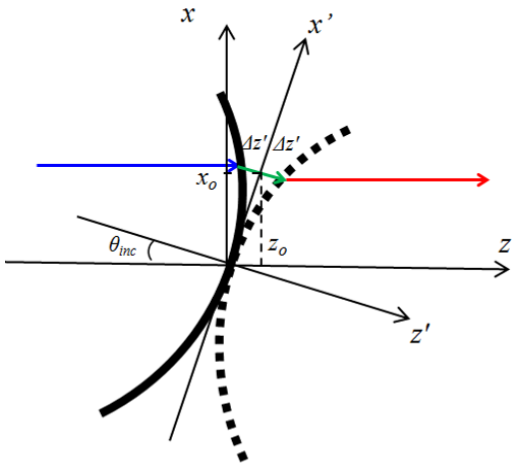

Fig. 6.7. Treating the mirror as an inclined phase transformation surface.

The phase transformation function can be found from the original mirror surface equation by shifting and rotating the axes such that:

$$\begin{aligned} x &= x'\cos\theta_{inc} + \Delta z'\sin\theta_{inc} = x_o + \Delta x \\ y &= y' = y_o \\ z &= x'\sin\theta_{inc} - \Delta z'\cos\theta_{inc} = z_o - \Delta z \end{aligned} \tag{6. 15}$$

b) The fields are assumed to be scalar in the form:

$$\begin{aligned} E_{in}(x',y',z') &= \sum_{n,m} A_{nm} E^{i}_{nm}(x',y',z') \\ E_{out}(x',y',z') &= \sum_{r,s} B_{rs} E^{o}_{rs}(x',y',z') \end{aligned} \tag{6. 16}$$

where A_{nm} and B_{rs} are the input and out modes coefficients respectively related by the scattering matrix and the free space modes $E^{i}_{nm}(x',y',z')$ and $E^{o}_{rs}(x',y',z')$ are related the Gaussian-optical approach discussed in the previous section.

c) The scattering from one mode to the others has two types:

I. The scattering due to the non-orthogonality of the incident and the reflected mode sets on the inclined plane. This scattering is described by the matrix β:

$$\beta_{glrs} = \iint h_r\left(\frac{\sqrt{2}x_o}{w_x}\right) h_g\left(\frac{\sqrt{2}x_o}{w_x}\right) h_s\left(\frac{\sqrt{2}y_o}{w_y}\right) h_l\left(\frac{\sqrt{2}y_o}{w_y}\right) e^{[i(r-g)\phi_{ox}]}\delta_{ls}\,dx_o\,dy_o \tag{6. 17}$$

where w_x and ϕ_{ox} vary as a function of x and y across the mirror surface and $h_n\left(\frac{\sqrt{2}x}{w}\right) = \frac{1}{\left(2^{n-0.5}\,n!\,\pi^{0.5}w\right)^{0.5}} H_n\left(\frac{\sqrt{2}x}{w}\right)\exp\left(\frac{x^2}{w^2}\right)$.

II. The scattering due to the variation of the beam amplitude and phase across the mirror surface described by the matrix α:

$$\alpha_{glmn} = \iint h_m\left(\frac{\sqrt{2}x_o}{w^i}\right) h_g\left(\frac{\sqrt{2}x_o}{w^o}\right) h_n\left(\frac{\sqrt{2}y_o}{w^i}\right) h_l\left(\frac{\sqrt{2}y_o}{w^o}\right) \exp\left[i(m+n+1)\phi^i{}_o - i(g+l+1)\phi^o{}_o\right] \exp\left[-ik\left(\frac{x^2+y^2}{R^i+\sqrt{R^{i^2}+x^2+y^2}} - \frac{x^2+y^2}{R^o+\sqrt{R^{o^2}+x^2+y^2}}\right)\right] \exp\left[2ik\Delta z'\cos\theta_{inc}\right] dx_o\,dy_o \tag{6. 18}$$

where the integration is carried out over the physical mirror size to account for beam truncation effect.

d) Finally the scattering matrix S is calculated by multiplying β^{-1} by α and the output modes coefficient vector B is calculated by multiplying the scattering matrix by the input modes coefficient vector A:

$$B = \beta^{-1}\alpha A = SA \qquad (6.\ 19)$$

The scattering-matrix technique based on treating the mirror as inclined phase transforming element has proven accuracy for off-axis angles of up to 45^{o} and down to an intensity level of -25 dB using 100 modes, compared to the physical optics simulations in the millimeter wavelength range [160]. We found that the scattering-matrix technique is not suitable for use with curved micro reflector in the near-infrared wavelength or shorter. For instance, consider the reflection of a GB on a spherical micromirror with a radius of curvature of 500 μm, incidence angle of 45 degrees and input distance of 175 μm. The incident beam min waist radius is 1.5 μm and the wavelength is 1550 nm. The simulated reflected beam profile in the tangential plane is depicted in Fig. 6.8 for different number of simulation modes. The obtained profile is not stable with increasing the number of modes used in the simulation. This indicates that a much larger of modes is needed, which is beyond the reasonable desktop computer capability. Therefore, there is a need for understanding and developing a model for the problem of GB off-axis reflection on curved micro reflectors.

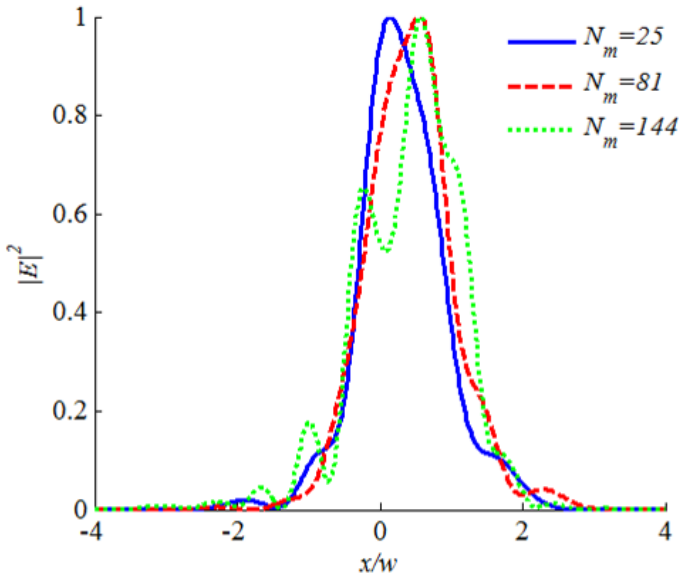

Fig. 6.8. Scattering-matrix based simulation for a reflected GB from micro spherical mirrors. The profile obtained is not stable with number of modes up to 144.

6.2 Simulation study using physical optics

In this section, a through simulation study is carried out using the student version of the Generalized Reflector Antenna farm analysis Software Package (GRASP9) simulator. The simulation is based on what is called the scattering analysis (not to be confused with the scattering-matrix technique in section 6.1.4). In this type of numerical analysis the source-equivalent surface currents are calculated on the reflector surface based on the Physical Optics (PO) relation:

$$\overline{J_S} = 2\bar{n}x\overline{H_i} \qquad (6.\ 20)$$

where $\overline{J_s}$ is the induced surface current on the reflector, $\bar{n}$ is the outward normal to the reflector and $\overline{H_i}$ is the incident magnetic field on the reflector. For non-planar surfaces, the PO is a good approximation to the actual current if both the diameter of the reflector and its radius of curvature are at least 5 times larger than the wavelength [161]. The field radiated by the calculated surface current is computed by means of the radiation integral carried out over the reflector surface [162]. The special behavior of the currents close to an edge of the reflector is not modeled by the PO relation and, therefore a correcting term based on the physical theory of diffraction (PTD) is added to the PO field for obtaining the total reflected field [163]:

$$\overline{E_r} = \overline{E^{PO}} + \overline{E^{PTD}} \qquad (6.\ 21)$$

The student version of GRASP9 has limited capabilities compared to the full industrial version. General conic mirror surfaces and numerically tabulated surface are not allowed and only surfaces of revolution are allowed. GB feed is an allowed source in the student version but with far field analysis only. In the following simulations, the wavelength is set to 1.55 μm serving as a mid value in the near infrared spectral regime.

6.2.1 Normal incidence

In this section, the accuracy of the Gaussian optics approach is examined for normal incidence of a GB on a spherical micromirror, when the beam spot size is comparable to the mirror radius of curvature. This situation is of particular interest for coupling back the beam to the source and for tight focusing of the beam as shown in Fig. 6.9 (a) and (b), respectively.

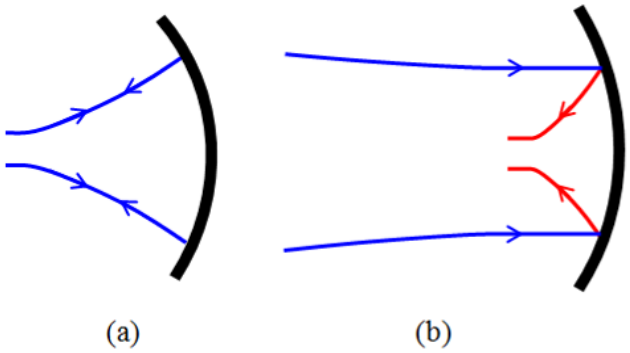

Fig. 6.9. Optical arrangement for normal incidence of a GB normally incident on a spherical reflector for the purpose of reflecting back the beam on itself in (a) and for focusing the incoming beam in (b).

For the coupling configuration shown in Fig. 6.9 (a), the beam waist is located approximately at the mirror center; i.e. is $d_{in} \approx R$, and the ratio between the beam spot radius on the mirror w_m and the mirror radius of curvature is given by:

$$\frac{w_m}{R} = \sqrt{\left(\frac{w_0}{R}\right)^2 + \left(\frac{\lambda}{\pi w_0}\right)^2} \qquad (6.\ 22)$$

The simulation study is carried out for w_m / R = 0.25, 0.5 and 1. The simulation was repeated for absolute values of R in the order of 10-100 μm. For a given R and for each value of w_m, the corresponding value of w_o was obtained from Eq. (6. 22). The simulation results are compared to Gaussian-optical and shown in Fig. 6.10 for the case of w_m / R = 0.5. For the sake of comparison, normalization is applied such that the input fields have equal power and the scale is normalized to unity. The x-axis of the plot represents the

paraxial angle normalized to the beam half-divergence angle. The paraxial angle is given by:

$$\theta = \sqrt{\frac{x^2 + y^2}{z^2}} \tag{6. 23}$$

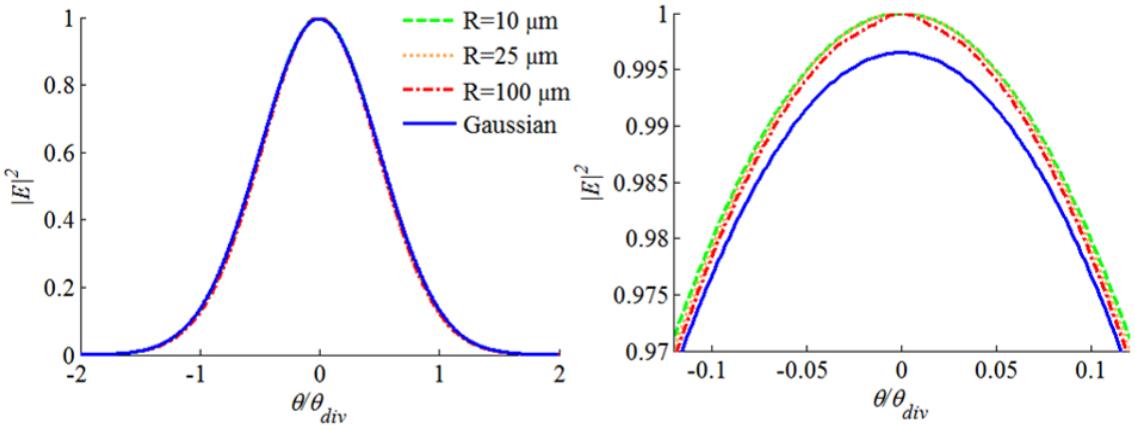

Fig. 6.10. GRASP9 simulation versus Gaussian-optics analysis at $w_m / R = 0.5$ for the optical arrangement shown in Fig. 6.9 (a).

An excellent agreement between the simulated and the Gaussian field for the case of $w_m/R=0.25$ while the deviation is largest for $w_m/R=1$. The simulated profiles were fitted to Gaussian profiles and the ratio between the fitting divergence angle and the divergence angle predicted by the Gaussian-optical analysis are listed in Table 6.2. The error in Gaussian-optical analysis is about 2% for the case $w_m / R = 0.5$ reaches about 10% for the $w_m / R = 1$ case.

Table 6.2. Simulation parameters used in the study for the optical arrangement shown in Fig. 6.9 (a).

R	w_m/R	$\theta_{fit} / \theta_{Gaussian}$
10	0.5	1
10	1	0.9
25	0.25	1
25	0.5	0.98
25	1	0.9
100	0.25	1
100	0.5	0.98
100	1	0.9

Table 6.3. Simulation parameters used in the study for optical arrangement in Fig. 6.9 (b).

R	w_m/R	$\theta_{fit} / \theta_{Gaussian}$
10	0.25	1.01
10	0.5	1.03
10	1	1.24
25	0.25	1.01
25	0.5	1.03
25	1	1.15
100	0.25	1.01
100	0.5	1.03
100	1	1.19

For the focusing configuration shown in Fig. 6.9 (b), the incident GB has its beam waist at the mirror surface; i.e. d_{in} = 0 and $w_o = w_m$, and the output beam waist locations is approximately at the focus of the mirror focus. The simulation study is carried out for w_m / R = 0.25, 0.5 and 1 and was repeated for absolute values of R in the order of 10-100 µm. The simulation results are compared to Gaussian-optical and shown in Fig. 6.10 for the case of w_m / R = 0.5. Again an excellent agreement between the simulated and the Gaussian field for the case of $w_m/R=0.25$ while the deviation is largest for $w_m/R=1$. The simulated profiles were also fitted to Gaussian profiles and the ratio between the fitting divergence angle and the divergence angle predicted by the Gaussian-optical analysis are listed in Table 6.3 .The error in Gaussian-optical analysis is about 3% for the case $w_m / R = 0.5$ reaches about 24 % for the $w_m / R = 1$ case. The error is in the opposite direction with respect to the coupling configuration.

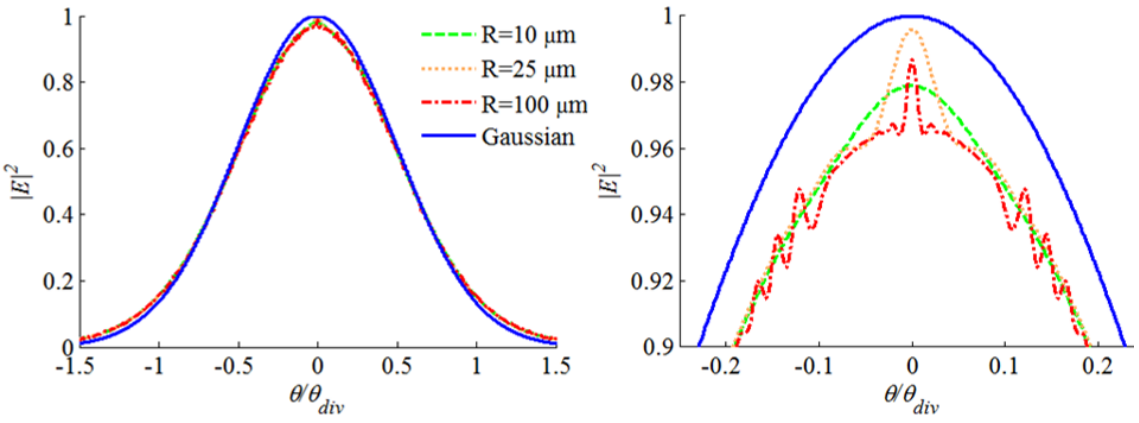

Fig. 6.11. GRASP9 simulation versus Gaussian-optics analysis at w_m / R = 0.5 for the optical arrangement shown in Fig. 6.9 (b).

6.2.2 Off-axis incidence

In this section, the resulting field from the inclined incidence of a GB on a spherical micromirror is examined, when the beam spot size is comparable to the mirror radius of curvature. The effect of the different parameters is studied including the incident beam divergence angle, mirror radius of curvature, the angle of incidence and the beam wave-front radius of curvature. The geometrical description of the off-axis incidence problem is shown in Fig. 6.12. One may define the effective radius of the mirror aperture, as seen by the incident beam, by:

$$r_{eff} = R(1-\sin\theta_{inc}) \qquad (6.\ 24)$$

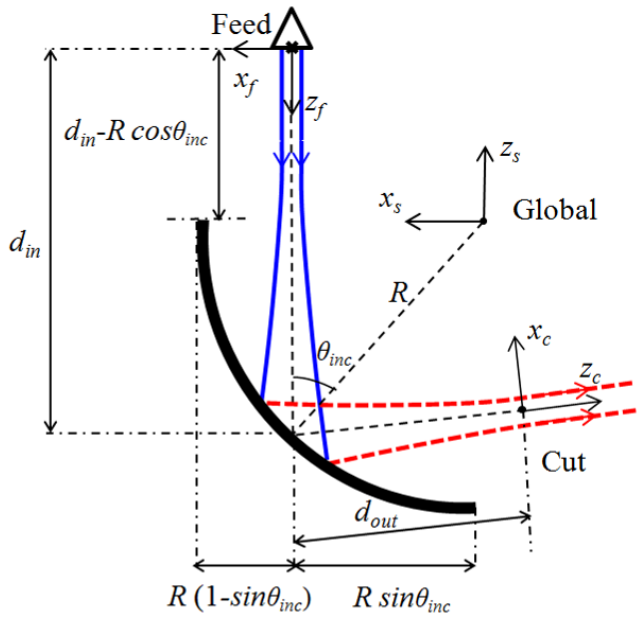

Fig. 6.12. The geometrical problem of inclined incidence of a GB on a spherical mirror.

6.2.2.1 Incident beam divergence angle effect

In this study, the incidence angle is fixed at 45 degrees, the mirror radius of curvature is fixed at 500 µm and the input beam waist is located at the tangential focal plane; i.e. $d_{in} = 0.5\ R\ cos(\theta_{inc})$. The incident beam waist is assigned the values of 1.5, 2.5 and 5 µm for the sake of observing the effect of different beam divergence on the GB distortion. The beam arrives at different spot sizes at the mirror (see Fig. 6.14 for illustration). The simulation parameters of this section are given in Table 6.4 where the ratio between the beams spots radius and the mirror radius as well as the mirror effective physical size radius are given. The simulation results are depicted in Fig. 6.14 and Fig. 6.15 for the tangential and sagittal planes, respectively.

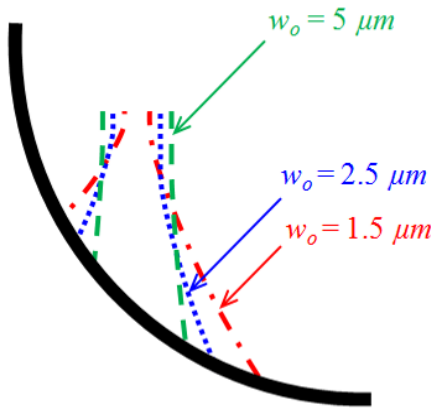

Fig. 6.13. Incident GB with a smaller beam waist arrives at the mirror with a larger spot size

Table 6.4. Simulation parameters for studying GB reflection from 45^o off-axis spherical mirror for different beam min beam waist launched from the effective focal point in the tangential plane.

w_o (μm)	w_m / R	w_m / r_{eff}
1.5	0.12	0.4
2.5	0.07	0.24
5	0.04	0.12

Two effects are observable in the tangential plane. First location of the maximum field is shifted from the zero location and, second, the appearance of side lobes. There is a small shift in the peak for w_o = 5 μm. The shift is larger and larger for w_o = 2.5 μm and w_o= 1.5 μm, respectively. The intensity profile of the beam is distorted and narrowed w_o= 5 μm and widened for w_o = 2.5 μm and w_o = 1.5 μm. The side lobes amplitude is relatively lager for smaller w_o. A fast decay is observed in the lobes for w_o = 2.5 μm while the degradation is much slower for w_o = 1.5 μm.

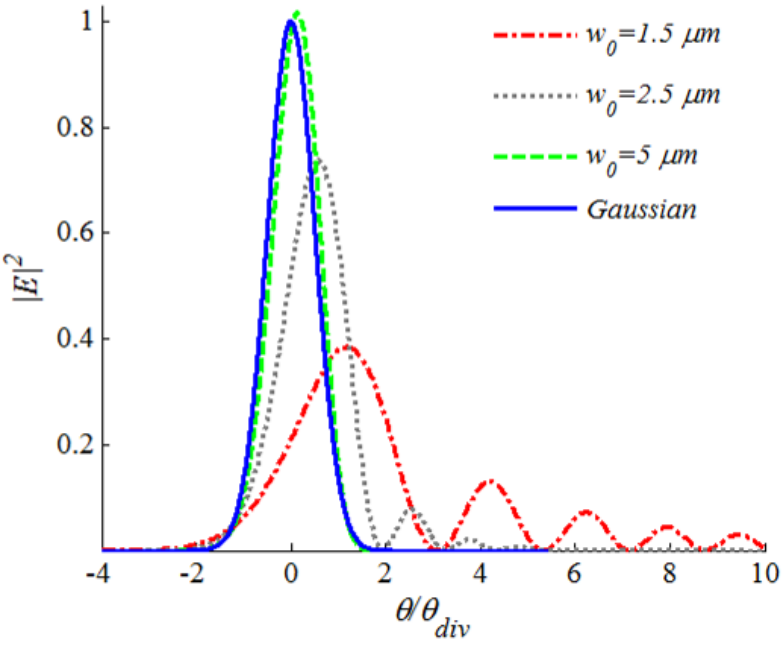

Fig. 6.14. GRASP9 simulation results in the tangential plane compared to Gaussian-optics analysis for mirror radius of curvature of 500 μm, incidence angle of 45 degree and different incident beam min spot waist radii.

The encountered results in the sagittal plane are completely different. The intensity profile is still having a central maximum and no side lobes appear in the profile. There is, however, a large deviation in the resulting beam divergence angle with respect to the Gaussian-optical analysis where the deviation is larger for smaller w_o. The predicated divergence angle is larger than the actual one. Gaussian profiles were fitted to the GRASP9 simulation data and their corresponding divergence angles θ_{fit} were obtained. The ratio between the fitting divergence angle and the angle predicted by the Gaussian-optic analysis is listed in Table 6.5. In addition to being closer to the Gaussian-optical prediction, it is to be noted also the resulting profile is more Gaussian in the case

of w_o = 5 µm than w_o = 2.5 µm and w_o = 1.5 µm. This can be deduced from the maximum error values between the Gaussian fitting and the profile given in Table 6.5.

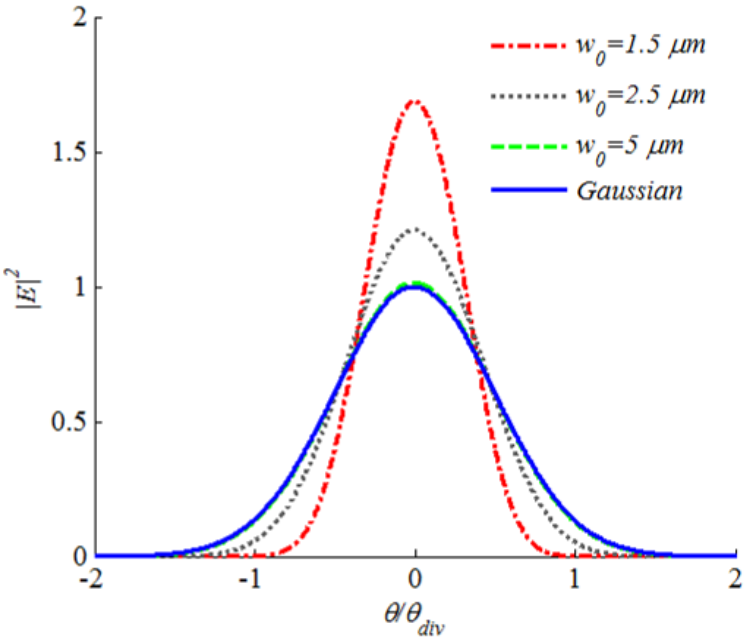

Fig. 6.15. GRASP9 simulation results in the tangential plane compared to Gaussian-optics analysis for mirror radius of curvature of 500 µm, incidence angle of 45 degree and different incident beam min spot waist radii.

Table 6.5. Gaussian fitting results for the sagittal plane profiles shown in Fig. 6.15.

w_o (µm)	$\theta_{fit}/\theta_{Gaussian}$	*Max error (%)*
1.5	0.59	1.4
2.5	0.82	0.65
5	0.99	0.008

6.2.3 Mirror radius of curvature effect

In this section, the study is carried out by varying the radius of curvature of the mirror from 25 μm to 1000 μm. The incident GB waist radius is w_o = 5 μm. The incident beam waist is also located at the tangential focal plane. The beam arrives at different spot sizes at the mirrors. The simulation parameters of this section are given in Table 6.6 and the results are depicted in Fig. 6.16 and Fig. 6.17 for the tangential and sagittal planes, respectively.

Table 6.6. Simulation parameters for studying GB reflection from 45^o off-axis spherical mirror for different mirror radius of curvature with the launched from the effective focal point in the tangential plane.

R (μm)	d_{in} (μm)	w_m / R	w_m / r_{eff}
25	9	0.2	0.7
100	35	0.06	0.21
500	177	0.04	0.12
1000	354	0.04	0.12

In the tangential plane, the smallest mirror with a radius of curvature 25 μm truncates the beam because the ratio of the beam spot radius to the mirror aperture radius is about 0.7 leading to the oscillation appearance in the beam profile, as shown in Fig. 6.16). The truncation effect disappears in the case of larger radii of curvatures. Increasing the mirror radius of curvature leads to shifting the maximum intensity location in addition to, first narrowing the profile and, then widening it. For R =1000 μm, multiple lobes start

to appear (not observable on a linear scale) but with much lower values than the central one.

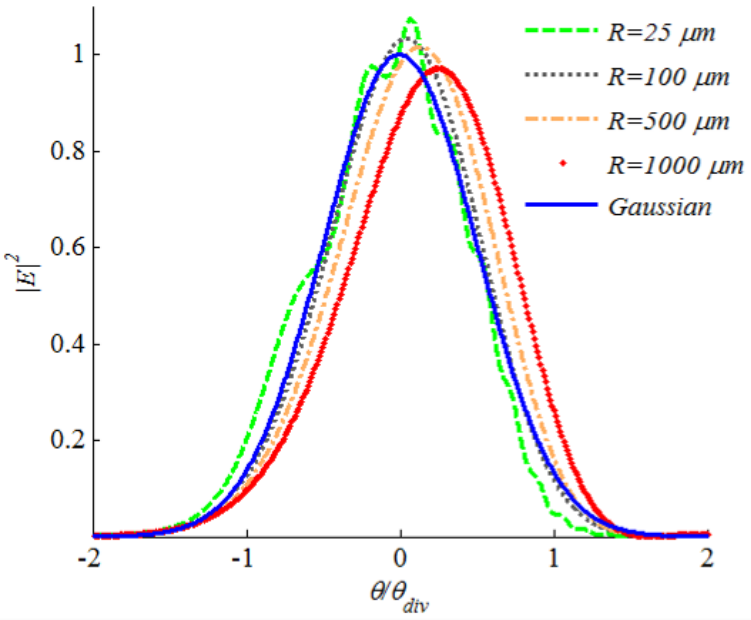

Fig. 6.16. GRASP9 simulation results in the tangential plane compared to Gaussian-optics analysis for incident beam waist of 5 μm, incidence angle of 45 degree and different mirror radii of curvature.

For the sagittal-plane intensity profile depicted in Fig. 6.15, there is a close agreement with the Gaussian profile for all mirror radii of curvature under study. There is a small deviation in the beam divergence angle between the simulation results and the predicated one from Gaussian-optical analysis. The encountered deviation gets smaller with increasing the radius of curvature of the mirror. In fact, the study considered many

intermediate values for radius of curvature and the same behavior was found both in the tangential and in the sagittal plane.

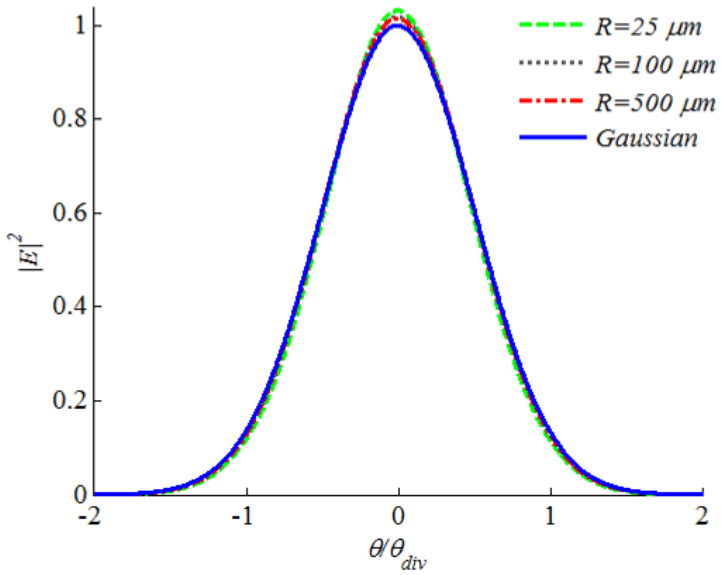

Fig. 6.17. GRASP9 simulation results in the sagittal plane compared to Gaussian-optics analysis for incident beam waist of 5 μm, incidence angle of 45 degree and different mirror radii of curvature.

6.2.4 Incidence angle effect

Two different cases are studied in this section. The first case when the mirror is used to collimate the beam in the tangential plane; i.e. $d_{in} = 0.5\ R\ cos(\theta_{inc})$. In this case varying the incidence angle implies corresponding variation in the input distance and the incident beam spot radius at the mirror. In the second case, the input distance is kept constant

independent of the incidence angle. This helps to understand the effect of changing the incidence angle only.

6.2.4.1 Collimated output beam

In this section, the angle of incidence of the GB is assigned the values 15^o, 45^o and 75^o while the radius of curvature of the mirror is kept constant at 500 μm. The incident beam waist is located at the tangential focal plane. The beam arrives at different spot sizes at the mirrors and the simulation parameters of this part are given in Table 6.7. The simulation results are depicted in Fig. 6.18 for the tangential plane. The maximum intensity location shifts more with increasing the incidence angle. For the 75-degree incidence angle, there is a significant deviation from the Gaussian profile for intensity levels below 20 dB (observable in log scale). The sagittal-plane simulation results showed generally good agreement with Gaussian-optical predications.

Table 6.7. Simulation parameters for studying GB reflection from off-axis spherical mirror with a 500 μm radius of curvature and incident beam waist in the focal plane for different angle of incidence.

θ_{inc} (degree)	d_{in} (μm)	w_m / R	w_m / r_{eff}
15	243	0.05	0.07
45	177	0.04	0.12
75	165	0.02	0.48

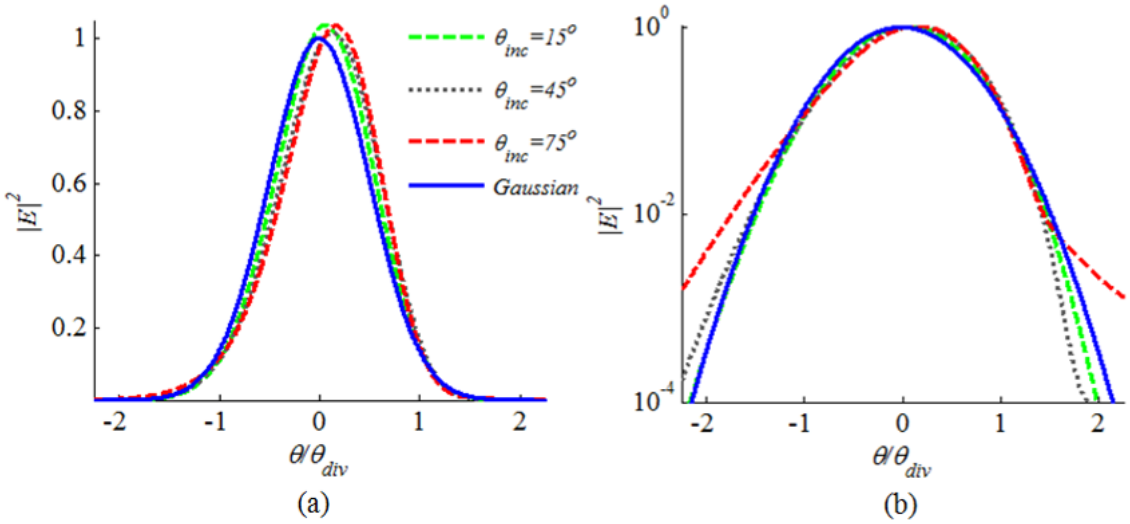

Fig. 6.18. GRASP9 simulation results in the tangential plane compared to Gaussian-optics analysis for incident beam waist of 5 µm, mirror radius of curvature of 500 µm, incidence beam waist in the focal plane with different incidence angles. Linear scale in (a) and log scale in (b).

6.2.4.2 Constant input distance

In this section, the effect of changing the incidence angle is studied for two given values of the input distance of 250 µm and 1000 µm. The simulation parameters of this part are given in Table 6.8. The simulation results in the tangential plane are depicted in Fig. 6.19 and Fig. 6.20 for 250 µm and 1000 µm, respectively. The common observation is the significant deviation from the Gaussian profile for intensity levels below 10 dB (observable in log scale). For the case of 250 µm input distance, the shift in the maximum intensity location is less for larger incidence angle. The agreement between the 15-degree and the 30-degree results with Gaussian-optical analysis is better in the case of 1000 µm

input distance. In contrast, the agreement is less for the 45-degree beam due to the significant truncation effect ($w_m / r_{eff} = 0.675$).

Table 6.8. Simulation parameters for studying GB reflection from off-axis spherical mirror with a 500 μm radius of curvature and input distance of 250 μm and 1000 μm for different angle of incidence.

θ_{inc} (degree)	d_{in} (μm)	w_m / R	w_m / r_{eff}
15	250	0.05	0.07
30	250	0.05	0.1
45	250	0.05	0.17
15	1000	0.2	0.27
30	1000	0.2	0.4
45	1000	0.2	0.68

There is a very good agreement between the simulation results and the Gaussian-optical analysis in the sagittal plane. However, a cross-polarization component was found to exceed -30 dB in comparison with the co-polarization. The amplitude of this cross-polarization component increases strongly with the incidence angle as shown in Fig. 6.21. The profile for the three cases has been normalized to unity peak and compared to the E_{01} mode profile where an excellent agreement could be found. The cross-polarization excitation of the E_{01} mode was reported in [155].

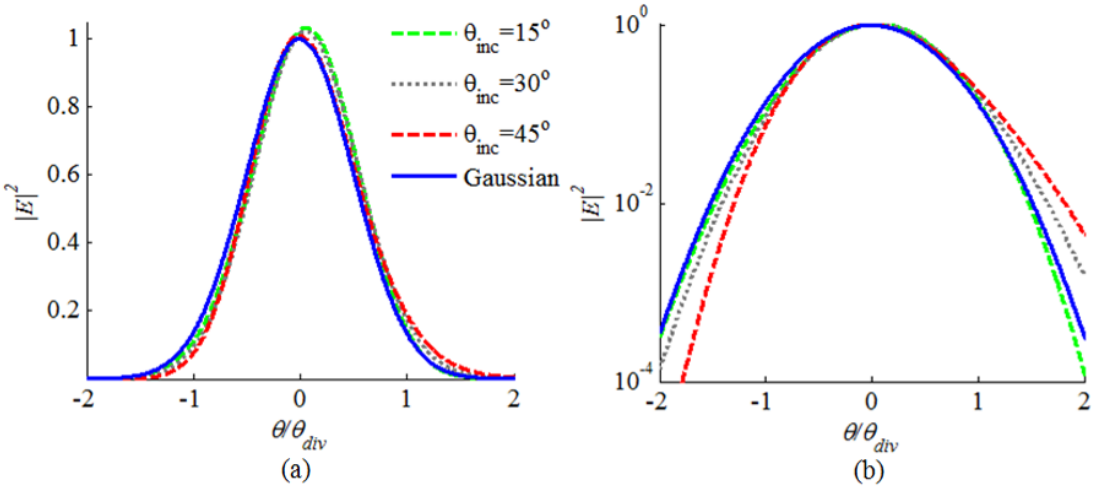

Fig. 6.19. GRASP9 simulation results in the tangential plane compared to Gaussian-optics analysis for incident beam waist of 5 μm, mirror radius of curvature of 500 μm and input distance of 250 μm with different incidence angle. Linear scale in (a) and log scale in (b).

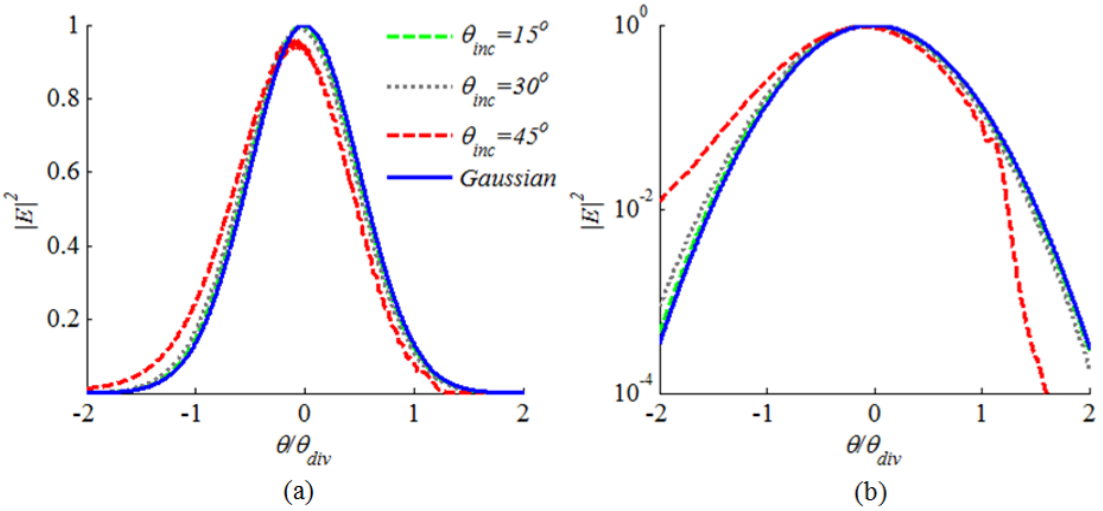

Fig. 6.20. GRASP9 simulation results in the tangential plane compared to Gaussian-optics analysis for incident beam waist of 5 μm, mirror radius of curvature of 500 μm and input distance of 1000 μm with different incidence angles. Linear scale in (a) and log scale in (b).

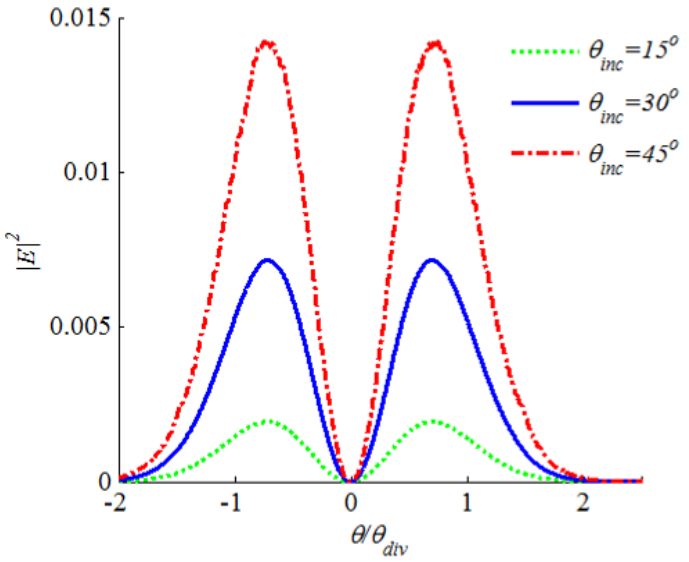

Fig. 6.21. GRASP9 simulation results in the sagittal plane for the cross-polarization field. The incident GB waist is 5 μm, the mirror radius of curvature is 500 μm and input distance is 1000 μm. The cross-polarization field amplitude increases with the incidence angle. The amplitude is normalized to co-polarization amplitude.

6.2.5 Wave-front radius of curvature effect

In this section, the angle of incidence of the GB and the radius of curvature of the mirror are kept constant at 45 degree and 500 μm, respectively. The distances between the beam waist and the mirror surface is assigned the values $0.1z_o$, z_o and $10z_o$ to screen the cases of large and small beam phase radius of curvatures. For the smallest distance the beam wave-front is similar to a plane wave, while it is more like a spherical wave for the largest distance. At z_o, the GB possess its minimum value for the wave-front radius of curvature, which is $2z_o$. The simulation parameters of this section are given in Table 6.9.

The simulation results in the tangential plane are depicted in Fig. 6.22 and the cross-polarization component in the sagittal plane is depicted in Fig. 6.23.

Table 6.9. Simulation parameters for studying GB reflection from off-axis spherical mirror with a 500 μm radius of curvature and input distance of 250 μm and 1000 μm for different angle of incidence.

d_{in} (μm)	w_m / R	w_m / r_{eff}
5	0.01	0.03
50	0.02	0.08
500	0.1	0.34

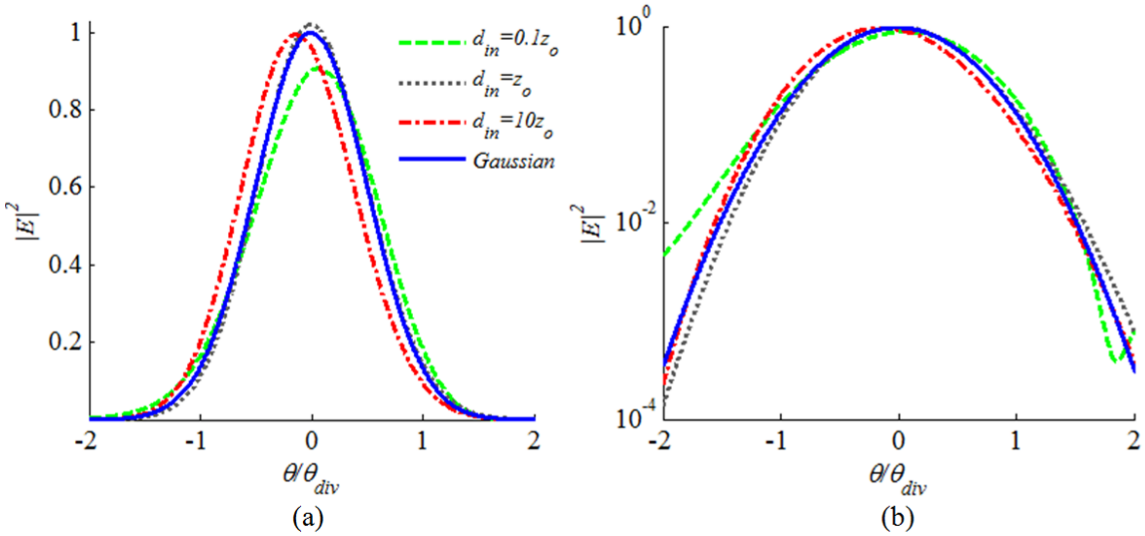

Fig. 6.22. GRASP9 simulation results in the tangential plane compared to Gaussian-optics analysis for incident beam waist of 5 μm, mirror radius of curvature of 500 μm and incidence angle of 45 degree for different input distance. Linear scale in (a) and log scale in (b).

In the tangential plane, the shift in the maximum intensity location is minimized for an input distance of z_o. The deviation from the Gaussian profile is largest for the smallest input distance. The shift direction in maximum intensity is toward the negative side. This is similar to the case of 45 degree incidence angle in Fig. 6.20 where significant beam truncation occurs. For the sagittal plane, the co-polarization component was agreeing well with the Gaussian-optical analysis. The cross-polarization component shown in Fig. 6.23 is well agreeing with the E_{01} mode and its amplitude increases with increasing the input distance.

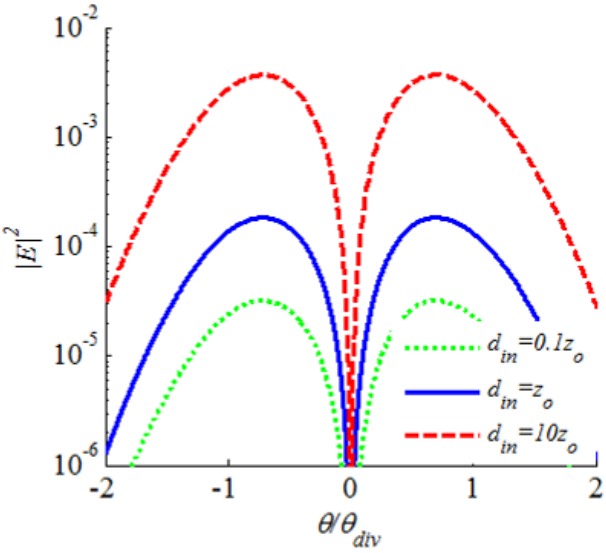

Fig. 6.23. GRASP9 simulation results in the sagittal plane for the cross-polarization field for incident beam waist of 5 μm, mirror radius of curvature of 500 μm and incidence angle of 45 degree for different input distance. The cross-polarization field amplitude increases with the input distance. The amplitude is normalized to co-polarization amplitude.

6.3 Developed model

In this section, a simple developed is presented and compared with GRASP9 results. The model is based on the treating the curved mirror as a phase transformer in which the phase transformation is composed of two components. The first component is calculated from the input beam side, which denoted by Δz_i in Fig. 6.24. The second component, denoted by Δz_o, is calculated from the output beam side. Each component is calculated by considering the phase variation across the beam propagation direction and round the point *O*. The transformation phase is given by:

$$\phi = \frac{2\pi}{\lambda}\left(\Delta z_i + \Delta z_o\right) \tag{6. 25}$$

In Fig. 6.24 the incident beam propagation direction and the direction across the beam are assumed to be aligned with the coordinate system of the mirror, which can be achieved by means of rotation of axes. The alignment of the axes can be always assumed in the case of a spherical mirror, which is the case at hand. The transformation phase is related to the radius of curvature of the mirror and the incidence angle by:

$$\begin{aligned}\phi &= \frac{2\pi}{\lambda}\left[z + z\cos(2\theta_{inc}) + x\sin(2\theta_{inc})\right] \\ &= \frac{2\pi}{\lambda}\left[\sqrt{R^2 - x^2 - y^2}\left(1 + \cos(2\theta_{inc})\right) + x\sin(2\theta_{inc})\right]\end{aligned} \tag{6. 26}$$

The transformation phase of a spherical mirror with a 500 μm radius of curvature in the tangential plane is depicted in Fig. 6.25. For normal incidence, the phase is symmetric around the central axis of the beam. In contrast, a significant asymmetry is encountered for the case of a 45 degrees inclination angle.

In addition to treating the mirror as a phase transformer, the incident beam suffers from unsymmetrical truncation on the mirror surface. Considering the geometry in Fig. 6.24, the left and right section of the mirror with respect to the incident beam central axes are R-x_o and x_o, respectively where $x_o = R\,(1-\sin\theta_{inc})$. This truncation can be considered as as a multiplication by a transmission function in the form:

$$T = u(x-R) - u(x) \qquad (6.\ 27)$$

where u is the unit step function. Note that the incident beam has a central axis x-coordinate of x_o which accounts for the unsymmetrical truncation.

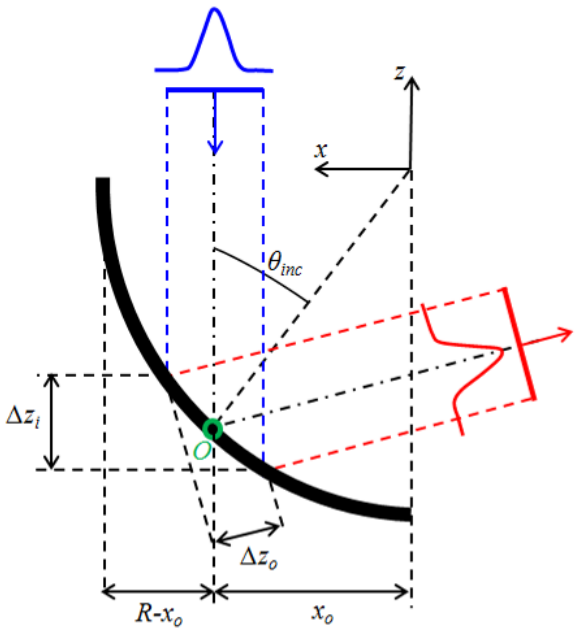

Fig. 6.24. Treating the curved mirror as a phase transformation element by in which the phase transformation has two components: Δz_i and Δz_o.

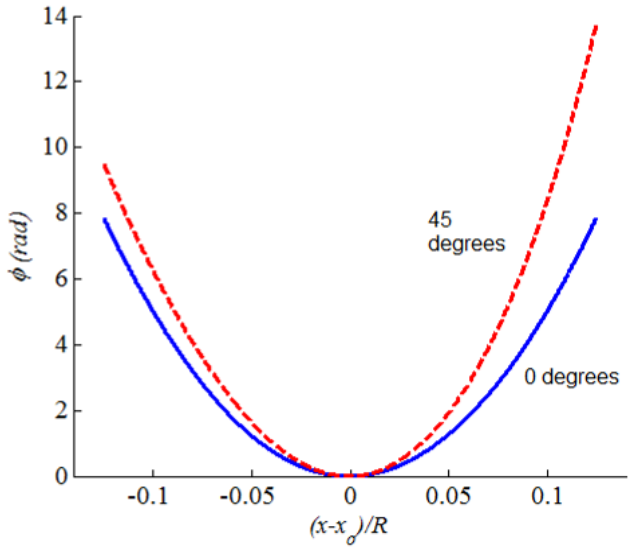

Fig. 6.25. Transforming phase of a spherical mirror with a 500 μm radius of curvature in the tangential plane for normal as well as 45-degree inclined incidences.

The propagation of the optical beam to and from the curved mirror surface in addition to the phase transformation/unsymmetrical truncation is all achieved using a Fourier-optics approach [164]. The overall simulation steps can summarized as follows:

a) Two-dimensional Fast Fourier Transform (FFT) is carried out for the input field in the spatial domain to get its spectral domain representation:

$$G_i(f_x, f_y, 0) = FFT\{E_i(x, y, 0)\} \tag{6. 28}$$

b) The propagation to the mirror is accounted for by phase multiplication:

$$G_i(f_x, f_y, d_{in}) = G_i(f_x, f_y, 0)\exp(-jk_z d_{in}) \tag{6. 29}$$

c) Inverse FFT to the field after propagation in the spatial domain:

$$E_i(x, y, d_{in}) = IFFT\{G_i(f_x, f_y, d_{in})\} \tag{6. 30}$$

d) Multiple the field by the phase transformation function and the amplitude truncation function:

$$E_o(x,y,d_{in}) = [u(x-R)-u(x)]E_i(x,y,d_{in})\exp(-j\phi) \quad (6.31)$$

e) FFT to get the output field in the spectral domain:

$$G_o(f_x,f_y,d_{in}) = FFT\{E_o(x,y,d_{in})\} \quad (6.32)$$

f) The propagation is accounted for by phase multiplication:

$$G_o(f_x,f_y,d_{out}) = G_o(f_x,f_y,0)\exp(-jk_z d_{in}) \quad (6.33)$$

g) Inverse FFT to the get the output field in the spatial domain:

$$E_o(x,y,d_{out}) = IFFT\{G_o(f_x,f_y,d_{out})\} \quad (6.34)$$

The developed model results were validated by comparison with GRASP9 results. In this comparison, the radius of curvature of the spherical mirror was taken to be 500 μm and the incidence angle is 45 degree. The input beam waist is located at the tangential focal plane; i.e. d_{in} = 0.5 $R\ cos(\theta_{inc})$. An incident beam waist of 1.5 μm was used that showed in the previous section a significant difference in the resulting beam profile between Gaussian optics and GRASP9. The reflected beam spot profile is shown in Fig. 6.26 and Fig. 6.27 in the near and far field, respectively. The spot profile is highly distorted and very far from the GB profile. The far field profile is compared to GRASP9 results in Fig. 6.28 and Fig. 6.29 with linear and log scale, respectively where an excellent agreement can be observed regarding the locations of the main and side lobes and there relative amplitudes. The comparison was repeated for many cases and a similar agreement was obtained.

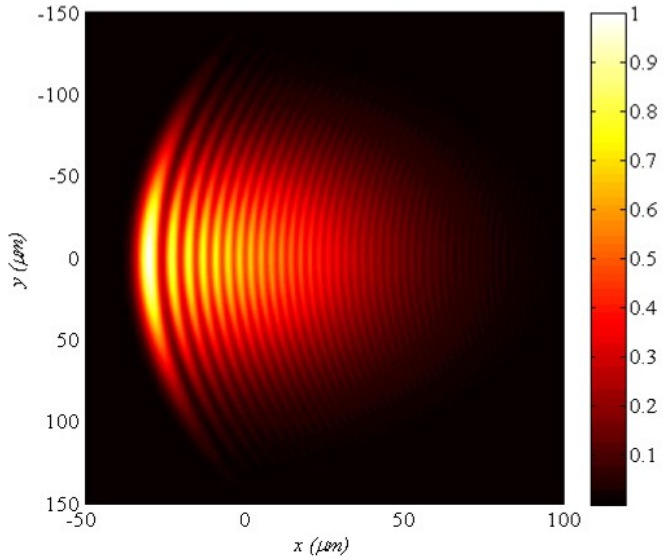

Fig. 6.26. Reflected beam profile for incident beam waist of 1.5 μm, incidence angle of 45 degree and 500 μm mirror radius of curvature. The profile is captured in the output tangential focal plane of the mirror; i.e. d_{out}=0.5 R $cos(\theta_{inc})$.

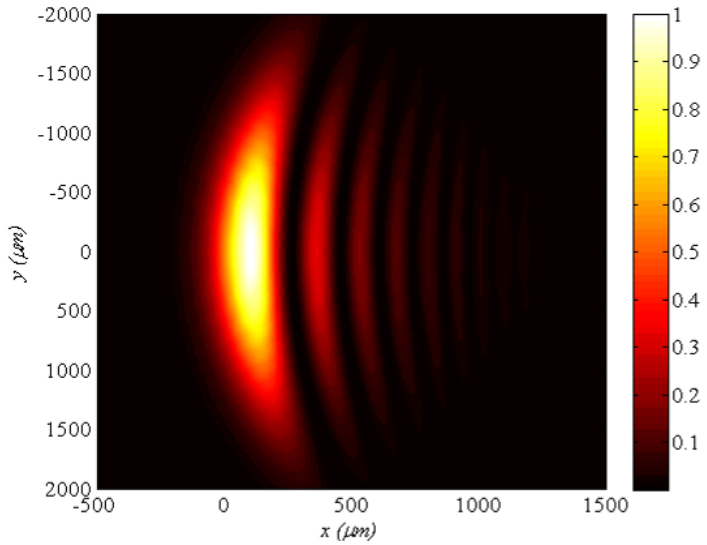

Fig. 6.27. Reflected beam profile for incident beam waist of 1.5 μm, incidence angle of 45 degree and 500 μm mirror radius of curvature. The profile is captured in the far field after 10 mm propagation distance.

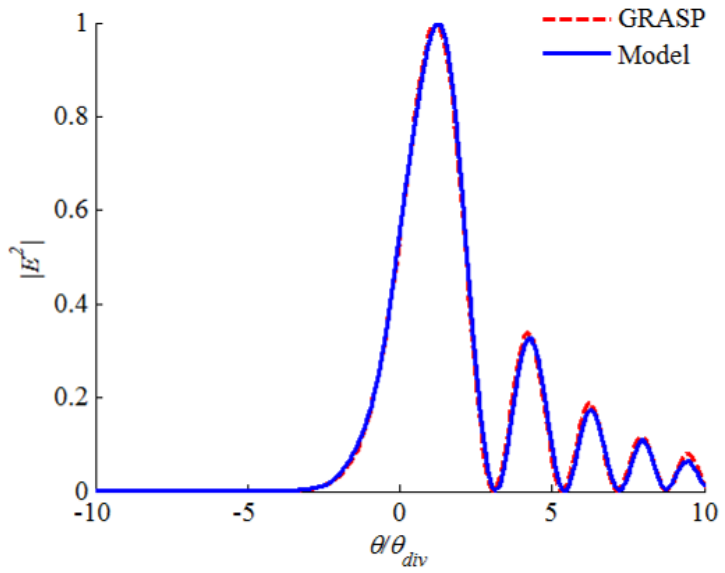

Fig. 6.28. Comparison on a linear scale between the developed model and GRASP9 for the reflected far field profile for incident beam waist of 1.5 μm, incidence angle of 45 degree and 500 μm mirror radius of curvature.

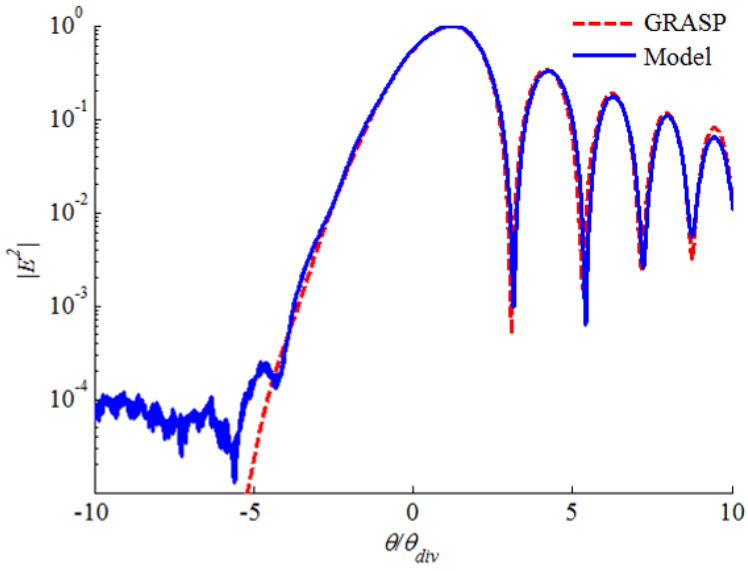

Fig. 6.29. Comparison on a log scale between the developed model and GRASP9 for the same conditions of Fig. 6.28.

6.4 Experimental study

The measurements in this section were carried out using single-mode optical fiber fed from a laser source such that a GB could be generated. Most of the measurements were carried out at the visible wavelength of 675 nm to facilitate the alignment and the detection of the reflected beam spot. In this, a special 4/125 single-mode optical fiber was used with datasheet mode-field diameter of 4 μm ± 0.5 μm and $1/e^2$ numerical aperture of 0.1 at 633 nm. In addition, some measurements were carried out at the near-infrared wavelength of 1550 nm using the standard 9/125 telecommunication optical fiber.

The optical beam intensity profile was measured using DataRay Inc. BeamScope^{TM}-P8 scanning slit beam profiling system. The output beams of the single-mode fibers were measured at different propagation distance by recording the spot profiles using the beam profiler. The corresponding beam widths were calculated based on the based on the second moment of the intensity distribution [85]. Due to the arbitrary shift than can exist between the beam central axis and the beam profiler zero position, the first moment of the intensity distribution was calculated and used to shift the beam to the zero position.

The normalized intensity profiles with after propagation are depicted in Fig. 6.30 and Fig. 6.31 for the 4 /125 fiber at 675 nm and 9/125 fiber at 1550 nm, respectively where the profiles are almost kept the same with propagation. The profiles were fitted to Gaussian profiles with root mean square error in the order of 1 %. A divergence angle of 5 degrees was deduced for 4/125 fiber at 675 nm with a corresponding minimum beam waist of 2.4 μm and beam Rayleigh range of 27 μm.

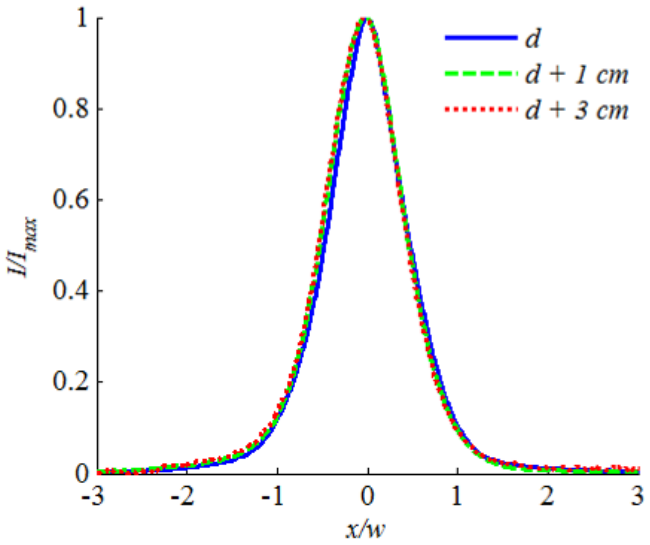

Fig. 6.30. Single-mode fiber output profile at 675 nm after propagation. The intensity is normalized and the x-axis is normalized with respect to the beam width.

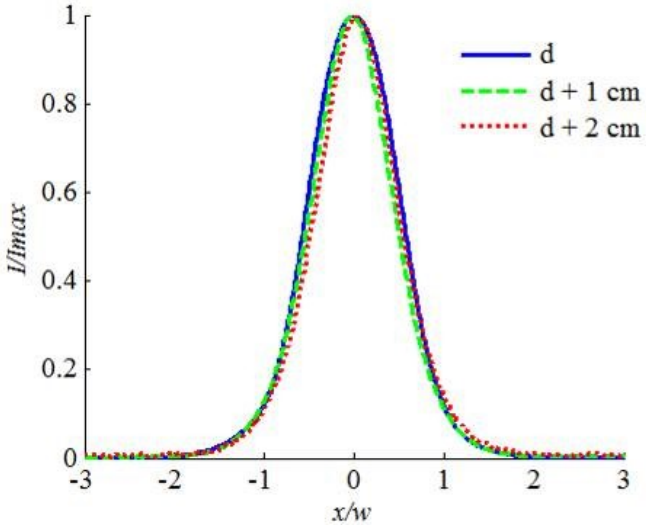

Fig. 6.31. Single-mode fiber output profile at 1550 nm after propagation. The intensity is normalized and the x-axis is normalized with respect to the beam width.

A divergence angle of 5.2 degrees was deduced for 9/125 fiber at 675 nm with a corresponding minimum beam waist of 5.4 μm and beam Rayleigh range of 60 μm.

The reflect intensity profile is close to the Gaussian profile for R = 400 μm while the profiles are significantly distorted for R = 200 μm and R = 100 μm where the latter exhibits the worst profile. Since the input distance is fixed at 100 μm, the ratio between the incident beam spot size and the mirror radius of curvature is inversely proportional to the mirror radius. Hence, the ratio is larger for smaller mirror radius of curvature leading to stronger effect on the beam profile. These highly distorted profiles are, however, not predictable by the physical optics simulation based on GRASP9 shown in Fig. 6.16 . The reflected intensity profile from a cylindrical micromirror with 500 μm radius of curvature was measured for different input distances as shown in Fig. 6.33. For a 300 μm input distance, the reflected beam is again highly distorted. The distortion is less for smaller input distance. It is important to mention here that the truncation effect is neglected for all of the input distance studied in Fig. 6.33. For instance, the incident beam should arrive at the mirror surface with a spot radius of about 28 μm for the 300 μm input distance case. The measured results are different from those obtained in Fig. 6.22 based on physical-optics simulations.

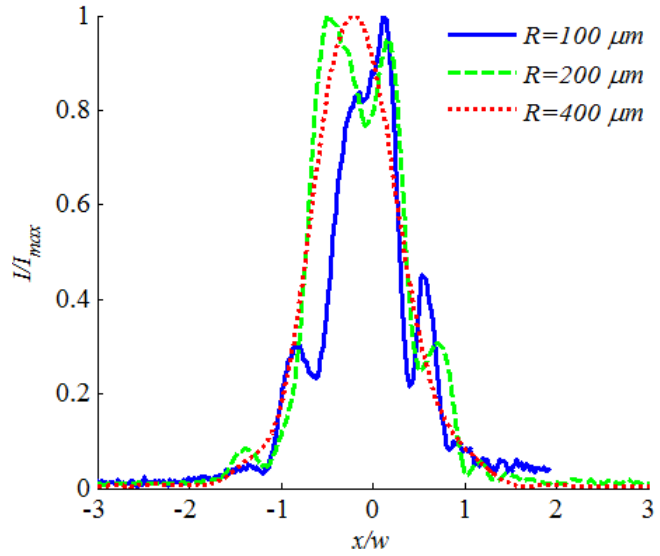

Fig. 6.32. Experimental results in the tangential plane using single-mode fiber at 675 nm for input distance of 100 μm, incidence angle of 45 degrees and different mirror radii of curvatures.

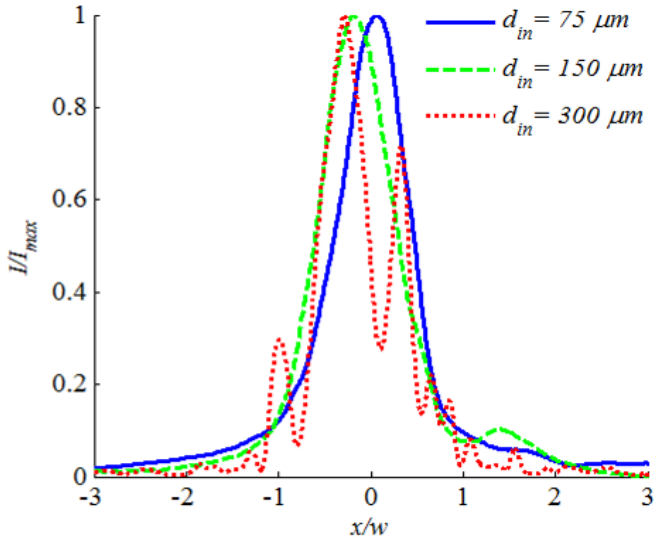

Fig. 6.33. Experimental results in the tangential plane using single-mode fiber at 675 nm for mirror radius of curvature of 500 μm, incidence angle of 45 degrees and different input distances.

The reflected intensity profile was measured also using the single-mode fiber at 1550 nm, by which the emitted GB has a Rayleigh range that is almost twice that of the single-mode fiber at 675 nm. The recorded intensity profile in both cases is depicted in Fig. 6.34. Less significant distortion was obtained in the 1550 nm due to the smaller spot size of the incident beam. However, the distortion in either case was not properly predictable by the physical-optics simulations.

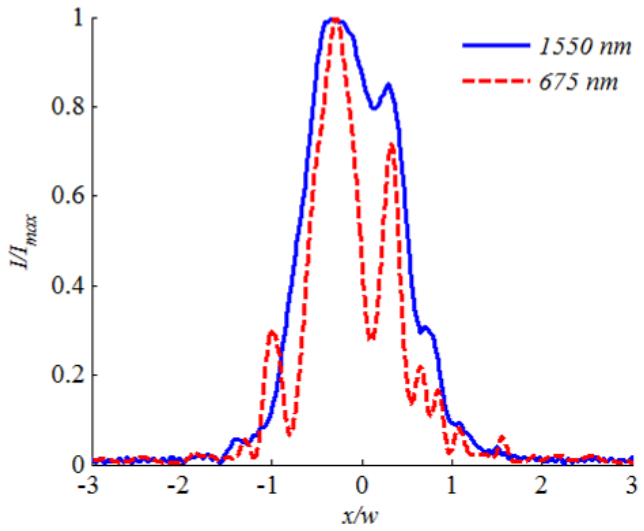

Fig. 6.34. Experimental results in the tangential plane using single-mode fiber at 675 nm and 1550 nm for mirror radius of curvature of 500 μm, incidence angle of 45 degrees and input distance of 300 μm.

Finally, the reflected intensity profile was measured for various incidence angles as shown in Fig. 6.35. The mirror radius of curvature and the input distance where fixed at 500 μm and 100 μm, respectively. The reflected beam profile distortion doesn't show

an increase in direct relation with the incidence angle; the same behavior was obtained using the physical-optics simulations. For the case at hand, the distortion is smaller for the larger incidence angle.

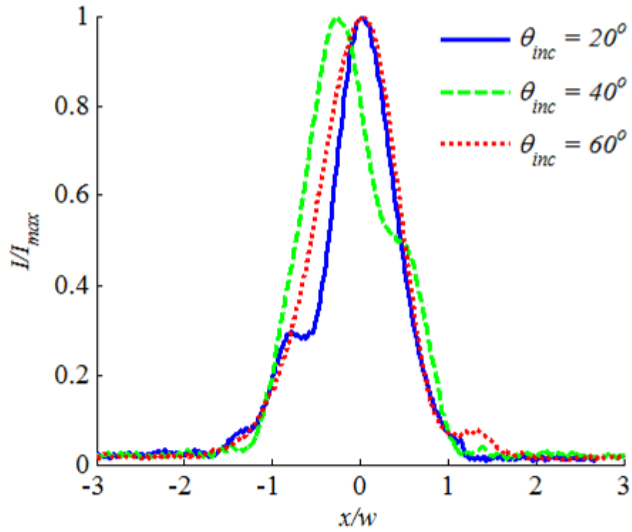

Fig. 6.35. Experimental results in the tangential plane using single-mode fiber at 675 nm for mirror radius of curvature of 500 μm, input distance of 100 μm and different incidence angles.

6.5 Discussion

The experimental results are not well-predicted by the previously presented simulation study carried out using GRASP9. We have also tried the direct solution of Maxwell's equations using finite element method. The simulation was carried out using HFSS simulator. The results, however, didn't add much value to the results obtained by

GRASP9. The main difference between the simulated and the measured micro reflectors are the non-ideal micromachined surface quality of the latter. The presence of surface roughness, or waviness with moderate spatial frequency, can be considered as a perturbation for the ideal surface. This perturbation can couple optical power from the fundamental Gaussian mode to the higher order HG modes. Together with the intrinsic distortion of the micro curved mirrors, the overall resulting beam profile can suffer from significant distortion. The deviation of the experimental data is more significant for the case of larger input distance, and consequently larger beam spot size on the mirror. Hence, this deviation can be attributed to optical surface waviness with spatial frequency that is comparable with order of magnitude of the spot size. To confirm this, we have added to our developed model, in section 6.3, a sinusoidal phase grating to simulate the waviness effect. The added terms is expressed by:

$$\Delta\phi = \frac{2\pi}{\lambda} R_a \sin\left(2\pi \frac{x}{R_p}\right) \qquad (6.\ 35)$$

where R_a is the waviness amplitude and R_p is its spatial period. A simulation was carried out for different input distance considering the reflected beam resulting from the incidence of a 2.4 μm waist radius Gaussian beam at a wavelength of 675 nm on a cylindrical micro mirror with a radius of curvature of 500 μm and with incidence angle of 45 degrees. The waviness amplitude and spatial period were assumed 35 nm and 20 μm, respectively. The results are shown in Fig. 6.36 where the effect of increasing beam distortion with the input distance is clearly captured. The exact beam profile is, of course, dependent on the actual surface topology of the micromachined cylindrical micromirrors.

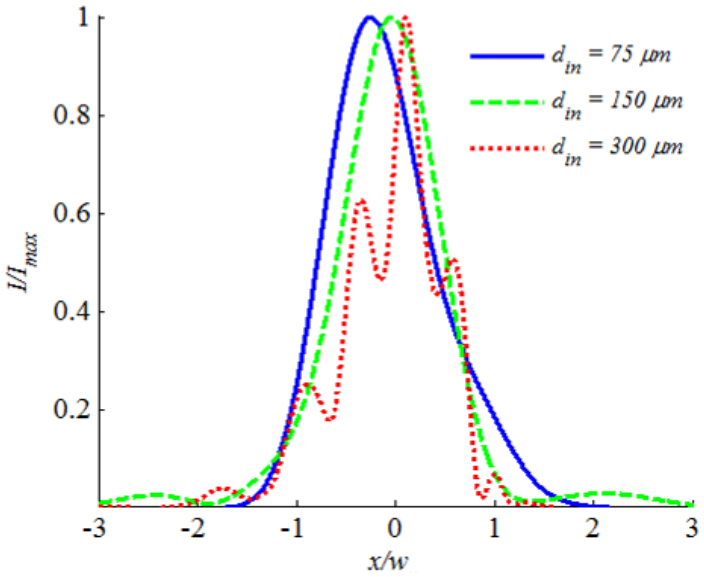

Fig. 6.36. Reflected beam from the incidence of a 2.4 μm waist radius Gaussian beam at a wavelength of 675 nm on a cylindrical micro mirror with a radius of curvature of 500 μm and with incidence angle of 45 degrees. The mirror profile waviness amplitude and spatial period are 35 nm and 20 μm, respectively.

6.6 Summary

GB reflection on curved micromirrors was thoroughly studied in this chapter. In Gaussian-optical treatment of optical systems, an incident GB is assumed to remain Gaussian after reflection or refraction from the optical element. For off-axis configuration, Gaussian-optical approach is based on the assumptions that the beam diameter is small relative to the beam phase radius of curvature and the radius of curvature of the off-axis optical elements. This assumption fails for micro reflectors where the incident beam diameter can be comparable to the reflector dimensions. The

scattering-matrix technique, used in the literature for the millimeter wavelength range, was reviewed in this chapter. It was applied on curved micro reflector in the near-infrared regime. The results were not satisfactory due to the larger number of modes needed in the simulation.

A simulation study for GB reflection from micro curved mirrors was carried out for both cases of normal and inclined incidence. The study has been carried out using the GRASP9 simulator, which is based on the physical-optics approach. In this study the wavelength was 1550 nm and a broad range of micromirror radius of curvature was considered from 10 μm and up to 1000 μm. For normal incidence, the simulated setups were the setup for coupling back the power on the source and the setup for focusing incoming collimated beam. The Gaussian-optical approach accuracy was found to be better than 98% when $w_m=0.5R$ while around 90% when $w_m=R$ where w_m is the GB waist radius at the mirror. The accuracy is measured by fitting the results of GRASP9 on Gaussian profiles and comparing the divergence angle of the fitting and the Gaussian-optical results. The error was positive in the focusing case ($\theta_{fit}/\theta_{Gaussian}>1$) and negative in the coupling case ($\theta_{fit}/\theta_{Gaussian}<1$).

For the inclined incidence case, the GB was found to undergo distortion and transformation that are not well predicted by the Gaussian-optical analysis in some cases, while other cases were found to be in a good enough match. For 45-degree incidence angle, the resulting beam was found to be close to Gaussian-optical analysis results in both the tangential and sagittal planes when the input beam waist is $w_0 = 5$ μm . For $w_0 =$ 1.5 μm, the tangential beam was completely distorted and the sagittal beam was found to

be still Gaussian but far from the Gaussian-optical. Keeping the ratio between the beam spot radius at the mirror and the mirror radius smaller than 10% ($w_m<0.1R$), the beam distortion was found a small peak shift and a little bit of beam widening (observed on log scale). The effect is more pronounced when the incidence angle is increased or the mirror radius of curvature is increased. The peak shift direction was found dependent on the input distance while being minimal when the beam is at its Rayleigh range (i.e. min phase radius of curvature). Cross polarization effect was found be always small (less than 20 dB or even smaller) and more pronounced when the incidence angle or the input distance is increased.

A simple model was developed based on the treating the curved mirror as a phase transformer in which the phase transformation is composed of two components; one is calculated from the input beam side and the second component is calculated from the output beam side. In addition, the model accounts for unsymmetrical truncation of the beam on the mirror surface. The propagation of the beam after reflection is carried out using Fourier-optics technique. The model was compared to the physical-optics results and excellent agreement was found.

Finally, an experimental study was carried using cylindrical micromirrors fabricated by deep reactive ion etching technology. The experimental results are not well-predicted by the physical-optics simulations, especially for relatively large distance between the incident beam waist and the mirror surface. We have attributed this discrepancy to the non-ideal measured surfaces that suffer from micromachining roughness and waviness. It was confirmed by a simple model based on sinusoidal phase

grating that waviness with a small amplitude of a few tens of nanometer is enough to couple optical power from the fundamental Gaussian mode to the higher order HG modes and, thus distorts the reflected beam profile.

CHAPTER 7
CONCLUDING REMARKS

7.1 Conclusions

In this PhD thesis the technology of micro-optical benches has been advanced, an integrated microscanner on a silicon chip has been demonstrated and the reflection of GB on micro reflectors has been thoroughly studied.

A deep etch fabrication process has been developed for realizing high optical throughput micro-optical benches. Micromirrors with verticality better than 0.1 degree and scalloping depth less than 75 nm have been demonstrated over a 300 μm etching depth, about 4*x* deeper than reported literature. A Miniaturized Michelson interferometer with a 200 μm depth has been demonstrated offering more than 12 dB improvement in the detected optical signal relative to a 90 μm depth. This improvement has brought this important miniaturized engine to the practical life.

A technological method has been presented for batch fabrication of three-dimensional curved microstructures with in-plane principal axis, which are compatible with micro-optical bench and lab-on-chip technologies. The method is based on multi-step etching and protection technique, in which all the steps are performed in an inductively-plasma reactors reactor without process interruption. Concave as well as convex microstructures with out-of-plane radius of curvature in the submillimeter range have been demonstrated. Fabricated spherical micromirror has been used in

demonstrating efficient wideband lens-less coupling of free-space light propagating in-plane with respect to the substrate. The fabricated micromirror has offered about 10*x* improvements in the quality factor of a micro-optical cavity and more than 10-dB reduction in the free-space propagation power loss.

Ultra-wide steering-angle integrated microscanner has been realized using the developed technology. The scanning has been achieved by displacing the principle axis of a curved silicon micromirror of acylindrical shape, with respect to the incident beam optical axis. We have demonstrated optical deflection angles up to 110 degrees using a one-degree-of-freedom MEMS system. Larger deflection angles, up to 160-180 degrees, are also predicated theoretically when two-degree-of-freedom MEMS system is used.

Detailed analytical study of free-space GB coupling using flat, cylindrical and spherical micromirrors has been performed. The study has focused on the regime where the confocal parameter of the GB is comparable to the micromirror radius of curvature. Non-deal effects, such as limited micromirror size, astigmatic spherical micromirror radii of curvature and optical axis misalignment have been taken into account.

A numerical study of GB distortion upon reflection on micro-curved surface has been carried out in the near-infrared spectral regime. The study has explored different methods based on physical-optics, scattering matrix and the developed methods based on phase transformation and Fourier-optics. The validity of the Gaussian-optical approach has been examined and its inadequacy has been highlighted in some cases. The study has been complemented using experimental data in the near-infrared spectral regime in addition to the visible regime using deeply etched micromirrors. A discrepancy has been

observed between the results of simulation and experimentation that has been attributed to the roughness/waviness of the fabricated micromirrors.

7.2 Recommendations

Based on the developed method in this thesis for batch-fabrication of 3-D curved microstructure having in-plane principal axis, a monolithic batch-fabricated 3-D micro optical bench system can be produced. The optical bench can have real 3-D elements like spherical mirrors\lenses that control light diffraction in both the in-plane and the out-of-plane directions, with respect to the wafer substrate. The flat surfaces and the curved surfaces are created in two successive cycles, monolithically on an SOI wafer. Flat surfaces can be optical, mechanical and/or electrical. This allows the optical elements to be actuated by MEMS actuator. The monolithic integration of movable 3-D curved elements in microsystems introduces a significant performance boost in a tremendous number of applications where free space propagation losses and coupling losses are significant. Among these applications interferometers, spectrometers, tunable optical cavities, optical switches, variable optical beam shapers, optical micro scanners, variable optical attenuators, tunable lasers and other applications in sensing and telecommunications domains.

Based on the integrated wide-angle microscanner developed in this thesis, many integrated miniaturized optical engines can built. The microscanner is a basic building block in various imaging systems including OCT, confocal microscopes and spectral imagers [165-166]. The integrability of the scanner is a major advantage, by which

combining the scanner with micro-optical components can produce miniaturized system on chip. In addition to the imaging domain, the scanner can be used to produce 1 x N beam-steering based optical fiber switches for reconfigurable optical networks. The switch is expected to have excellent insertion loss uniformity and, therefore can be arranged to produce N x N switch.

The study of GB reflection on curved micromirrors needs to be complemented by accounting for micromachining non-idealities such as surface roughness and waviness. These parameters have to be well controlled and characterized. These roughness and waviness are not affecting only the reflectivity of the micromirror but also affecting the wavefront of the reflected beam. The polarization of the GB has to be controlled while carrying the optical experiments. This control will removes any ambiguity about cross-polarization effects that may occur and affect the overall profile of the reflected beam.

AUTHOR'S PUBLICATIONS

Pending patents

1. Y. M. Sabry, T. E. Bourouina, B. A. Saadany, and D. A. M. Khalil, "Integrated monolithic optical bench containing 3-D curved optical elements and methods of its fabrication," U.S. patent application 20130100424, 2013.
2. Y. M. Sabry, D. A. M. Khalil, B. A. Saadany, and T. E. Bourouina, "Aspherical optical surfaces and optical scanners," U.S. patent application 61676336, 2012.

Journal papers

3. Y. M. Sabry, B. Saadany, D. Khalil, and T. Bourouina, "Silicon micromirrors with three-dimensional curvature enabling lens-less efficient coupling of free-space light," Light Sci. Appl. **2**, e94, Nature Publishing Group, 2013.
4. Y. M. Sabry, D. Khalil, B. Saadany and T. Bourouina, "Integrated wide-angle scanner based on translating a curved mirror of acylindrical shape," Opt. Express **21**, 13906-13916, Optical Society of America, 2013.
5. Y. M. Sabry, D. Khalil, B. Saadany and T. Bourouina, "Multi-step etching of three-dimensional sub-millimetre curved silicon microstructures with in-plane principal axis," Microelectron. Eng. **114**, 78-84 (2014).
6. Y. M. Sabry, D. Khalil, B. Saadany and T. Bourouina, "In-plane external fiber Fabry–Perot cavity comprising silicon micromachined concave mirror," J. Micro-Nanolith. MEM., **13**, 011110, International society for optics and photonics (SPIE), 2014.

7. Y. Sabry, M. Medhat, B. Saadany, T. Bourouina, and D. Khalil, "Parameter extraction of MEMS comb-drive near-resonance equivalent circuit: physically-based technique for a unique solution," J. Micro-Nanolith. MEM. **11**, 021205-1, International society for optics and photonics (SPIE), 2012.

Conference contributions

8. Y. M. Sabry, D. Khalil, B. Saadany, and T. Bourouina, "Wide steering angle microscanner based on curved surface," in Proceedings of SPIE Photonics West, pp. 86160F, 2013. **(Best student paper award)**
9. Y. M. Sabry, D. Khalil, B. Saadany, and T. Bourouina, "Inclination-independent transformation of light beams using high-throughput uniquely-curved micromirrors," accepted in IEEE MEMS 2014.
10. Y. M. Sabry, T. Bourouina, B. Saadany and D. Khalil, "In-plane diffraction loss free optical cavity using coated optical fiber and silicon micromachined spherical mirror," in Proceedings of SPIE Photonics West, pp. 86160P, 2013.
11. D. Khalil, Y. Sabry, H. Omran, M. Medhat, A. Hafez and B. Saadany, "Characterization of MEMS FTIR spectrometer," in Proceedings of SPIE Photonics West, pp. 79300J, 2011.
12. Y. M. Sabry, D. Khalil, B. Saadany, and T. Bourouina, "Three-dimensional collimation of in-plane-propagating light using silicon micromachined mirror" accepted in SPIE Photonics West 2014.

BIBLIOGRAPHY

1. H. V. Jansen, M. J. De Boer, S. Unnikrishnan, M. C. Louwerse and M. C. Elwenspoek, "Black silicon method X: a review on high speed and selective plasma etching of silicon with profile control: an in-depth comparison between Bosch and cryostat DRIE processes as a roadmap to next generation equipment," J. Micromech. Microeng. **19**, 033001, 2009.
2. C. Marxer, C. Thio, M. A. Gretillat, N. F. de Rooij, R. Battig, O. Anthamatten,... and P. Vogel, "Vertical mirrors fabricated by deep reactive ion etching for fiber-optic switching applications," J. Microelectromech. Syst. **6**, 277,1997.
3. C. Marxer and N. F. de Rooij, "Micro-opto-mechanical 2× 2 switch for single-mode fibers based on plasma-etched silicon mirror and electrostatic actuation," J. Lightw. Technol. **17**, 2-6. 1999.
4. C. Marxer, P. Griss and N. F. de Rooij, "A variable optical attenuator based on silicon micromechanics," IEEE Photon. Technol. Lett. **11**, 233, 1999.
5. A. Bashir, P. Katila, N. Ogier, B. Saadany and D. A. Khalil, "A MEMS-based VOA with very low PDL," IEEE Photon. Technol. Lett. **16**, 1047, 2004.
6. B. Saadany, F. Marty, Y. Mita, D. Khalil and T. Bourouinam "A MEMS tunable optical filter based on vertical DBR architecture" In Symposium on Design, Test, Integration and Packaging of MEMS/MOEMS, pp.317-321, 2004.
7. B. Saadany, M. Malak, M. Kubota, F. Marty, Y. Mita, D. Khalil and T. Bourouina, "Free-space tunable and drop optical filters using vertical Bragg mirrors on silicon," IEEE J. Sel. Top. Quant. Electron. **12**,1480-1488, 2006.
8. J. Masson, R. St-Gelais, A. Poulin and Y. A. Peter, "Tunable fiber laser using a MEMS-based in plane Fabry-Pérot filter," IEEE J. Quantum Electron. **46**, 1313, 2010.
9. M. Medhat, B. Saadany, D. Khalil and B. Mortada, "Opto-Mechanical Optical Path Retardation Multiplier for Optical MEMS Applications," U.S. patent application No. 12/762,068, 2010.
10. O. Manzardo, R. Michaely, F. Schädelin, W. Noell, T. Overstolz, N. De Rooij and H. P. Herzig, "Miniature lamellar grating interferometer based on silicon technology," Opt. Lett. **29**, pp. 1437, 2004.
11. D. Khalil, H. Omran, M. Medhat and B. Saadany, "Miniaturized tunable integrated Mach-Zehnder MEMS interferometer for spectrometer applications" In SPIE MOEMS-MEMS, 75940T, 2010.

12. H. Omran, M. Medhat, B. Mortada, B. Saadany and D. Khalil, "Fully Integrated Mach-Zhender MEMS Interferometer With Two Complementary Outputs" IEEE J. Quantum Electron. **48**, 244-251, 2012

13. B. Saadany, H. Omran, M. Medhat, F. Marty, D. Khalil and T. Bourouina, "MEMS tunable Michelson interferometer with robust beam splitting architecture," In IEEE/LEOS International Conference on Optical MEMS and Nanophotonics pp. 49-50, 2009.

14. Y. Sabry, M. Medhat, B. Saadany, A. Safwat and D. Khalil, "Optical characterization technique for MEMS comb-drive resonators," In IEEE/LEOS International Conference on Optical MEMS and Nanophotonics, pp. 127-128, 2009.

15. M. Malak, F. Marty, N. Pavy, Y. A. Peter, A. Q. Liu and T. Bourouina, "Cylindrical Surfaces Enable Wavelength-Selective Extinction and Sub-0.2 nm Linewidth in 250 μm-Gap Silicon Fabry-Perot Cavities," J. Microelectromech. Syst. **21**, 171-180, 2012.

16. R. R. Syms and A. Lohmann, "MOEMS tuning element for a Littrow external cavity laser," J. Microelectromech. Syst. **12**, pp. 921, 2003.

17. A. Q. Liu, A. Q and X. M. Zhang, "A review of MEMS external-cavity tunable lasers", J. Micromech. Microeng. **17**, R1, 2007.

18. O. Manzardo, H. P. Herzig, C. Marxer and N. F. Rooij," Miniaturized time-scanning Fourier transform spectrometer based on silicon technology", In SPIE symposium on Micromachining and Microfabrication, pp. 39-47, 1999.

19. O. Manzardo, Y. Petremand, H. P. Herzig, W. Noell, N. De Rooij, S. Kittaka, ... and E. T. Rodriguez, "Micro-sized Fourier spectrometer" Diffractive optics and micro-optics **75**, 134, 2002.

20. O. Manzardo, H. P. Herzig, C. R. Marxer, and N. F. de Rooij, "Miniaturized time-scanning Fourier transform spectrometer based on silicon technology," Opt. Lett. **24**, 1705–1707, 1999.

21. K. Yu, D. Lee, U. Krishnamoorthy, N. Park, and O. Solgaard, "Micromachined Fourier transform spectrometer on silicon optical bench platform," Sensor. Actuat. A-Phys. **130-131**, 523–530, 2006.

22. D. Khalil, Y. Sabry, H. Omran, M. Medhat, A. Hafez and B. Saadany, "Characterization of MEMS FTIR spectrometer," In SPIE MOEMS-MEMS, pp. 79300J-79300J, 2011.

23. M. C. Wu, L. Y. Lin, S.S. Lee and K. S. J. Pister, "Micromachined free-space integrated micro-optics," Sensor. Actuat. A-Phys. **50**, 127-134, 1995.

24. R. R. Syms, "Surface tension powered self-assembly of 3-D micro-optomechanical structures," J. Microelectromech. Syst. **8**, 448-455, 1999.

25. S. Bargiel, K. Rabenorosoa, C. Clevy, C. Gorecki and P. Lutz, "Towards micro-assembly of hybrid MOEMS components on a reconfigurable silicon free-space micro-optical bench" J. Micromech. Microeng. **20**, 045012, 2010.

26. K. S. Chen, A. A. Ayón, X. Zhang and S. M. Spearing, "Effect of process parameters on the surface morphology and mechanical performance of silicon structures after deep reactive ion etching (DRIE), "J. Microelectromech. Syst. **11**, 264-275, 2002.

27. H. C. Liu, Y. H. Lin and W. Hsu, "Sidewall roughness control in advanced silicon etch process," Microsyst. technologies **10**, 29-34, 2003.

28. W. H. Juan and S. W. Panga, "Controlling sidewall smoothness for micromachined Si mirrors and lenses," Vac. Soc. J. Vacuum Science Technol. B **14**, 4080–4084, 1996.

29. M.M. Lee and M. Wu, "Thermal annealing in Hydrogen for 3D profile transformation on silicon on insulator and sidewall roughness reduction", J. Microelectromech. Syst. **15,** 338-343, 2006.

30. A. A. Avon, R. L. Bayt and K. S. Breuer, "Deep reactive ion etching: a promissing technology for micro and nanosatellites" Smart Mater. Struct. **10,** 1135-1144, 2001.

31. D. Nilsson, S. Jensen and A. Menon, "Fabrication of silicon mold for polymer optics," J. Micromech. Microeng. **13**, S57, 2003.

32. A. Lipson and E. M. Yeatman, "A 1-D photonic band gap tunable optical filter in (110) silicon" J. Microelectromech. Syst. **16**, 521-527, 2007.

33. D. Lee, K. Yu, U. Krishnamoorthy and O. Solgaard, "Vertical mirror fabrication combining KOH etch and DRIE of (110) silicon," J. Microelectromech. Syst. **18**, 217-227, 2009.

34. R. Agarwal, S. Samson and S. Bhansali, "Fabrication of vertical mirrors using plasma etch and KOH: IPA polishing," J. Micromech. Microeng. **17**, 26, 2007

35. X. M. Zhang, A. Q. Liu, D. Y. Tang and C. Lu, "Discrete wavelength tunable laser using microelectromechanical systems technology," Appl. Phys. Lett. **84**, 329-331, 2004.

36. Y. Uenishi, K. Honma and S. Nagaoka, "Tunable laser diode using a nickel micromachined external mirror," IEEE Electron. Lett. **32**, 1207-1208, 1996.

37. E. Geerlings, M. Rattunde, J. Schmitz , G. Kaufel, J. Wagner , B. Bläsi B, D. Jallweit and H. Zappe, "Widely tunable micro-mechanical external-cavity diode laser emitting around 2.1 μm," IEEE J. Quantum. Electron. **44**, 1071-1075, 2008.

38. S. S. Lee, L. Y. Lin, M. C. Wu, "Surface-micromachined free-space micro-optical systems containing three-dimensional micrograting," App. Phys. Lett. **67**, 2135-2137, 1995.

39. L. Y. Lin, J. L. Shen, S. S. Lee and M. C. Wu, "Surface-micromachined micro-xyz stages for free-space micro-optical bench," IEEE Photonic. Tech. Lett. **9**, 345-347, 1997.

40. D. C. Flanders, P. S. Whitney, M. Masghati and L. M. Racz, "Mounting and alignment structures for optical components," US patent No. 6,625,372, 2003.

41. K. Do, J. E. Sell, R. Kono, D. S. Jones, R. de la Torro and W. J. Kozlovsky, "Micro optical bench for mounting precision alighned optics, optical assembly and method of mounting optics," US patent No. 6,775,076, 2005.

42. M. Hu, H. Du, S. Ling, B. Liu and G. Lau, "Fabrication of a rotary micromirror for fiber-optic switching,". Microsys. technologies **11**, 987-990, 2005.

43. M. T. K. Hou, L. Y. Huang, S. S. Jiang and J. A. Yeh, "In-plane rotary comb-drive actuator for a variable optical attenuator," J. Micro-Nanolith. MEM. **7**, 043015-043015, 2008.

44. C. P. B. Siu, H. Zeng, and M. Chiao, "Magnetically actuated MEMS microlens scanner for in vivo medical imaging," Opt. Express **15**, 11154-11166, 2007.

45. H. C. Park, C. Song, and K. H. Jeong, "Micromachined lens microstages for two-dimensional forward optical scanning," Opt. Express **18**, 16133-16138, 2010.

46. J. B. Chou, Y. Kyoungsik and M. C. Wu, "Electrothermally Actuated Lens Scanner and Latching Brake for Free-Space Board-to-Board Optical Interconnects," J. Microelectromech. Syst. **21**, 1107-1116, 2012.

47. J. M. Zara, S. Yazdanfar, K. D. Rao, J. A. Izatt and S. W. Smith, "Electrostatic micromachine scanning mirror for optical coherence tomography," Opt. Lett. **28**, 628-630, 2003.

48. P. H. Tran, D. S. Mukai, M. Brenner and Z. Chen, "In vivo endoscopic optical coherence tomography by use of a rotational microelectromechanical system probe," Opt. Lett. **29**, 1236-1238, 2004.

49. X. Mu, G. Zhou, H. Yu, Y. Du, H. Feng, J. M. L. Tsai and F. S. Chau, "Compact MEMS-driven pyramidal polygon reflector for circumferential scanned endoscopic imaging probe," Opt. Express **20**, 6325-6339, 2012.

50. T. Iseki, M. Okumura and T. Sugawara, "High Speed and Wide Angle Deflection Optical MEMS Scanner Using Piezoelectric Actuation," IEEJ T. Electr. Electr. **5**, 361-368, 2010.

51. J. Sun, S. Guo, L. Wu, L. Liu, S-W. Choe, B.S. Sorg, and H. Xie, "3D In Vivo optical coherence tomography based on a low-voltage, large-scan-range 2D MEMS mirror," Opt. Express **18**, 12065-12075, 2010.

52. A .D. Yalcinkaya, O. Ergeneman and H. Urey, "Polymer magnetic scanners for bar code applications," Sensor. Actuat. A-Phys. **135**, 236-243, 2007.

53. F. Marty, L. Rousseau, B. Saadany, B. Mercier, O. Français, Y. Mita and T. Bourouina, "Advanced etching of silicon based on deep reactive ion etching for silicon high aspect ratio microstructures and three-dimensional micro-and nanostructures", Microelectr. J. **36**, 673, 2005.

54. C. Chang, Y. F. Wang, Y. Kanamori, J. J. Shih, Y. Kawai, C. K. Lee, K. C. Wu and M. Esashi, "Etching submicrometer trenches by using the Bosch process and its

application to the fabrication of antireflection structures", J. Micromech. Microeng. **15**, pp. 580, 2005.

55. R. Abdolvand and F. Ayazi, "An advanced reactive ion etching process for very high aspect-ratio sub-micron wide trenches in silicon", Sensor Actuat. A-Phys. **144**, pp. 109, 2008
56. A. Summanwar, "Deep Silicon Etching Using High Density Plasma", PhD thesis Paris-Est Universite, 2009.
57. P. Griffiths and J. A. De Haseth, Fourier transform infrared spectrometry, Wiley-Interscience, 2007.
58. M. J. Madou, Fundamentals of microfabrication: the science of miniaturization, CRC PressI Llc, 2002.
59. A. W. Snyder and J. Love, Optical waveguide theory, Springer, 1983.
60. D. A. Khalil, B. Mortada, M. Nabil, M. Medhat and B. A. Saadany, "Compensated MEMS FTIR Spectrometer Architecture," U.S. patent application No. 12/877,888, 2010
61. C. M. Waits, B. Morgan, M. Kastantin and R. Ghodssi, "Microfabrication of 3D silicon MEMS structures using gray-scale lithography and deep reactive ion etching," Sensor Actuat. A-Phys. **119**, pp. 245, 2005.
62. Z. Yaqoob and N. A. Riza, "Free-Space Wavelength-Multiplexed Optical Scanner Demonstration," Appl. Opt. **41**, 5568-5573, 2002.
63. S. A. Boppart, T. F. Deutsch and D. W. Rattner. "Optical imaging technology in minimally invasive surgery," Surg. Endos. **13**, 718-722, 1999.
64. T. Matsuda, F. Abe, and H. Takahashi, "Laser printer scanning system with a parabolic mirror," Appl. Opt. **17**, 878-884, 1978.
65. G. Zacharakis, J. Ripoll, R. Weissleder and V. Ntziachristos, "Fluorescent protein tomography scanner for small animal imaging", IEEE Trans. on Med. Imaging **24**, 878-885, 2005.
66. M. H. Kiang, O. Solgaard, R. S. Muller and K.Y. Lau, "Surface-micromachined electrostatic-comb driven scanning micromirrors for barcode scanners," in Proceedings of the ninth annual international workshop on Micro Electro Mechanical Systems, pp. 192-197m 1996.
67. W. O. Davis, R. Sprague and J. Miller, "MEMS-based pico projector display," in Proceedings of IEEE/LEOS international conference on Optical MEMs and Nanophotonics, pp. 31-32, 2008.
68. H. Ra, W. Piyawattanametha, Y. Taguchi, D. Lee, M.J. Mandella and O. Solgaard, "Two-dimensional MEMS scanner for dual-axes confocal microscopy," IEEE/ASME J. Microelectromech. Syst. **16**, 969-976, 2007.

69. C. L. Arrasmith, D. L. Dickensheets and A. Mahadevan-Jansen, "MEMS-based handheld confocal microscope for in-vivo skin imaging," Opt. Express **18**, 3805-3819, 2010.

70. S. D. Senturia, Microsystem Design, Kluwer Academic Publishers, 2001.

71. O. Solgaard, Photonic microsystems: Micro and nanotechnology applied to optical devices and systems, Springer, 2008.

72. Y. Wang, K. Kumar, L. Wang and X. Zhang, "Monolithic integration of binary-phase Fresnel zone plate objectives on 2-axis scanning micromirrors for compact microscopes," Opt. Express **20**, 6657-6668, 2012.

73. D. A. Khalil and H. Haddara, "Ultra-wide angle MEMS scanner architecture," U.S. patent No. 8411340 B2, 2013.

74. Y. Sabry, D. Khalil, B. Saadany, and T. Bourouina, "Wide steering angle microscanner based on curved surface" In SPIE MOEMS-MEMS, pp. 86160F-86160F, 2013.

75. Y. Sabry, D. Khalil, B. Saadany, and T. Bourouina, "Aspherical optical surfaces and optical scanners," U.S. patent application No. 20130100424, 2013.

76. Y. M. Sabry, B. Saadany, D. Khalil and T. Bourounia, "Integrated wide angle optical microscanner" Optic. Express, 21, 13906-13916 (2013).

77. Y. M. Sabry, D. Khalil, B. Saadany, and T. Bourouina, "Inclination-independent transformation of light beams using high-throughput uniquely-curved micromirrors", The 27th IEEE International Conference on Micro Electro Mechanical Systems, January 2014.

78. Y. Nada, M. Medhat, M. Nagi, F. Marty, B. Saadany and T. Bourouina, "Mechanical displacement multiplier: 250 μm stable travel range MEMS actuator using frictionless simple compliant structures" in Proceedings of IEEE Conference on Micro Electro Mechanical Systems, pp. 1161-1164, 2012.

79. M. Medhat, Y. Nada, B. Mortada and B. Saadany, "Long Range Travel MEMS Actuator," U.S. patent application No. 12761621, 2010.

80. R. Legtenberg, A.W. Groeneveld and M. Elwenspoek, "Comb-drive actuators for large displacements," J. Micromech. Microeng. **6**, 320, 1999.

81. Y. Sabry, M. Medhat, B. Saadany, T. Bourouina and D. Khalil, "Parameter extraction of MEMS comb-drive near-resonance equivalent circuit: physically-based technique for a unique solution," J. Micro-Nanolith. MEM. **11**, 021205-1, 2012.

82. A.E. Siegman, Lasers University Science Books, Mill Valley, 1986.

83. P. Goldsmith, Quasioptical systems: Gaussian beam quasi-optical propagation and applications, Wiley-IEEE Press, 1997.

84. Y. Sabry, T. Bourouina, B. Saadany D. Khalil, "Integrated monolithic optical bench containing 3-D curved optical elements and methods of its fabrication," U.S. patent application No. 1261078, 2011.

85. ISO Standard 11146, "Lasers and laser-related equipment – Test methods for laser beam widths, divergence angles and beam propagation ratios", 2005.

86. M. E. Motamedi, W. H. Southwell, R. J. Anderson, L. G. Hale, W. J. Gunning III and M. Holz, "High-speed binary optic microlens array in GaAs," In SPIE San Diego, pp. 33-44, 1991.

87. S. Zissi, A. Bertsch, J. Y. Jézéquel, S. Corbel, D. J. Lougnot and J. C. Andre, "Stereolithography and microtechniques,". Microsystem. technologies **2**, 97-102, 1995.

88. T. J. Suleski and D. C. O'Shea, "Gray-scale masks for diffractive-optics fabrication: I. Commercial slide imagers," Appl. Opt. **34**, 7507-7517, 1995.

89. W. Däschner, P. Longm R. Stein, C. Wu and S. H. Lee, "Cost-effective mass fabrication of multilevel diffractive optical elements by use of a single optical exposure with a gray-scale mask on high-energy beam-sensitive glass,"Appl. Opt. **36**, 4675-4680, 1997.

90. T. Bourouina, T. Masuzawa and H. Fujita, "The MEMSNAS process: microloading effect for micromachining 3-D structures of nearly all shapes," J. Microelectromech. Syst. **13,** 190-199, 2004.

91. T. K. Chou and K. Najafi, "Fabrication of out-of-plane curved surfaces in Si by utilizing RIE lag," In Micro Electro Mechanical Systems, pp. 145-148, 2002.

92. C. S. Lee and C. H. Han, "A novel refractive silicon microlens array using bulk micromachining technology," Sensor Actuat. A-Phys. **88**, 87-90, 2001.

93. H. O. Sankur, R. L. Hall, M. E. Motamedi, W. J. Gunning III and W. E. Tennant, "Fabrication of microlens arrays by reactive ion milling," In SPIE Miniaturized Systems with Micro-Optics and Micromechanics **2687**, pp. 150, 1996.

94. M. Eisner and J. Schwider, "Transferring resist microlenses into silicon by reactive ion etching," Opt. Eng. **35**, 2979-2982, 1996.

95. T. Y. Wang, "Graded thickness optical element and method of manufacture therefor," U.S. Patent No. 6,606,199. 12, 2003.

96. T. M. Bloomstein and D. J. Ehrlich, "Laser-chemical three-dimensonal writing of multimaterial structures for microelectromechanics," In Micro Electro Mechanical Systems, pp. 202-203, 1991.

97. J. D. Madden and I. W. Hunter, "Three-dimensional microfabrication by localized electrochemical deposition," J. Microelectromech. Syst. **5**, 24-32, 1996.

98. J. Gobet, F. Cardot, J. Bergqvist and F. Rudolf, "Electrodeposition of 3D microstructures on silicon," J. Micromech. Microeng. **3**, 123, 1993

99. Z. Y. Yu, T. Masuzawa and M. Fujino, "Micro-EDM for three-dimensional cavities-development of uniform wear method," CIRP Ann. Manuf. Technol. **47**, 169-172, 1998.

100. P. H. S. Heeren, D. Reynaerts, H. Van Brussel, C. Beuret, O. Larsson and A. Bertholds, "Microstructing of silicon by electro-discharge machining (EDM)—part II: applications," Sensor Actuat. A-Phys. **61**, 379-386, 1997.

101. X. Q. Sun, T. Masuzawa and M. Fujino, "Micro ultrasonic machining and its applications in MEMS," Sensor Actuat. A-Phys. **57**, 159-164, 1996.

102. M. T. Gale, M. Rossi, J. Pedersen and H. Schuetz, "Fabrication of continuous-relief micro-optical elements by direct laser writing in photoresists," Opt. Eng. **33**, 3556-3566, 1994.

103. E. B. Kley, B. Schnabel and U. D. Zeitner, "E-beam lithography: an efficient tool for the fabrication of diffractive and micro-optical elements." In SPIE Photonics West'97, pp. 222-232, 1997.

104. H. K. Leung, "Multiple step trench etching process," U.S. Patent No. 4,729,815. 8, 1988.

105. H. S. Liu, J. Y. Lee, J. K. Wang, C. S. Yoo and P. J. Wang, "Tapered opening sidewall with multi-step etching process," U.S. Patent No. 5,180,689. 19, 1993.

106. K. A. Shaw, Z. L. Zhang and N. C. MacDonald, "SCREAM I: a single mask, single-crystal silicon, reactive ion etching process for microelectromechanical structures," Sensor Actuat. A-Phys. A **40**, 63-70, 1994.

107. M. J. de Boer, R. W. Tjerkstra, J. W. Berenschot, H. V. Jansen, G. J. Burger, J. G. E. Gardeniers, M. Elwenspoek and A. van den Berg, "Micromachining of buried micro channels in silicon," J. Microelectromech. Syst. **9,** 94-103, 2000.

108. H. L. Gardeniers, R. Luttge, E. J. Berenschot, M. J. De Boer, S. Y. Yeshurun, M. Hefetz, R. Van't Oever and A. van den Berg, "Silicon micromachined hollow microneedles for transdermal liquid transport," J. Microelectromech. Syst. **12**, 855-862 ,2003.

109. R. Gómez-Martínez, A. Sánchez, M. Duch, J. Esteve and J.A. Plaza, "DRIE based technology for 3D silicon barcodes fabrication," Sensor Actuat. B-Chem. **154,** 181-184, 2011.

110. Y. M. Sabry, B. Saadany, D. Khalil, and T. Bourouina, "Silicon micromirrors with three-dimensional curvature enabling lens-less efficient coupling of free-space light," Light Sci. Appl. 2, e94, 2013.

111. Y. M. Sabry, D. Khalil, B. Saadany and T. Bourouina, "Multi-step etching of three-dimensional sub-millimetre curved silicon microstructures with in-plane principal axis," Microelectron. Eng. 114, 78-84 (2014).

112. S. L. Lai, D. Johnson and R. Westerman, "Aspect ratio dependent etching lag reduction in deep silicon etch processes," J. Vac. Sci. Technol., A **24**, 1283-1288, 2006.

113. X. Zhu, D. W. Greve and G. K. Fedder, "Characterization of silicon isotropic etch by inductively coupled plasma etch in post-CMOS processing," In IEEE Micro Electro Mechanical Systems, pp. 568-573, 2000.

114. K. P. Larsen, D. H. Petersen and O. Hansen, "Study of the roughness in a photoresist masked, isotropic, SF6-based ICP silicon etch," J. Electrochem. Soc. **153,** G1051-G1058, 2006

115. D. M. Gaugel, CMOS-Compatible Fluidic Chip Cooling Using Buried Channel Technology, Doctoral dissertation, Carnegie Mellon University, 2001.

116. Z. Moktadir, E. Koukharenka, M. Kraft, D. M. Bagnall, H. Powell, M. Jones and E. A. Hinds, "Etching techniques for realizing optical micro-cavity atom traps on silicon," J. Micromech. Microeng. **14**, S82, 2004

117. J. Bartl and M. Baranek, "Emissivity of aluminium and its importance for radiometric measurement. Measurement of Physical Quantities," **43**, 3136, 2004

118. P. Bienstman, S. Assefa, S. G. Johnson, J. D. Joannopoulos, G. S. Petrich and L. A. Kolodziejski, "Taper structures for coupling into photonic crystal slab waveguides," JOSA B **20**, 1817-1821, 2003.

119. G. Roelkens, D. Vermeulen, F. V. Laere, S. Selvaraja, S. Scheerlinck, D. Taillaert, W. Bogaerts, P. Dumon, D. Van Thourhout, and R. Baets, "Bridging the gap between nanophotonic waveguide circuits and single mode optical fibers using diffractive grating structures," Journal of Nanoscience and Nanotechnology **10,** 1551-1562, 2010.

120. N. Meinzer, M. Konig, M. Ruther, S. Linden, G. Khitrova, H. M. Gibbs, K. Busch and M. Wegner, "Distance-dependence of the coupling between split-ring resonators and single-quantum-well gain," App. Phys. Lett. **99**, 111104, 2011.

121. M. Zickar, W. Noell, C. Marxer and N. de Rooij, "MEMS compatible micro-GRIN lenses for fiber to chip coupling of light," Opt. Express **14**, 4237-4249, 2006.

122. H. M. Presby, A. F. Benner and C. A. Edwards, "Laser Micromachining Of Efficient Fiber Microlenses," Appl. Opt. **29**, 2692-2695, 1990.

123. C. A. Edwards, H. M. Presby and C. Dragone, "Ideal microlenses for laser to fiber coupling," IEEE J. Lightw. Technol. **11**, 252-257, 1993.

124. M. Thual, P. Chanclou, O. Gautreau, L. Caledec, C. Guignard and P. Besnard, "Appropriate micro-lens to improve coupling between laser diodes and singlemode fibres," Electron. Lett. **39**, 1504-1506, 2003.

125. L. Liu, M. Pu, K. Yvind and J. M. Hvam, "High-efficiency, large-bandwidth silicon-on-insulator grating coupler based on a fully-etched photonic crystal structure," App. Phys. Lett. **96**, 051126-051128, 2010.

126. Q. Wang , T. H. Loh, K. T. Ng and S. T. Ho, "Design and analysis of optical coupling between silicon nanophotonics waveguide and standard single-mode fiber

using an integrated asymmetric Super-GRIN lens," IEEE J. Sel. Top. Quant. Electron. **17**, 581-589, 2011.

127. C. Kopp, S. Bernabé, B. Ben Bakir, J. M. Fedeli, R. Orobtchouk, F. Schrank, H. Porte. L. Zimmermann and T. Tekin, "Silicon photonic circuits: on-CMOS integration, fiber optical coupling, and packaging," IEEE J. Sel. Top. Quant. Electron. **17**, 498-509, 2010.

128. T. H. Loh, Q. Wang, J. Zhu, K. T. Ng, Y. C. Lai, Y. Huang and S. T. Ho, "Ultra-compact multilayer Si/SiO2 GRIN lens mode-size converter for coupling single-mode fiber to Si-wire waveguide," Opt. Express **18**, 21519-21533, 2010.

129. J. F. Tao, A. B. Yu, H. Cai, W. M. Zhu, Q. X. Zhang, J. Wu, K. Xu, J. T. Lin, and A. Q. Liu, "Ultra-high coupling efficiency of MEMS tunable laser via 3-dimensional micro-optical coupling system." In IEEE Micro Electro Mechanical Systems, pp. 13-16, 2011

130. D. Miller, "Device requirements for optical interconnects to silicon chips," Proceedings of the IEEE **97**, 1166-1185, 2009.

131. M. Yano, F. Yamagishi and T. Tsuda, "Optical MEMS for photonic switching-compact and stable optical crossconnect switches for simple, fast, and flexible wavelength applications in recent photonic networks," IEEE J. Sel. Top. Quant. Electron. **11**, 383-394, 2005.

132. R. Heming, L. C. Wittig, P. Dannberg, J. Jahns, E. B. Kley and M. Gruber, "Efficient planar-integrated free-space optical interconnects fabricated by a combination of binary and analog lithography," IEEE/OSA J. Lightw. Technol. **26**, 2136-2141, 2008.

133. S. S. Lee, L. S. Huang, C. J. Kim, M. C. Wu, "Free-space fiber-optic switches based on MEMS vertical torsion mirrors," IEEE/OSA J. Lightw. Technol. **17**, 7-13, 1999.

134. M. C. Wu, L.Y. Lin, S. S. Lee and K. S. J. Pister, "Micromachined freespace integrated micro-optics," Sensor Actuat. A-Phys. **50**, 127-134, 1995.

135. D. Marcuse, "Loss Analysis of Single-Mode Fiber Splices," Bell Syst Tech J **56,** 703-718, 1977.

136. Yasser Sabry, Tarik Bourouina, Bassam Saadany, and Diaa Khalil, "In-plane diffraction loss free optical cavity using coated optical fiber and silicon micromachined spherical mirror" SPIE MOEMS-MEMS, Photonics West 2013, pp. 86160P-86160P (2013) .

137. Y. M. Sabry, D. Khalil, B. Saadany and T. Bourouina, "In-plane external fiber Fabry–Perot cavity comprising silicon micromachined concave mirror," J. Micro/Nanolith. MEMS MOEMS **13**, 011110 (2014).

138. Y. M. Sabry, D. Khalil, B. Saadany and T. Bourouina, "Three-dimensional collimation of in-plane-propagating light using silicon micromachined mirror", SPIE MOEMS-MEMS, Photonics West 2014, USA, February 2014.

139. N. Hodgson and H. Weber, Laser Resonators and Beam Propagation: Fundamentals, Advanced Concepts and Applications, Springer, 2005.

140. H. T. Yura and T. S. Rose, "Gaussian beam transfer through hard-aperture optics," Appl. Opt. **34,** 6826-6828, 1995.

141. J. Ye, T. W. Lynn, "Applications of optical cavities in modern atomic, molecular, and optical physics," Adv. At., Mol., Opt. **49**, 1-83, 2003.

142. X. Zhou and Q. Yu, "Wide-Range Displacement Sensor Based on Fiber-Optic Fabry–Perot Interferometer for Subnanometer Measurement," IEEE Sens. J. **11**, 1602-1606, 2011.

143. C. L. Lee, W. Y. Hong, H. J. Hsieh and Z. Y. Weng, "Air gap fiber Fabry–Pérot interferometer for highly sensitive micro-airflow sensing," IEEE Photonic. Tech. L., **23**, 905-907, 2011.

144. M. Zhang, L. L. Chen, C. Zhou, Y. Cai, L. Ren and Z. G. Zhang, "Mode-locked ytterbium-doped linear-cavity fiber laser operated at low repetition rate," Laser Phys. Lett. **6,** 657-660, 2009.

145. J. Stone and L.W. Stulz, "Pigtailed high-finesse tunable fibre Fabry-Perot interferometers with large, medium and small free spectral ranges," Electron. Lett. **23**, 781, 1987.

146. A. Muller, E. B. Flagg, M. Metcalfe, J. Lawall and G. S. Solomon, "Coupling an epitaxial quantum dot to a fiber-based external-mirror microcavity," Appl. Phys. Lett. **95**, 173101, 2009.

147. Y. Yeh and S. H. Park, "Fiber-optic tunable filter with a concave mirror," Opt. Lett. **37**, 626, 2012.

148. O. Kilic, M. J. Digonnet, G. S. Kino and O. Solgaard, "Asymmetrical spectral response in fiber Fabry–Perot interferometers," J. Lightwave Technol., **27,** 5648-5656, 2009.

149. A. E. Siegman, "Defining, measuring, and optimizing laser beam quality," In Proc. SPIE **1868**, p. 2, 1993.

150. A. E. Siegman, "New developments in laser resonators," In Proc. SPIE 1224, pp. 2–14, 1990.

151. S. Collins, "Analysis of optical resonators involving focusing elements," Appl. Opt. **3**, 1263-1276, 1964.

152. G. Massey and A. Siegman, "Reflection and refraction of Gaussian light beams at tilted ellipsoidal surfaces," Appl. Opt. **8**, 975-978, 1969.

153. J. Sokoloff, S. Bolioli, and P. Combes, "Gaussian beam expansion for radiation analysis of metallic reflectors illuminated under oblique incidence," IEEE Trans. Magn. **38,** 697-700, 2002.

154. A. Rohani, A. Shishegar and S. Naeini, "A fast Gaussian beam tracing method for reflection and refraction of general vectorial astigmatic Gaussian beams from general curved surfaces," Opt. Commun. **232,** 1-10, 2004.

155. J. Murphy, "Distortion of a simple Gaussian beam on reflection from off-axis ellipsoidal mirrors," Int. J. infrared Milli. **8**, 1165-1178, 1987.

156. A. Gomez-Vieyra and D. Malacara-Hernández, "Geometric theory of wavefront aberrations in an off-axis spherical mirror," Appl. Opt. **50**, 66-73, 2001.

157. H. Kogelnik and T. Li, "Laser Beams and Resonators," Appl. Opt. **5**, 1550-1566, 1966.

158. J. Murphy and S. Withington, "Perturbation analysis of Gaussian-beam-mode scattering at off-axis ellipsoidal mirrors", Infrared Phys. Technol. **37**, 205-219, 1996.

159. S. Withington, J. Murphy, and K. Isaak, "Representation Of mirrors in beam waveguides as inclined phase-transforming surfaces" Infrared Phys. Technol. **36**, 723-734, 1995.

160. T. Finn, N. Trappe, J. Murphy, S. Withington, "The Gaussian beam mode analysis of off-axis aberrations in long wavelength optical systems", Infrared Phys. Technol. **51,** 351–359, 2008.

161. TICRA Engineering Consultants, GRASP9 Technical Description, 2005.

162. R. Collin and F. Zucker, Antenna Theory parts 1 and 2, McGraw-Hill,1969.

163. P. Johansen, "Uniform physical theory of diffraction equivalent edge currents for truncated wedge strips", IEEE Trans. Antennas Propagat. **AP-44**, 989–995, 1996.

164. D. G. Voelz, Computational Fourier Optics: A MATLAB Tutorial, SPIE Press Book, 2011.

165. A. E. El Hady, Y. M. Sabry, M. Yehia, and D. Khalil, "Dual-fiber OCT measurements," SPIE BiOS, 2014.

166. H. Omran , Y. M. Sabry, M. Sadek, K. Hassan, M. Y. Shalaby, and D. Khalil, "MEMS optical tunable filter based on free-standing sub-wavelength silicon layers," SPIE MOEMS-MEMS, 2014.

Résumé Cette thèse a pour objectif ultime d'améliorer notre compréhension de la réflexion de la lumière sur des surfaces micro-courbes, en particulier lorsque les dimensions physiques des surfaces (rayons de courbure de l'ordre de 50-300 µm) sont comparables aux paramètres dimensionnels d'un faisceau optique Gaussien, typique des faisceaux issus d'une fibre optique ou d'un microlaser.
A cet effet, une étude théorique et des simulations numériques ont été menées ; elles ont été confrontées à une étude expérimentale. Pour ce faire, la réalisation des micro-miroirs à concavité contrôlée n'étant pas chose aisée, un premier jalon de cette thèse a consisté à atteindre les avancées technologiques nécessaires à la réalisation de tels micro-miroirs (par procédé de gravure plasma de type DRIE) en vue de leur caractérisation expérimentale.
Une motivation importante du choix de ce sujet est son potentiel applicatif à la réalisation de micro-bancs optiques sur puce silicium, de sorte à augmenter les capacités de couplage et de manipulation de lumière de façon intégrée dans un espace ultra-compact. A titre d'illustration des possibilités de la nouvelle micro-instrumentation optique que nous proposons, nous avons conçu et réalisé un microsystème de balayage spatial à grand angle (110°) d'un faisceau laser dont le spot optique ne se déforme pas tout au long de l'opération de balayage, ce qui en fait, entre autres, la pièce maitresse de systèmes portables d'imagerie médicale par tomographie à cohérence optique.

Mot-Clés : Micro-miroirs incurvés, acylindrique, asphérique, efficacité de couplage, micro-bancs optiques, photonique sur silicium, gravure DRIE 3D.

Abstract The ultimate objective of this thesis is to improve our understanding of light reflection on micro-curved surfaces, especially when the physical dimensions of the surfaces (radii of curvature in the order of 50-300 microns) are comparable to typical dimensional parameters of a Gaussian optical beam, such as those coming from an optical fiber or from a micro-laser.
To this end, a theoretical study and numerical simulations were conducted; they were confronted with an experimental study. To do this, the realization of micro-mirrors controlled concavity being not easy, a first step of this thesis was to achieve the technological advances necessary for the realization of such micro-mirrors (by plasma etching method of DRIE type) for their subsequent experimental characterization.
An important motivation for choosing this topic is its potential application in the production of micro-optical benches on a silicon chip, so as to increase the coupling efficiencies and capabilities of manipulation of light, in an integrated way and in an ultra-compact space. As an illustration of the new micro-optical instrumentation which is attainable, we have designed and implemented a micro-device able of wide-angle (110 °) spatial scanning of a laser beam, the optical spot being not deformed during the scanning operation, which makes this device, the centerpiece of portable medical imaging systems by optical coherence tomography, among others.

Keywords: Micro-curved mirrors, acylindrical, aspherical, coupling efficiency, micro-optical benches, Silicon photonics, 3D DRIE.